CHARACTERIZATION OF WATER OXIDATION CATALYSTS FOR IMPLEMENTATION IN A DYE-SENSITIZED PHOTOELECTROSYNTHESIS CELL (DSPEC)

KATHERINE E. MICHAUX

A dissertation submitted to the faculty at the University of North Carolina at Chapel Hill in partial fulfillment of the requirements for the degree of Doctor of Philosophy in the Department of Chemistry.

Chapel Hill
2015

Approved by:

Royce W. Murray

James W. Jorgenson

R. Mark Wightman

Alexander J. M. Miller

Andrew M. Moran

ABSTRACT

Katherine E. Michaux: CHARACTERIZATION OF WATER OXIDATION CATALYSTS FOR
IMPLEMENTATION IN A DYE-SENSITIZED PHOTOELECTROSYNTHESIS CELL (DSPEC)
(Under the direction of Royce W. Murray)

Chapter One is an introduction to solar energy conversion and the Dye-Sensitized

Photoelectrosynthesis Cell (DSPEC). It goes into detail about the development of the individual

parts of the DSPEC, including the semiconductor electrodes, photosensitizers and catalysts that

have been implemented in similar devices. It then gives a brief history of the use of iridium

oxide nanoparticles as water oxidation catalysts.

Chapter Two describes the film formation process for iridium oxide nanoparticles,

focusing particularly on the electroflocculation technique. Studies were performed which

determined the mechanism of electroflocculation, focusing on the short electroflocculation time

periods. Three different electroflocculation methods – constant potential, potential pulsing and

potential cycling – were implemented and the resulting iridium oxide nanoparticle films were

compared electrochemically and microscopically. Electroflocculation was also compared to

chemical flocculation and a direct pH change method of film formation.

Chapter Three is a general characterization chapter on iridium oxide nanoparticles,

using a variety of analytical techniques to probe the structure, surface chemistry and reactivity of

these nanoparticles. It probes the pH effect on electroflocculated NPs electrochemically and

relates it to its reactivity as a water oxidation catalyst. UV-Vis spectroelectrochemistry of the

iridium oxide nanoparticles is discussed and the individual spectra of each Ir oxidation state is

presented. Raman spectroscopy of the freely diffusing iridium oxide nanoparticles and

electroflocculated nanoparticles demonstrates the increase in crystallinity via electroflocculation. SEM demonstrates the morphology of the electroflocculated films. Change in surface charge of the iridium oxide nanoparticles with respect to pH is depicted with zeta potential measurements. Finally, XPS of various forms of the iridium oxide nanoparticles shows the different forms of iridium within the nanoparticles, likely distinguished by surface and core iridium sites.

Chapter Four details the behavior of iridium oxide nanoparticles in organic media through a few different methods. First, the behavior of an electroflocculated iridium oxide nanoparticle film is examined in an aprotic solvent, as well as the changes in the electrochemical behavior when a proton source is added. A hot injection thermal degradation synthesis of iridium oxide nanoparticles is also explored. Exchange into organic media via valeric acid capping ligands is discussed. This leads to the ferrocenation of the iridium oxide nanoparticles using a Click reaction with a phosphate terminated ligand. Electrochemical tagging of the iridium oxide nanoparticles elaborates on the surface chemistry and diffusion coefficient in aprotic media.

Chapter Five explores a dip-coated layer-by-layer synthesis of a chromophore-catalyst photoanode assembly consisting of a Ru(II) polypyridal dye and iridium oxide nanoparticle catalyst. Preparation of Ru(II) polypyridyl-iridium oxide nanoparticle (IrO_x NP) chromophore-catalyst assemblies on a FTO|*nano*ITO|TiO_2 core/shell by a layer-by-layer procedure is described for application in Dye Sensitized Photoelectrosynthesis Cells (DSPEC). Significantly enhanced, bias-dependent photocurrents with Lumencor 455 nm 14.5 mW/cm^2 irradiation are observed for core/shell structures compared to TiO_2 after derivatization with $[Ru(4,4'-PO_3H_2bpy)_2(bpy)]^{2+}$ (RuP_2) and uncapped IrO_X NPs at pH 1 and pH 5.8 in $HClO_4$ and $NaSiF_6$ buffers, respectively, with a Pt cathode. Photocurrents arising from photolysis of the resulting photoanodes,

FTO|$nano$ITO|TiO$_2$|-RuP$_2$,IrO$_2$, are dependent on TiO$_2$ shell thickness and applied bias, reaching 0.2 mA/cm^2 at 0.5 V vs AgCl/Ag with a shell thickness of 6.6 nm. Long term photolysis in the NaSiF$_6$ buffer results in a marked decrease in photocurrent over time due to surface hydrolysis and loss of the chromophore from the surface. Long term stability, with sustained photocurrents, has been obtained by Atomic Layer Deposition (ALD) of overlayers of TiO$_2$ to stabilize surface binding of -RuP$_2$ prior to the addition of the IrO$_X$ NPs.

Chapter Six focuses on the electrochemical characterization of three novel Ru(II) quaterpyridine complexes and the assessment of their potential for benzyl alcohol oxidation catalysis. The terminal ligands for these complexes are varied between CH$_3$CN, Cl and vinyl pyridine. Their electrochemical behavior in acetonitrile and aqueous media are reported. When dissolved in aqueous media, an exchange of the CH$_3$CN ligands with H$_2$O allows the complexes to reach higher oxidation states, suggesting potential for water oxidation catalysis. Benzyl oxidation catalysis is also explored; two of the three complexes are catalysts for this reaction.

To my brother, Woody. Thanks for growing up with me and tolerating my older sibling abuse. This dissertation is for you and I can't wait to read yours.

achievement of my graduate school career. I hope graduate school doesn't break you and that you're able to mentor a student who is even half as brilliant as you are.

To all of the scientists I've had the opportunity to collaborate with through the Energy Frontier Research Center for Solar Fuels at UNC – thank you. You have my deepest gratitude. This includes, but probably isn't limited to, Paul Giokas, Dennis Ashford, Rob Binstead, Leila Alibabei, Ben Sherman, Kyle Brennaman and Alex Lapides. These experiences have prepared me for my career in ways you can't imagine.

To all of my friends, both from home and here at UNC – I would never had made it through these past five years without you. I would especially like to thank James Treadway, Will Black, Katie Moga and Jenna Ogden. James – Our late night study sessions with Moga are what got me through our first year of grad school. For that and your incredibly patience, I will be forever grateful. Will – You have been a wonderful friend. I will always cherish our bourbon drinking and Derby parties and I can't wait to trash talk you in 2020 when VT beats Michigan. Moga – I don't know what I would've have done in graduate school without my other Katie. I'm sure I would've given up long ago. After all, we do come in pairs. I hope, one day, we're able to finish Covert Affairs. JMO – While there have been over 700 miles between us, I am so thankful for all of the time we've been lucky enough to spend together. You are my best friend and your support has meant the world to me. You have been the one person who was never afraid to tell me the truth, even when I was about to run my car into a bush. I excitedly await for the day when we finally live in the same city again.

To my incredible family, including, but not limited to, my parents, my brothers, my sister and my grandparents. Mom and Dad – Thank you for your daily encouragement and advice. I really appreciate you instilling in me that I can do anything I set my mind to. Thank you for still

taking my phone calls, even if I do call you excessively. Grandma, Papa S. and Papa M. – You are all wonderful inspirations in everything you do. I love every visit that I get with you and look forward to visiting more often once I'm done with school. Thank you for being the best role models a person could ask for, both personally and professionally. Woody – You are an inspiration. Your hard work in everything you do has been my motivation to finish this thing. As I said in the dedication, I look forward to reading your dissertation one day, even if it is in physics. Sidney – Thank you for sending me daily pictures of cats. I hope it's not too sad to say that they're the highlight of my day. I am so proud of you. You're going to make a wonderful physical therapist. Last, but certainly not least, Chip – You are a hoot. Thank you for FaceTiming me any time you find your way to an iPad. I love our conversations about science and I hope that you keep your natural curiosity through the rest of your life.

To my fiancé Brendan – I don't even know if I can put into words how much your support has meant to me. It has been so wonderful to have you as my friend and partner over the past five years. You were the one who had to listen to all of my self-doubt and every time I thought I should give up. Each and every time you told me exactly what I needed to hear, whether or not I wanted to hear it at the time. It has been an incredible experience going through this journey with you. I am so excited to see where the next step takes us. Maybe one day, we'll even get married.

And finally, I would like to thank Panera Bread Company. 90% of this dissertation was written at a table in one of their restaurants and I can confidently say it would never have come to fruition without. I would particularly like to thank the unnamed employee who helped me clean up my mess when I spilled water on my computer five days before my dissertation was due. You are a kind and thoughtful person, wherever you are.

LIST OF SCHEMES

LIST OF ABBREVIATIONS AND SYMBOLS

A	Area of the Electrode
A (unit)	Ampere
Å	Angstrom
AFM	Atomic Force Microscopy
$AgBF_4$	Silver Tetrafluoroborate
Ag/AgCl	Silver/Silver Chloride Reference Electrode
ALD	Atomic Layer Deposition
Al_2O_3	Aluminum Oxide
Ar	Argon
Au	Gold
BDD	Boron Doped Diamond Electrode
BF_4^-	Tetrafluroborate Anion
BnOH	Benzyl Alcohol
bpy	2,2'-bipyridine
BTU	British Thermal Unit
C	Carbon, Elemental
C_O	Concentration of the Catalyst
C_S	Concentration of the Substrate
ca.	Circa
CAN	Cerium Ammonium Nitrate
Ce	Cerium
Cd	Cadmium

Ce(OH)$_3$	Cerium (III) Hydroxide
CH$_4$	Methane
CH$_3$CH$_2$OH	Ethanol
CHCl$_3$	Chloroform
CH$_3$CN	Acetonitrile
CH$_3$OH	Methanol
Cl	Chloride, Chloro
cm	Centimeter
cm^{-2}	Inverse Centimeter
Co	Cobalt
CO$_2$	Carbon Dioxide
Co$_3$O$_4$	Cobalt Oxide
Cu	Copper
CuSO$_4$	Copper Sulfate
CV	Cyclic Voltammetry
D	Diffusion Coefficient in cm^2/s
dia.	Diameter
DCM	Dichloromethane
DMF	Dimethylformamide
DMSO	Dimethyl Sulfoxide
dpp	2,0-di(pyrid-2'-yl)-1,10-phenanthroline
dppi	3,6-di-(4-methylpyrid-2-yl) pyridazine
DPV	Differential Pulse Voltammetry

DSA	Dimensionally Stable Anode
DSPEC	Dye-Sensitized Photoelectrosynthesis Cell
DSSC	Dye-Sensitized Solar Cell
e^-	Electron
E	Potential
E^0	Formal Potential
$E_{1/2}$	Measured Half-Wave Potential in Cyclic Voltammetry
E_p	Measure Peak Potential
EC'	Electrochemical Reaction Followed by a Chemical Reaction
EDS	Energy Dispersive X-Ray Spectroscopy
EIROF	Electrodeposited Iridum Oxide Film
eQCM	Electrochemical Quartz Crystal Microbalance
ET	Electron Transfer
EtOH	Ethanol
eV	Electron Volt
EXAFS	Extended X-Ray Absorption Fine Structure
F	Faraday's Constant, 96485 coulombs/mole
Fc	Ferrocene
Fc^+	Ferrocenium
$FcIrO_X$	Ferrocenated Iridium Oxide Nanoparticles
Fe	Iron, Elemental
Fe_2O_3	Iron Oxide
Fe_3O_4	Iron Oxide

FTO	Fluorine-Doped Tin Oxide
FTO│*nano*ITO	Nanoscopic Tin-Doped Indium Oxide Film on a Fluorine-Doped Tin Oxide Coated Glass Slide
Ga	Gallium
GaP	Gallium Phosphide
GC	Glassy Carbon Electrode
H^+	Proton
H_2	Hydrogen, Molecular
$HClO_4$	Perchloric Acid
HER	Hydrogen Evolution Reactoin
HNO_3	Nitric Acid
HPT	Hydride Proton Transfer
hr	Hour
hr^{-1}	Inverse Hour
H_2O	Water
H_2O_2	Hydrogen Peroxide
HOMO	Highest Occupied Molecular Orbital
H_2SO_4	Sulfuric Acid
H_2PO_3	Phosphonic Acid
H_3PO_4	Phosphoric Acid
$H_2PO_4^-$	Monobasic Phosophate Anion
HPO_4^{-2}	Dibasic Phosphate Anion
PO_4^{-3}	Tribasic Phosphate Anion
i_c	Catalytic Current

i_L	Limiting Current for a Catalytic Reaction
i_{lim}	Limiting Current for a Microelectrode CV Experiment
i_p	Peak Current
I_{SS}	Steady-State Current
In	Indium
iR	Current Times Resisitance
Ir	Iridium, Elemental
Ir^{III}	Iridium (III) Oxidation State
Ir^{IV}	Iridium (IV) Oxidation State
Ir^{V}	Iridium (V) Oxidation State
Ir^{VI}	Iridium (VI) Oxidation State
$Ir^{IV/III}$	Iridium 3+, 4+ redox couple
$Ir^{V/IV}$	Iridium 4+, 5+ redox couple
Ir $4f_{5/2}$	Iridium $4f_{5/2}$ Electron Orbital
Ir $4f_{7/2}$	Iridium $4f_{7/2}$ Electron Orbital
$Ir(acac)_3$	Iridium Acetylacetonate
$[IrCl_6]^{-2}$	Iridium(IV) Chloride Anion
IrO_X	Iridium Oxide Nanoparticles
$IrO_X \cdot nH_2O$	Hydrated Iridium Oxide Nanoparticles
IrO_2	Iridium Oxide, Bulk Material
$[Ir(OH)_6]^{-2}$	Iridium(IV) Hydroxide Anion
ITO	Tin-doped Indium Oxide
j	Current Density

j_0	Exchange Current Density
k	Boltzmann Constant in J/K
k_{cat}	Catalytic Rate Constant
k_{obs}	Observed Rate Constant
K_2IrCl_6	Potassium hexachloroiridate
L	Liter
LED	Light Emitting Diode
LUMO	Lowest Unoccupied Molecular Orbital
M	Molar (mol/L)
mA	Milliamp
mC	Millicoulomb
Mebimpy	2,6-bis(1-methylbenziidazol-2-yl)pyridine
MeCN	Acetonitrile
mg	Milligram
$MgSO_4$	Magnesium Sulfate
MHz	Megahertz
min	Minute
mL	Milliliter
mM	Millimolar (mmol/L)
mmol	Millimole
mol	Moles
mV	Millivolt
mW	Milliwatt

n	Number of Electrons
n_c	Number of Electrons Involved in the Catalytic Reaction
n_p	Number of Electrons Involved in the Peak Reaction
N	Number of Moles
N_2	Nitrogen, Molecular
Na	Sodium
$NaHCO_3$	Sodium Bicarbonate
NaN_3	Sodium Azide
*nano*ITO	Nanoscopic Tin-Doped Indium Oxide Films
NaOH	Sodium Hydroxide
Na_2SiF_6	Sodium Hexafluorosilicate
$(NH_4)_2Ce(NO_3)_6$	Cerium Ammonium Nitrate
NHE	Normal Hydrogen Electrode
Ni	Nickel
NiO	Nickel Oxide
N_3IrO_x	Iridium Oxide Nanoparticles with Azide Terminated Capping Ligand
nm	Nanometer
NP	Nanoparticles
O	Oxygen, Elemental
O_2	Oxygen, Molecular
OER	Oxygen Evolution Reaction
Os	Osmium
PCET	Proton Coupled Electron Transfer

PEC	Photoelectrolysis Cell
PhCHO	Benzaldehyde
PhCHOH	Benzyl Alcohol
pic	Picoline
PMAA	Poly(methacrylic acid)
PO_4^{-3}	Phosphate Anion
$POCl_3$	Phosphoryl Chloride
PSII	Photosystem II
Pt	Platinum
Q	Charge in coulombs
QCM	Quartz Crystal Microbalance
qpy	Quaterpyridine
r	Hydrodynamic Radius of a Nanoparticle
r_0	Radius of a Microdisk Electrode
R	Gas Constant in J/mol K
Rh	Rhodium
RHE	Reversible Hydrogen Electrode
RMS	Root Mean Square
rpm	Rotations Per Minute
RRDE	Rotating Ring Disk Electrode
RT	Room Temperature (ca. 25 °C)
Ru	Ruthenium
RuO_2	Ruthenium Oxide

RuP$_2$	[Ru(4,4'-PO$_3$H$_2$bpy)$_2$(bpy)]$^{2+}$
s	Second
[S]$_{bulk}$	Concentration of Substrate in Bulk Solution
SAM	Self-Assembled Monolayer
SEM	Scanning Electron Microscopy
Si	Silicon
SIROF	Sputtered Iridium Oxide Films
SnO$_2$	Tin Oxide
Sn:In$_2$O$_3$	Tin-Doped Indium Oxide (ITO)
T	Temperature
TBAOH	Tetrabutylammonium Hydroxide
TBAP	Tetrabutylammonium Perchlorate
TBAPF$_6$	Tetrabutylammonium Hexafluorophosphate
TDMAT	Tetrakis(dimethylamido)titanium
TEM	Transmission Electron Microscopy
TFA	Trifluoroacetic Acid
THF	Tetrahydrofuran
Ti	Titanium
TiO$_2$	Titanium Dioxide
TO	Turnover
trpy	2,2′:6′,2″-terpyridine
UV-Vis	Ultraviolet-Visible Spectroscopy
V	Volts

VP	Vinyl Pyridine
WE	Working Electrode
WO_3	Tungsten Oxide
WOC	Water Oxidation Catalyst
XANES	X-Ray Absorption Near Edge
XAS	X-Ray Absorption Spectroscopy
XPS	X-Ray Photoelectron Spectroscopy
vs.	Versus
ZnO	Zinc Oxide
α	Transfer Coefficient
Γ_{cat}	Coverage of Catalyst
Γ_{Ir}	Coverage of Iridium in mol/cm^2
ΔE_p	Difference in Potential of the Oxidative and Reductive Peak for a Redox Couple
ΔG	Gibbs Free Energy
η	Viscosity in cP
μA	Microamp
μg	Microgram
μL	Microliter
μm	Micrometer
μM	Micromolar
ν	Scan Rate
ω	Rotation Rate
% w/w	Percent weight by weight

°C   Degrees Celsius

CHAPTER 1: Introduction to the Dye-Sensitized Photoelectrosynthesis Cell (DSPEC)

1.1 SOLAR ENERGY AS A RENEWABLE SOURCE

Over the past few decades, the global energy demand has significantly increased due to growing economies, advances in technology and increased access to that technology. Figure 1.1, from the International Energy Outlook of 2013 published by U.S. Energy Information Administration, depicts this trend and further predicts how this demand will increase through 2040.[1] There is need for a renewable efficient energy source to meet this perpetually increasing demand.

Research has focused on developing and improving renewable energy sources, such as wind, hydroelectric and solar energy sources. As almost 600 quadrillion BTU hits the earth's surface every hour directly from the sun, improving solar energy conversion techniques to harvest this energy has been a major focus of current research. Photovoltaic devices are the current technology that has reached commercial use. However, their use of semiconductor material limits the maximum efficiency at which these devices can function. This limit is based on the Shockley-Quiesser limit, and the maximum efficiency of a silicon photovoltaic device is ca. 29%.[2] Most modern photovoltaic cells are close to achieving this value. On top of this, they also present the dilemma of their electrical output being directly proportional to the influx of sunlight. As the majority of energy consumption occurs at times after the sun has set, a method of storing this energy must also be obtained.
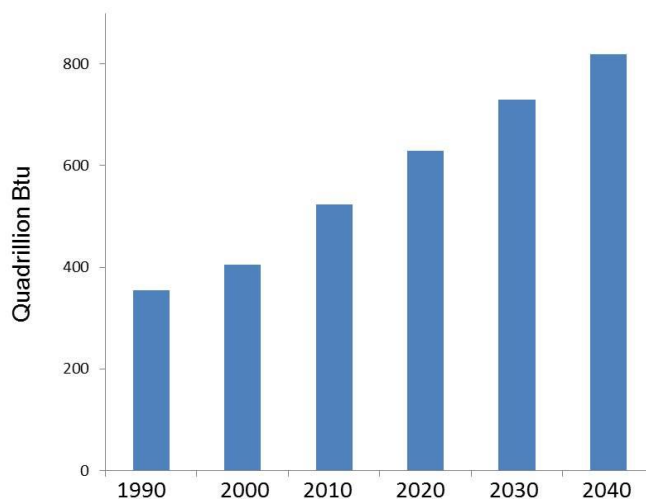
Figure 1.1: Annual global energy demand by decade since 1990, as well as the predicted increase over the next 35 years.

Battery materials have been proposed as a storage method for solar energy. Most recently, Tesla Motors announced the production of at-home versions of their car batteries, Powerwall©, that can pair with photovoltaic materials for solar energy storage.[3] However, the materials for such high power density batteries can become quite expensive. Batteries are also prone to losing their charging and discharging ability over time, largely due to loss of structural integrity of the cathodes and anodes. An alternative to this is to use a different method of storing solar energy, by mimicking plants and storing this energy in chemical bonds, as is done in photosynthesis.

One of the most sought after reactions for storing energy in chemical bonds is the splitting of water into molecular oxygen and hydrogen. Per its mass, hydrogen has one of the highest energy densities of any molecule. As a fuel, it has the added benefit of producing water as its only side product, eliminating the production of greenhouse gases. Generating hydrogen from the splitting of water involves two half reactions: the oxidation of water to oxygen gas and protons and the reduction of those protons to hydrogen gas. The major obstacle in this reaction is the large activation energy of water oxidation required in the thermodynamically uphill

reaction. While the free energy change (ΔG) of this reaction corresponds to 1.23 eV, an energy within the solar spectrum, it often requires more energy (i.e. overpotential, η) due to a large kinetic obstacle from the multielectron process. This large overpotential results in a need for either a semiconductor with a large enough band gap energy to compensate for this increase in energy requirement or a catalyst to lower the overpotential of the water oxidation reaction.

The semiconductor requirements for water splitting involve a large band gap energy, a conduction band energy with a potential more negative than the formal potential (E^0) of the H^+/H_2 reaction and a valence band energy with a potential more positive than the formal potential of the O_2/H_2O reaction. One such material that fits these requirements is TiO_2, which has a band gap of ca. 3 eV. In 1972, Honda and Fujishima first demonstrated solar water splitting via illumination of a TiO_2 semiconductor photoanode coupled with a Pt cathode.[4] However, the conduction band of TiO_2 is just barely more negative than that of the proton reduction reaction, which leads to slow overall water splitting. Finding a semiconductor material that is efficient and stable in the conditions for both the oxygen evolution reaction (OER) and the hydrogen evolution reaction (HER) has been a challenge. Because of this, dual band gap cells have been explored, where a p-type semiconductor material is combined with an n-type semiconductor material to more efficiently split water.[2] The use of two different semiconductor materials in one cell with complementary band gaps to absorb different regions of the solar spectrum results in an increase of overall efficiency of these devices.
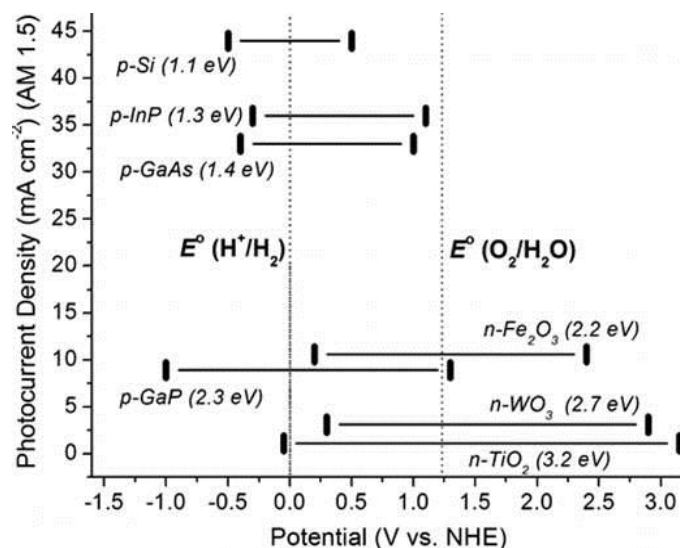
Figure 1.2: Band gaps of common semiconductor materials. The negative limit on the left corresponds to the conduction band energy and the positive limit on the right corresponds to the valence band energy. The dotted lines represented the potentials required for water oxidation and proton reduction.

The development of photocathode semiconductor materials has largely focused on phosphide, sulfide, telluride and selenide materials, consisting of various ratios of Ga, Cd and In.[5,6,7,8,9,10,11,12,] This focus is due to their conduction band being sufficiently negative, as shown in Figure 1.2. Due to the large overpotential, the addition of a Pt catalyst to the semiconductor/liquid interface has been implemented.[5a,13] It was found that using catalytic metal particles, instead of a metal film, improved efficiency for H_2 production, likely because a continuous metal film blocks light absorption by the semiconductor. By limiting the coverage of the catalyst to island-like structures, the electrode material is essentially transparent.[2]

Conversely, photoanode semiconductor materials for water oxidation have been largely oxide based. The valence band on these materials consist of O 2p orbitals, with the valence orbitals of the metals serving as the conduction band.[2] Because of this, the valence band of these materials are all very similar, while the conduction band is varied based on which metal ions are present; examples include TiO_2, Fe_2O_3, WO_3 and ZnO (Figure 1.2).[14,15] Because the valence

band energies tend to be significantly higher than the OER potential, the excess energy that is absorbed escapes via thermal relaxation, resulting in poor efficiency.

Unassisted solar water splitting has been widely reported using a combination of the n-type TiO_2 semiconductor electrode combined with the p-type GaP.[16,17,18,19,20] Efficiencies up to 1% were reported, largely due to the instability of the p-GaP photocathode. These were all examples of some of the first photoelectolysis cells (PEC). Combination of a PEC device with a photovoltaic (PV) device has also been explored, where the light that isn't absorbed by the PEC semiconductor is instead absorbed by the PV. This provides a bias that is required to split water.[21]

In a similar manner, Grätzel combined a dye-sensitized solar cell (DSSC) with a WO_3 photoanode to increase efficiency.[22,23,24] DSSC devices generally contain a high surface area semiconductor, such as TiO_2, with dyes bound to the surface to absorb light and inject the resulting excited electron into the semiconductor material. This, in turn, can create a bias which is sufficient to split water. By implementing a molecular dye, DSSC devices incorporate a material with a tunable absorption.[25] It is difficult to control the band gap energies of metal oxide semiconductor materials. Organometallic complexes, however, have much greater tunability, as changing the metal center and surrounding ligands can adjust the lowest unoccupied molecular orbtail (LUMO) and highest occupied molecular orbital (HOMO). Manipulating the structure of these complexes or organic dyes can be seen as the equivalent of changing the band gap of the semiconductor material. With the addition of a dye, the absorption characteristic of the device can be shifted towards the visible region of the solar spectrum and the need for an external bias can be decreased or eliminated.[26]

DSSC devices have other advantages as well. The implementation of the dye splits the duties of the semiconductor material. The dye serves the purpose of absorption, while the semiconductor electrode's sole responsibility is charge separation of the injected electron and the resulting holes. Most DSSC devices implement a high surface area, mesoporous semiconductor structure, which results in high loading of the dye,[27] and use TiO_2 as their base, which is a relatively cheap material, reducing cost of the overall device.[28,29,30] Because of this, they also are simple to fabricate, lightweight and are flexible in design.[25] The use of a dye attached to mesoporous semiconductor base has also been applied to the photocathode as well, with NiO serving as the base.[31,32,33,34,35] The combination of both an n-type DSSC with a p-type DSSC has also been explored for its advantages. By manipulating the absorption of each dye molecule so that they're complementary to each other, the theoretical maximum efficiency is greater than 40%, significantly higher than a single device.[25] Currently, the efficiency is much less ideal, but strides have been made to further improve the function of these devices.

While strides have been made to improve the stability and efficiency of photoanode and cathode materials for water splitting, the large overpotentials required, especially for water oxidation, result in higher energy requirements needed for water splitting. To reduce these high overpotentials, electrocatalysts have been added on the surfaces of both semiconductor electrodes. Pt has proven to be the ideal electrocatalyst for the HER, with a low overpotential of 50 mV at 10 mA/cm^2. Electrocatalysts for the OER have proven to be more elusive; some examples of these are discussed in Section 1.4. The DSSC, when combined with electrocatalysts for water oxidation and reduction, leads to the development of the Dye-Sensitized Photoelectrosynthesis Cell (DSPEC), discussed below.

1.2   THE DYE-SENSITIZED PHOTOELECTROSYNTHESIS CELL (DSPEC)

The Dye-Sensitized Photoelectrosynthesis Cell (DSPEC) was originally proposed by

Thomas J. Meyer in 2005.[36] The goal of these devices is to take common resources, such as

H_2O and CO_2 and yield a fuel entirely from sunlight to store solar energy for later use. This

device consists of two semiconductor electrodes with chromophore catalyst assemblies, as

pictured in Figure 1.3. At the photoanode, a chromophore is excited via sunlight and injects an

excited electron into the semiconductor material. The chromophore then oxidizes the catalyst,

attached by a bridging ligand, which in turn oxidizes water to O_2 and H^+. The protons then travel

across a membrane to the photocathode, where they are reduced to some type of fuel by another

chromophore-catalyst assembly. The fuel that is produced can be manipulated based on what

catalyst is present at the cathode. Examples include H_2, CH_4, CH_3OH and CH_3CH_2OH. The

example shown in Figure 1.3 illustrates the flow of electrons throughout the device, from the
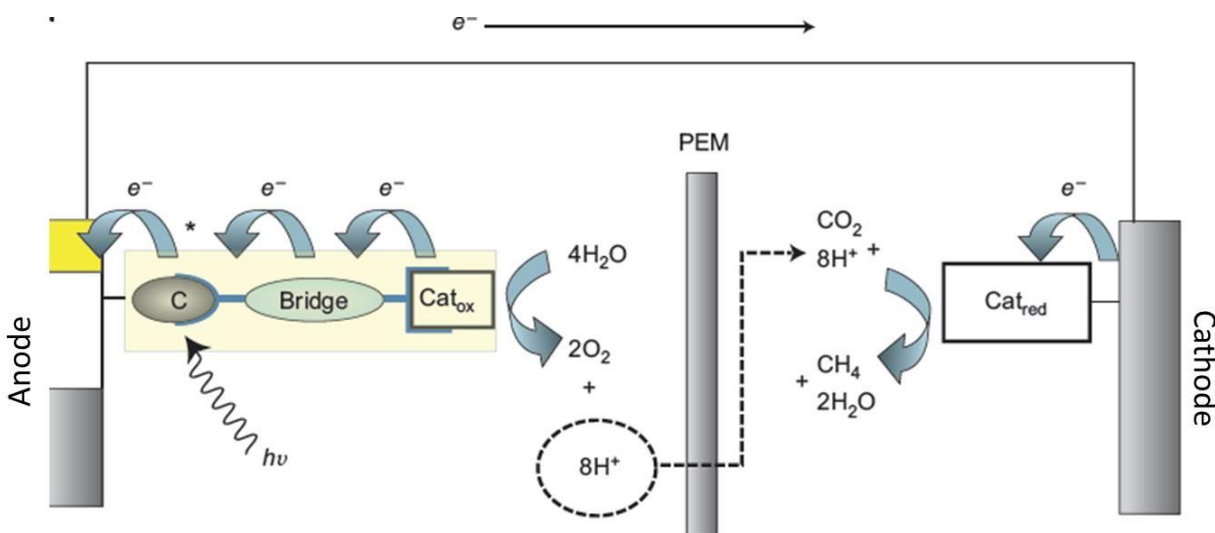
Figure 1.3: Schematic of the Dye-Sensitized Photoelectrosynthesis Cell, where sunlight is used to oxidize water and use the resulting protons to reduce CO_2 to CH_4.

7

excitation of the photoanode chromophore over to the photocathode, where the catalyst specifically reduces CO_2 and H^+ to form CH_4.

DSPEC devices are very similar in structure to the DSSC devices discussed above. They both consists of the mesoporous semiconductor material for high surface area electrodes, as well as high loading concentrations of each dye. The major difference between the two is the addition of electrocatalysts at both the photoanode and photocathode in the DSPEC. DSSC devices use an electron mediator in order to regenerate the ground state of each dye. In a DSPEC, the catalyst is responsible for regenerating the ground state of the dye. On the photoanode side of the device, the catalyst reduces the chromophore back to its ground state by donating an electron. After successive electron donations, the catalyst then oxidizes the desired reagent, in this case water, to form molecular O_2 and H^+. This dependence on the catalyzed reaction to regenerate the chromophore is what distinguishes the DSPEC from the DSSC.

There are major challenges to be overcome on both sides of the DSPEC device, including efficient absorption by the chromophore, limiting back electron transfer within the system, photoanode and photocathode stability and lowering the overpotential required for both the cathodic and anodic reactions.[26,37,38,39] As the topic of this dissertation focuses on the photoanode half of this device, this introduction will focus on the development of that half of the device.

1.3 THE PHOTOANODE

There are many requirements for the photoanode and its individual parts that must be met, in order for the DSPEC device to function and split water.[24,40,41, 42,43,44,45,46,47,48,49,50] The first condition is relatively obvious: the semiconductor electrode, photosensitizer dye and water oxidation catalyst must all be photo- and electrochemically stable under the conditions of the

8

device. This is easier said than done, as the stability conditions for the dye can be very different than those for the catalyst and the semiconductor material. The second requirement is that the sensitizer must absorb in the visible part of the solar spectrum, in order to maximize how much of the light is going to towards water splitting and not waste. Ideally, the dyes would be fixed to the semiconductor surface by a linker that is stable under aqueous conditions. Finally, the HOMO and LUMO of the dye must be at sufficient energies for the flow of electrons that is required for water oxidation in this setup. The HOMO must be at a potential more positive than of the onset of water oxidation for the particular catalyst it is paired with. Conversely, the LUMO energy level must be more negative than the conduction band of the semiconductor in order to be able to inject excited electrons.

Examples of some popular chromophores in the literature that have been utilized in DSSC and DSPEC devices are featured in Figure 1.4.[26] All of these dyes incorporate highly conjugated pi systems for efficient molecular absorption in the UV-Visible region of the solar spectrum and then electron transfer into the desired semiconductor surface. Most of the dyes consist of polypyridal ligands paired with Ru centers and are derivatized from $[Ru(bpy)_3]^{2+}$, a gold standard for a chromophore in these types of devices. Most importantly, all of these photosensitizers have a linker which can anchor them to the metal oxide semiconductor surface. The linkers are generally either carboxylic acid or phosphonic acid groups, which are known to interact with metal oxide surfaces. Carboxylic acids are generally considered a weaker interaction than the phosphonic acid groups, which form covalent bonds with metal oxide surfaces. Phosphonic acid groups, however, are prone to hydrolysis attack as pH increases.[51] Because of this, significant research has been focused on ways to further stabilize the chromophore linkage to the semiconductor surface, especially in higher pH media, where the

thermodynamic potential of water oxidation is shifted to more negative potentials and should

require less potential bias to proceed.
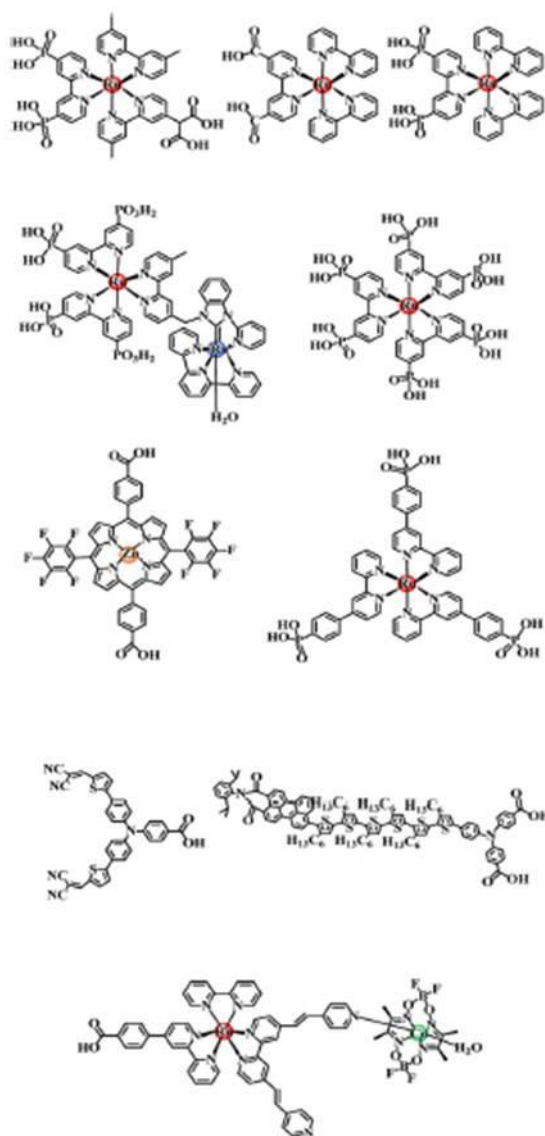
Figure 1.4: Examples of the structures of commonly used chromophores for DSSC and DSPEC devices.

Stabilization of these linkers has been thoroughly explored. One proposed method is to

cover the chromophore with an electronically and ionically conductive material, such as Nafion

or other electropolymerized films.[52] Modifying the ligands of the chromophores to include vinyl

groups is another method. When the potential of an electrode is cycled with these chromophores

10

freely diffusing in solution, the vinyl groups will polymerize and form a film on the electrode surface, stabilizing the chromophore in the process.[53,54,55,56,57] More recently, physically blocking the anchoring group with a metal oxide material, such as Al_2O_3 or TiO_2, has been explored.[58,59,60,61,62,63,64,65,66,67] Atomic layer deposition was implemented in order limit the metal oxide film growth to less than 1 nm in thickness. By limiting film growth to this thickness, the linker is covered, but not the entire chromophore, in order to maintain both the maximum absorption and ET to the catalyst.. These thin films have shown promise is stabilizing phosphonic acid groups at pH values up to 13.[68]

Improvements in the semiconductor electrode have also been made by altering the structure. Nanostructured semiconductors, such as rods, have shown enhancement in photocurrent.[69,70] This is due to the decreased path length for the excited electron to travel from injection to the conductive circuit. Because this is shorter, there is less chance of recombination.[3] Core/shell electrodes have also been developed, which involve a thin semiconductor shell surrounding a conductive core. [71,72] This maintains the high surface area of the mesoporous titania with nanostructured optically transparent conductive materials such as tin-doped indium oxide.[74] The thin semiconductor layer limits back electron transfer to the dye and improves electron injection into the circuit.

1.4 CATALYSTS FOR WATER OXIDATION

Choosing the right catalyst for water oxidation is imperative for improving the overall efficiency for a DSPEC device. One of the major hurdles in developing an effective device is the overpotential required for water oxidation. A higher overpotential results in an increase in the energy required for reaction to proceed, meaning less of the solar spectrum can be employed. By implementing a water oxidation catalyst with a lower overpotential, light with longer

wavelengths, i.e. in the visible region and near IR region, have the potential to be used to split water. This improves the solar energy conversion efficiency, as more of the solar spectrum can be applied towards water splitting.

There are two major requirements for an efficient water oxidation catalyst.[2] The first is that it must be able to create a sufficient amount of O_2, at a low overpotential, i.e. this reaction should occur at the rate at which the chromophore is injecting electrons into the semiconductor electrode. This means electron transfer must be fast between the chromophore and catalyst and within the catalyst to oxidize water. The other condition is that the catalyst must be photo- and electrochemically robust under the conditions of water oxidation for extended periods of time. Both molecular, homogeneous catalysts and heterogeneous catalysts have been explored. This dissertation delves into the characterization of IrO_X NPs, a heterogeneous water oxidation catalyst, and three new Ru polypyridal complexes, which have shown potential as water oxidation catalysts.

1.4.1 Homogeneous Catalysts

Orginially, catalysts for water oxidation were synthesized to structurally mimic Photosystem II (PSII), the main player in natural photosynthesis that produces oxygen gas (O_2). In this system, O_2 is generated from splitting water molecules. H_2O is oxidized by manganese sites within the complex that are bonded together by μ-oxo bridges. Using this as an inspiration, various mono-, di-, tri- and tetrametallic complexes have been suggested as catalysts using ruthenium, manganese, rhodium, osmium and iridium metal centers.[74,75,76,77,78,79,80,81,82,83,84,85,86,87,88,89,90,91,92,93] They have polypyridal ligands, such as bipyridine, tripyridine, and phenanthraline which are good oxidizers due to their ability to accept electrons in the conjugated pi system and transfer them to the metal centers. Some of the more prominent molecular catalysts are featured in Figure 1.5.

12
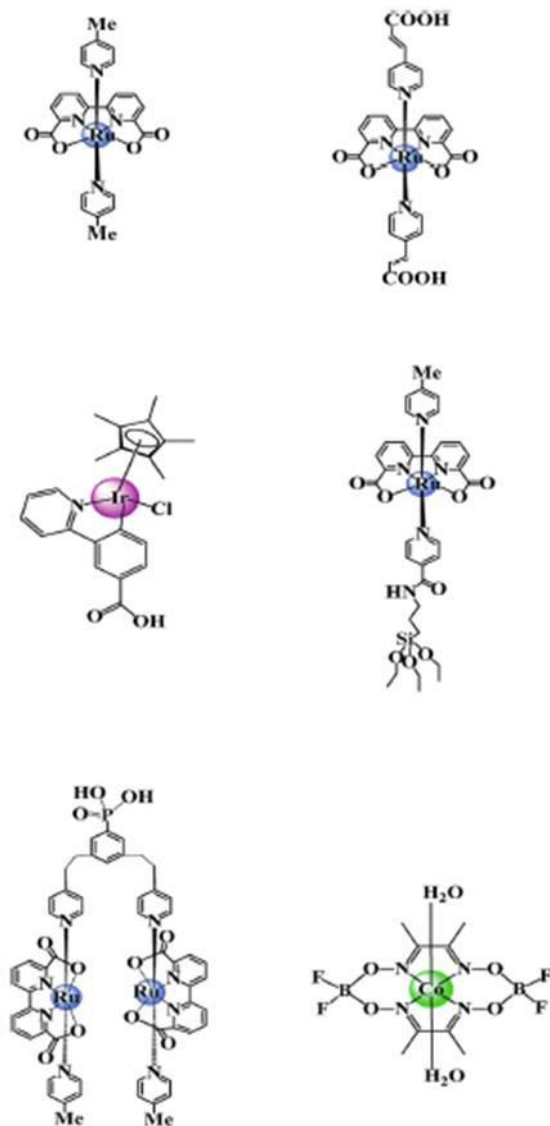
Figure 1.5: Examples of more recent molecular complexes that have served as water oxidation catalyssts.

All of these molecular catalysts consist of a metal center that can access high oxidation states, such as 4+, 5+ or higher. These high oxidation states are required for water oxidation catalysis. Organometallic complexes which cannot access these states have repeatedly shown lack of catalytic activity.[26] A relatively new trend in research has been to synthesize seven coordinate Ru complexes, where there is an open site on the metal center that can react with H_2O. Licheng Sun et al. has observed fast water oxidation rates with Ce(IV) as a chemical oxidant with complexes with this structure, seen in the top two complexes in Figure 1.5, although

13

their stability as a monomer has been questioned. Ir complexes, such as the one in the middle of Figure 1.5, have also shown promise as water oxidation catalyts. However, their stability is limited and they have shown to decompose into the heterogeneous water oxidation catalyst, iridium oxide nanoparticles (IrO$_X$ NPs).[75, 76, 88]

The most successful molecular water oxidation catalysts developed have largely consisted of precious metal centers, such as Ru, Rh, Ir and Os. However, there has been a push recently to explore complexes derived of first row transition metals, such as Co, Cu, Ni and Fe, in order to reduce the cost of the DSPEC devices.[94,95,96,97,98,99,100] The Meyer laboratory, in particular, has had luck with Co, Cu and Fe complexes showing water oxidation electrocatalytic properties. The overpotentials for these complexes, however, need to be much higher than their Ru complex equivalent in order to observe the same rate of activity.

1.4.2   Metal Oxide Heterogeneous Catalysts

While these systems are able to catalyze the water oxidation reaction, they are complex to synthesize, requiring multiple step syntheses, especially in the case of the tri- and tetrametallic complexes. An alternative and still effective catalyst choice is a metal oxide heterogeneous catalyst. Due to the high density of oxygen sites on the surface of these materials, they have a propensity towards water oxidation catalysis. However, it has been found that not all metal oxides catalyze water oxidation to the same extent. Rasiyah and Tseung proposed in 1984 that redox potentials for the metal oxidation states in the materials affect their ability to effectively oxidize water.[101] Those whose redox potentials closely aligned with the formal potential of the water oxidation reaction would have the highest activity. They were able to establish a linear relationship between the redox couple potentials of the metal oxide catalysts and the overpotential required for water oxidation catalysis. A volcano plot, depicted in Figure 1.6, demonstrates the relationship between the overpotential required for water oxidation catalysis

and the metal-oxygen bond strength at the surface of these materials. Essentially, there is a

minimum overpotential reached with the materials whose metal-oxygen bond strength is ca. -100

kJ/mol, with the ideal materials being RuO_2 and IrO_2. For those materials whose bond strength

is more positive than the maximum, the materials are less readily oxidized, thereby increasing

the overpotential required for water oxidation. Those with more negative bond strengths are

very easily oxidized, which results in an abundance of the absorbed intermediate and thus an

increased overpotential.

While less expensive materials, such as Co_3O_4, NiO_2 and Fe_2O_3 have been explored as

water oxidation catalysts,[102,103,104,105,106,107,108,109] they have yet to achieve comparable activity to

their more expensive counterparts. Both IrO_2 and RuO_2 are currently used as commercially

available dimensionally stable anodes (DSAs), where they are thermally deposited onto a metal
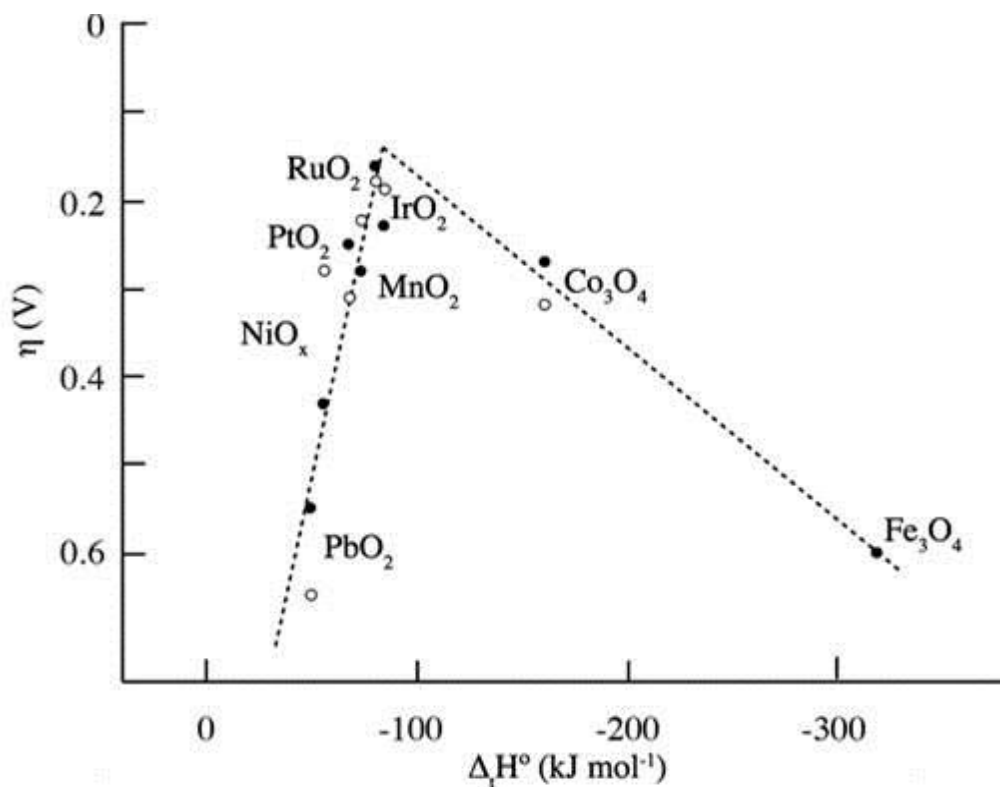
Figure 1.6: "Volcano plot", developed by S. Trasatti, relating the metal-oxygen bond strength of each material to the overpotential required for water oxidation catalysis.

oxide semiconductor, such as TiO_2 or SnO_2.[2] Both IrO_2 and RuO_2 bulk materials have the

advantage of being highly reactive, especially in acidic media, but RuO_2 in particular can have

stability issues at high overpotentials and in more alkaline solutions. To make the film more

stable, RuO_2 can be mixed with IrO_2 or deposited at higher temperatures to form a more

crystalline structure. As a film becomes more crystalline, however, the number of exposed

active catalytic sites decreases due to decreased surface area, resulting in a decrease in catalytic

activity. In this respect, increasing the active surface area of the film should increase the

catalytic activity, thus giving rise to the contribution of nanoscience – most specifically iridium

oxide nanoparticles – in the area of water oxidation research.

1.5   IRIDIUM OXIDE NANOPARTICLES

Iridium oxide nanoparticles (IrO_X NPs), both freely diffusing and deposited as films,

have been explored as electrocatalysts for water oxidation and have proven to be very

efficient.[52,69,70,110,111,112,1,113,114,115,116,117,118,119,120,121,122,123,124,125,126] In a study performed by Yagi

et al., the electrocatalytic effects on water oxidation of colloidal IrO_X nanoparticles (50 – 100

nm diameter) as an amorphous monolayer on an tin-doped indium oxide (ITO) electrode were

studied and the turnover frequency for this system was determined to be between 2.3 x 10^4 and

3.5 x 10^4 h^{-1}.[115] In comparison, electrodes modified with ruthenium complexes, which are the

homogeneous catalysts with the next most efficient turnover frequency, have reported turnover

rates that are smaller by an order of magnitude or more than that of this system. The Ru-red/Pt-

black system, for example, demonstrated a turnover frequency of 1500 h^{-1} and the complex

$[(NH_3)_3Ru^{II}(\mu-Cl)_3Ru^{III}(NH_3)_3]^{2+}$ was only shown to have a turnover rate of around 200 h^{-1} in

conjunction with a Ce^{IV} oxidant. Furthermore, the overpotential needed for the oxidation of

water using the colloidal IrO_X nanoparticles was about 0.4 V, which was much lower than others previously reported.[115]

More recently, IrO_X nanoparticles of a smaller size have been explored as electrocatalysts by numerous groups, in particular those of Murray and Mallouk.[27, 38, 42, 71, 110-113, 116] Because of the nanoparticle's small size, generally in the 1 – 2 nm range, their reactivity differs from that of the larger colloidal IrO_2 nanoparticles, due to the increase in surface area. Murray and coworkers demonstrated that the nanoparticles can be deposited onto the electrode by electroflocculation; the nanoparticles retain their individual shape and size, as determined by TEM of the dislodged film. Electroflocculation is a film formation technique, where the nanoparticles flocculate, not aggregate, together when a potential bias is applied. Studies of the pH dependence of the redox couples from the film, Ir^V/Ir^{IV} and Ir^{IV}/Ir^{III} revealed that as the pH of the solution increased, the formal potentials of the couples shift proportionally according to the Nernst equation, and are thus Nernstian behaved. As the thermodynamic potential of water oxidation is also Nernstian behaved, the overpotential for water oxidation was nearly independent of pH, revealing that the nanoparticles retain their catalytic activity across a wide range of pH.[110-111]

A relationship between the production of O_2 and the thickness of the film was also demonstrated by Murray *et al*.[111] As the coverage, Γ, of IrO_X nanoparticles increased, the production of O_2 increased proportionally, indicating that the kinetics are not adversely affected by the increasing thickness of the film. At a Γ_{Ir} of 7 x 10^{-8} mol/cm^2 and applied potential of 1.3 V vs. Ag/AgCl, a steady state current of 91 mA/cm^2 was achieved, which is about 40 times higher than that reported previously. In addition, the turnover frequency achieved by the films was similar to those earlier reported, between 1.6 x 10^4 and 2.2 x 10^4 hr^{-1}. These films are quite thick, comparatively, and are charged to the Ir^{VI} state throughout very quickly, indicating that the

electron transfer through the film is fast. This is due to a mesoporous structure of the film, which allows transport of water and ions to flow easily through the film, and the increased surface area, which results in an increase of accessible reactive sites. Futhermore, this film had an overpotential of 0.25 V vs. Ag/AgCl at a current density of 0.5 mA/cm^2 for the OER, which was significantly lower than the 0.4 V reported by Yagi et al.[111]

While the nanoparticles of Murray and coworkers were prepared in a basic solution at pH 13, the nanoparticles synthesized by Mallouk and coworkers were synthesized using the same method and then were adjusted to a pH of 1 by the addition of HNO$_3$.[27, 38, 71, 114, 116] The proposed mechanism involves the formation of $[Ir(OH)_6]^{2-}$ and $IrO_X \cdot nH_2O$ from $[IrCl_6]^{-2}$ in a basic solution. As the pH of the solution is lowered, the $[Ir(OH)_6]^{2-}$ condenses to form $IrO_X \cdot nH_2O$. The partial condensation of the iridium centers of the nanoparticles led to slightly increased electrocatalytic activity for the nanoparticle electroflocculated films, which decreased the overpotential for the oxidation of water to 0.22 V vs. Ag/AgCl independent of pH, roughly 30 mV less than that of Murray et al. Mallouk et al. suggested this was due to consumption of the Ir^{IV} in the acidic condensation method, although the difference in overpotential could be considered negligible in comparison.[27, 116]

IrO$_X$ NPs freely diffusing in solution have also proven to be efficient heterogeneous electrocatalysts.[110,112] It was found that the current produced from water oxidation catalysis when rotating the electrode was almost independent of the rotation rate, ω. This suggests the rate determining step in the process is the electron transfer between the Ir^{VI} and the H$_2$O. The current efficiency was found to be nearly 100% at a current density of 0.5 mA/cm^2. The overpotential needed for the 100% current efficiency was determined to be 0.29 V vs. Ag/AgCl, which is comparable to that of the IrO$_X$ film made of the same nanoparticles. The turnover frequency of

O$_2$ was also similar to that of the nanoparticle films and independent of the concentration of IrO$_X$. Consequently, it was concluded that the kinetics are very similar in both the film and freely diffusing NPs, indicating that the reaction is limited by its kinetics, not by mass transport.[110,111]

While it has been established that these 2 nm IrOx NPs are excellent catalysts for water oxidation based on their low overpotential and high turnover rate, little is known about the NPs themselves or how they behave. The Murray lab has investigated this, including the research in this dissertation. In the same study mentioned above, 96% of the known concentration of Ir sites present in solution were able to undergo reduction from Ir^{VI} to Ir^{III}. This suggests that the entire nanoparticle is electrochemically reactive, where each Ir site is able to undergo redox chemistry. This may be due to the small size of the nanoparticle, which facilitates electron transfer between iridium sites. Because the electron transfer is fast, each one of the Ir sites is able to be reduced and oxidized.[111]

The Murray lab also studied the same IrOx NPs in solution, when stabilized by phosphate ligands.[112] In a Pourbaix diagram of formal potential, $E^{0'}$, vs. pH, the Ir$^{V/IV}$ E^0 and Ir$^{IV/III}$ $E^{0'}$ at low pH of the NPs in solution followed a similar pattern as that of the electroflocculated NPs. They each had a slope of around 70 mV/pH, suggesting a one e$^-$, one H$^+$ transfer. The Ir$^{IV/III}$ $E^{0'}$ in solutions above pH 6, however, differed by having a slope of 116 mV/pH, which implies a one e$^-$, two H$^+$ transfer in basic media. It is thought that this change from the film is due to the surface oxide acid-base sites of the NPs; when the NPs are electroflocculated, these sites become inactive, resulting in a one e$^-$, one H$^+$ process at the pH values above 6.

Another important observation from this study is that both phosphates and carboxylates ligate and stabilize the IrOx NPs.[1] This led to a study by the Murray lab as well where the NPs

were attached to a Au slide via a self-assembled monolayer (SAM) of carboxylated alkanethiolates.[113] The longer carbon chains lead to decreased electron transfer (ET) for the monolayers, as measured by a change in ΔE_{peak}, which increased with increasing chain length. The overpotential for water oxidation also shifts with increasing chain length. A higher overpotential was required to reach the same current level for longer alkane chains. This change in overpotential demonstrates that the kinetics of water oxidation can be controlled by varying the chain length of the SAMs, opening up a new way to study the kinetics of water oxidation.

The research presented in this dissertation largely focuses on these small iridium oxide nanoparticles. Film formation and characterization of IrO_X NPs will be discussed, as well as their behavior in non-aqueous media. By fully understanding the behavior, structure and surface chemistry of IrO_X NPs, we can learn more about what makes them such efficient catalysts for the OER and apply that knowledge towards the development of less expensive materials. The implementation of these catalysts into a DSPEC device will also be discussed, including a novel assembly method with a Ru(II) polypyridal based chromophore on core/shell electrodes. Finally, the last chapter will take a left turn and discuss the electrochemical characterization of three novel Ru(II) quaterpyridine complexes, as well as their potential to serve as benzyl alcohol oxidation and water oxidation catalysts.

REFERENCES

(1)   Administration, U. S. E. I., International Energy Outlook 2013. Energy, D. o., Ed. Office of Energy Analysis: 2013.

(2)   Walter, M. G.; Warren, E. L.; McKone, J. R.; Boettcher, S. W.; Mi, Q.; Santori, E. A.; Lewis, N. S., *Chem. Rev.* **2010,** *110*, 6446-6473.

(3)   Motors, T., Tesla Energy. http://www.teslamotors.com/presskit, 2015.

(4)   Fujishima, A.; Honda, K., *Nature* **1972,** *238*, 37.

(5)   (a) Aharon-Shalom, E.; Heller, A., *J. Electrochem. Soc.* **1982,** *129*, 2865; (b) Aspnes, D. E.; Studna, A. A., *Phys. Rev. B* **1983,** *27*, 985.

(6)   Baglio, J. A.; Calabrese, G. S.; Harrison, D. J.; Kamieniecki, E.; Ricco, A. J.; Wrighton, M. S.; Zoski, G. D., *J. Am. Chem. Soc.* **1983,** *105*, 2246.

(7)   Dominey, R. N.; Lewis, N. S.; Bruce, J. A.; Bookbinder, D. C.; Wrighton, M. S., *J. Am. Chem. Soc.* **1980,** *102*, 5142.

(8)   Khaselev, O.; Turner, J. A., *Science* **1998,** *280*, 425.

(9)   Kocha, S. S.; Turner, J. A.; Nozik, A. J., *J. Electroanal. Chem.* **1994,** *367*, 27.

(10)   Memming, R.; Schwandt, G., *Electrochim. Acta* **1968,** *13*, 1299.

(11)   Nakato, Y.; Yano, H.; Nishiura, S.; Ueda, T.; Tsubomura, H., *J. Electroanal. Chem.* **1987,** *228*, 97.

(12)   Price, M. J.; Maldonado, S., *J. Phys. Chem. C* **2009,** *113*, 11988.

(13)   (a) Bocarsly, A. B.; Bookbinder, D. C.; Dominey, R. N.; Lewis, N. S., *J. Am. Chem. Soc.* **1980,** *102*, 3628; (b) Heller, A.; Aspnes, D. E.; Porter, J. D.; Sheng, T. T.; Vadimsky, R. G., *J. Phys. Chem.* **1985,** *89*, 4444.

(14)   Scaife, D. E., *Sol. Energy* **1980,** *25*, 41.

(15)   Matumoto, Y., *J. Solid State Chem.* **1996,** *126*, 227.

(16)   Yoneyama, H.; Sakamoto, H.; Tamura, H., *Electrochim. Acta* **1975,** *20*, 341.

(17)   Nozik, A. J., *J. Appl. Phys. Lett.* **1976,** *29*, 150.

(18)   Nozik, A. J., *J. Appl. Phys. Lett.* **1977,** *30*, 567.

(19)   Ohashi, K.; McCann, J.; Bockris, J. O. M., *Nature* **1977,** *266*, 610.

(20)   Ohashi, K.; McCann, J.; Bockris, J. O. M., *J. Hydrogen Energy* **1977,** *1*, 259.

(21)   Miller, E. L.; Paluselli, D.; marsen, B.; Rocheleau, R. E., *Sol. Energy Mater. Sol. Cells* **2005,** *88*, 131.

(22)   Gratzel, M., *Nature* **2001,** *414*, 338.

(23)   O'Regan, B.; Gratzel, M., *Nature* **1991,** *353*, 737-740.

(24)   Hagfeldt, A.; Gratzel, M., *Acc. Chem. Res.* **2000,** *33*, 269-277.

(25)   Hagfeldt, A.; Boschloo, G.; Sun, L.; Kloo, L.; Pettersson, H., *Chem. Rev.* **2010,** *110*, 6595-6663.

(26)   Yu, Z.; Li, F.; Sun, L., *Energy Environ. Sci.* **2015,** *8*, 760-775.

(27)   Lee, S.-H. A.; Abrams, N. M.; Hoertz, P. G.; Barber, G. D.; Halaoui, L. I.; Mallouk, T. E., *J. Phys. Chem. B* **2008,** *112*, 14415-14421.

(28)   Gratzel, M., *Acc. Chem. Res.* **2009,** *42*, 1788-1798.

(29)   Yu, Z.; Vlachopoulos, N.; Gorlov, M.; Kloo, L., *Dalton Trans.* **2011,** *40*, 10289-10303.

(30)   Tian, H.; Sun, L., *J. Mater. Chem.* **2011,** *21*, 10592-10601.

(31)   He, J.; Lindstrom, H.; Hagfeldt, A.; Lindquist, S.-E., *J. Phys. Chem. B* **1999,** *103*, 8940-8943.

(32)   Qin, P.; Zhu, H.; Edvinsson, T.; Boschloo, G.; Hagfeldt, A.; Sun, L., *J. Am. Chem. Soc.* **2008,** *130*, 8570-8571.

(33)   Nattestad, A.; Mozer, J. A.; Fischer, M. K. R.; Cheng, Y. B.; Mishra, A.; Bauerle, P.; U., B., *Nat. Mater.* **2010,** *9*, 31-35.

(34)   Odobel, F.; Pellegrin, Y.; Gibson, E. A.; Hagfeldt, A.; Smiegh, A. L.; Hammarstrom, L., *Coord. Chem. Rev.* **2012,** *256*, 2414-2423.

(35)   Odobel, F.; Pellegrin, Y., *J. Phys. Chem. Lett.* **2013,** *4*, 2551-2564.

(36)   Alstrum-Acevedo, J. H.; Brennaman, M. K.; Meyer, T. J., *Inorg. Chem.* **2005,** *44*, 6802-6827.

(37)   Song, W.; Glasson, C. R. K.; Luo, H.; Hanson, K.; Brennaman, M. K.; Concepcion, J. J.; Meyer, T. J., *J. Phys. Chem. Lett.* **2011,** *2*, 1808-1813.

(38)   Swiek, J. R.; McCool, N. S.; Saunders, T. P.; Barber, G. D.; Strayer, M. E.; Vargas-Barbosa, N. M.; Mallouk, T. E., *J. Phys. Chem. C* **2014,** *118*, 17046-17053.

(39)   (a) Alibabaei, L.; Luo, H.; House, R. L.; Hoertz, P. G.; Lopez, R.; Meyer, T. J., *J. Mater. Chem. A* **2013,** *1*, 4133-4145; (b) Song, W.; Chen, Z.; Glasson, C. R. K.; Hagfeldt, A.; Luo, H.; Norris, M. R.; Ashford, D. L.; Concepcion, J. J.; Brennaman, M. K.; Meyer, T. J., *Chem. Phys. Chem.* **2012,** *13*, 2882-2890.

(40)   Duan, L.; Tong, L.; Xu, Y.; Sun, L., *Energy Environ. Sci.* **2011,** *4*, 3296-3313.

(41)   Young, K. J.; Martini, L. A.; Milot, R. L.; Snoeberger III, R. C.; Batista, V. S.; Schumuttenmaer, C. A.; Crabtree, R. H.; Brudvig, G. W., *Coord. Chem. Rev.* **2012,** *256*, 2503-2520.

(42)   Swiek, J. R.; Mallouk, T. E., *Chem. Soc. Rev.* **2013,** *42*, 2357-2387.

(43)   Argazzi, R.; Murakami Iha, Y.; Zabri, H.; Odobel, F.; Bignozzi, C. A., *Coord. Chem. Rev.* **2004,** *248*, 1299-1316.

(44)   Polo, A. S.; Itokazu, M. K.; Murakami Iha, N. Y., *Coord. Chem. Rev.* **2004,** *248*, 1343-1361.

(45)   Mishra, A.; Fischer, M. K. R.; Bauerle, P., *Angew, Chem. Int. Ed.* **2009,** *48*, 2474-2499.

(46)   Galoppini, E., *Coord. Chem. Rev.* **2004,** *248*, 1283-1297.

(47)   Wasylenko, D. J.; Palmer, R. D.; Berlinguette, C. P., *Chem. Commun.* **2013,** *49*, 218-227.

(48)   Hetterschied, D. G. H.; Reek, J. N. H., *Angew. Chem. Int. Ed.* **2012,** *51*, 9740-9747.

(49)   Cao, R.; Lai, W.; Du, P., *Energy Environ. Sci.* **2012,** *5*, 8134-8157.

(50)   Concepcion, J. J.; Jurss, J. W.; Brennaman, M. K.; Hoertz, P. G.; Patrocinio, A. O. T.; Murakami Iha, N. Y.; Templeton, J. L.; Meyer, T. J., *Acc. Chem. Res.* **2009,** *42*, 1954-1965.

(51)   Hyde, J. T.; Hanson, K.; Vannucci, A. K.; Lapides, A. M.; Alibabaei, L.; Norris, M. R.; Meyer, T. J.; Harrison, D. P., *ACS Appl. Mater. Interfaces* **2015,** *7*, 9554-9562.

(52)   Lattach, Y.; Rivera, J. F.; Bamine, T.; Deronzier, A.; Moutet, J.-C., *ACS Appl. Mater. Interfaces* **2014,** *6*, 12852-12859.

(53)   Ashford, D. L.; Sherman, B. D.; Binstead, R. A.; Templeton, J. L.; Meyer, T. J., *Angew, Chem. Int. Ed.* **2015,** *16*, 4778-4781.

(54)   Ashford, D. L.; Lapides, A. M.; Vannucci, A. K.; Hanson, K.; Torelli, D. A.; Harrison, D. P.; Templeton, J. L.; Meyer, T. J., *J. Am. Chem. Soc.* **2014,** *136*, 6578-6581.

(55)   Fang, Z.; Keinan, S.; Alibabaei, L.; Luo, H.; Ito, A.; Meyer, T. J., *Angew, Chem. Int. Ed.* **2014,** *53*, 4872-4876.

(56)   Lapides, A. M.; Ashford, D. L.; Hanson, K.; Torelli, D. A.; Templeton, J. L.; Meyer, T. J., *J. Am. Chem. Soc.* **2013,** *135*, 15450-15458.

(57)   Harrison, D. J.; Lapides, A. M.; Binstead, R. A.; Concepcion, J. J.; Mendez, M. A.; Torelli, D. A.; Templeton, J. L.; Meyer, T. J., *Inorg. Chem.* **2013,** *52*, 4747-4749.

(58)   Alibabaei, L.; Sherman, B. D.; Norris, M. R.; Brennaman, M. K.; Meyer, T. J., *Proc. Nat. Acad. Sci.* **2015,** *112*, 5899-5902.

(59)   Hanson, K.; Losego, M. D.; Kalanyan, B.; Ashford, D. L.; Parsons, G. N.; Meyer, T. J., *Chemistry of Materials* **2013,** *25*, 3.

(60)   Hanson, K.; Losego, M. D.; Kalanyan, B.; Parsons, G. N.; Meyer, T. J., *Nano Lett.* **2013,** *13*, 4802.

(61)   Vannucci, A. K.; Alibabaei, L.; Losego, M. D.; Concepcion, J. J.; Kalanyan, B.; Parsons, G. N.; Meyer, T. J., *Proc. Nat. Acad. Sci.* **2013,** *110*, 20918.

(62)   Jeong, N. C.; Son, H.-J.; Prasittichai, C.; Lee, C. Y.; Jensen, R. A.; Farha, O. K.; Hupp, J. T., *J. Am. Chem. Soc.* **2012,** *134*, 19820.

(63)   Katz, M. J.; Vermeer, M. J. D.; Farha, O. K.; Pellin, M. J.; Hupp, J. T., *Langmuir* **2012,** *29*, 806.

(64)   Martinson, A. B. F.; Elam, J. W.; Liu, J.; Pellin, M. J.; Marks, T. J.; Hupp, J. T., *Nano Lett.* **2008,** *8*, 2862.

(65)   Son, H.-J.; Wang, X.; Prasittichai, C.; Jeong, N. C.; Aaltonen, T.; Gordon, R. G.; Hupp, J. T., *J. Am. Chem. Soc.* **2012,** *134*, 9537.

(66)   Williams, V. O.; Jeong, N. C.; Prasittichai, C.; Farha, O. K.; Pellin, M. J.; Hupp, J. T., *Nano Lett.* **2012,** *6*, 6185.

(67)   Son, H.-J.; Prasittichai, C.; Mondloch, J. E.; Luo, L.; Wu, J.; Kim, D. H.; Farha, O. K.; Hupp, J. T., *J. Am. Chem. Soc.* **2013,** *135*, 11529.

(68)   Son, H.-J.; Prasittichai, C.; Mondloch, J. E.; Luo, L.; Wu, J.; Kim, D. H.; Farha, O. K.; Hupp, J. T., Dye Stabilization and Enhanced Photoelectrode Wettability in Water-based Dye-sensitized Solar Cells through Post-assembly Atomic Layer Deposition of TiO2. *J. Am. Chem. Soc.* **2013,** *135* (31), 11529 - 11532.

(69) Cong, Y.; Park, H. S.; Wang, S.; Dang, H. X.; Fan, F.-R. F.; Mullins, C. B.; Bard, A. J., *J. Phys. Chem. C* **2012,** *116*, 14541-14550.

(70) Tilley, S. D.; Cornuz, M.; Sivula, K.; Gratzel, M., *Angew, Chem. Int. Ed.* **2010,** *49*, 6405-6408.

(71) Lee, S.-H. A.; Zhao, Y.; Hernandez-Pagan, E. A.; Blasdel, L.; Youngblood, W. J.; Mallouk, T. E., *Faraday Discuss.* **2012,** *155*, 165-176.

(72) Alibabaei, L.; Farnum, B. H.; Kalanyan, B.; Brennaman, M. K.; Losego, M. D.; Parsons, G. N.; Meyer, T. J., *Nano Lett.* **2014,** *14*, 3255-3261.

(73) Hoertz, P. G.; Chen, Z.; Kent, C. A.; Meyer, T. J., *Inorg. Chem.* **2010,** *49*, 8179-8181.

(74) Junge, H.; Marquet, N.; Kammer, A.; Denurra, S.; Bauer, M.; Wohlrab, S.; Gartner, F.; Pohl, M.-M.; Sapnnenberg, A.; Gladiali, S.; Beller, M., *Chem. Eur. J.* **2012,** *18*, 12749-12758.

(75) Blakemore, J. D.; Schley, N. D.; Kushner-Lenhoff, M. N.; Winter, A. M.; D'Souza, F.; Crabtree, R. H.; Brudvig, G. W., *Inorg. Chem.* **2012,** *51*, 7749-7763.

(76) Blakemore, J. D.; Mara, M. W.; Kushner-Lenhoff, M. N.; Schley, N. D.; Konezyny, S. J.; Rivalta, I.; Negre, C. F. A.; Snoeberger III, R. C.; Kokhan, O.; Huang, J.; Stickrath, A.; Tran, L. A.; Parr, M. L.; Chen, L. X.; Tiede, D. M.; Batista, V. S.; Crabtree, R. H.; Brudvig, G. W., *Inorg. Chem.* **2013,** *52*, 1860-1871.

(77) Sala, X.; Poater, A.; Romero, I.; Rodriguez, M.; Llobet, A.; Solans, X.; Parella, T.; Santos, T. M., *Eur. J. Inorg. Chem.* **2004**, 612-618.

(78) Zong, R.; Wang, B.; Thummel, R. P., *Inorg. Chem.* **2012,** *51*, 3179-3185.

(79) Sens, C.; Rodriguez, M.; Romero, I.; Llobet, A., *Inorg. Chem.* **2003,** *42*, 8385.

(80) Chanda, N.; Mondal, B.; Puranik, V. G.; Lahiri, G. K., *Polyhedron* **2002,** *21*, 2033-2043.

(81) Dobson, J. C.; Meyer, T. J., *Inorg. Chem.* **1988,** *27*, 3283-3291.

(82) Che, C.-M.; Wong, K.-Y.; Leung, W.-H.; Poon, C.-K., *Inorg. Chem.* **1986,** *25*, 345-348.

(83) Liu, Y.; Ng, S.-M.; Yiu, S.-M.; Lam, W. W. Y.; Wei, X.-G.; Lau, K.-C.; Lau, T.-C., *Angew, Chem. Int. Ed.* **2014,** *53*, 1-5.

(84) Muckerman, J. T.; kowalczyk, M.; Badiei, Y. M.; Polyanksy, D. E.; Concepcion, J. J.; Zong, R.; Thummel, R. P.; Fujita, E., *Inorg. Chem.* **2014,** *53*, 6904-6913.

(85) Geneste, F.; Moinet, C., *New. J. Chem.* **2004,** *28*, 722-726.

(86) Chan, C.-W.; Lai, T.-F.; Che, C.-M., *J. Chem. Soc. Dalton Trans.* **1994**, 895.

(87) Guadalupe, A. R.; Chen, X.; Sullivan, B. P.; Meyer, T. J., *Inorg. Chem.* **1993,** *32*, 5502-5512.

(88) Blakemore, J. D.; Schley, N. D.; Olack, G. W.; Incarvito, C. D.; Brudvig, G. W.; Crabtree, R. H., *Chem. Sci.* **2011,** *2*, 94.

(89) Concepcion, J. J.; Tsai, M.-K.; Muckerman, J. T.; Meyer, T. J., *J. Am. Chem. Soc.* **2010,** *132*, 1545-1557.

(90) Chen, Z.; Concepcion, J. J.; Hu, X.; Wang, W.; Hoertz, P. G.; Meyer, T. J., *Proc. Nat. Acad. Sci.* **2010,** *107*, 7225-7229.

(91) Jurss, J. W.; Concepcion, J. J.; Norris, M. R.; Templeton, J. L.; Meyer, T. J., *Inorg. Chem.* **2010,** *49*, 3980-3982.

(92) Chen, A.; Concepcion, J. J.; Meyer, T. J., *Dalton Trans.* **2011,** *40*, 3789-3792.

(93) Ashford, D. L.; Brennaman, M. K.; Brown, R. J.; Keinan, S.; Concepcion, J. J.; Papinikolas, J. M.; Templeton, J. L.; Meyer, T. J., *Inorg. Chem.* **2015,** *54*, 460-469.

(94) Chen, Z.; Meyer, T. J., *Angew, Chem. Int. Ed.* **2012,** *52*, 700-703.

(95) Zhang, M.-T.; Chen, Z.; Kang, P.; Meyer, T. J., *J. Am. Chem. Soc.* **2013,** *135*, 2048-2051.

(96) Kent, C. A.; Concepcion, J. J.; Dares, C. J.; Torelli, D. A.; Rieth, A. J.; Miller, A. S.; Hoertz, P. G.; Meyer, T. J., *J. Am. Chem. Soc.* **2013,** *135*, 8432-8435.

(97) Coggins, M. K.; Zhang, M.-T.; Vannucci, A. K.; Dares, C. J.; Meyer, T. J., *J. Am. Chem. Soc.* **2014,** *136*, 5531-5534.

(98) Coggins, M. K.; Zhang, M.-T.; Vannucci, A. K.; Dares, C. J.; Meyer, T. J., *J. Am. Chem. Soc.* **2014,** *136*, 7186.

(99) Coggins, M. K.; Zhang, M.-T.; Chen, Z.; Song, N.; Meyer, T. J., *Angew, Chem. Int. Ed.* **2014,** *53*, 12226-122230.

(100) Du, J.; Chen, Z.; Ye, S.; Wiley, B. J.; Meyer, T. J., *Angew, Chem. Int. Ed.* **2015,** *54*, 2073-2078.

(101) Rasiyah, P.; Tseung, A. C. C., *J. Electrochem. Soc.* **1984,** *131*, 803.

(102) Kay, A.; Cesar, I.; Gratzel, M., *J. Am. Chem. Soc.* **2006,** *128*, 15714.

(103)   Kanan, M. W.; Nocera, D. G., *Science* **2008,** *321*, 1072.

(104)   Lutterman, D. A.; Surendranath, Y.; Nocera, D. G., *J. Am. Chem. Soc.* **2009,** *131*, 3838.

(105)   McAlpin, J. G.; Surendranath, Y.; Dinca, M.; Stich, T. A.; Stoian, S. A.; Casey, W. H.; Nocera, D. G.; Britt, R. D., *J. Am. Chem. Soc.* **2010,** *131*, 6882.

(106)   Surendranath, Y.; Dinca, M.; Nocera, D. G., *J. Am. Chem. Soc.* **2009,** *131*, 2615.

(107)   Kanan, M. W.; Surendranath, Y.; Nocera, D. G., *Chem. Soc. Rev.* **2009,** *38*, 109.

(108)   Cook, T. R.; Dogutan, D. K.; Reece, S. Y.; Surendranath, Y.; Teets, T. S.; Nocera, D. G., *Chem. Rev.* **2010,** *110*, 6474-6502.

(109)   Gorlin, Y.; Jaramillo, T. F., *J. Am. Chem. Soc.* **2010,** *132*, 13612-13614.

(110)   Nakagawa, T.; Beasley, C. A.; Murray, R. W.; , *J. Phys. Chem. C* **2009,** *113* (30), 12958.

(111)   Nakagawa, T.; Bjorge, N. S.; Murray, R. W.; , *J. Am. Chem. Soc.* **2009,** *131*, 15578.

(112)   Gambardella, A. A.; Bjorge, N. S.; Alspaugh, V. K.; Murray, R. W., *J. Phys. Chem. C* **2011,** *115*, 21659.

(113)   Gambardella, A. A.; Feldberg, S. W.; Murray, R. W., *J. Am. Chem. Soc.* **2012,** *134* (13), 5774.

(114)   Zhao, Y.; Hernadez-Pagan, E. A.; Vargas-Barbosa, N. M.; Dysart, J. L.; Mallouk, T. E.; , *J. Phys. Chem. Lett.* **2011,** *2*, 402.

(115)   Yagi, M.; Tomita, E.; Sakita, S.; Kuwabara, T.; Nagai, K.; , *J. Phys. Chem. B* **2005,** *109*, 21489.

(116)   Youngblood, W. J.; Lee, S.-H. A.; Kobayashi, Y.; Hernadez-Pagan, E. A.; Hoertz, P. G.; Moore, T. A.; Moore, A. L.; Gust, D.; Mallouk, T. E., *J. Am. Chem. Soc.* **2009,** *131*, 926-927.

(117)   Ouattra, L.; Fierro, S., *J. Appl. Electrochem.* **2009,** *39*, 1361-1367.

(118)   Lee, Y.; Suntivich, J.; May, K. J.; Perry, E. E.; Shao-Horn, Y., *J. Phys. Chem. Lett.* **2012,** *3*, 388-404.

(119)   Frame, F. A.; Townsend, T. K.; Chamousis, R. L.; Sabio, E. M.; Dittrich, T.; Browning, N. D.; Osterloh, F. E., *J. Am. Chem. Soc.* **2011,** *133*, 7264-7267.

(120)   Casalongue, H. G. S.; Ng, M. L.; Kaya, S.; Friebel, D.; Ogasawara, H.; Nilsson, A., *Angew, Chem. Int. Ed.* **2014,** *53*, 7169-7172.

(121)   Chuang, M.-C.; Ho, J. A., *RSC Adv.* **2012,** *2*, 4092-4096.

(122)   Hu, W.; Chen, S.; Xia, Q., *Int. J. of Hydrogen Energy* **2014,** *39*, 6967-6976.

(123)   Mirbagheri, N.; Chevallier, J.; Kibsgaard, J.; Besenbacher, F.; Ferapontova, E. E., *Chem. Phys. Chem.* **2014,** *15*, 2844-2850.

(124)   Busch, M.; Ahlberg, E.; Panas, I., *J. Phys. Chem. C* **2013,** *117*, 288-292.

(125)   Badia-Bou, L.; Mas-Marza, E.; Rodena, P.; Barea, E. M.; Fabregat-Santiago, F.; Gimenez, S.; Peris, E.; Bisquert, J., *J. Phys. Chem. C* **2013,** *117*, 3826-3833.

(126)   Pauporte, T.; Andolfatto, F.; Durand, R., *Electrochimica Acta* **1999,** *45*, 431-439.

CHAPTER 2: Film formation of Iridium Oxide Nanoparticles

2.1 INTRODUCTION

Iridium oxide nanoparticles ($Ir^{IV}O_X$ NPs) deposited as films are highly efficient electrocatalysts for the oxidation of water.[1-10] Yagi *et al.*[127g] showed that colloidal IrO_X nanoparticles (50 – 100 nm diameter) spontaneously adsorb as an amorphous monolayer on an indium tin oxide (ITO) electrode surface. These coated surfaces electrocatalyzed water oxidation at 1.3V vs Ag/AgCl at a turnover frequency (mol O_2/mol Ir) of ca. 6.6 s^{-1} (23,000 hr^{-1}) and at pH 5.3, with an overpotential of water oxidation reaction of ca. 0.4 V. While the turnover rate and over-potential were attractive, only a small percentage of the Ir sites in the film were electrochemically activate.

Thermal hydrolysis of K_2IrCl_6 solutions produces much smaller (ca. 2 nm dia.) $Ir^{IV}O_X$ nanoparticles which in films on electrodes are also very active water oxidation catalysts, as our laboratory[1,2,5,6] and that of Mallouk[4,9,10] have shown. The TO frequencies of Ir sites for water oxidation by these nanoparticles are similar to those observed by Yagi[127g] but the electrochemical over-potentials are significantly smaller. Additionally, nearly 100% of the Ir centers undergo electrochemical transformations, reflecting[5,6] facile transport of electronic and ionic charge throughout the nanoparticle films.

The formation of IrO_X nanoparticle films on electrodes occurs by their electroflocculation,[5] in which the nanoparticles retain their individual shape and size (as opposed to aggregation to form larger nanoparticles by the cementing together of smaller ones.) IrO_X nanoparticle films can also be formed by anodic electrolysis of $[Ir(OH)_6]^{-2}$ solutions.[10] The

quantities of nanoparticles deposited in their electroflocculated films—expressed as Γ_{IrO2}, mol Ir/cm^2—can be adjusted by the duration of the electroflocculation process.[5] The rate of production of O_2 by water oxidation is proportional to nanoparticle coverage over a ca. 300-fold range, indicating that charge and ion transport kinetics are somewhat tolerant to increasing film thickness. Deposition of an Ir oxide like material has also been reported from the decomposition of a soluble Ir complex upon oxidation.[11]

While the previous research shows that films of IrO$_X$ NPs are efficient catalysts for water oxidation, little is known about how electroflocculation of the NPs occurs. The electroflocculation process may influence structure and catalytic activity. Because of the key connection of water oxidation rate to nanoparticle coverage, a fuller understanding of the electroflocculation process than now available is desirable. The research presented seeks further insights based on voltammetry and microscopy techniques, notably scanning electron microscopy (SEM), atomic force microscopy (AFM), and an electrochemical quartz crystal microbalance (eQCM). We will show the topography of these films and propose a mechanism of flocculation based on these techniques.

Three different electroflocculation methods were also explored, including constant potential, potential pulsing and potential cycling. The electrochemistry and microscopy of these films are presented below as a comparison of the different electroflocculation techniques. Finally, two alternative flocculation methods not involving any applied potential will be discussed; they provide further insight to the film formation process of IrO$_X$ NPs. Understanding the film formation process is key in developing efficient heterogenous water oxidation catalyst films and the research presented delves into how different methods affect this film formation process as well as the film itself.

2.2 EXPERIMENTAL

2.2.1 Electrochemical Experimental Setup

Electrochemical experiments were performed in a conventional three electrode cell with Au-coated slide working, Pt wire auxiliary, and 3 M Ag/AgCl reference (BASi) electrodes, using a CH Instruments 760c potentiostat. This reference electrode, relative to RHE, is 0.2881 V. The Au-coated glass slides (Evaporated Metal Films, 239 Cherry St, Ithaca, NY 14850) had a 5 nm Ti layer on the glass over-coated by a 100 nm Au layer. Electroflocculating while rotating the electrode at 500 rpm was performed using a Pt ring, GC disk rotating ring disk electrode (RRDE). Changes in mass of IrO_X films upon electroflocculation were monitored with a Gamry eQCM 10M^{TM} Quartz Crystal Microbalance.

2.2.2 Iridium Oxide Nanoparticle Synthesis

The $Ir^{IV}O_X$ nanoparticles were synthesized using a Wohler method,[12] in which a 2.5 mM solution of K_2IrCl_6 (99%, Strem Chemicals) in nanopure H_2O was adjusted to pH 13 with 25% w/w NaOH (50% w/w, Fisher Scientific). The solution was heated at 90 °C for 20 minutes and then allowed to cool to RT and to rest for at least 24 hours after the synthesis.

For studies at lowered pH, the above nanoparticle solutions were adjusted to lower pH with either concentrated $HClO_4$ (GSF Chemicals), to a final pH of 2.5, or H_3PO_4 (Fisher Scientific), to a final pH of 1.5. For pH 7 and 10 NP solutions, concentrated H_3PO_4 was added to create 1.0 M PO_4^{-3} solutions and then adjusted to their respective pH with 50% w/w NaOH.

2.2.3 Electroflocculation of Iridium Oxide Nanoparticles

For electroflocculations not monitored by QCM, Au slides were first cleaned by exposure to piranha solution (3:1 concentrated H_2SO_4 (Fisher Scientific) to H_2O_2 (30% w/w, Fisher Scientific)), and then rinsed with nanopure H_2O and dried under a stream of Ar gas. Piranha solution is highly oxidizing and should therefore be handled with care. For electroflocculation of

31

films monitored by QCM, Gamry Au coated and C coated 10 MHz crystals were used as delivered, without prior cleaning in order to reduce exposure of the crystal to harsh environments.

The films were formed from unstirred pH 13 IrO$_X$ nanoparticle solutions by applying a potential of 0.9 V *vs*. Ag/AgCl. The duration of the applied potential was varied to generate different nanoparticle coverages. The films were rinsed with nanopure H$_2$O and then CV was performed in 0.1 M NaOH to verify the presence of a film.

Three different electroflocculation techniques were further explored: constant potential, potential pulsing and potential cycling. The methods to determine the most efficient film formation process are discussed below. In order to accurately compare each technique, the total time spent at potentials more positive than the onset of water oxidation (0.6 V vs. Ag/AgCl at pH 13) was kept constant at 10 minutes. After electroflocculation, all films were analyzed using cyclic voltammetry in a clean pH 13 buffer. The charge (Q) under the Ir$^{IV/III}$ and Ir$^{V/IV}$ waves were calculated. Using Faraday's Law (Equation 2-1), where n, F and N are the number of electrons, Faraday's constant and the number of moles of analyte respectively, the coverage of Ir (Γ_{Ir}) was found.

Equation 2-1

$$Q = nFN$$

2.2.3.1   Electroflocculation via Constant Potential

In the constant potential experiments, a potential more positive than the onset of water oxidation was held for ten minutes. This potential varied from 0.6 to 1.9 V vs. Ag/AgCl. The time was also varied, while keeping the potential applied constant at 1.2 V vs. Ag/AgCl.

2.2.3.2   Electroflocculation via Potential Pulsing

Electroflocculation via potential pulsing involved pulsing between two potentials, one more positive than the onset of water oxidation and one more negative than the onset of water oxidation. For the remainder of this chapter, these will be referred to as the upper and lower potential limits, respectively. The upper potential limits explored were 0.6, 0.9 and 1.2 V vs. Ag/AgCl and the lower potential limits were 0, 0.2 and 0.6 V vs. Ag/AgCl. The pulse length of the upper potential limit was varied between 0.1, 0.2 and 0.5 s; the total time spent at the upper potential limit, however, remained constant at 10 minutes.

2.2.3.3   Electroflocculation via Potential Cycling

Electroflocculation via potential cycling consisted of cycling the potential between the upper and lower potential limits listed in the above section. The scan rates were varied between 0.01, 0.1 and 1 V/s. The number of sweep segments was adjusted so that the total time spent more positive than the onset of water oxidation was kept at 10 minutes.

2.2.4   Microscopy of the IrOx NP Films

Images of films were obtained from a Hitachi S-4700 Cold Cathode Field Emission Scanning Electron Microscope (SEM) and an Asylum Research MFP3D Atomic Force Microscope (AFM).

2.2.5   Chemical Flocculation of Iridium Oxide Nanoparticles

The nanoparticles were chemically flocculated from homogeneous solutions by either adding a solid oxidant $NH_4Ce(NO_3)_6$ (Aldrich) salt to an as synthesized pH 13 nanoparticle solution, or by adding a 1 mM solution of $NH_4Ce(NO_3)_6$ to the nanoparticle solution in 50 μL increments.

2.2.6 Direct pH Change for Iridium Oxide Nanoparticle Precipitation

A solution of as-synthesized IrO_X NPs was adjusted to ~pH 1 with the addition of concentrated $HClO_4$ so that the final solution was 0.1 M $HClO_4$. After sitting at room temperature for 24 hours, electroactive slides were dipped vertically in the solution for 1.5 hours in order to form a film on the surface.

2.3 RESULTS AND DISCUSSION

2.3.1 Electroflocculation of Iridium Oxide Nanoparticles via Constant Potential

As noted earlier, electroflocculation of IrO_X nanoparticles onto an electrode is accomplished by applying a potential sufficiently positive to induce water oxidation catalysis. An example is shown in Figure 2.1 and Figure 2.2 where the film-forming applied potential was 0.9 V, for 10 minutes, in an as-synthesized pH 13 solution of nanoparticles. Voltammetry of a film of $Ir^{IV}O_X$ nanoparticles in 0.1M NaOH solution (pH 13) is illustrated in Figure 1. The nanoparticles undergo two Ir-centered redox reactions, $Ir^{IV/III}$ and $Ir^{V/IV}$. At potentials more
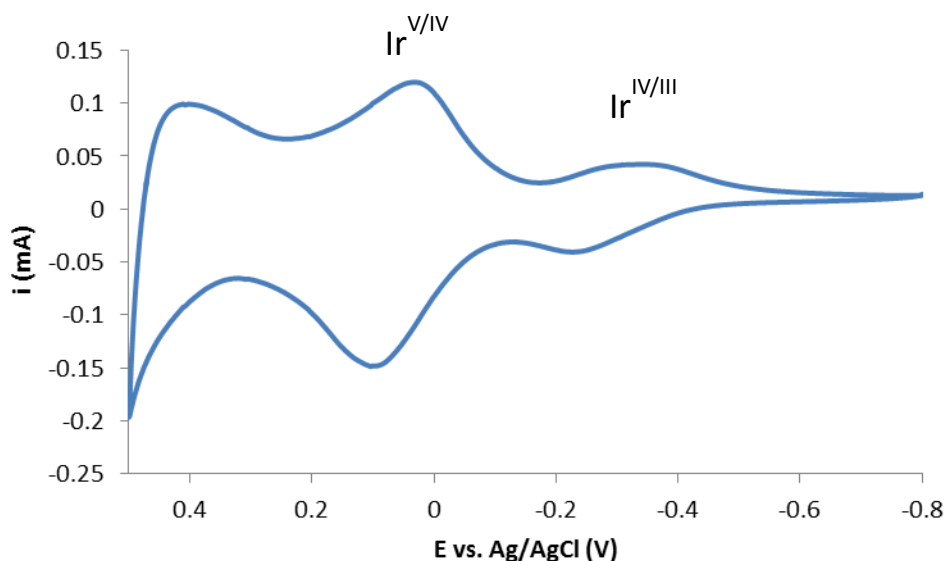
Figure 2.1: Cyclic voltammetry of an electroflocculated IrO_X NP film, depicting the $Ir^{V/IV}$ and $Ir^{IV/III}$ redox waves and the onset of water oxidation in 0.1 M NaOH solution (pH = 13). Electrode area 0.071 cm^2.

positive than the latter reaction, large currents for water oxidation immediately appear. (These

electrochemical processes are also seen when the nanoparticles are solutes in the electrolyte
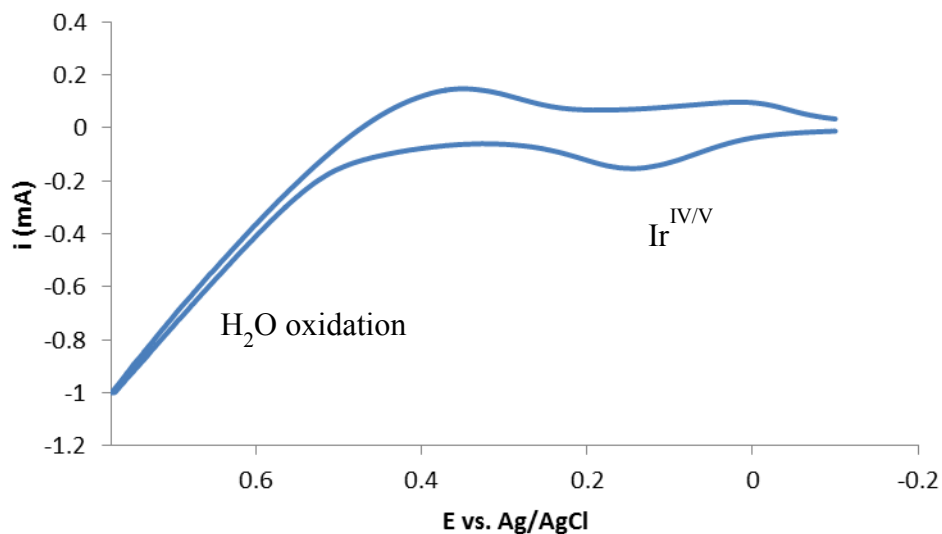
Figure 2.2: Cyclic voltammetry of an electroflocculated IrO_X NP film, depicting the $Ir^{IV/V}$ redox wave and water oxidation catalysis region in 0.1 M NaOH solution (pH = 13). Electrode area 0.071 cm^2.

solution, and oxygen is evolved at a similar rate and over-potential.) The solution pH

dependences of the formal potentials of the Ir^V/Ir^{IV} and Ir^{IV}/Ir^{III} couples of the nanoparticles, and

of the onset of water oxidation (associated with the Ir^{VI}/Ir^V reaction), are all *ca*. 60 mV/pH unit.

The overpotential for water oxidation, *ca*. 250 mV at 0.5 mA/cm^2, is independent of pH from

1.5 to 13, revealing a constant level of catalytic reactivity across pH.[2] Coulometry of

nanoparticle solutions shows that ca. 100% of the Ir nanoparticle sites undergo the Ir^V/Ir^{IV} and

Ir^{IV}/Ir^{III} reactions.[2]

The IrO_X film formation process is general with respect to electrode material, including

gold, glassy carbon (GC), platinum, tin-doped indium oxide (ITO) and titanium dioxide (TiO$_2$)

surfaces. The formation of a film is readily confirmed by cyclic voltammetry in 0.1 M NaOH

solution, in which two film redox couples are observed (Figure 2.1). The two waves are

attributed to $Ir^{IV/III}$ and $Ir^{V/IV}$ oxidation state changes, and can also be seen in solutions of IrO_X

nanoparticles. The $Ir^{IV/III}$ peak in a nanoparticle film occurs at a somewhat more positive

potential for the IrOx films, as described previously.[2,5] Once formed, the films are stable to exposure to various buffers and organic solvents within the limits described.
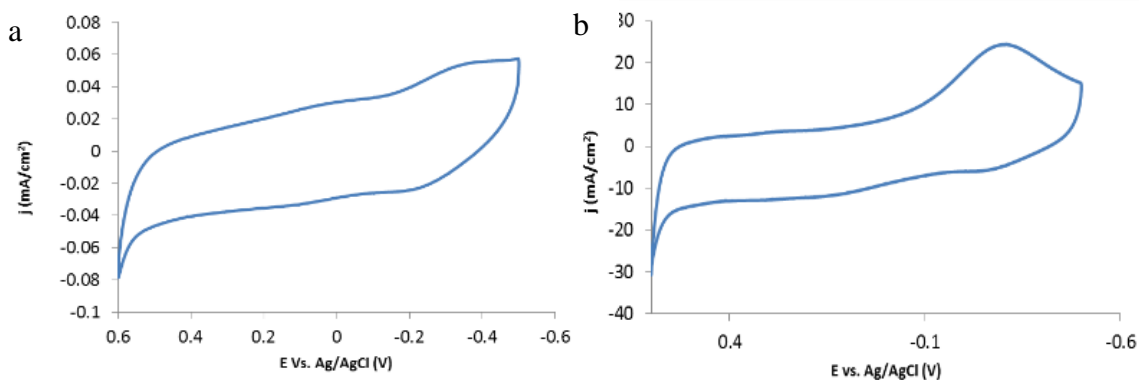
Figure 2.3: Cyclic voltammetry in 0.1 M NaOH of the GC disk (a) and Pt ring (b) after electroflocculation of pH 13 IrOx NPs while rotating at 500 rpm.

2.3.1.1   Electroflocculation with Rotation of Electrode

The film-forming process diminished by convection. Rotating the disk electrode during film-forming results in appearance of $Ir^{IV/III}$ and $Ir^{V/IV}$ waves in subsequent voltammetry, but the charge (Q) under the waves (which are proportional to the number of Ir sites present on the electrode) is significantly reduced (Figure 2.3). When using a rotating ring-disk electrode (500 rpm RRDE, Pt disk and GC ring), holding the disk potential in a pH 13 nanoparticle solution at 0.9 V for 10 minutes, film formation occurred on both disk and ring electrodes as evidenced by subsequently observed water oxidation catalysis. (Applying potential only to the Pt ring of the RRDE deposited IrOx film only on the ring.) This phenomenon is due to the convection created by rotating the electrode. The NPs flocculate at whichever electrode is polarized. When it is generated at the disk, some of the flocculated NPs are swept past the ring and therefore IrOx film formation is observed at both the disk and the ring. When the ring is polarized, the convection due to rotating doesn't cause the flocculated NPs generated at the ring to pass the disk, so there is no precipitation observed at the disk. There is still NP precipitation at the ring because the flocculated NPs are created there.

36
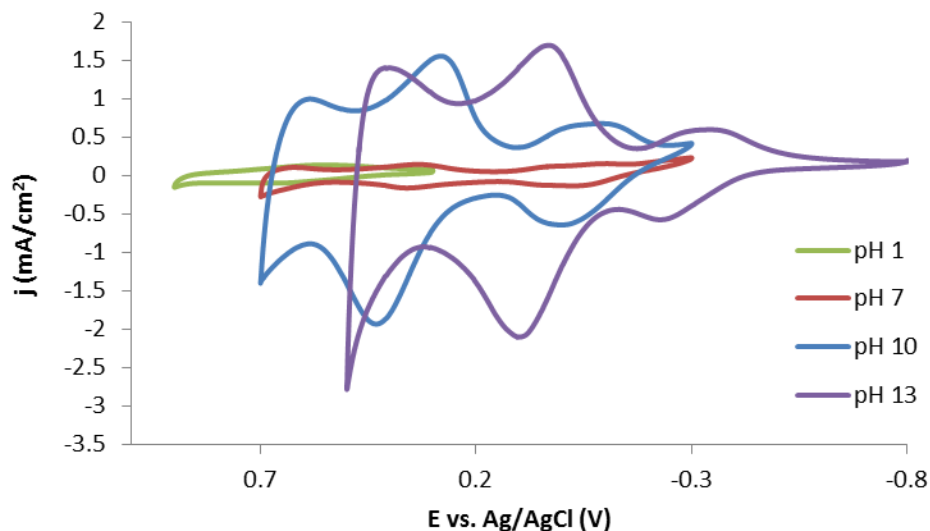
Figure 2.4: Cyclic voltammetry after the electrofloccultion onto Au coated slides of different pH IrO$_X$ NPs. CVs were performed in pH 1 phosphate buffer (pH 1 NPs), pH 10 phosphate buffer (pH 7 and 10 NPs) and 0.1 M NaOH (pH 13 NPs).

From these observations, it can be concluded that while applied potential is essential for nanoparticle flocculation into a film, the flocculation process is moderately slow, allowing film formation on an electrode (the ring) to which potential is not applied but which is exposed to a bath of (disk-charged) nanoparticles.

2.3.1.2   Electroflocculation at Varying pH

Electroflocculation onto Au film electrodes was attempted from nanoparticle solutions at lowered pH (pH 1, 7 and 10), with varying degrees of success, as seen in Figure 2.4. The NPs in pH 10 solution appeared to flocculate just as readily as the as-synthesized pH 13 NPs, with comparable coverages seen in the CVs from charge (Q). The NPs in pH 1 and pH 7 solutions, however, did not electroflocculate as readily, as their CVs showed a significant decrease in Q, presumably corresponding to a decrease in coverage. This suggests that the H$^+$ formation at high pH is essential for flocculation. Also of note, the surface of the NPs at different pH values changes significantly, which greatly impacts the electroflocculation.

37

2.3.1.3 eQCM Monitoring of Electroflocculation

Observations during electroflocculation using an electrochemical quartz crystal microbalance (eQCM) were very informative. Figure 2.5 shows an example of electroflocculation onto a Au coated quartz crystal at an applied 0.9 V potential. While current flow commences immediately upon the potential application, the quartz crystal frequency, whose decrease reflects growth of nanoparticle mass rigidly bound to the Au surface, interestingly exhibits a delayed response, for a relatively prolonged period (indicated by the black arrow in Figure 2.5). This delay, or induction period, occurred only for the initial stage of film formation; if the applied potential was removed and then re-applied, mass changes were observed immediately. The lack of delay in mass accumulation occurred whether the same nanoparticle solution was used or was replaced by a fresh one. It appears that once formed, a nanoparticle film builds upon itself with relative ease. The induction period of the electroflocculation process was seen at different IrO_X nanoparticle concentrations and electrodes.
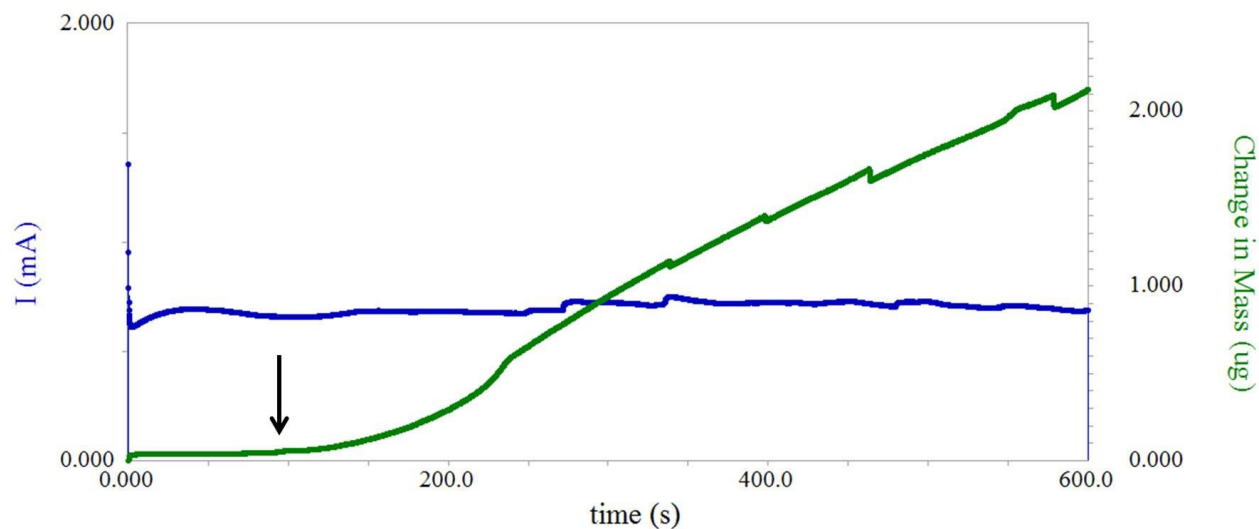
Figure 2.5: Electroflocculation of IrO_X NPs ([Ir] = 2.5 mM, pH 13) at 0.9 V vs. Ag/AgCl onto a Au coated quartz crystal, as monitored by eQCM. The measured current is the blue line; green corresponds to the change in mass obtained from the change in frequency of the quartz crystal. The black arrow indicates the end of the observed induction period. 1 µg increase in mass corresponds to roughly 1.67×10^{-10} mol IrO_X NPs/cm^2.

38
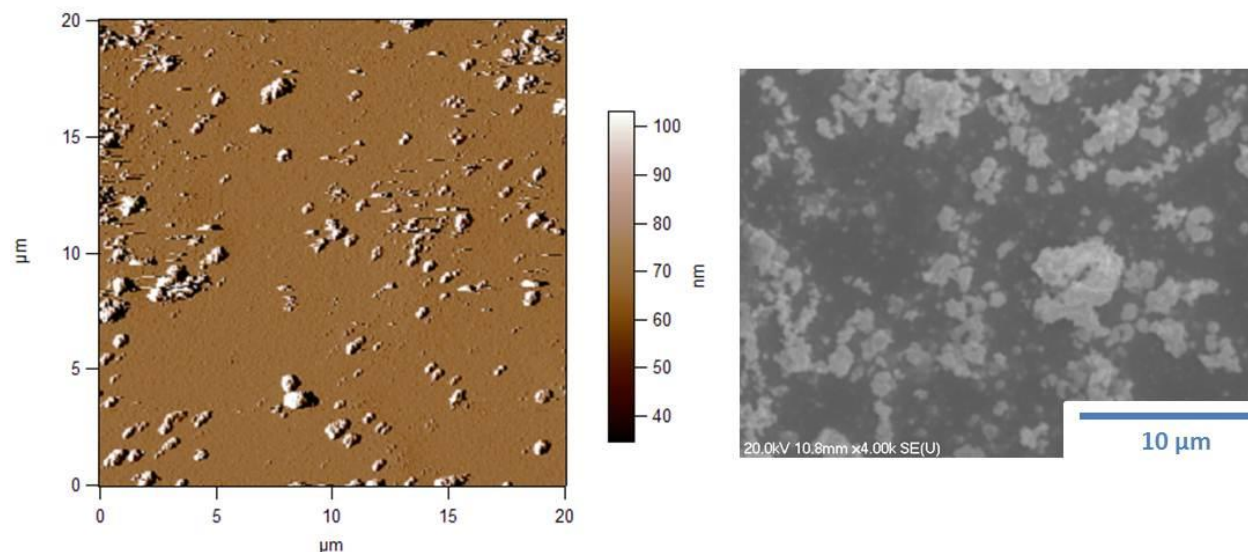
Figure 2.6: AFM (left) and SEM (right) images of electroflocculated IrO$_X$ NP films depicting the "islands" of NPs that form initially on the $0.209\ cm^2$ electrode surface. Both samples were electroflocculated onto a Au coated glass slide for 5 minutes.

The length of time for the induction phase could vary with conditions, but the total charge passed during it was crudely similar between films, averaging *ca.* 85 ± 8 mC, regardless of nanoparticle concentration. This suggests a common scenario of the trigger for film deposition, such as a buildup of a local pH gradient at the electrode due to prolonged water oxidation. The currents are rather substantial. The above water oxidation charge corresponds to an average of 2×10^{-7} moles of generated protons, which would neutralize an equivalent amount of base in the electrode interphase. The ca. 200 seconds of proton generation would create, roughly, a 0.01 cm thick diffusion layer at the electrode surface and a proton concentration of 0.1 M at the surface, i.e. sufficient to neutralize the 0.1 M NaOH near the electrode surface and create a pH gradient. This change in pH at the interface may trigger the initial flocculation of NPs and precipitation onto the electrode surface.

2.3.1.4   Microscopy of IrO$_X$ NP Films at Early Electroflocculation Times

Atomic force micrscopy (AFM) and scanning electron microscopy (SEM) were performed on various electroflocculated films of IrO$_X$ NP films. For longer electroflocculation
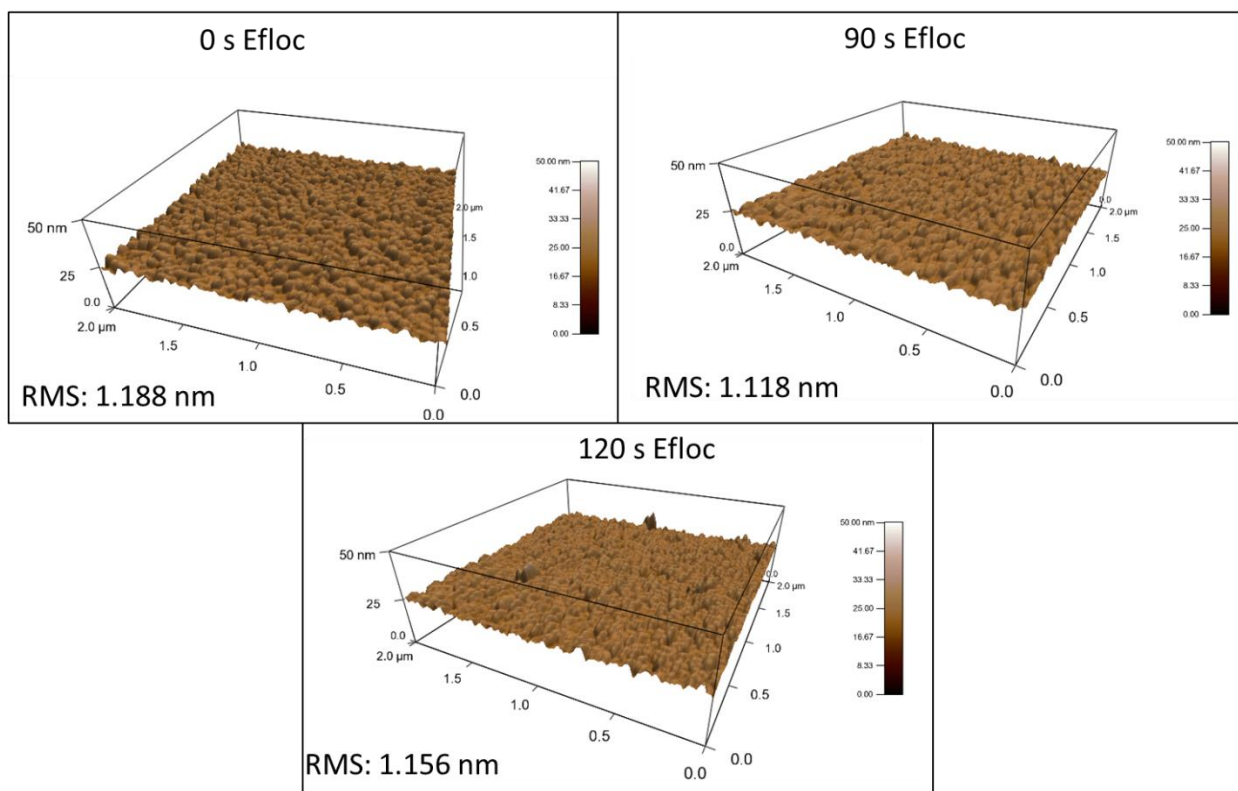
Figure 2.7: AFM of Au coated glass slides after varying times of electroflocculation in pH 13 IrO$_X$ NPs. Very little change in surface roughness (seen by the RMS) and topography is seen in the first 120 s of electroflocculation.

times, 5 minutes or longer, both SEM and AFM showed porous, non-uniform islands of NPs, as seen in Figure 2.6.

Atomic Force Microscopy (AFM) was implemented to study the topography of the films, specifically as a function of electroflocculation time; AFM was chosen as an alternative to SEM for these experiments due to its higher spatial resolution. AFM agrees with the eQCM data reported above. AFM images of films after 0, 90 and 120 s of electroflocculation are in the Figure 2.7. Films electroflocculated for 120 seconds and shorter times all very closely resemble a blank gold slide, in terms of topography and roughness factor (RMS), with the 120 second film appearing slightly rougher than the rest. These results support the eQCM data where there was no net increase in mass for films electroflocculated for 120 seconds or less, again suggesting an induction phase. Figure 2.8 depicts a film electroflocculated for 180 seconds at 0.9 V in pH 13 IrO$_X$ NP solution. Small islands of what is presumed to be IrO$_X$ NPs are visible at this point, as

indicated by the blue boxes. This corresponds with the induction period seen in the QCM data, as for the first two minutes or so, there is very little change in topography.

RMS: 1.188 nm

RMS: 1.418 nm
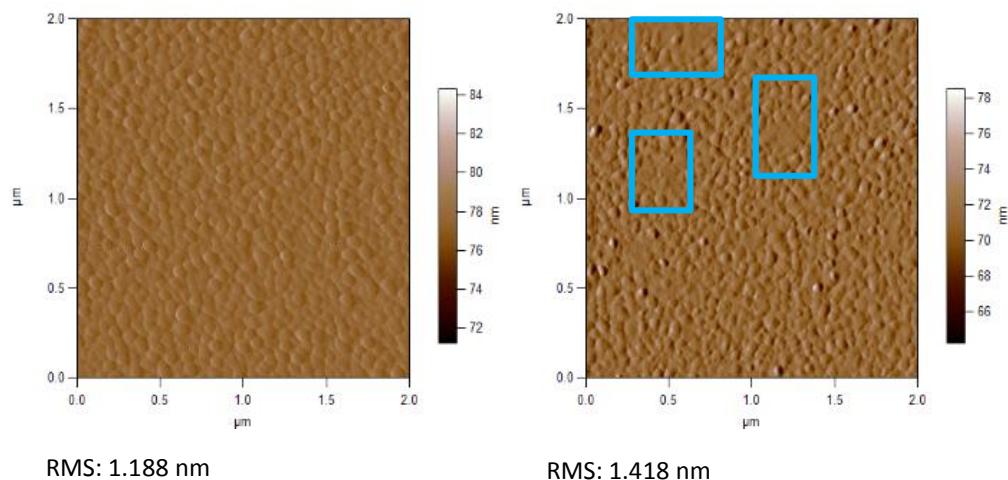
Figure 2.8: AFM images of Au coated glass slides subjected to 0 s (left) and 180 s (right) of electroflocculation. After 180 s, patches of IrO_X NPs are visible, as indicated by the blue squares.

2.3.2   Different Methods of Electrofloccuation

2.3.2.1   Constant Potential

Figure 2.9 depicts the coverages of Ir in mol/cm^2 obtained after electroflocculation at different potentials via constant potential by integrating both the $Ir^{IV/III}$ and $Ir^{V/IV}$ redox waves obtained by cyclic voltammetry in a pH 13 NaOH solution. Various scan rates were used and integrated and the standard deviation is representative of the variance of the Q over the difference scan rates. Ideally, there would be no variance and the coverage of iridium would be the same for both the $Ir^{IV/III}$ and $Ir^{V/IV}$ couples.

The overall trend for coverage of iridium with respect to electroflocculation potential is an increase of coverage with increase in potential. This is evident in the coverages calculated from the waves of both redox couples. This agrees with the proposed method of flocculation mentioned above, where the precipitation is induced via a local change in pH caused by water oxidation catalysis. As the applied potential increases, the rate of catalysis also increases and

protons are generated more quickly. This would lead to a larger localized pH change and theoretically, a greater number of precipitated nanoparticles.
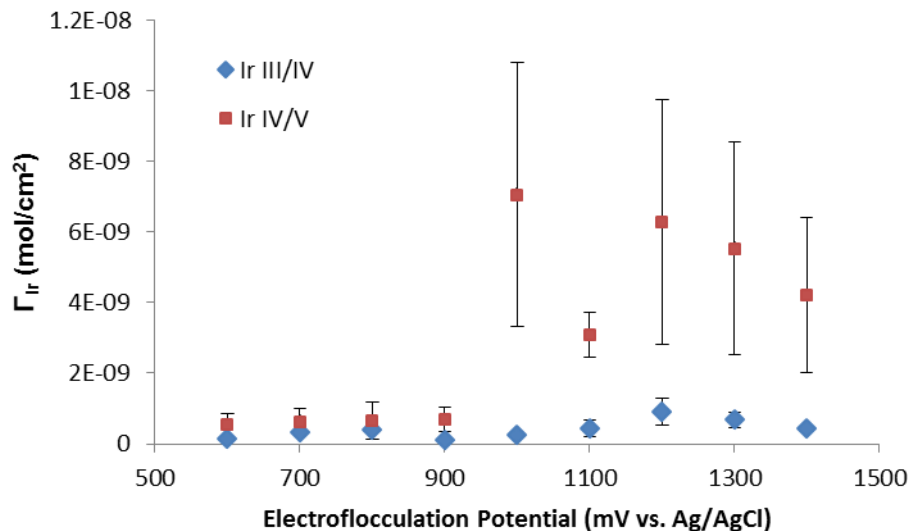
Figure 2.9: Coverage of Ir (Γ_{Ir}) after electroflocculation at different potentials, using the chronoamperometry method. The coverages calculated from the Ir$^{IV/III}$ couple is represented in blue and the coverages calculated from the Ir$^{V/IV}$ couple are in red.

At potentials above 1.2 V vs. Ag/AgCl, however, the trend breaks and we see a decrease in coverage. This is can also be explained through water oxidation catalysis. Another product of water oxidation is O_2 and if it is produced at a faster rate than which it can diffuse away, it will start to accumulate at the electrode surface. If the solution then becomes saturated past the solubility of O_2 in water, then the remaining O_2 will form bubbles at the electrode surface. These bubbles, which are visible during electroflocculation, will inhibit precipitation onto the electrode surface. At the higher applied potentials, enough bubbles are likely formed that it inhibits film formation, so we see a decrease in coverage.

The high applied potentials also resulted in a larger discrepancy between the coverages calculated from the Ir$^{V/IV}$ and those from the Ir$^{IV/III}$ waves. The average coverages for the Ir$^{V/IV}$ wave of films formed at applied potentials greater than 1 V were an order of magnitude larger than those for the Ir$^{IV/III}$ wave of the same films. These films agree with other findings from the

Murray lab[129], where there is an increase in conductivity between the two couples, resulting in a larger current and charge for the $Ir^{V/IV}$ wave. What is unique about this finding, however, is that
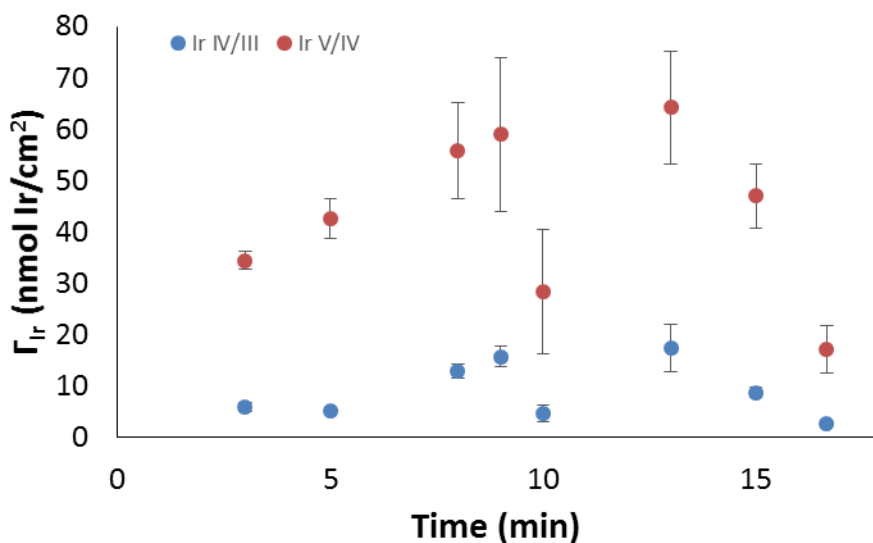
Figure 2.10: Coverage of iridium (Γ_{Ir}) for the $Ir^{V/IV}$ (red) and $Ir^{IV/III}$ (blue) waves with respect to length of electroflocculation in min at 1.2 V vs. Ag/AgCl.

there is a correlation between whether this effect is observed and the applied potential during electroflocculation. This can also be due to bubble formation during the water oxidation catalysis. As mentioned above, at higher applied potentials, bubbles result from a build-up of O_2 at the electrode surface. As the IrO_X NP films are mesoporous, these bubbles can also form within the film itself. This would cause breaks within the film and the decrease in connectivity between the different areas of IrO_X NPs would lead to a decrease in conductivity. This would result in a discrepancy between the Q passed by the $Ir^{IV/III}$ and $Ir^{V/IV}$ waves.

Figure 2.10 depicts how coverage changes of the IrO_X NP films with respect to how long the applied potential is held at 1.2 V vs. Ag/AgCl in as-synthesized pH 13 IrO_X NP solution. At electroflocculation times shorter than 10 minutes, there is a trend of increasing film coverage with increasing electroflocculation time. Starting at 10 minutes, however, there is no trend with

length of electroflocculation time. This is likely due to the high applied potential creating

bubbles at the electrode surface and inhibiting film formation.

From these studies, it was concluded that the best conditions for electroflocculating IrO_X

NP films via the constant potential method were potentials below 1.0 V vs. Ag/AgCl in pH 13

IrO_X NP solution. The reduced applied potential decreases the rate of water oxidation which

creates bubbles that inhibit film formation at the electrode surface. The bubbles can also affect

the conductivity throughout the film; when these films are used in potential devices, higher

conductivity is preferable.

2.3.2.2   Pulsing the Potential

Compared to a typical cyclic voltammogram of IrO_X NP films featured in Figure 2.1,

pulsing the potential to induce electroflocculation yielded oddly shaped cyclic voltammetry (CV)

of the films depending on the pulse length. These CVs are shown in Figure 2.11. The longest

pulse length (0.5 s at the upper potential limit) yielded CVs most closely resembling that of those

formed using the constant potential method. Two redox waves are observed, likely the same

$Ir^{IV/III}$ and $Ir^{V/IV}$ waves identified previously. The shorter pulse lengths, however, formed films

with slightly different electrochemistry. The two main redox waves at -0.3 and 0.1 V vs.

Ag/AgCl are still both present, corresponding to the $Ir^{IV/III}$ and $Ir^{V/IV}$ redox couples. However,

there also appears to be a third couple at 0.3 V vs. Ag/AgCl that previously wasn't present in

these films. This couple appears to be more diffusional in character, compared to the other two

redox couples. The ΔE_p is much closer to the standard 60 mV separation expected for a diffusing

species as opposed to the near 0 mV separation for species on the electrode surface. As the

nanoparticle films are mesoporous, one explanation for these species could be unbound IrO_X NPs

diffusing through the film. In larger films, such as those formed via the constant potential
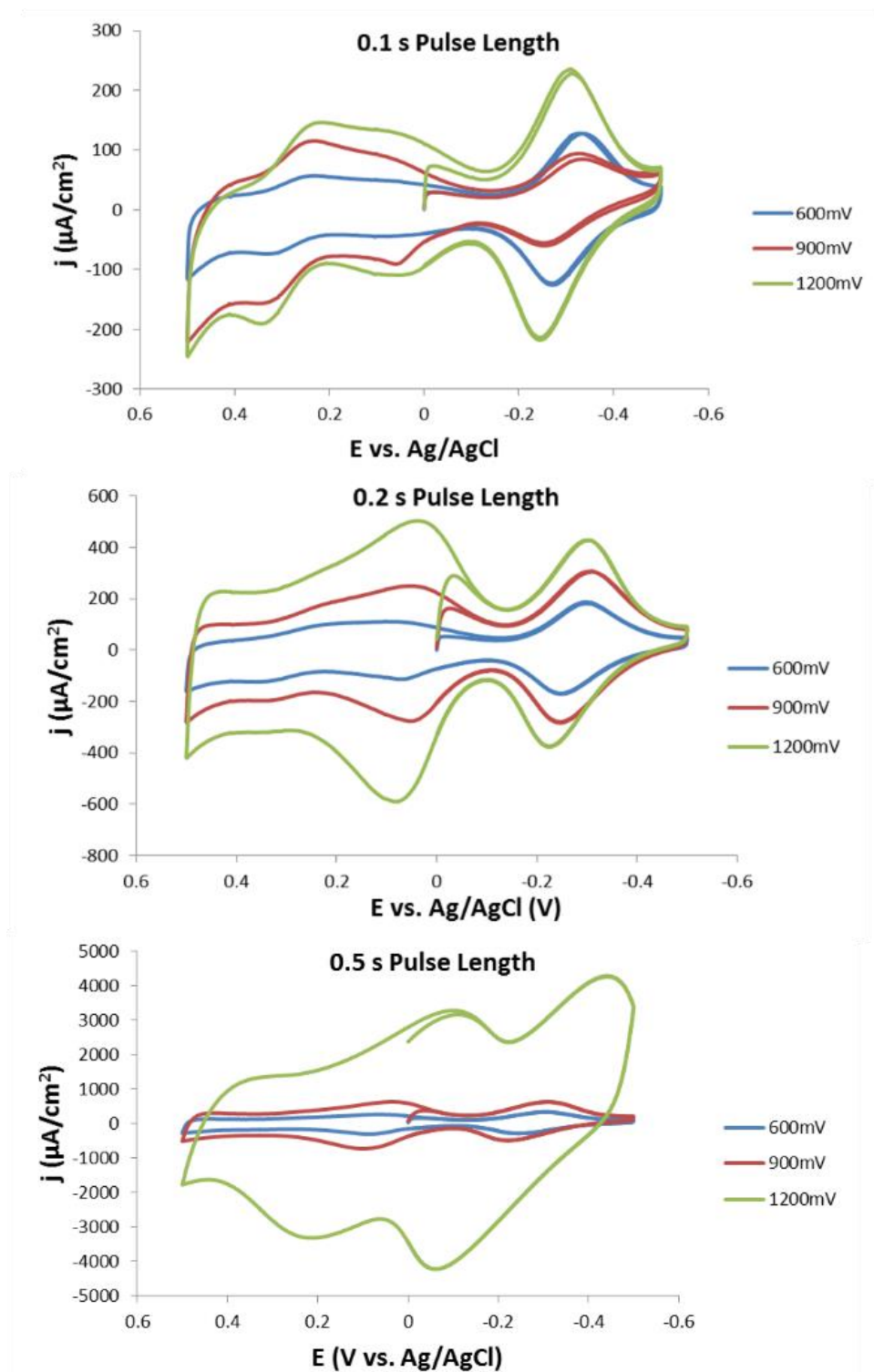
Figure 2.11: Cyclic voltammetry of the IrO$_X$ NP films formed via potential pulsing. The lower potential limit was 0 V vs. Ag/AgCl and the upper potential limit was varied between 1.2 V (green), 0.9 V (red) and 0.6 V (blue). The different pulse lengths were 0.1, 0.2 and 0.5 s at the upper potential limit. CVs were performed in fresh 0.1 M NaOH solution and the CVs shown above are at $v = 50$ mV/s.

method and at longer pulse lengths, these could blend into the Ir$^{V/IV}$ wave for the film, thus

accounting for the appearance of a much larger $Ir^{V/IV}$ wave compared to the $Ir^{IV/III}$ wave. The $Ir^{IV/III}$ wave for the diffusional species is much more negative than that of the film and therefore wouldn't be seen in the potential window above.

The other thing to notice is the significantly higher coverages associated with the longest pulse length (0.5 s). If an induction phase is still present for this method of electroflocculation, the longer pulse lengths would create a larger pH gradient at the electrode surface, which would lead to more flocculation and an increase in coverage of Ir. The coverage of each film with respect to the upper potential limit is shown in Figure 2.12. Also of interest, is the ratio of the coverage of $Ir^{IV/III}$ compared to that of $Ir^{V/IV}$. Previously, that ratio for most films was less than one, as the $Ir^{V/IV}$ wave was much larger than the $Ir^{IV/III}$ wave. With the pulsing, however, it is the $Ir^{IV/III}$ wave that is larger, and therefore has a higher coverage. The ratio of $Ir^{IV/III}$ to $Ir^{V/IV}$ for nearly all of the films formed by pulsing the potential is greater than one. The difference in ratio could be due to the ability to distinguish the waves at 0.1 V and 0.3 V vs Ag/AgCl. If both of these waves are present in the thicker films and are indistinguishable from the each other, than integrating the two together would lead to the appearance of a higher coverage of Ir from the $Ir^{V/IV}$ wave. The combined film and diffusional wave effect appears largely in films
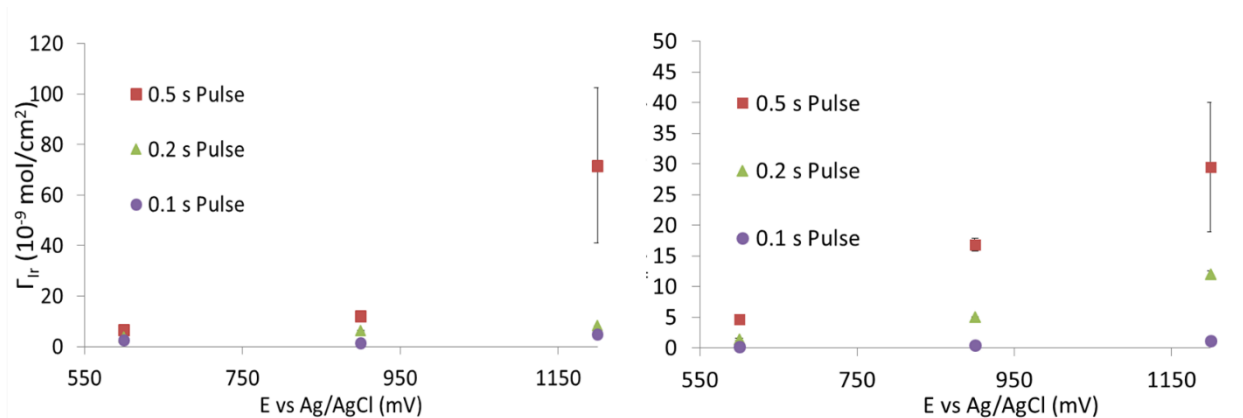
Figure 2.12: Coverage of iridium (Γ_{Ir}) with respect to the upper potential limit. Coverage for the $Ir^{IV/III-}$ couple is on the left and that for the $Ir^{V/IV}$ couple is on the right. The lower potential limit was 0 V vs. Ag/AgCl, while the upper potential limit is featured along the x-axis. Each pulse length is represented by a different symbol, 0.5 s as red squares, 0.2 s as green triangles and 0.1 s as purple circles.

electroflocculated with high upper potential limits or applied potentials. These diffusional peaks

may be caused by bubble formation within the film, which break off part of the IrO_X NP

flocculate, resulting in diffusional species within the film.

The lower potential limit was also varied for the same upper potential limits and pulse

lengths discussed above. The CVs of the varied potentials are similar to those featured in Figure

2.11. The coverages from these films formed with a lower potential limit of 0.2 V vs. Ag/AgCl

are shown in Figure 2.13. Those of the films flocculated with a lower potential limit of 0.6 V vs.

Ag/AgCl are in Figure 2.14.
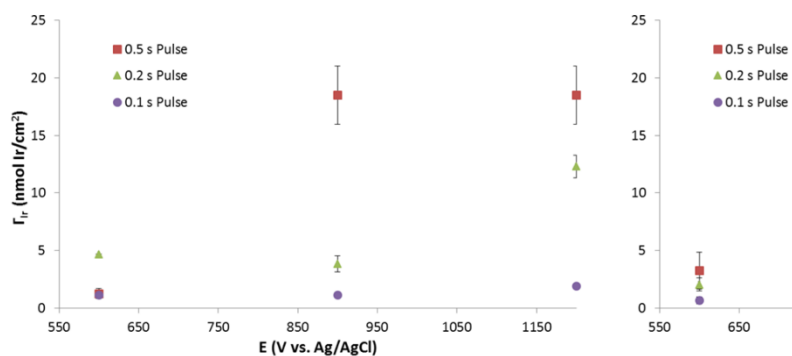
Figure 2.13: Coverages of iridium (Γ_{Ir}) for the $Ir^{IV/III}$ (left) and $Ir^{V/IV}$ (right) couples with a lower potential limit of 0.2 V vs. Ag/AgCl. The upper potential limit is shown on the x-axis and the different pulse lengths are in different colors, 0.5 s in red, 0.2 s in green and 0.1 s in purple.

By increasing the lower potential limit to 0.2 V from 0 V vs. Ag/AgCl, the ratio of $Ir^{IV/III}$

to $Ir^{V/IV}$ is much closer to one. The coverages calculated for each species are not statistically

different from one another. The same trend is observed for the pulse length, where an increase in

pulse length leads to higher coverage of Ir in both species. The upper potential limit, itself,

however, doesn't appear to have a significant effect on Ir coverage past 0.9 V vs. Ag/AgCl.

Comparing the lower potential limit of 0.2 V to 0 V vs. Ag/AgCl, there is a slight decrease in

iridium coverage by increasing the lower potential limit by 200 mV.

Only two upper potential limits were explored for the lower potential limit of 0.6 V vs.

Ag/AgCl, as keeping the upper potential limit at 0.6 V vs. Ag/AgCl would be the same
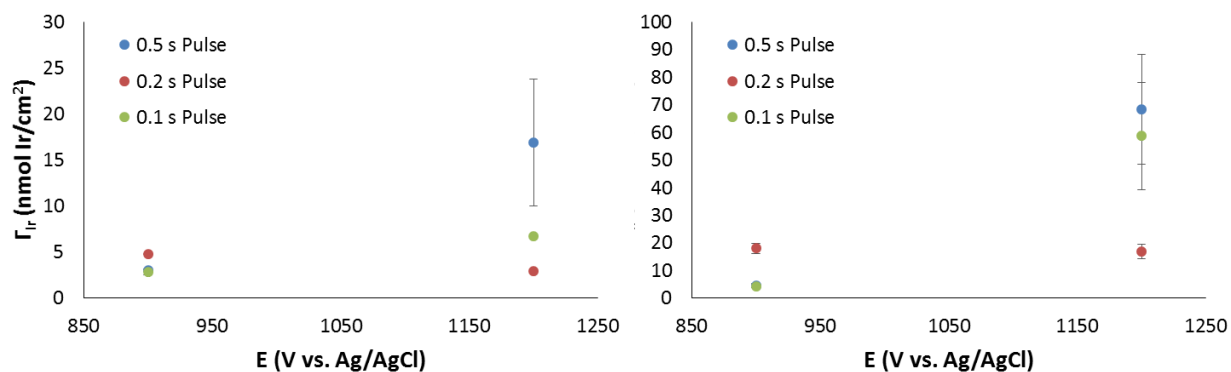
Figure 2.14: Coverages of iridium (Γ_{Ir}) for the $Ir^{IV/III}$ (left) and the $Ir^{V/IV}$ couples formed via potential pulsing with a lower potential limit of 0.6 V vs. Ag/AgCl. The upper potential limit is represented along the x-axis and the pulse length is represented by different colors, 0.5 s as blue, 0.2 s as red and 0.1 s as green.

experiment as the constant potential experiment at 0.6 V Ag/AgCl. The CVs of these films appear to have gone back to the usual trend seen in the constant potential flocculations, where the ratio of $Ir^{IV/III}$ to $Ir^{V/IV}$ is less than one. This makes sense, as the potential never dips below the onset of water oxidation catalysis. While there may be a decrease in the rate of catalysis at the lower potential limit, water oxidation is still occurring throughout the electroflocculation process and the films formed would be expected to behave similarly to those formed via the constant potential method. The increase in upper potential limit for these films still yields a higher coverage (although only two potentials were explored) and the longer pulse lengths yield higher Ir coverages as well.

2.3.2.3   Cycling the Potential

The films formed via cycling the potential in an as-synthesized IrO_X NP solution all yielded similar cyclic voltammetry when put into a new 0.1 M NaOH solution. An example of these CVs are in Figure 2.15, where each CV is from a different film formed by cycling the potential at different scan rates. The examples shown have a lower potential limit of 0 V vs. Ag/AgCl and an upper potential limit of 0.9 V vs. Ag/AgCl during electroflocculation. The
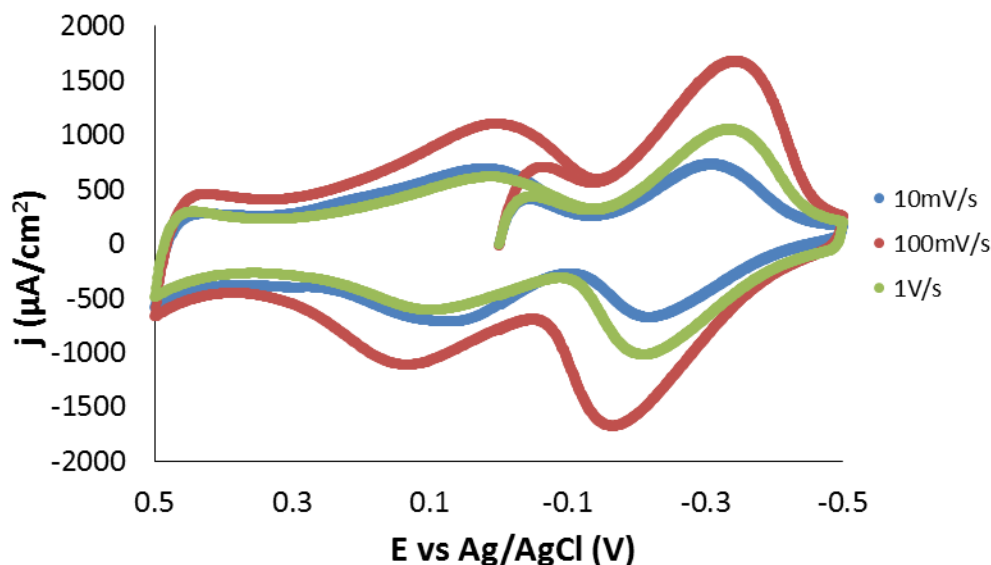
Figure 2.15: Cyclic voltammetry of three different films formed via potential cycling and different scan rates: 10 mV/s in blue, 100 mV/s in red and 1 V/s in green. Each CV was taken in a new 0.1 M NaOH solution at 50 mV/s.

waves for the Ir$^{IV/III}$ and Ir$^{V/IV}$ couples are relatively equal for this method, with the ratio of the two being slightly larger than one. The wave at 0.3 V vs. Ag/AgCl that is present in the pulsing method is not present in these cyclic voltammagrams. This suggests that the freely diffusing IrO$_X$ NPs, if those are responsible for the couple at 0.3 V, are not trapped within the mesoporous film.

The coverages obtained for the Ir$^{IV/III}$ and Ir$^{V/IV}$ waves via potential cycling with a lower potential limit of 0 V vs. Ag/AgCl are shown in Figure 2.16. As hinted at in the previous paragraph, the coverage for the Ir$^{IV/III}$ couple is slightly higher than that of the Ir$^{V/IV}$. For the fastest scan rate (1 V/s), Ir coverage increases with increasing upper potential limit, as expected. With the slower scan rates (10 and 100 mV/s), there is no apparent trend with upper potential limit, with the exception of the Ir$^{IV/III}$ coverage for the 10 mV/s cycling which decreases with increasing upper potential limit. This could be the equivalent to the high applied potentials in the constant potential method, as the slower scan rate results in longer continuous time at potentials

49

above the onset of water oxidation catalysis. This could lead to accumulation of O_2 at the electrode surface and therefore, film formation inhibition due to bubble formation.

Another important feature to note is the relatively small scatter in coverage with respect to scan rate, represented by the standard deviation on the graphs. These films are behaving more ideally, where the same charge is passed regardless of scan rate.

The lower potential limit was also varied for the potential cycling electroflocculation processes and the coverages obtained from the 0.4 V vs. Ag/AgCl lower potential limit are featured in Figure 2.18.

For the fastest scan rate (1 V/s), there is a slight increase in Ir coverage with increasing upper potential limit, although the difference in the $Ir^{IV/III}$ wave is statistically insignificant. There is no apparent trend for the film formed at 100 mV/s and the coverages for the slowest scan rate (10 mV/s) decrease with increasing upper potential limit. These are likely due to the same effect mentioned about the 0 V lower potential limit, where a slower scan rate can lead to the formation of bubbles at the electrode surface that inhibit electroflocculation. However, there are only two data points, so this should all be taken with a large grain of salt.
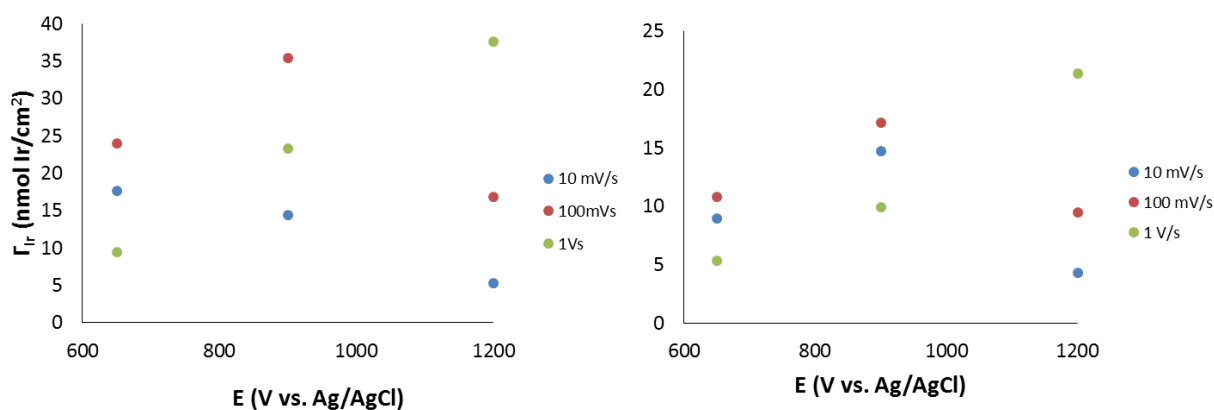
Figure 2.16: Coverages of iridium (Γ_{Ir}) from film formed via potential cycling with a lower potential limit of 0 V vs. Ag/AgCl for the $Ir^{IV/III}$ (left) and $Ir^{V/IV}$ (right) couples. The upper potential limit is represented along the x-axis and the scan rates are represented by different colors, 10 mV/s in blue, 100 mV/s in red and 1 V/s in green.

50
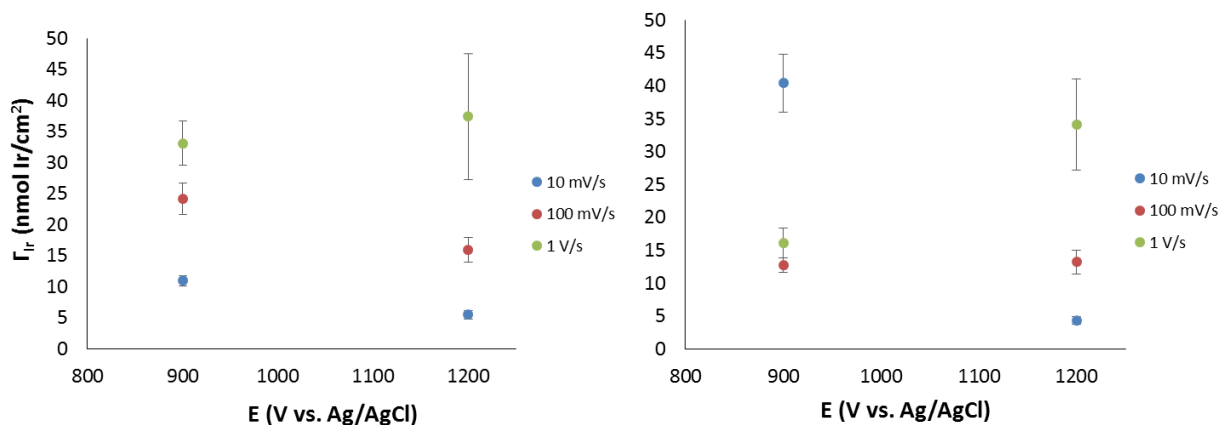
Figure 2.18: Coverages of iridium (Γ_{Ir}) from film formed via potential cycling with a lower potential limit of 0.4 V vs. Ag/AgCl for the $Ir^{IV/III}$ (left) and $Ir^{V/IV}$ (right) couples. The upper potential limit is represented along the x-axis and the scan rates are represented by different colors, 10 mV/s in blue, 100 mV/s in red and 1 V/s in green.

The coverages of Ir for the lower potential limit of 0.6 V vs. Ag/AgCl is exhibited in Figure 2.17. There is no apparent trend for upper potential limit or variance in scan rate. Again, there are only two data points so these "trends" are only so accurate. However, there does appear to be a trend for the lower potential limit and ratio of coverage of the $Ir^{IV/III}$ to $Ir^{V/IV}$ couples. The ratio of the $Ir^{IV/III}$ to $Ir^{V/IV}$ coverages for the films formed with a lower potential limit of 0 V vs. Ag/AgCl most closely resembled those of the potential pulsing, where the ratio is greater than one. The Ir coverages of the films electroflocculated with a lower potential limit of 0.6 V, however, more
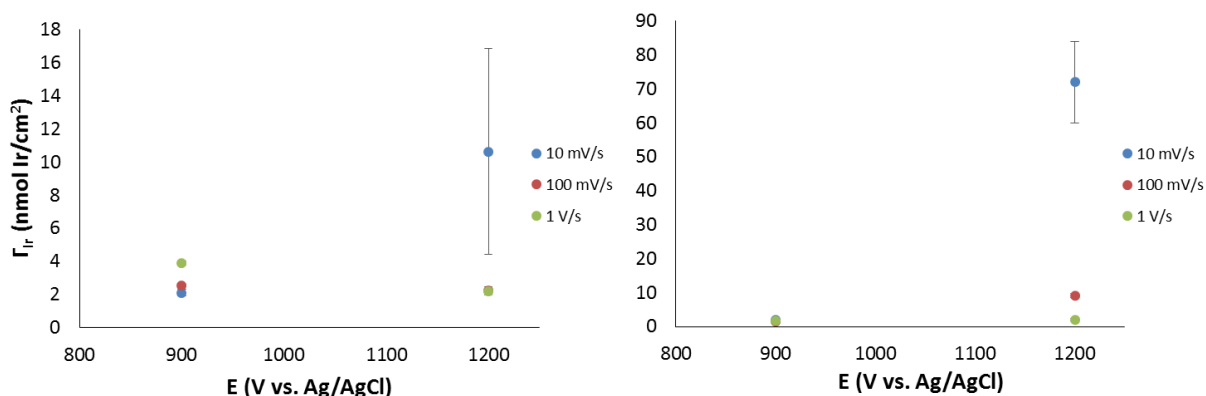
Figure 2.17: Coverages of iridium (Γ_{Ir}) from film formed via potential cycling with a lower potential limit of 0.6 V vs. Ag/AgCl for the $Ir^{IV/III}$ (left) and $Ir^{V/IV}$ (right) couples. The upper potential limit is represented along the x-axis and the scan rates are represented by different colors, 10 mV/s in blue, 100 mV/s in red and 1 V/s in green.

51

closely resemble the films formed via the constant potential method, where the ratio of $Ir^{IV/III}$ to $Ir^{V/IV}$ is less than one. The films deposited with the lower potential limit of 0.4 V are right in the middle of these two extremes, where the ratio of $Ir^{IV/III}$ to $Ir^{V/IV}$ is very close to one. This trend is likely due to the time spent not above the onset of water oxidation. For the most negative lower potential limit (0 V vs. Ag/AgCl), there is more continuous time spent not at potentials above the onset of water oxidation. This time is equivalent to the lower potential limit pulse in the pulsing technique, so the electroflocculation methods create similar films. In these cases, there is more time for O_2 to diffuse away from the electrode surface, resulting in a decrease in bubble formation.

On the opposite side of the spectrum, the films formed via cycling with a lower potential limit of 0.6 V vs. Ag/AgCl never spend any time below the onset of water oxidation catalysis. There is a slight change in rate of catalysis, but this method is essentially identical to the constant potential method and they therefore deposit similar IrO_x NP films. Bubble formation in the more positive lower potential limit case results in film breakage which contributes to the high $Ir^{V/IV}$ charge and coverage, as seen in the constant potential films.

2.3.2.4 Comparison of Various Electroflocculation Methods
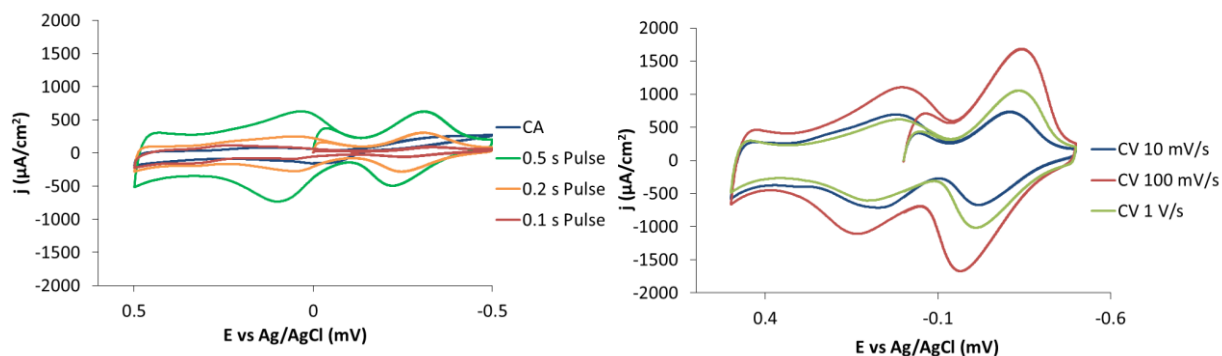
Figure 2.19: Cyclic voltammetry of films formed via different methods of electroflocculation. Constant potential and potential pulsing is represented on the left and potential cycling on the right. The different pulse lengths and scan rates for the potential pulsing and potential cycling respectively are noted in the legend. Each film was electroflocculated with the same amount of time spent above the onset of water oxidation catalysis. Each of these CVs is taken in 0.1 M NaOH at 50 mV/s.

2.3.2.4.1 Cyclic Voltammetry and Coverages of Ir of Different Electroflocculation Methods

Cyclic voltammetry of a representative film from each electroflocculation method is depicted Figure 2.19. Each of these films has an upper potential limit of 0.9 V vs. Ag/AgCl and a lower potential limit of 0 V vs. Ag/AgCl and they each spent an equivalent amount of time above the onset of water oxidation (10 minutes), although not continuously for the potential cycling and pulsing techniques. At first glance, the current passed for the film formed via the constant potential method is the lowest out of all of the films, followed by the shortest pulse length of potential cycling through the longest pulse length. The potential cycling appears to yield the thickest film (based off of current), although there is no trend within the potential cycling films with regard to scan rate. The overall shape is important to note as well. The film formed with the constant potential method exhibits a larger $Ir^{V/IV}$ wave than $Ir^{IV/III}$. The films formed via potential pulsing have relatively equivalent $Ir^{V/IV}$ and $Ir^{IV/III}$ waves. The potential cycling films, however, have larger $Ir^{IV/III}$ waves compared to the $Ir^{V/IV}$ waves.
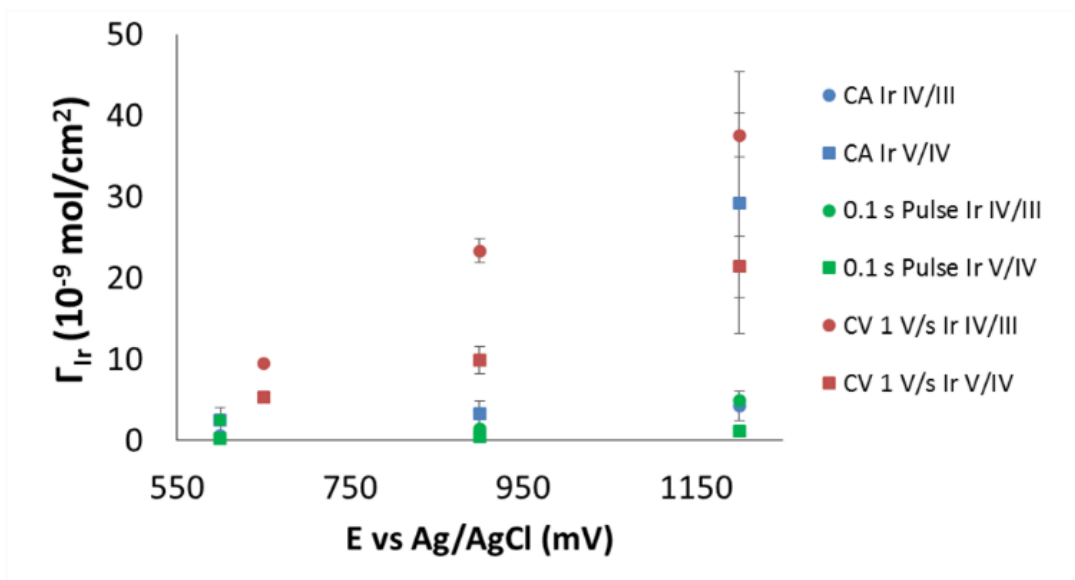
Figure 2.20: Coverages of iridium (Γ_{Ir}) for films formed via different electroflocculation methods, depicted in the legend on the right. The $Ir^{IV/III}$ values are represented by circles, while the $Ir^{V/IV}$ values are squares. The blue data points denote values obtained from a film formed via constant potetial, while the green data points are from films flocculated by potential pulsing and the red from potential cycling. The lower potential limit is 0 V vs. Ag/AgCl for all films.

The Ir coverages for the films created via the constant potential method, 0.1 s potential pulses and 1 V/s scan rates are displayed in Figure 2.20, as well as those from the upper potential limits of 0.6-0.65 V and 1.2 V vs. Ag/AgCl. Potential pulsing and cycling methods had a lower potential limit of 0 V vs. Ag/AgCl. Looking at the difference in coverage between the $Ir^{V/IV}$ and $Ir^{IV/III}$ waves, the potential pulsing remained the most consistent for each applied potential, where there was a slight discrepancy between coverage, but the overall ratio of the $Ir^{IV/III}$ and $Ir^{V/IV}$ waves was very close to one. The difference between the $Ir^{IV/III}$ and $Ir^{V/IV}$ waves increases with increasing upper potential limit for the potential cycling and constant potential methods; however, the ratio of $Ir^{IV/III}$ and $Ir^{V/IV}$ changes in opposite directions. For the potential cycling methods, the ratio increases, as the $Ir^{IV/III}$ couple becomes significantly larger than the $Ir^{V/IV}$ couple. For the constant potential methods, the ratio of $Ir^{IV/III}$ and $Ir^{V/IV}$ decreases with increasing applied potential as the $Ir^{V/IV}$ wave becomes much larger than the $Ir^{IV/III}$ wave.

Also of importance is the variance of calculated coverage with respect to scan rate, denoted by the standard deviations in Figure 2.20. As the upper potential limit and/or applied potential increases, the standard deviation also increases. If these were ideally behaved films, there would be no change in the charge passed, and therefore coverage of Ir, with respect to scan rate. Therefore, the most ideal films are formed at the lower applied potentials and/or upper potential limits.

There are significant changes to the IrO_X NP films that are formed via different methods of electroflocculation, based on the shape of the cyclic voltammetry and the charge passed for each Ir redox couple. Ideally, the ratio of the two Ir redox couples would be equal and the charge underneath each of this couples would not vary with respect to scan rate. Based on these two criteria, the preferred method of electroflocculation would involve a low applied potential or

54

upper potential limit. However, this must be balanced with thickness of film, as a higher

coverage of catalyst would result in higher rates of catalysis. Taking this into consideration, an

upper potential limit of 0.9 V for either the potential cycling or potential pulsing method meets

both the ideal electrochemical film behavior and film thickness requirements.

2.3.2.4.2 SEM of Film Formed via Different Electroflocculation Methods

Examples of images obtained by scanning electron microscopy (SEM) of the IrO_X NP

films are seen in Figure 2.21. The top row of images (a, b and c) are all films made using the

constant potential technique, with varying applied potential. A, b and c correspond to an applied

potential of 0.6, 0.9 and 1.2 V vs. Ag/AgCl. The middle row (d and e) are both films deposited

using the potential pulsing technique. D corresponds to a film electroflocculated with an upper

potential limit of 0.9 V vs. Ag/AgCl and a lower potential limit of 0.6 V vs. Ag/AgCl, while e

was formed with an upper potential limit of 0.9 V vs. Ag/AgCl and lower potential limit of 0 V

vs. Ag/AgCl. The bottom images (f, g and h) are of films flocculated via the potential cycling

method, with upper and lower potential limits of 0.9 and 0 V vs. Ag/AgCl. Each letter

corresponds to a different scan rate; 10 mV/s, 100 mV/s and 1 V/s are depicted in images f, g and

h, respectively.

Looking at the images of the films formed via the constant potential technique, there is a

distinct increase of film coverage with increase applied potential. The film formed at 0.6 V vs.

Ag/AgCl is still quite sparse throughout the electrode surface, with only small islands of IrO_X NP

flocculates randomly space across the surface. It resembles a film formed at a higher potential

over a short amount of time (< 5 min). For the films formed at 0.9 and 1.2 V vs Ag/AgCl, the

entire electrode is covered with IrO_X NPs. What started out as islands (as seen in Figure 2.6), has

grown together to create a mesoporous film on the Au surface. Elemental analysis via Energy

Dispersive X-ray Spectroscopy (EDS) confirmed the presence of Ir throughout the surface, as well as the high atomic concentration (3-6%), indicating a fairly thick film on the electrode surface.

Images of the films electroflocculated with the potential pulsing method demonstrated that the films still form islands in the beginning stages of deposition. This indicates that there is similarity to the mechanism of electroflocculation compared to the constant potential technique. EDS confirmed that that the brighter spots in the images are the IrO_X NP flocculates, based on the Ir atomic concentration (4-5%). The darker areas still had some Ir present, although the Ir
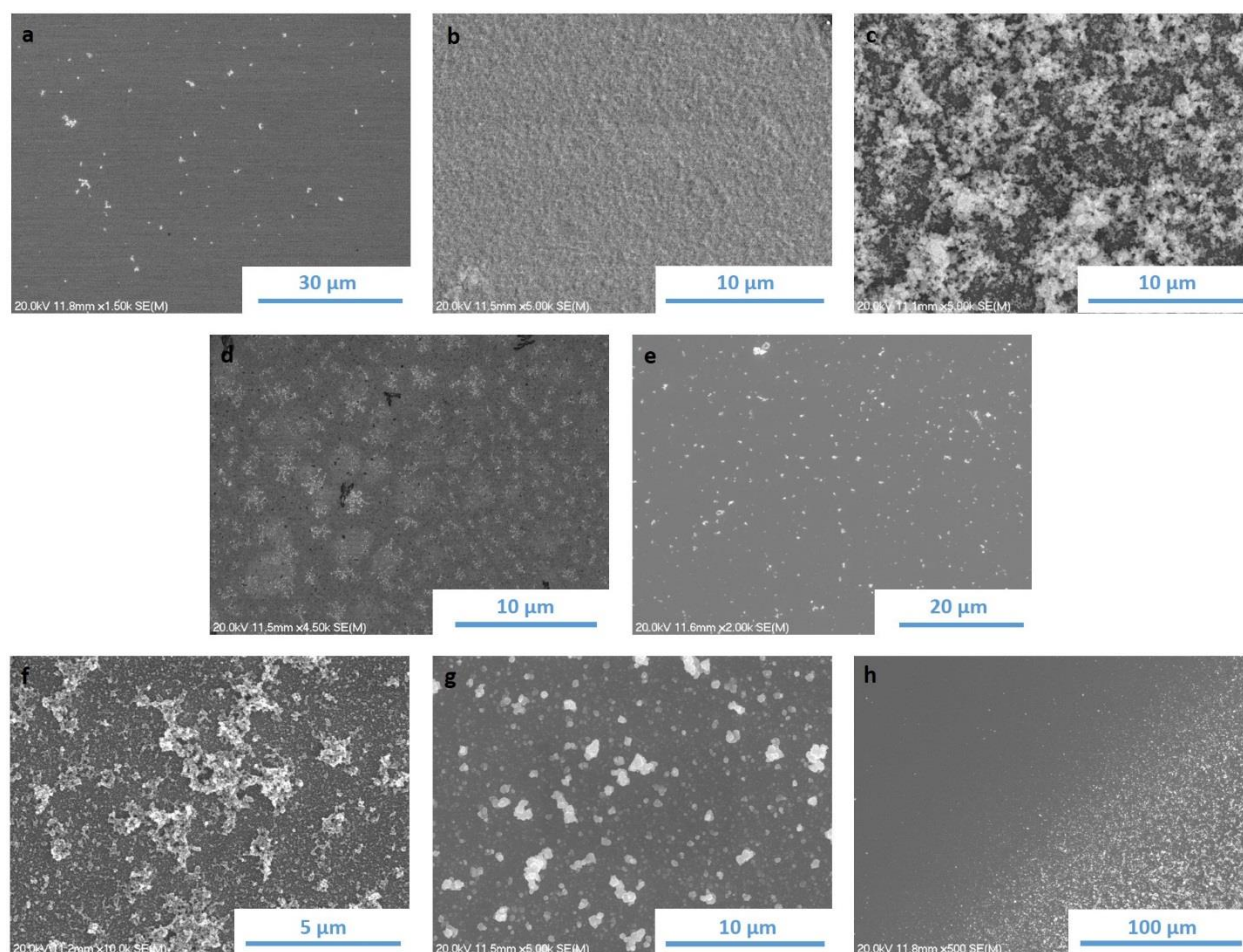
Figure 2.21: SEM images of electroflocculated IrO_X NP films formed via different electroflocculation methods.. (a) Constant potential with applied potential of 0.6 V. (b) Constant potential with applied potential of 0.9 V. (c) Constant potential with applied potential of 1.2 V. (d) Potential pulsing, 0.5 s pulse, upper potential limit of 0.9 V and lower potential limit of 0.6 V. (e) Potential pulsing, 0.5 s pulse, upper potential limit of 0.9 V and lower potential limit of 0 V. (f) Potential cycling, 10 mV/s scan rate, upper potential limit of 0.9 V and lower potential limit of 0 V. (g) Potential cycling, 100 mV/s scan rate, upper potential limit of 0.9 V and lower potential limit of 0 V. (h) Potential cycling, 1 V/s scan rate, upper potential limit of 0.9 V and lower potential limit of 0 V. All potentials are versus a Ag/AgCl reference electrode.

56

atomic concentration was low (< 2%). It is likely that if the pulsing method were performed for longer periods of time (> 10 total min more positive than the onset of water oxidation catalysis), the islands would eventually grow together to form films similar to those seen in Figure 2.21b and Figure 2.21c.

The films electroflocculated via potential cycling (Figure 2.21f, g and h) appear to also deposit in IrO_X NP islands initially as well, particularly seen in the films formed at the faster scan rates (100 mV/s and 1 V/s). EDS ratified that the brighter areas in the images were IrO_X NPs. For the film formed at 1 V/s, the darker areas of the electrode showed very little Ir concentration (< 1% Ir). The darker areas of the film flocculated at 100 mV/s exhibited higher concentrations of Ir (~2%), compared to the faster scan rate. At the slowest scan rate, the film morphology resembles that of a film formed via the constant potential method, where it's starting to cover the entire electrode surface. EDS confirmed this with an atomic concentration ranging from 4-6% Ir.

2.3.3 Chemical Flocculation of Iridium Oxide Nanoparticles

For comparison, a chemical flocculation was attempted, using Ce(IV) as an oxidant. When a four-fold excess of Ce(IV) was added (i.e., four times the charge accumulated during the
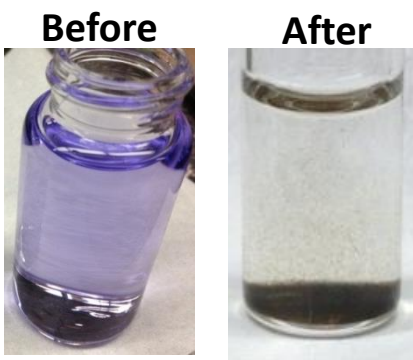
Figure 2.22: IrO_X NP solution as-synthesized as pH 13 (left) and after the addition of CAN (right). The solution changes from a clear, purple solution to a colorless solution with a brown precipitate.

57

induction phase of electroflocculation), the normally purple solution turned colorless and a brown precipitate formed at the bottom of the vessel, as seen in Figure 2.22.

In another test, a 1 mM solution of Ce(IV) oxidant was added gradually to the pH 13 IrO$_X$ NP solution. A color change was observed, first to a pale blue and then to a light brown, neither with any visible precipitate. However, addition of excess oxidant to the solution produced a brown precipitate; the solution remained brown as well. When left at room temperature for 15 hours, the solution turned colorless to resemble the resulting solution of the first chemical flocculation test.

X-ray Photoelectron Spectroscopy (XPS) performed on both precipitates reveal a similar spectrum for each. The spectrum for the precipate formed in the second trial is seen in Figure 2.23. The expected signals for Ir, Ce, Na, O and Au were all present. The atomic ratio of Ce to Ir was roughly 2:1; this corresponds with the expected reaction, where two Ce(IV) would be needed to oxidize Ir^{IV} to Ir^{VI} which then flocculate. The precipitate included Ce due to the insolubility of Ce(OH)$_3$, as the NPs are synthesized in a pH 13 solution. Chemical flocculation by Ce(IV), therefore, is a less clean way to flocculate the IrO$_X$ NPs. The presence of Ir in the
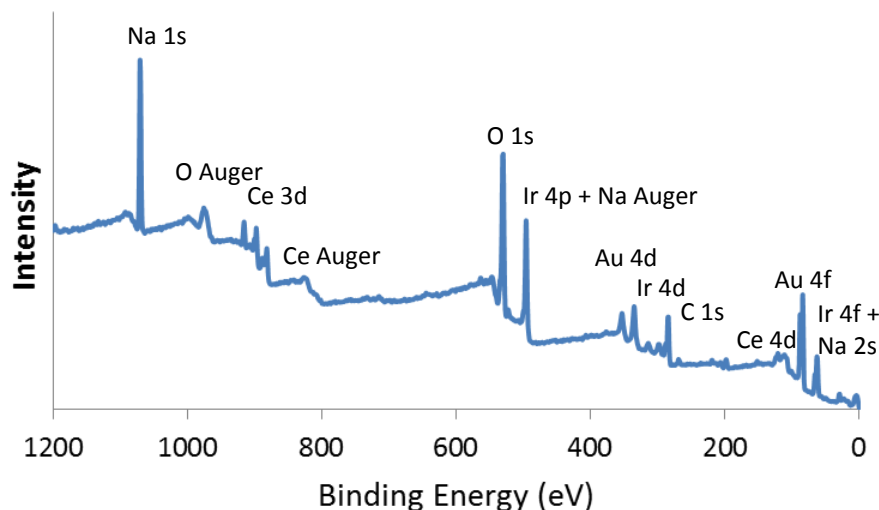
Figure 2.23: XPS of the precipitate formed via "chemical flocculation" of the IrO$_X$ NPs with Ce(IV). The precipitate was drop-cast onto a Au coated glass slide.

precipitate is consistent with the precipitation mechanism of the electroflocculation discussed above, where enough charge must be passed in order for the NPs to flocculate and fall out of solution.

2.3.4 Direct pH Change for Iridium Oxide Nanoparticle Precipitation

From the hypothesis that a localized change in pH was triggering the flocculation and and film formation of the IrO_X NPs, directly changing the pH of the solution was explored as a means to deposit a film. A non-coordinating acid, $HClO_4$, was chosen, as previous studies had shown that coordinating acids, such as H_3PO_4, can stabilize IrO_X NPs in solution, which would defeat the purpose.[1] A sufficient concentration of acid was added in order to neutralize the 0.1 M NaOH present in the as-synthesized IrO_X NP solution and it was allowed to sit at RT for 24 hours in order to stabilize. Different electrode slides were then dipped into the pH adjusted solution. Films were successfully formed on *nano*ITO, TiO_2, Au and *nano*ITO/TiO_2 core/shell electrodes, as well as on top of two different Ru polypyridal complexes. Film formation was unsuccessful for Au surfaces that were not previously cleaned via piranha solution and on a film comprised of a porphryin based complex. This is likely due to the more hydrophobic nature of these surfaces, suggesting that the IrO_X NP films are preferential to hydrophilic surfaces. More on this is discussed in Chapter 5. There does appear to be a time window of deposition where this dip-coating method works. Films will not form within the first 24 hours after adding the acid and after 72 hours of sitting on the benchtop, the IrO_X NPs have completely precipitated out of solution onto the bottom of the vial. Once they have reached this phase, they are no longer viable to create films on other surfaces. The ideal window for this method is between 24 and 48 hours after acid addition.

2.4 CONCLUSIONS

The above results demonstrate how the electroflocculation of IrO_X NPs is a precipitation process. The induction period observed via eQCM and AFM correlates to an amount of charge passed in order for the NPs to flocculate. The charge, in turn, is related to the acidification of the interface by the water oxidation process, initiating the NP flocculation. Electroflocculation in lower pH solutions yields significantly smaller films, suggesting that the mechanism has changed, possibly due to the change of surface of the IrO_X NPs. The NPs precipitate onto whatever surface is present, creating a film.

Three different electroflocculation methods were explored: constant potential, potential pulsing and potential cycling. Based off of their electrochemistry and micrscopy, the most ideal films were formed via the potential cycling and pulsing techniques. There appears to be a balance of H^+ formation to induce flocculation and O_2 formation that inhibits film deposition onto the electrode surface that is met by varying the potential applied by the electrode.

Flocculation via chemical methods and direct pH change further endorses the localized pH change mechanism for electroflocculation. All of these methods create IrO_X NP films without any stabilizing ligand, which could lead to an increase in catalytic activity. The data provide deeper insight into the creation of these films and how the structure could affect their catalytic properties for water oxidation.

2.5 ACKNOWLEDGEMENT

of the SEM, AFM and XPS facilities at the Chapel Hill Anatlytical and Nanofabrication

Laboratories. The exploration of different electroflocculation techniques was performed by

Robert Kieber (undergraduate researcher), including the preparation and cyclic voltammetry of

all of the films, as well as the integrations and conversions to coverage.

REFERENCES

(1)   Gambardella, A. A.; Bjorge, N. S.; Alspaugh, V. K.; Murray, R. W. *J. Phys. Chem. C* **2011**, *115*.

(2)   Gambardella, A. A.; Feldberg, S. W.; Murray, R. W. *J. Am. Chem. Soc.* **2012**, *134*, 5774.

(3)   Lee, Y.; Suntivich, J.; May, K. J.; Perry, E. E.; Shao-Horn, Y. *J. Phys. Chem. Lett.* **2012**, *3*, 299.

(4)   Morris, N. D.; Suzuki, M.; Mallouk, T. E. *J. Phys. Chem. A* **2004**, *108*, 9115.

(5)   Nakagawa, T.; Beasley, C. A.; Murray, R. W. *J. Phys. Chem. C* **2009**, *113*, 12958.

(6)   Nakagawa, T.; Bjorge, N. S.; Murray, R. W. *J. Am. Chem. Soc.* **2009**, *131*.

(7)   Ouattara, L.; Fierro, S. *J. Appl. Electrochem.* **2009**, *39*, 1361.

(8)   Yagi, M.; Tomita, E.; Sakita, S.; Kuwabara, T.; Nagai, K. *J. Phys. Chem. B* **2005**, *109*, 21489.

(9)   Zhao, Y.; Hernadez-Pagan, E. A.; Vargas-Barbosa, N. M.; Dysart, J. L.; Mallouk, T. E. *J. Phys. Chem. Lett.* **2011**, *2*, 402.

(10)   Zhao, Y.; Vargas-Barbosa, N. M.; Hernandez-Pagan, E. A.; Mallouk, T. E. *Small* **2011**, *7*, 2087.

(11)   Schley, N. D.; Blakemore, J. D.; Subbaiyan, N. K.; Incarvito, C. D.; D'Souza, F.; Crabtree, R. H.; Brudvig, G. W. *J. Am. Chem. Soc.* **2011**, *133*, 10473.

(12)   Chow, K. F.; Carducci, T. M.; Murray, R. W. *J. Am. Chem. Soc.* **2014**, *136*, 3385.

CHAPTER 3: Characterization of Iridium Oxide Nanoparticles

3.1   INTRODUCTION

While the catalytic activity of iridium oxide nanoparticles has been thoroughly explored, little is known about the surface chemistry and why these nanoparticles are such efficient catalysts. There has been extensive research on the bulk counterpart, IrO_2, in terms of traditional characterization techniques, such as Raman, UV-Vis and X-ray photoelectron spectroscopy.[1-17] However, little of it has been applied to the IrO_X NPs. Due to their very small size (< 2 nm in diameter), these nanoparticles have a high surface area to volume ratio. Because of this, understanding the surface chemistry and how it affects the catalytic ability of the IrO_X NPs is paramount.

The bulk material IrO_2 has gained a lot of attention for use as a durable anode material.[1,4,5,7,13,17-21] It can also catalyze the water oxidation reaction, though at a higher overpotential compared to its high surface area nanoparticle counterpart.[22-28] These films can be prepared by a variety of methods, most involving the metallic Ir species undergoing oxidizing conditions. These materials have been extensively characterized using microscopy, spectroscopy and other methods, all with similar results.

Raman spectroscopy, in particular, has proven a useful tool for elucidating structural features of a material. Extensive research has been performed on various iridium oxide materials, including sputtered iridium oxide films (SIROF), electrodeposited iridium oxide films (EIROF), IrO_2 formed via thermochemical methods and single crystal IrO_2.[3,7-9,13-16,29] The large majority of these films exhibited tetragonal rutile structure, where the B_{1g}, E_g, A_{1g} and B_{2g} modes

are Raman active. These Raman shifts appear at 145, 561, 752 and 728 cm^{-1}, respectively.

Additional Raman peaks have been observed at 366 and 456 cm^{-1}, which correspond to the Ir=O

and Ir-O stretching modes. In most Raman spectra collected of IrO$_2$ films, the rutile structure is

confirmed by the presence of two major peaks, corresponding to the E$_g$ and combined A$_{1g}$ and

B$_{2g}$ modes. These peaks are always present, though their exact peak position and full width half

max can vary depending on the surface on which it has been deposited.[7,12] The one exception to

this is the EIROF, which exhibits multiple overlapping peaks from 445 to 744 cm^{-1}.[8] While

some of these peaks overlap with the rutile peaks addressed above, the other peaks suggest that

there is limited crystalline structure to these EIROFs.

IrO$_2$ is tetragonal rutile in crystalline structure and it has long been assumed that the IrO$_X$

NPs have chemical aspects similar to IrO$_2$. There are some literature examples that refer to them

as IrO$_2$ NPs, though largely without any experimental justification.[25,30-32] The NPs are typically

synthesized using a Woehler method,[33] where an Ir^{IV} chloride salt undergoes a basic hydrolysis

to form IrO$_X$ NPs at relatively low temperatures. Because of the lack of oxidative or reductive

conditions, it was largely assumed that the Ir maintained its Ir^{IV} oxidation state. The research

presented below sets out to compare the Raman spectra of these NPs to their bulk counterparts

and determine whether the assumption is valid.

X-ray analysis methods, such as x-ray absorption spectroscopy (XAS), X-ray absorption

near-edge structure (XANES), extended x-ray absorption fine structure (EXAFS) and x-ray

photoelectron spectroscopy (XPS), have been used to further probe the structure of bulk IrO$_2$

and, more recently, larger IrO$_X$ NPs.[2,5,6,10,11,34,35] X-ray techniques are popular for both elemental

analysis and determining the oxidation states and surrounding environment of each element. In

particular, XANES has been used to demonstrate a shift in the Ir L$_3$-edge towards higher energies

as it is electrochemically oxidized.[2] Similarly, when the IrO_2 films are formed on other

substrates, the Ir L_3-edge can shift depending on whether the substrate acts as a reducing or

oxidizing agent.[10] EXAFS was also able to demonstrate structural disorder in electrodeposited

bulk material IrO_2 films, as well as identify two different Ir-O bond lengths within the sample

(1.995 and 1.959 Å). These bond lengths also changed with applied potential; as the IrO_2 films

were oxidized, the Ir-O bond lengths shortened.[2]

XPS, conversely, has largely been used to examine the oxidation states of various iridium

oxide materials, focusing on thermally deposited and electrochemically deposited IrO_2 films.[6,34]

A doublet is usually observed at 62 and 65 eV, corresponding to the Ir $4f_{7/2}$ and Ir $4f_{5/2}$ orbital

electrons. Tailing is also observed with these doublets, attributed to the 5d electron screening.[6,36]

More recently, the Nilsson laboratory developed an ambient-pressure XPS in order to

incorporate electrochemical experiments.[5] They applied this to the study of water oxidation

catalysis via IrO_X NPs (50-80 nm in diameter) and determined that the surfaces of the IrO_X NP

films was a mixture of both the oxide and hydroxide species. They also determined that water

oxidation undergoes a deprotonation mechanism, where the hydroxide is oxidized to the oxide

species on the surface of the catalyst.[35] The research presented below aims to demonstrate how

the small IrO_X NPs (< 2 nm in diameter) compare to both the bulk IrO_2 and larger IrO_X NPs

using XPS, as well as demonstrate how the surrounding environment can deeply impact the

spectra obtained.

Previous work by the Murray laboratory has focused on trying to characterize small IrO_X

NPs by altering their surface chemistry with capping ligands such as carboxylates.[37] These

capped NPs were then analyzed using techniques such as mass spectrometry and NMR. While

the exchange into non-aqueous solvents was successful, the constant exchange of the capping

ligands resulted in difficult quantification. In the work presented below, the goal was to largely characterize them either in aqueous media, to remove the solvent entirely by electroflocculating the NPs into a film, or precipitating them using a variety of methods. Eliminating this uncertainty simplifies analysis of the IrO_X NPs. Presented below are electrochemical, microscopic, spectroscopic and zeta potential investigations with the aim to better understand the surface chemistry behavior of small IrO_X NPs.

3.2 EXPERIMENTAL

3.2.1 Aqueous Hydrolysis of IrO$_X$ NPs

The $Ir^{IV}O_X$ nanoparticles were synthesized using a Wohler method,[33] in which a 2.5 mM solution of K_2IrCl_6 (99%, Strem Chemicals) in nanopure H_2O was adjusted to pH 13 with 25% w/w NaOH (50% w/w, Fisher Scientific). The solution was heated at 90 °C for 20 minutes and then allowed to cool to RT and to rest for at least 24 hours after the synthesis, before electroflocculation.

3.2.2 Electroflocculation of IrO$_X$ NP Films

For electroflocculations on Au coated glass slides, Au slides were first cleaned by exposure to piranha solution (3:1 concentrated H_2SO_4 (Fisher Scientific) to H_2O_2 (30% w/w, Fisher Scientific)), and then rinsed with nanopure H_2O and dried under a stream of Ar gas. Piranha solution is highly oxidizing and should therefore be handled with care.

The films were formed from unstirred pH 13 IrOx nanoparticle solutions by applying a potential bias of 0.9 V *vs*. Ag/AgCl for 10 minutes. The films were rinsed with nanopure H_2O and then cyclic voltammetry (CV) was performed in 0.1 M NaOH to verify the presence of a film.

3.2.3 Precipitation of Iridium Oxide Nanoparticles

Precipitation of the iridium oxide nanoparticles was induced using one of three methods:

direct lowering of the pH using a non-coordinating acid, addition of a chemical oxidation, and addition of isopropanol. The first two are previously discussed in Chapter 2, where the acidification of the IrO$_X$ NPs with no coordinating ligand results in precipitation. The third method involves adding an excess of isopropanol (3:1 isopropanol:IrO$_X$ NP solution), which in turn changes the polarity of the solution. This mixture is then centrifuged at 6000 rpm for 10 minutes, which results in precipitation of the nanoparticles.

3.2.4 Electrochemistry of Iridium Oxide Nanoparticles

Electrochemical measurements were performed using a three electrode set-up, with a Au coated glass slide as a working electrode, a Pt wire as an auxiliary electrode and a 3 M Ag/AgCl reference electrode. A CH Instruments 760c potentiostat was used for these experiments. All cyclic voltammetry was performed either in 0.1 M NaOH (from 50 % w/w NaOH, Fisher Scientific) or in various phosphate buffers that each had a constant phosphate concentration (0.1 M PO$_4^{-3}$).

3.2.5 UV-Vis Spectroelectrochemistry of Iridium Oxide Nanoparticles

IrO$_X$ NP films were deposited on FTO|*nano*ITO conductive films using the pH adjusted dip-coating method discussed in Chapter 2. The as-synthesized pH 13 IrO$_X$ NPs were adjusted to pH 1 using concentrated HClO$_4$ (GSF Chemicals). After 24 hours, the FTO|*nano*ITO glass slides were dipped in the IrO$_X$ NP solution for 1.5 hours, then rinsed thoroughly with nanopure H$_2$O and dried with Ar. The pH 5.8 buffers that were used in the aforementioned experiments were composed of 37.5 mM Na$_2$SiF$_6$ (Aldrich) and 80 mM NaHCO$_3$ (Aldrich) in nanopure water.

Spectroelectrochemical characterizations were conducted at pH 5.8 in a three electrode cell with a 1 cm path length cuvette by using a CHI 670 potentiostat, and an Agilent UV-Vis spectrometer. The potential was varied in 0.02 V increments from -0.2 to 1.2 V vs. Ag/AgCl

with spectra recorded at each increment after holding the potential for 60 s. (The Ag/AgCl reference is +0.199V vs NHE.) The data were analyzed by using SpecFit.

3.2.6   Raman Spectroscopy of Iridium Oxide Nanoparticles

All Raman Spectra were obtained using a Renishaw Invia Raman Microscope, using a 633 nm laser. Spectra were obtained of the as-synthesized pH 13 IrO_X NPs in solution, drop cast on a glass slide, the isopropanol precipitated IrO_X NPs as a solid on a glass slide and the electroflocculated IrO_X NPs on a Au coated glass slide.

3.2.7   Microscopy of Iridium Oxide Nanoparticle Films

Microscopic images of IrO_X NP films were obtained from a Hitachi S-4700 Cold Cathode Field Emission Scanning Electron Microscope (SEM) and an Asylum Research MFP3D Atomic Force Microscope.

3.2.8   Zeta Potential Measurements of Iridium Oxide Nanoparticles

Zeta potential measurements were collected on a Malvern Zetasizer Nano-ZS. To resuspend the IrO_X NPs in a solution with lower electrolyte concentration, an excess of isopropanol was added to the as-synthesized pH 13 IrO_X NPs and the resulting solution was centrifuged using an Eppendorf 5810 centrifuge with a fixed angle rotator at 6000 rpm for 10 minutes. The excess liquid was decanted and the precipitate was then resuspended in 0.01 M phosphate solutions, which varied in pH.

3.2.9   X-Ray Photoelectron Spectroscopy of Iridium Oxide Nanoparticles

X-ray photoelectron spectra were obtained on a Kratos Axis Ultra DLD system with monochromatic Al Kα x-ray source. High resolution scans were taken at pass energy of 20 eV and the spectral energy axis was aligned at the C 1s peak (284.6 eV). The IrO_X NPs were prepared in four different ways for analysis via XPS. The first preparation involved drop-casting the as-synthesized IrO_X NPs in 0.1 M NaOH onto a piranha cleaned (described in section 3.2.2)

Au coated glass slide. The second was electroflocculation onto a Au coated glass slide, as described above. The third preparation used a chemical oxidant ($NH_4Ce(NO_3)_6$), which resulted in precipitated IrO_X NPs. This precipitate suspension was drop cast onto a piranha cleaned (as discussed in Section 3.2.2) Au coated glass slide. The fourth preparation involved exchanging the pH 13 IrO_X NPs into dichloromethane (DCM), using valeric acid as a capping ligand. The exchanged NPs were then drop-cast onto a piranha cleaned (described above) Au coated glass slide.

3.3 RESULTS AND DISCUSSION

3.3.1 Electrochemistry of Iridium Oxide Nanoparticles

3.3.1.1 Electrochemical Behavior of IrO_X NP Films at Different pH
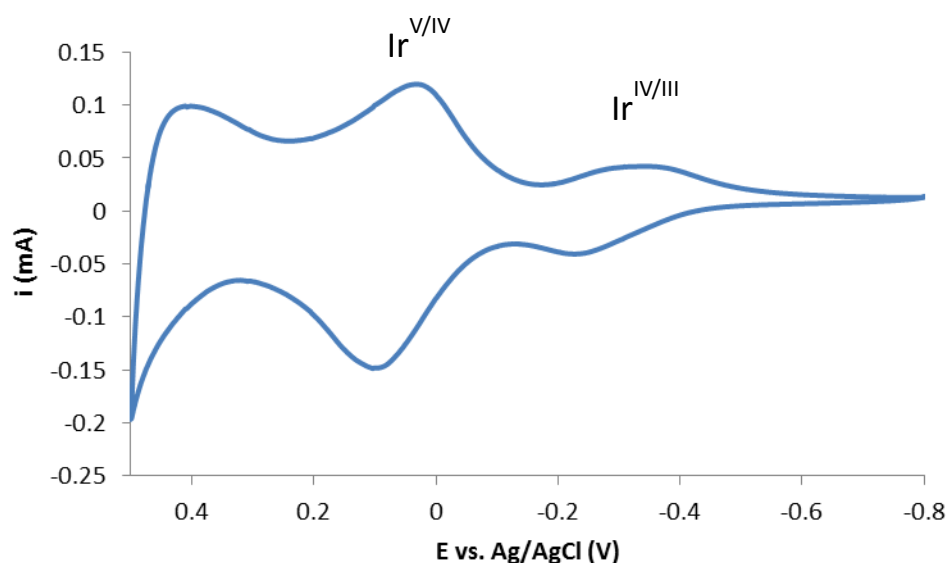
Figure 3.1: Cyclic voltammetry of an electroflocculated IrO_X NP film, depicting the $Ir^{V/IV}$ and $Ir^{IV/III}$ redox waves and the onset of water oxidation in 0.1 M NaOH solution (pH = 13). Electrode area 0.071 cm^2.

As discussed in Chapter 2, there are three electrochemical areas of interest for the electroflocculated IrO_X NP films, the $Ir^{IV/III}$ redox couple, the $Ir^{V/IV}$ redox couple and the water oxidation catalysis region, as seen in Figure 3.1. All of these regions are Nernstian behaved, shifting ca. 70 mV/pH.[24,26-28] Studying the electrochemical behavior of these NPs as

electroflocculated films also gives the added advantage of being able to integrate the charge under the $Ir^{IV/III}$ and $Ir^{V/IV}$ waves to find the coverage of Ir on the surface of the electrode.

During these studies, the apparent Ir coverage of the films was observed to change between phosphate buffers of different pH. When the same film was observed in a more acidic buffer (pH 2) and then in a more basic solution (pH 13), the coverage drastically changed by an order of magnitude, as seen in Table 3.1. The calculated coverage from the Ir IV/V wave was much larger at higher pH values and a trend was seen: as pH increased, the calculated coverage increased as well. Furthermore, when the same film (Film 3) was transferred back to the lower pH buffer, the coverage decreased back to a value comparable with the originally measured coverage at the same pH. This enormous change could be due to an increased resistance within the film itself at lower pH, resulting in a higher iR effect, and in turn, a lower apparent coverage, as discussed below.

Table 3.1: Examples of how the measured coverage of Ir of the same film can vary between different pH solutions. Γ_{Ir} is in mol Ir/cm^2 and is determined by integrating the $Ir^{V/IV}$ oxidation wave.

Film	Γ_{Ir} at pH 1.8	Γ_{Ir} at pH 12.7	Γ_{Ir} at pH 1.8
1	7.99×10^{-9}	1.60×10^{-8}	----
2	3.19×10^{-8}	5.56×10^{-8}	----
3	1.77×10^{-9}	5.60×10^{-8}	3.58×10^{-9}

Because of this iR effect, the change in coverage with respect to potential scan rate was also studied and the results are listed in Table 3.2. In a system lacking resistance, the charge (Q) from the $Ir^{V/IV}$ peak would remain constant with scan rate. However, as scan rate increased, the charge - and thus apparent coverage - of a given film decreased. Such an observation is indicative of a larger resistance in the film, preventing the flow of ions within. This iR effect,

therefore, hinders the oxidation of Ir sites that are not easily accessible by ions (i.e. those not on or near the surface of the NP film) at faster scan rates, resulting in a lower observed coverage.

Table 3.2: Change in charge (Q) of the Ir IV/V wave with varying scan rate (v) at pH 3.

Scan rate, v	5 mV/s	20 mV/s	50 mV/s
Q of Ir IV/V wave	7.42 x 10^{-4} C	4.87 x 10^{-5} C	No peak observed

In all buffers, especially those at the lower pH values, an iR effect was apparent at higher overpotentials (η). As the overpotential increased, the turnover rate decreased, resulting in an almost non-existent change in current with respect to coverage at the highest measured overpotential, 0.6 V. Such results suggest there is a limiting factor at higher overpotentials where an increase in nanoparticle coverage no longer increases the overall catalytic activity. One might suspect the increased resistance in the films to be the limiting factor, as was observed with the change in coverage mentioned above because this would limit the amount of water accessing the active Ir sites within the film. While the driving force for the reaction increases with overpotential, the amount of water able to flow through the film would be limited by the resistance, resulting in little or no change in activity with increasing film coverage. Another possibility is that all of the films were too thick. In general, the dependence of catalytic reactivity on coverage follows a logarithmic trend, where at higher coverages of catalysts, the reactivity levels off. Thus, the films analyzed may have already reached their limit in reactivity and any slight difference seen in coverage was negligible.

To gain a better understanding of the iR effects, the conductivity of each phosphate buffer was measured and the results are shown in Table 3.3. All of the buffers had similar conductivities, ranging from 29 mS/cm to 52 mS/cm. Since the conductivities were all very similar, the solution resistance between the buffers must also be very similar. This demonstrates that while there is a significant iR drop in the lower pH buffers seen in the data, there is a

minimal effect from the actual solution regardless of buffer. This observation implies that the resistance is within the film, as opposed to in the solution.

Table 3.3: Conductivity measurements (mS/cm) of each of the phosphate buffers. pH 3 and 5 are both 1.0 M phosphate and pH 7.5, 10 and 12 are 0.1 M phosphate.

Buffer	1.0 M pH 3	1.0 M pH 5	0.1 M pH 7.5	0.1 M pH 10	0.1 M pH 12
Conductivity (mS/cm)	39.0	27.0	42.8	45.0	52.8

3.3.1.2 Kinetic Studies of Water Oxidation Catalysis vis IrO_X NP Films

The advantage of using a film in an electrochemical experiment is that it eliminates any solution mass transport effects on the kinetic activity of the redox species. This makes the kinetics, and the studies of them, much less complex compared to if the redox species were freely diffusing. In an unpublished message, Stephen Feldberg discussed the theory behind using an electrocatalyst as a film in order to determine the rate constant for a given reaction.[38] The equation that he derived is below:

Equation 3-1

$$I_{SS} = nAFk_{cat}\Gamma_{cat}[S]_{bulk}$$

In this equation, the steady state current (I_{SS}) is proportional to the area of the electrode (A), the turnover rate constant of the catalyst (k_{cat}), the coverage of the catalyst (Γ_{Ir}), and the concentration of the substrate from the catalyzed reaction in the bulk solution ($[S]_{bulk}$). In order for this relationship to be true, it makes three major assumptions: $k_{cat}[S]_{bulk}$ follows pseudo-first order kinetics, electron transfer (ET) is facile between the electrode surface and the redox species, and electron hopping is fast within the film. All of these conditions are assumed to be met with the IrO_X nanoparticles when catalyzing water oxidation in an aqueous solution.

The films were created via electroflocculation, holding the potential of the electrode at 0.9 V in a solution of pH 13 nanoparticles. The length of time for the potential hold was varied from three to fifteen minutes in order to create a range of "coverages;" the process is not solely dependent on time, thus coverage may vary for films electroflocculated for equivalent times. The coverages themselves were determined from the charge (Q) of the $Ir^{V/IV}$ redox wave obtained using linear sweep voltammetry. In order to mimic the work of Nakagawa et al.,[24] the films were originally subjected to a linear sweep through the $Ir^{V/IV}$ wave out to water oxidation, where the potential was held for 200 seconds and then swept back through the $Ir^{V/IV}$ wave. It was observed that using this technique led to a drastic decrease in calculated coverage for the film, presumably due to loss of nanoparticles from O_2 gas formation (Table 3.4). From this, it was concluded that the coverage determined in the initial linear sweep was not representative of actual number of active Ir sites when the I_{SS} was taken.

Table 3.4: Examples of how the coverage of Ir can change before and after potentials more positive the onset of water oxidation are applied. Γ_{Ir} is in mol Ir/cm^2 and is determined by integrating the $Ir^{V/IV}$ oxidation wave.

pH 13		pH 7		pH 1	
Γ_{Ir} **Before**	Γ_{Ir} **After**	Γ_{Ir} **Before**	Γ_{Ir} **After**	Γ_{Ir} **Before**	Γ_{Ir} **After**
6.8 x 10^{-9}	3.5 x 10^{-9}	1.7 x 10^{-9}	2.2 x 10^{-9}	2.8 x 10^{-9}	8.9 x 10^{-10}
4.9 x 10^{-8}	1.8 x 10^{-8}	4.6 x 10^{-9}	5.0 x 10^{-10}	3.7 x 10^{-8}	1.9 x 10^{-9}
2.7 x 10^{-7}	3.3 x 10^{-8}	2.8 x 10^{-8}	2.3 x 10^{-9}	2.0 x 10^{-8}	NA

To ensure that the coverage determined by the $Ir^{V/IV}$ wave accurately represented the NPs that are catalytically involved in water oxidation, the current at different overpotentials (η) from a fast potential scan rate linear sweep were used as "I_{SS}" in lieu of a true steady state current. By limiting the time spent at the potentials where O_2 is produced, there is less time for the NP film to be disturbed, allowing the coverage measured at the IV/V wave to be a better representation of

the NPs present when water oxidation values are measured. Due to the observed change in coverage due to scan rate at low pH, the linear sweep of the $Ir^{V/IV}$ couple was performed at a slower scan rate of 5 mV/s. This was then followed by a faster linear sweep (100 mV/s) into water oxidation to obtain the current values, "I_{SS}", at different overpotentials (η).
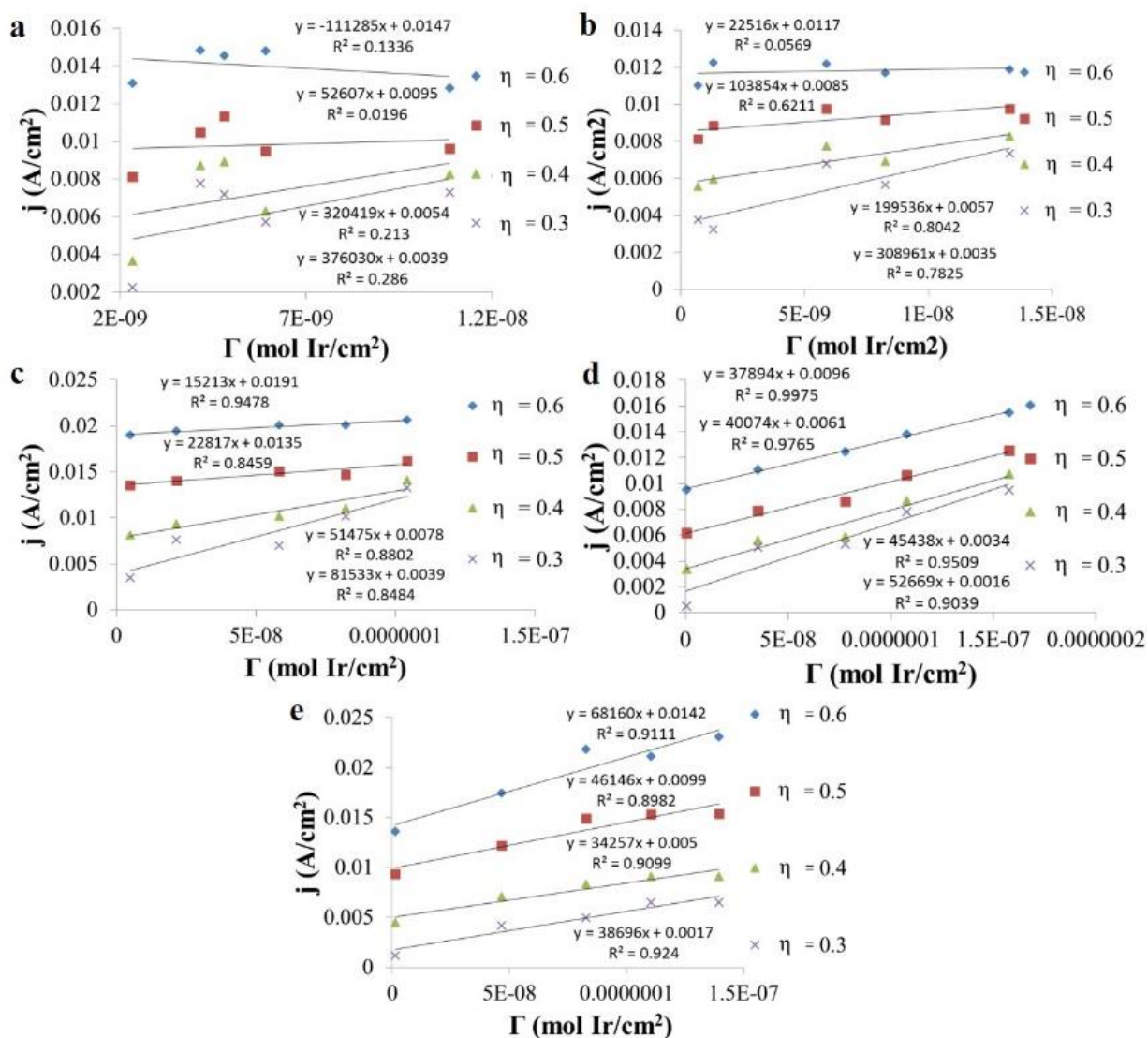
Figure 3.2: j (A/cm^2) vs. Γ_{Ir} (mol Ir/cm^2) for four different overpotentials (η), indicated by the different symbols in each graph. a) Plot for IrO$_X$ NP films in pH 3 phosphate buffer. b) Plot for IrO$_X$ NP films in pH 5 phosphate buffer. c) Plot for IrO$_X$ NP films in pH 7.5 phosphate buffer. d) Plot for IrO$_X$ NP films in pH 10 phosphate buffer. e) Plot for IrO$_X$ NP films in pH 12 phosphate buffer.

The results for the aforementioned experiments are seen in Figure 3.2, where current density, j, at a given overpotential η, is plotted versus the coverage in moles of Ir (Γ_{Ir}). The plots demonstrate a linear relationship where the slope is proportional to the rate constant of the catalytic reaction (k_{cat}), as per the equation mentioned above. However, at the higher

Table 3.5 k_{cat} (s^{-1}) of water oxidation catalysis for two different overpotentials in 0.1 M phosphate buffers of varying pH.

η	pH				
	3	5	7.5	10	12
0.3	0.97	0.80	0.21	0.14	0.10
0.4	0.52	0.83	0.13	0.12	0.09

overpotentials, the currents converge. Instead of showing the expected increase in rate with an increase in driving force, the apparent rate decreases and levels off at these higher potentials. This could be due to a number of reasons, including an iR effect, as previously mentioned, or a higher O_2 production, which in turn creates noise that distorts the values obtained. A third
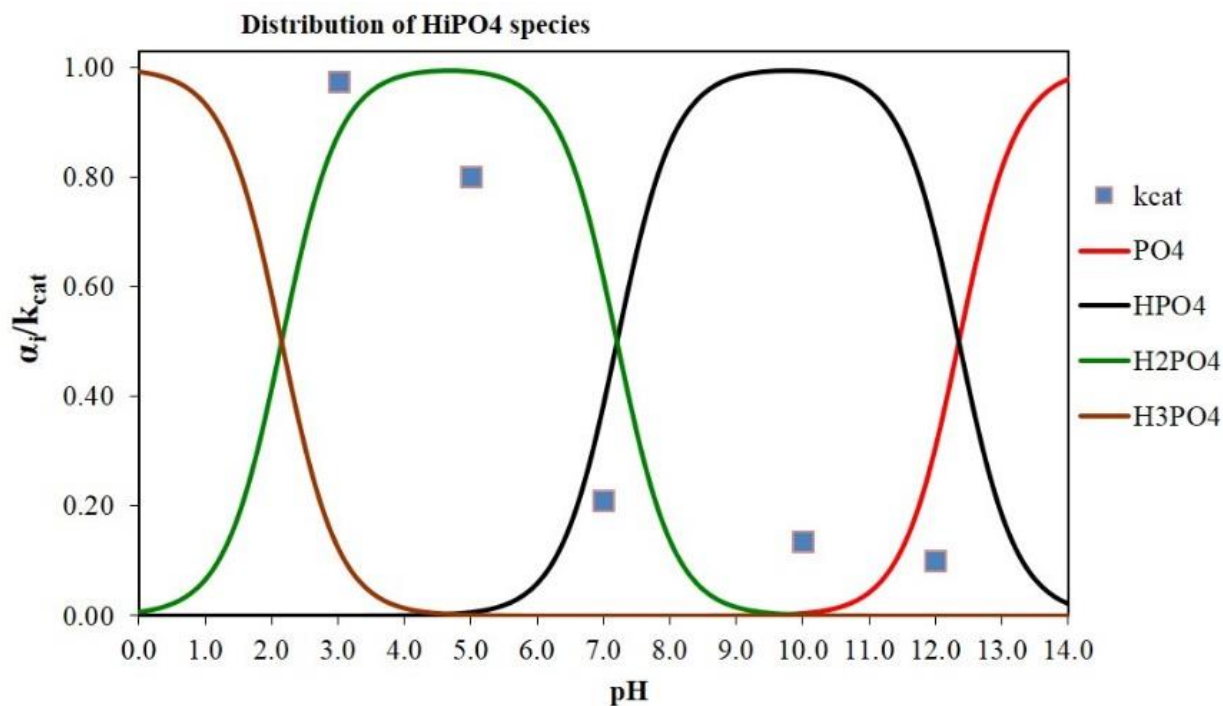
Figure 3.3: Distribution plot of the different phosphate species with respect to pH. The k_{cat} values for the 5 different buffers are plotted, as well, for comparison.

reason that could cause the current to converge is that the buffers may not have the capacity to handle such high rates of water oxidation. If the buffer capacity is not sufficient, then the pH at the electrode surface may not be the same as that of the bulk solution. Because of this, the rates at lower overpotentials, such as $\eta = 0.3$ and 0.4, are a more accurate representation of the kinetics of water oxidation catalysis, where both the iR effect and water oxidation is minimal.

Using Figure 3.2, the turnover rate constants, k_{cat} were determined at overpotentials of 0.3 and 0.4 V from the slopes, as shown in Table 3.5. Overall, the turnover rates from the lower pH buffers were much higher than that for the higher pH buffers, with an order of magnitude in change between pH 3 and pH 12, from 0.97 to 0.10 s^{-1}. A distribution diagram of phosphoric acid and its dissociated products is shown in Figure 3.3. The calculated k_{cat} values are overlaid on this diagram. There does not appear to be a trend in the k_{cat} values with respect to which phosphate anion is predominate in the buffer. Instead, there is a general decrease in rate with respect to pH. This trend, however, is not linear with respect to the concentration of H$^+$ or pH.

3.3.1.3   Catalytic Tafel Plots

The Tafel equation, shown below, is another way of analyzing irreversible electrochemical reactions and in this case, it overcomes the difficulty of analyzing higher overpotentials with j vs. Γ_{Ir} plots by extrapolating to smaller overpotentials.

Equation 3-2

$$\eta = \left(\frac{2.3RT}{\alpha nF}\right) \log(\frac{j}{j_0})$$

It relates the overpotential, η, to the logarithm of the ratio of the current density, j, to the exchange current density, j_0. Catalytic Tafel plots, as discussed in a review by Nathan Lewis, use a simplified version of this equation, substituting $\left(\frac{2.3RT}{\alpha nF}\right)$ for a constant b.[22] When plotted η
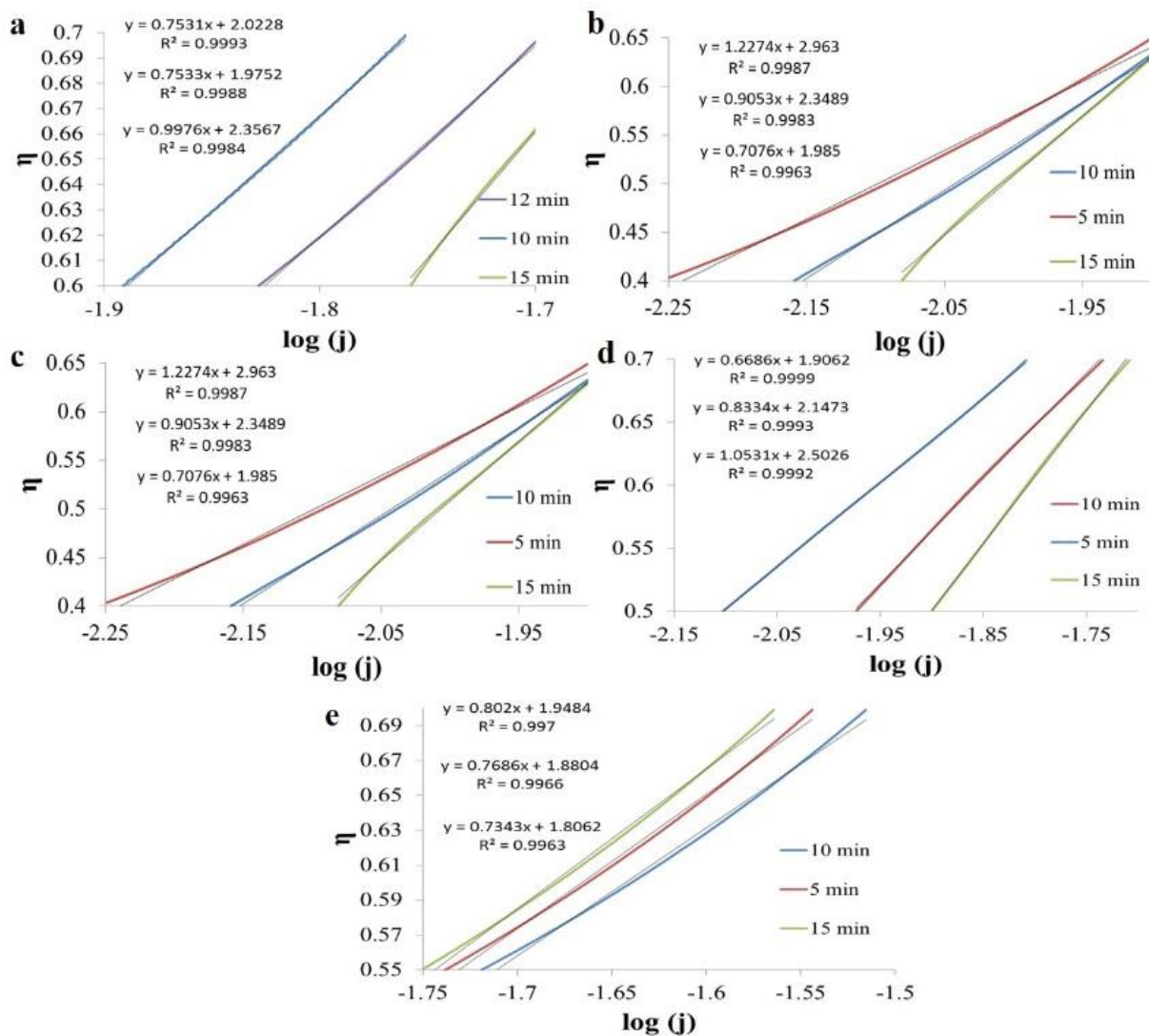
Figure 3.4: Catalytic Tafel plots for IrO$_X$ NP films, electroflocculated for various lengths of time (indicated by the different colors) in different pH buffers. a) IrO$_X$ NP films in pH 3 phosphate buffer. b) IrO$_X$ NP films in pH 5 phosphate buffer. c) IrO$_X$ NP films in pH 7.5 phosphate buffer. d) IrO$_X$ NP films in pH 10 phosphate buffer. e) IrO$_X$ NP films in pH 12 phosphate buffer.

versus $log(j)$, the slope is b and the y-intercept is $-b\log(j_0)$. This slope is a function of the

rate of the reaction, in this case k_{cat}, the iR drop experienced at high overpotentials, as well as the

other parameters shown in the Tafel equation above. When compared with other catalysts, the

slope can be a qualitative evaluation of whether the catalysts have similar mechanisms and if the

solutions have similar resistances. The y-intercept, on the other hand, is related to the exchange

current density, j_0, which is a measure of how the electrode surface behaves at zero overpotential.

j_0 is dependent on the electrode and catalyst material, the surface roughness of both, and the

concentration of the reactants and products in the catalyzed reaction, in this case H_2O and O_2.

Figure 3.4 a through e are the catalytic Tafel plots for films of different

electroflocculation times for a given pH. With the exception of pH 5, films exposed to the same

buffer have similar slopes at higher overpotentials. This implies that they have similar iR effects

and k_{cat}, which is expected considering they have the same parameters, with the exception of

coverage. From this, it can be inferred that the mechanism of water oxidation doesn't change

with increased coverage at each specific pH. The j_0 for each of the pH buffers increases with

electroflocculation time, or increased coverage, however, not significantly. This is due to the

fact that the coverages of IrO_X NPs are high enough that they may have reached their maximum

catalytic potential, as discussed earlier. So while the exchange current density changes

somewhat between the different coverages, they are essentially the same considering these

values are extrapolated from higher overpotentials. The abnormality of the pH 5 Tafel plots

(Figure 3.4b) could be due to the poor buffer capacity at this pH. This could greatly affect the
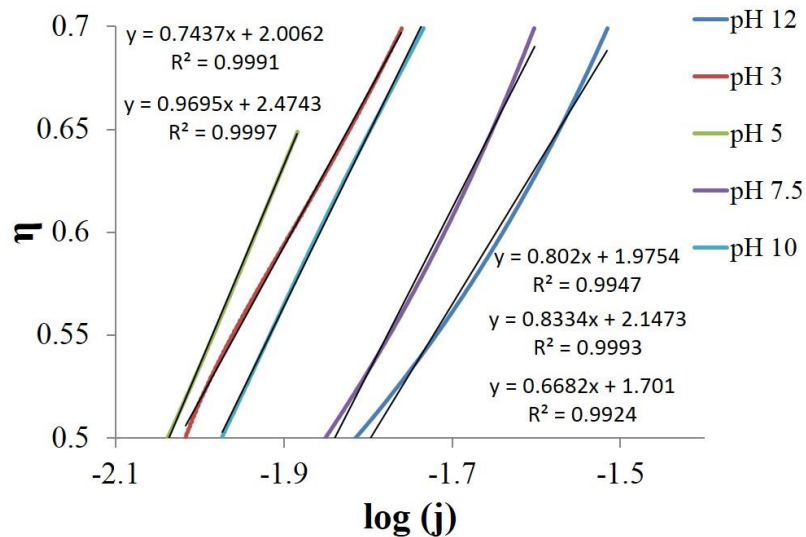
Figure 3.5: Catalytic Tafel plot of similar coverage IrO_X NP films in different pH phosphate buffers, represented by the different colors. The slope corresponds to the k_{cat} and mechanism of catalysis, while the y-intercept corresponds to the exchange current density.

shape of the Tafel plot as the pH of the solution is more than likely changing with water oxidation.

Table 3.6: The slopes (b) and exchange current values (j_0) for the IrOx NP films at different pH values taken from the catalytic Tafel plot. Each film was electroflocculated for 10 minutes.

pH	3	5	7.5	10	12
slope (b)	0.7531	0.9053	0.802	0.8334	0.7343
j_0	0.0021	0.0025	0.0034	0.0027	0.0035

Figure 3.5 overlays the Tafel plots of films that have the same electroflocculation time (similar coverages) but were exposed to different pH buffers. The slopes of these are similar, however, the lines are not as parallel as the films compared in the same buffer. This suggests that there is a difference in either the k_{cat} or the resistance within the film, as seen in Table 3.5. There is also an effect seen by the difference in conductivity of the solutions, referring back to Table 3.3. The less conductive buffers, pH 3 and pH 5, have steeper slopes because of the smaller change in current with applied potential, due to a higher resistance. The exchange current densities in all of the buffers, on the other hand, were very similar and clustered around 0.003 A/cm^2 (Table 3.6). They also followed no trend with respect to pH, inferring that a H$^+$ is not involved in the rate determining step. This discovery suggests that while the measured coverages of Ir found from the integration of the Ir$^{V/IV}$ wave varied drastically, the active electrode area (or volume in this case with a permeable film) and roughness of the said film are fairly similar at $\eta = 0$. The variance between these values can be explained by non-uniformity of the films and also by the long extrapolation from a high overpotential back to zero.

3.3.2 UV-Vis Spectroelectrochemistry of Iridium Oxide Nanoparticles

UV-Vis difference spectra of the dip-coated IrO$_X$ NPs on FTO|*nano*ITO conductive films are presented in Figure 3.6 with respect to change in potential. The potential was held for 60 s, prior to each spectra being collected. The IrO$_X$ NP films were prepared by adjusting the pH of
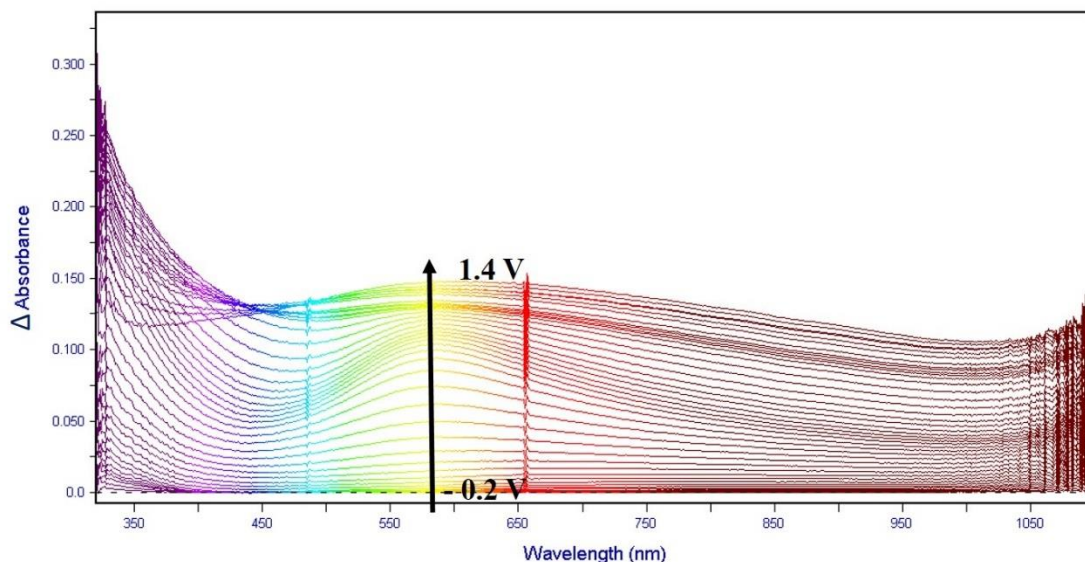
Figure 3.6: UV-Vis difference spectra for the precipitated IrO_X NP films on a *nano*ITO buffer in pH 5.8 $NaSiF_6$ buffer. The potential was varied in 20 mV increments from -0.2 to 1.4 V vs. Ag/AgCl and was held for 60 s before each absorbance spectra was obtained.

the NP solution with a non-coordinating acid ($HClO_4$), as previously described in Chapter 2. The addition of a non-coordinating acid lowers the pH which induces precipitation of the IrO_X NPs in the absence of a stabilizing ligand.

From the change in these spectra, a concentration gradient with respect to applied potential was created, as seen in Figure 3.7a. The intersects of each species corresponds to the $E_{1/2}$ of each iridium redox couple. Difference spectra for each individual iridium oxidation species can be extrapolated from this information and that is seen in Figure 3.7b. Starting in the Ir^{III} state, an absorbance peak at 600 nm grows in as the iridium is oxidized to the Ir^{IV} oxidation state. This peak continues to grow in intensity as the nanoparticles are oxidized to the Ir^V state. At more positive potenials, the IrO_X NPs become black absorbers as they transition into the Ir^{VI} oxidation state, observed by the increase in absorbance at all wavelengths. These changes in absorbance correspond to the color of the nanoparticles in solution at each oxidation state: the reduced $Ir^{III}O_X$ NPs are generally observed to have a yellow-green color, the as- synthesized

80

Ir^{IV}O$_X$ NPs are purple and as they are oxidized to higher oxidation states, they transition from a darker purple color to black. Also note that the Ir^{VI} oxidation state appears at potentials that are positive enough to
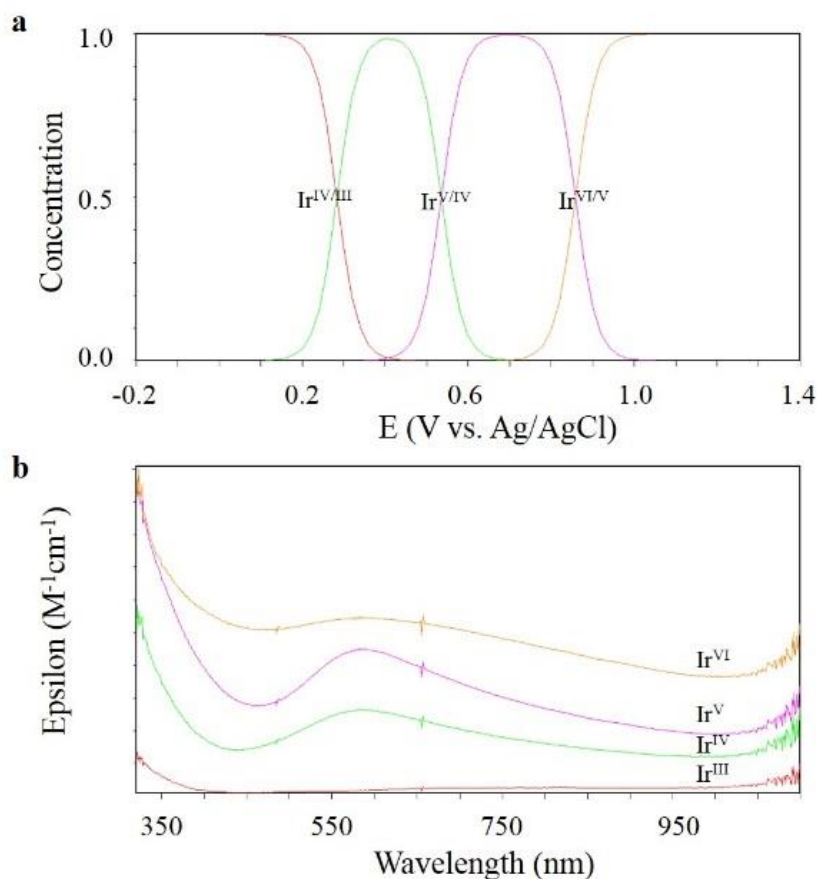
Figure 3.7: a) Distribution plot of each Ir oxidation state with respect to applied potential (V vs. Ag/AgCl), derived from the difference spectra in Figure 3.6. b) The difference spectra of each individual Ir oxidation state.

induce water oxidation electrocatalysis, indicating that the Ir^{VI} species is an active participant in this reaction. Similar behavior has been reported for the bulk IrO$_2$ material, which has shown promise as an electrochromic sensor material.[130a, 130i]

3.3.3 Zeta Potential Measurements of Iridium Oxide Nanoparticles

Zeta potential measurements were collected for IrO$_X$ NPs in different pH phosphate buffers. The method of adding 0.1 M H$_3$PO$_4$ and adjusting using NaOH to the as-synthesized pH 13 IrO$_X$ NPs proved to affect the zeta potential measurements due to the high electrolyte
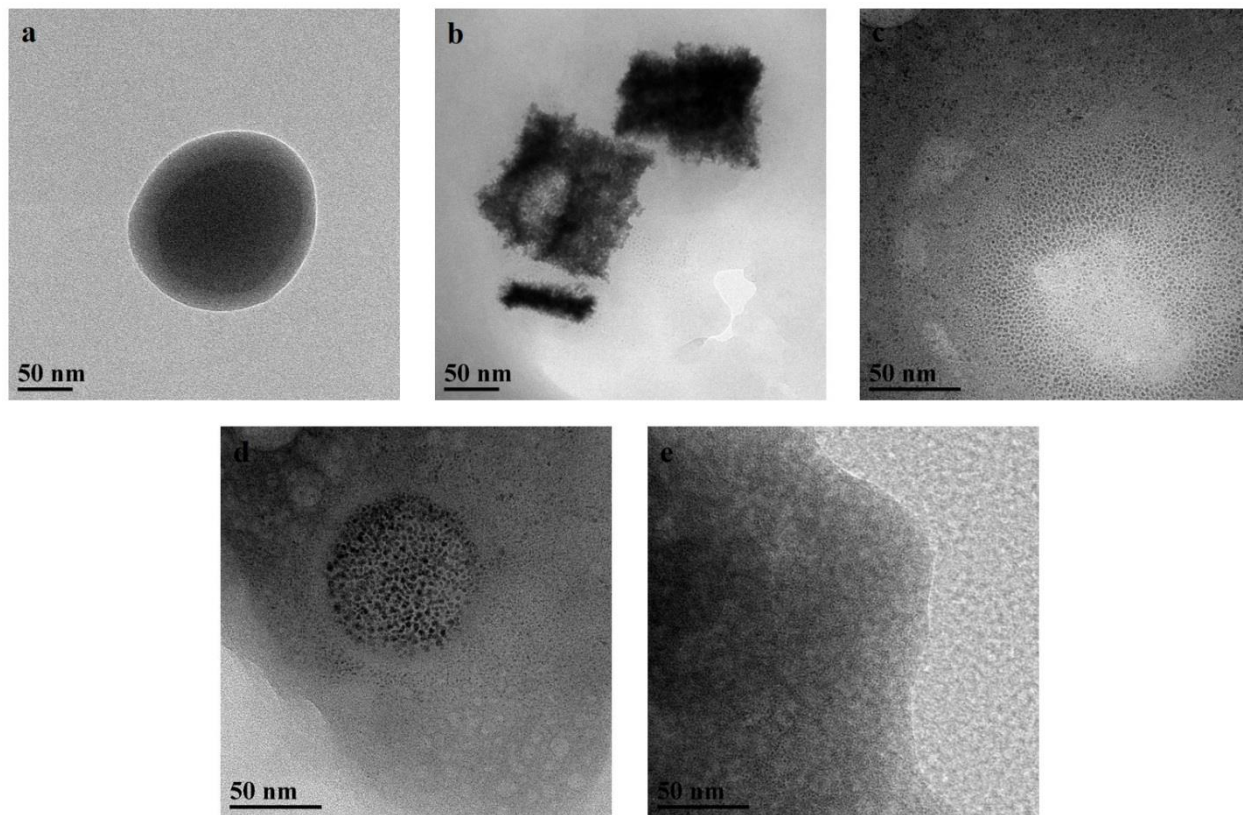
Figure 3.8: TEM images of the isopropanol precipitated IrO_X resuspended in various 0.1 M phosphate buffer:. a) pH 3.3 b) pH 7.7 d) pH 11 e) pH 12.

concentration. In order adjust the pH of the NPs with a decrease in electrolyte concentration, an excess of isopropanol was added to the pH 13 IrO_X NPs and the resulting solution was centrifuged at 6000 rpm to induced precipitation. The precipitate was then resuspended in 0.01 M phosphate buffers of various pH. Presence of nanoparticles in the new solutions was confirmed via TEM, as seen in Figure 3.8.

The distributions of zeta potentials of the various pH IrO_X NPs are presented in Figure 3.9 and the zeta potential values are in Table 3.7. At pH 2, the zeta potential is slightly positive, but centered ca. 0 mV. This is likely due to the species of phosphate present at pH 2, as previously presented in Figure 3.3. This is predominantly H_3PO_4, a neutral state. There is also a high concentration of H^+, which may explain the slightly positive zeta potential.

The IrO$_X$ NPs in pH 3.3 and 5.8 phosphate buffers have very similar zeta potentials at -44.9 ± 2.7 and -48.5 ± 2.4 mV, respectively. As both pH values are between the first and second pK$_a$s of phosphoric acid, the dominant phosphate species is H$_2$PO$_4^-$. This would lead to a similar surface charge, and therefore zeta potential for these nanoparticles. This potential is negative due to the negative charge on the H$_2$PO$_4^-$ species, which is likely the capping ligand present at these two pH values.
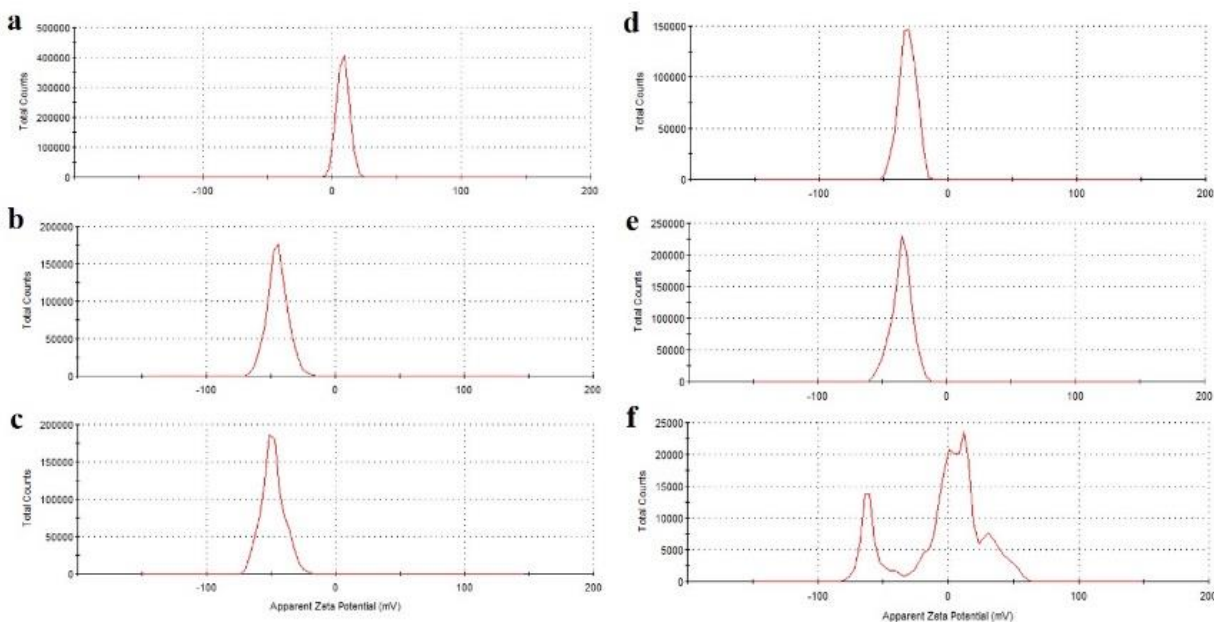
Figure 3.9: Zeta potential distributions for the isopropanol precipitated IrO$_X$ NPs, resuspened in various phosphate buffers: a) pH 2 b) pH 3.3 c) pH 5.8 d) pH 7.7 e) pH 11 and f) pH 12.

The IrO$_X$ NPs in pH 7.7 and 11 phosphate solutions also exhibited similar zeta potentials, at -31.3 ± 4.2 and -33.4 ± 3.3 mV. At both of these pH values, the predominant phosphate species is HPO$_4^{-2}$, which is also negatively charged like H$_2$PO$_4^-$. While it is more negatively charged than H$_2$PO$_4^-$, the zeta potentials for these nanoparticles are more positive than the ones at the lower pH. This suggests that fewer of these capping ligands are required to stabilize the nanoparticles in solution, so a decrease in zeta potential is not observed.

Table 3.7: Zeta potentials for IrO$_X$ NPs, resuspended in 0.01 M Phosphate buffers of various pH.

	pH					
	2	3.3	5.8	7.7	11	12
Zeta Potential (mV)	8.2 ± 0.93	-44.9 ± 2.7	-48.5 ± 2.4	-31.3 ± 4.2	-33.4 ± 3.3	-6.5 ± 3.4

The zeta potential for the IrO$_X$ NPs at pH 12 shifts even further positive, but still remains negative. At this pH, the predominant phosphate species is PO$_4^{-3}$, however, there is also an abundance of OH$^-$ groups in solution as well. The OH$^-$ groups are presumed to be the stabilizing ligands method for the as-synthesized pH 13 IrO$_X$ NPs, so it is likely that they are also interacting with the NP surface in the phosphate buffers at this pH, as well. Looking at the distribution of the zeta potential measurements in Figure 3.9f, it no longer follows the Lorentzian distribution observed in the other pH solutions. Instead, there are two distinct distributions, a Lorentzian shaped one at -60 mV and an oddly shaped one centered ca. 0 mV. Because of this,
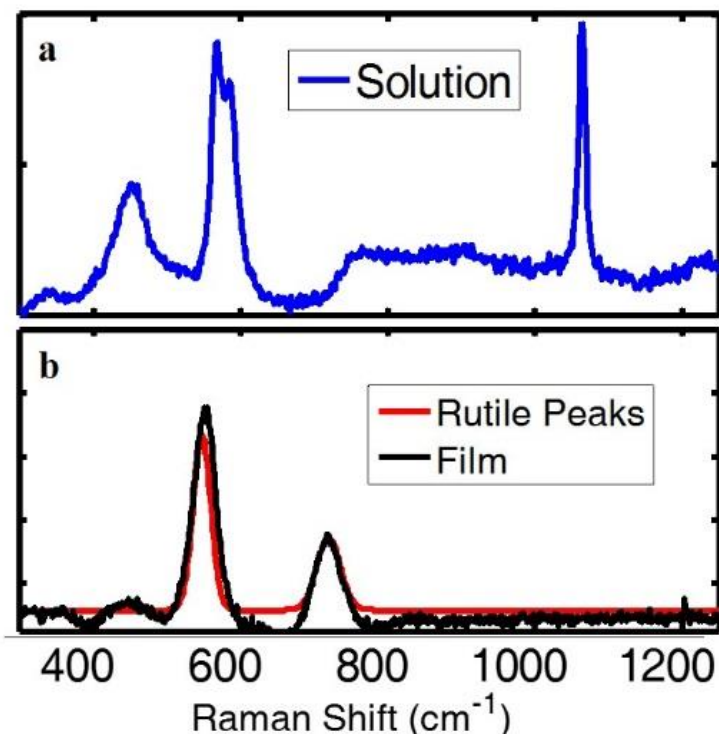
Figure 3.10: Raman spectra of the IrO$_X$ NPs in two different states. a) As-synthesized IrO$_X$ NPs in 0.1 M NaOH. b) Electroflocculated IrO$_X$ NP film on Au slide.

the overall zeta potential is -6.74 mV, however, it does appear that this value should be more negative. This may be explained by the nature of the experiment for measuring the zeta potential. For these measurements, a potential difference is applied across two electrodes to induce migration of the charged nanoparticles. However, it is known that when a potential is applied to the IrO_X NPs in high pH solutions, the NPs will flocculate together. The peak at the more neutral potential may be due to the flocculated IrO_X NPs, while the other peak at -60 mV is more representative of the IrO_X NPs in pH 12 phosphate buffer.

3.3.4   Raman Spectroscopy of Iridium Oxide Nanoparticles

Raman spectra were obtained of the IrO_X NPs in three different states, the as-synthesized pH 13 solution IrO_X NPs, an electroflocculated IrO_XNP film and the IrO_X NPs precipitated via isopropanol. The spectra of the freely diffusing IrO_X NPs and the electroflocculated IrO_X NP film are shown in Figure 3.10. In the Raman spectrum of the pH 13 solution IrO_X NPs, there is an abundance of peaks, some of which correlate to the rutile structure of bulk IrO_2 at ca.560 and 750 cm^{-1}.[3,7,14,15] However, the presence of other Raman shifts suggests that the as synthesized
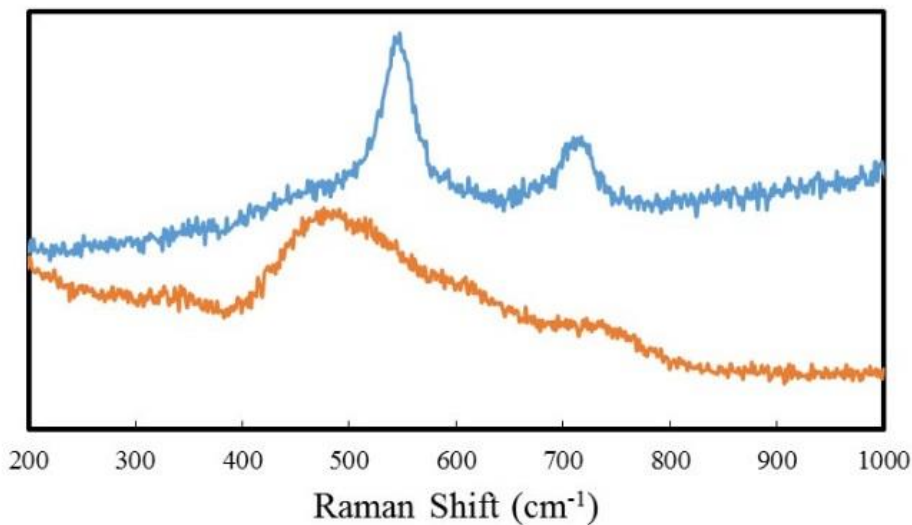
Figure 3.11: Before (blue) and after (orange) Raman spectra of the same electroflocculated IrO_X NP film, which presents a decrease in crystallinity over time.

85

IrO$_X$ NPs are not the only Ir species present. It is likely that not all of the starting material (K$_2$IrCl$_6$) is converted to IrO$_X$ and there are some other Ir species, likely either Cl or OH salts, also in solution.

When the IrO$_X$ NPs are electroflocculated onto a Au plated glass slide, as seen in Figure 3.10b, there are two predominate Raman peaks observed at 550 and 720 cm^{-1}, both indicative of the tetragonal rutile structure of IrO$_2$. It appears that the act of electroflocculation avoids the addition of other Ir species that are present in solution and also increases the crystalline structure of the nanoparticles. This is also the first indication that these IrO$_X$ NPs have a crystalline structure and that it closely agrees with the rutile IrO$_2$ structure found in other bulk iridium oxide films.

Unfortunately, the rutile peaks are short lived in these films. Figure 3.11 shows the before and after of the same electroflocculated IrO$_X$ NP film. The before spectrum (in blue)
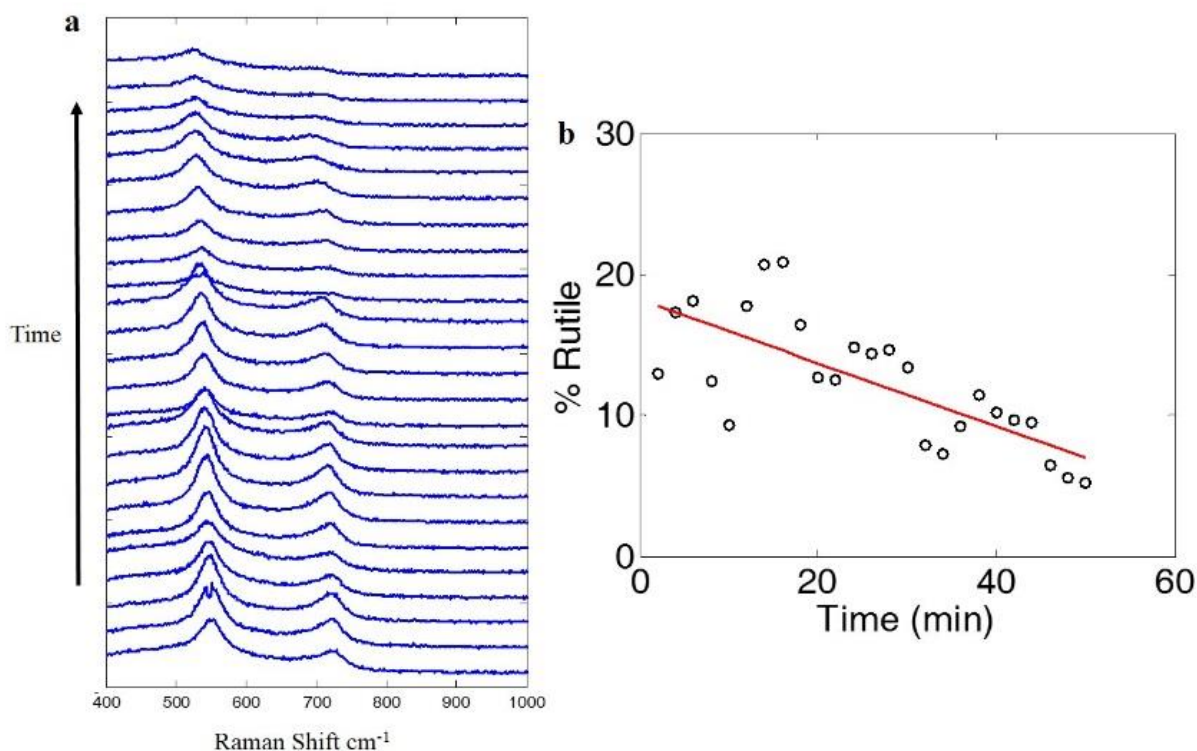
Figure 3.12: a) Raman spectra of an electroflocculated IrO$_X$ NP film over time as a 633 nm laser continuously illuminated the sample. b) % area of the spectra that is rutile over time, while the film is illuminated.

86

clearly exhibits the rutile peaks expected of an IrO_2 film. However, after laser exposure, these peaks decrease in intensity and other peaks overlap, resulting in the more blob like peak seen in orange of the same figure. This peak more closely resembles that of the EIROF discussed above in the introduction, which exhibits limited crystallinity.[8,12] In order to determine what was causing this decrease in crystallinity, Raman spectra were collected every two minutes while the laser was continuously illuminated the sample. The results are displayed in Figure 3.12.

While the two rutile peaks are dominant in the initial spectrum in Figure 3.12a, they decrease in intensity overtime. To quantify this, the Raman spectra were fit to 5 different Gaussian peaks and the area of the two rutile peaks was compared to the area of the other three peaks over time. There is a distinct decrease in this value, as shown in Figure 3.12b, indicating that the film becomes less crystalline over time when illuminated by the 633 nm laser. It is possible that the high laser power (50% power) could be changing the structure of the IrO_X NP film to a more amophorous form over exposure time.

As a comparison, the Raman spectrum of the isopropanol precipitated IrO_X NPs was also collected and is presented in Figure 3.13. There are significantly fewer Ir species present in this spectrum, compared to that of the pH 13 solution IrO_X NPs, and the rutile peaks at 550 and 720
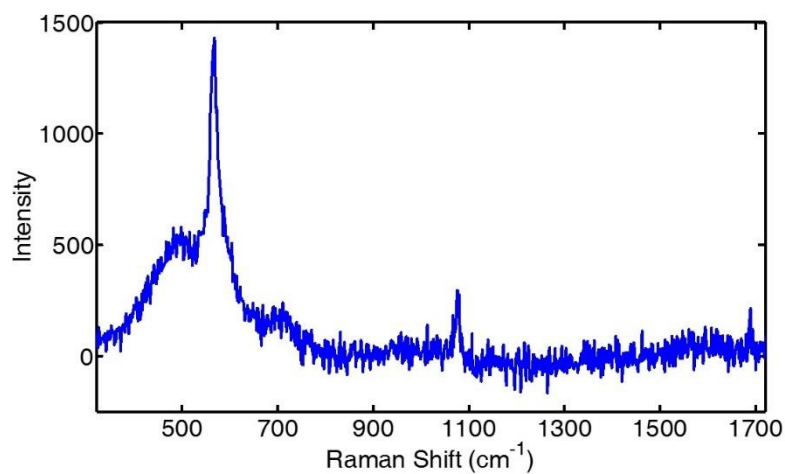
Figure 3.13: Raman spectrum of the isopropanol precipitated IrO_X NPs.

cm^{-1} both appear to be present. There also appears to be a broader peak around 500 cm^{-1} which matches the Ir-O stretching mode reported by Mo *et al* for the EIROFs.[12] We still observe the increase in crystallinity from the pH 13 solution IrO$_X$ NPs, however, the two rutile peaks are
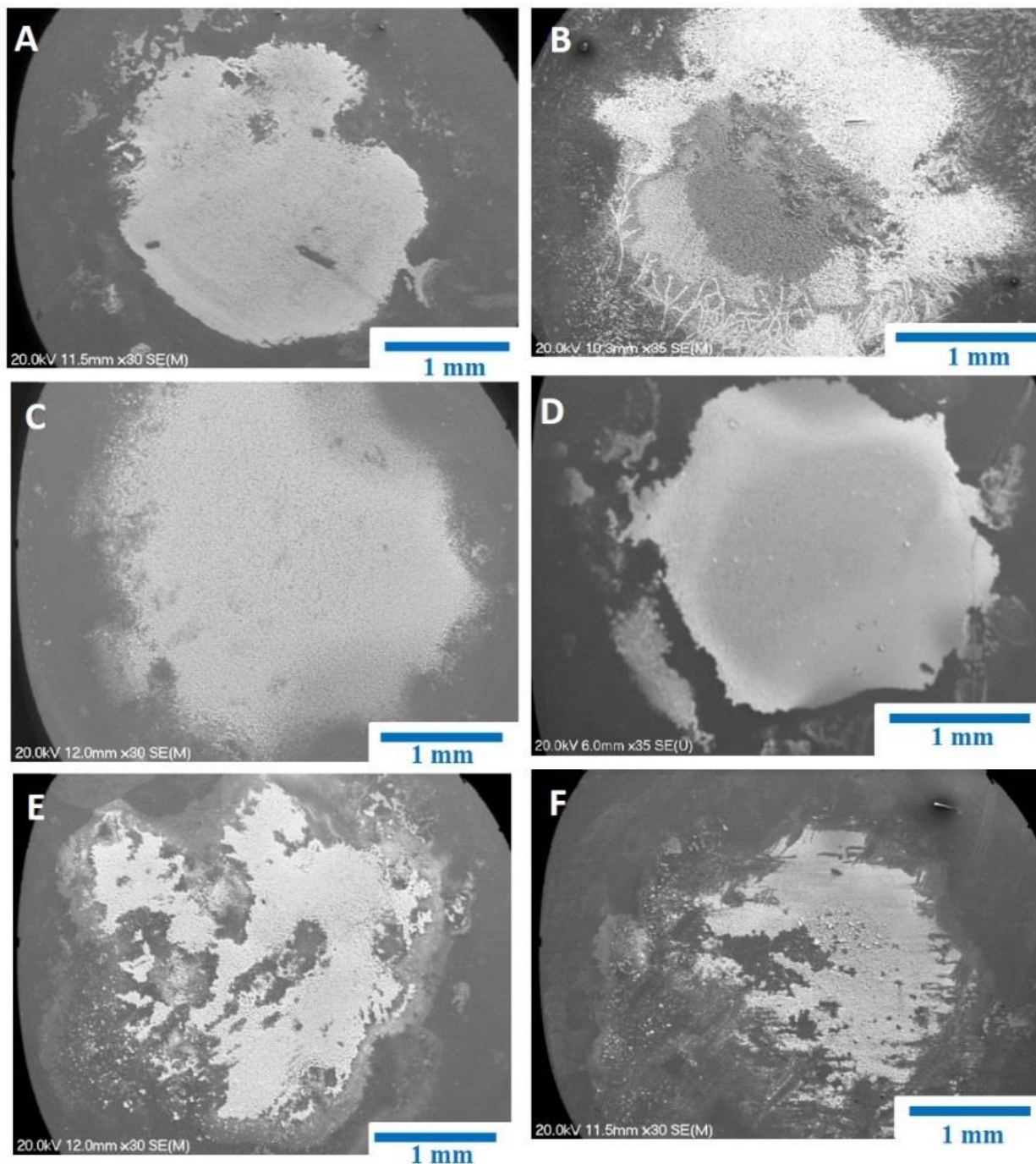
Figure 3.14: SEM images at 30 and 35x magnification of electroflocculated IrO$_X$ NP films after exposure to various phosphate buffers and electrochemical experiments. a) Immediately after electroflocculation, no phosphate buffer. b) After pH 12 phosphate buffer. c) After pH 10 phosphate buffer. d) After pH 7.5 phosphate buffer. e) After pH 5 phosophate buffer. f) After pH 3 phosphate buffer.

not as distinct as in the electroflocculated film. This suggests that there is an increase in crystalline order via electroflocculation that isn't observed when the NPs are simply precipitated from solution.
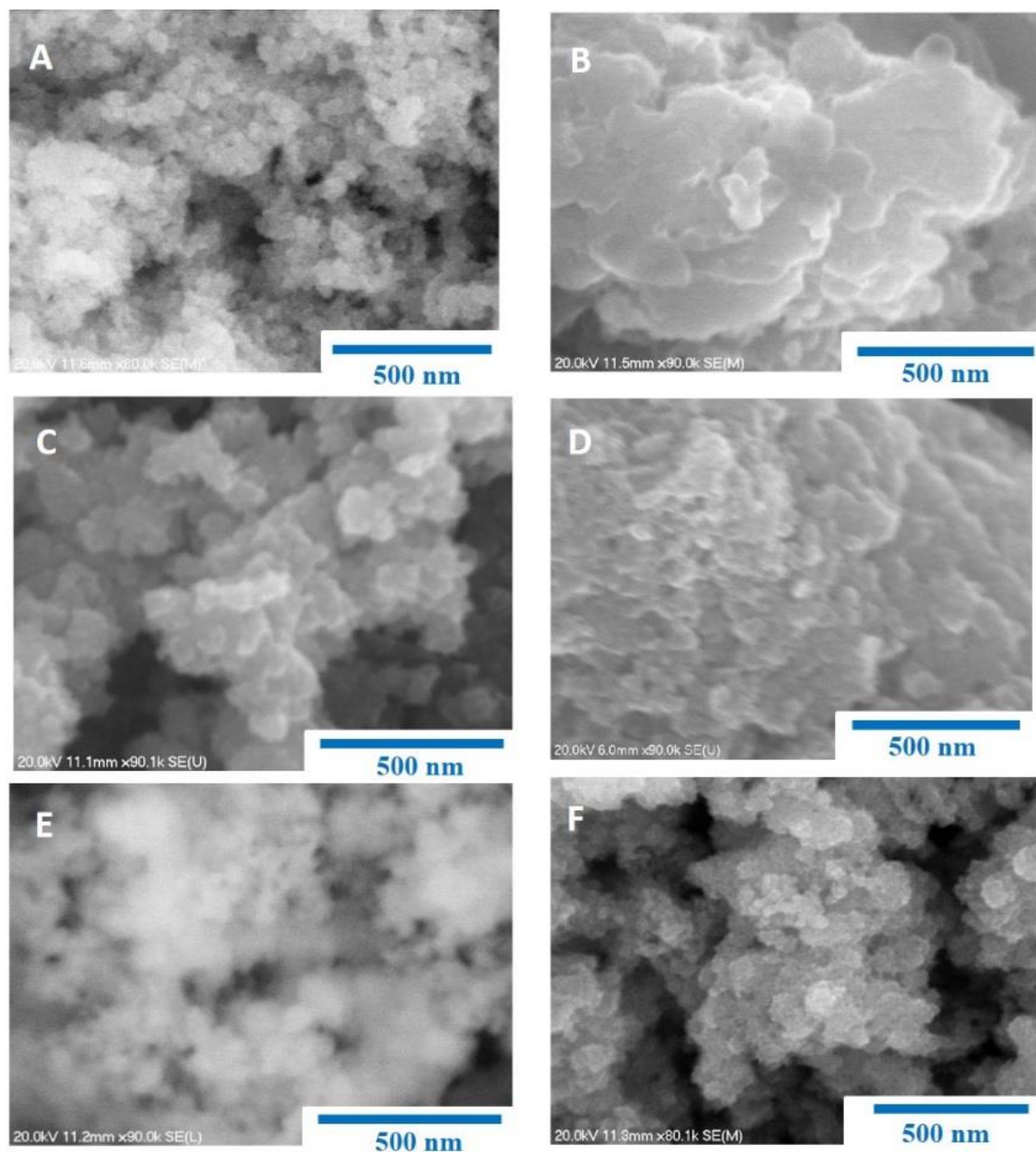
Figure 3.15: SEM images at 80,000 and 90,000x magnification of electroflocculated IrO$_X$ NP films after exposure to various phosphate buffers and electrochemical experiments. a) Immediately after electroflocculation, no phosphate buffer. b) After pH 12 phosphate buffer. c) After pH 10 phosphate buffer. d) After pH 7.5 phosphate buffer. e) After pH 5 phosophate buffer. f) After pH 3 phosphate buffer.

3.3.5 Microscopy of Iridium Oxide Nanoparticles

Figure 3.14 is a collection of images of the IrOx NP films exposed to the different phosphate buffers taken via Scanning Electron Microscopy (SEM). Each film was electroflocculated for 10 minutes at 0.9 V and then placed in the specified buffer to perform the linear sweep program previously mentioned in Section 3.3.1.2. At 30x and 35x magnification, there are no apparent differences in the films based on the pH of the buffer. One difference, however, is that films that underwent the linear sweep program presented more bare spots than
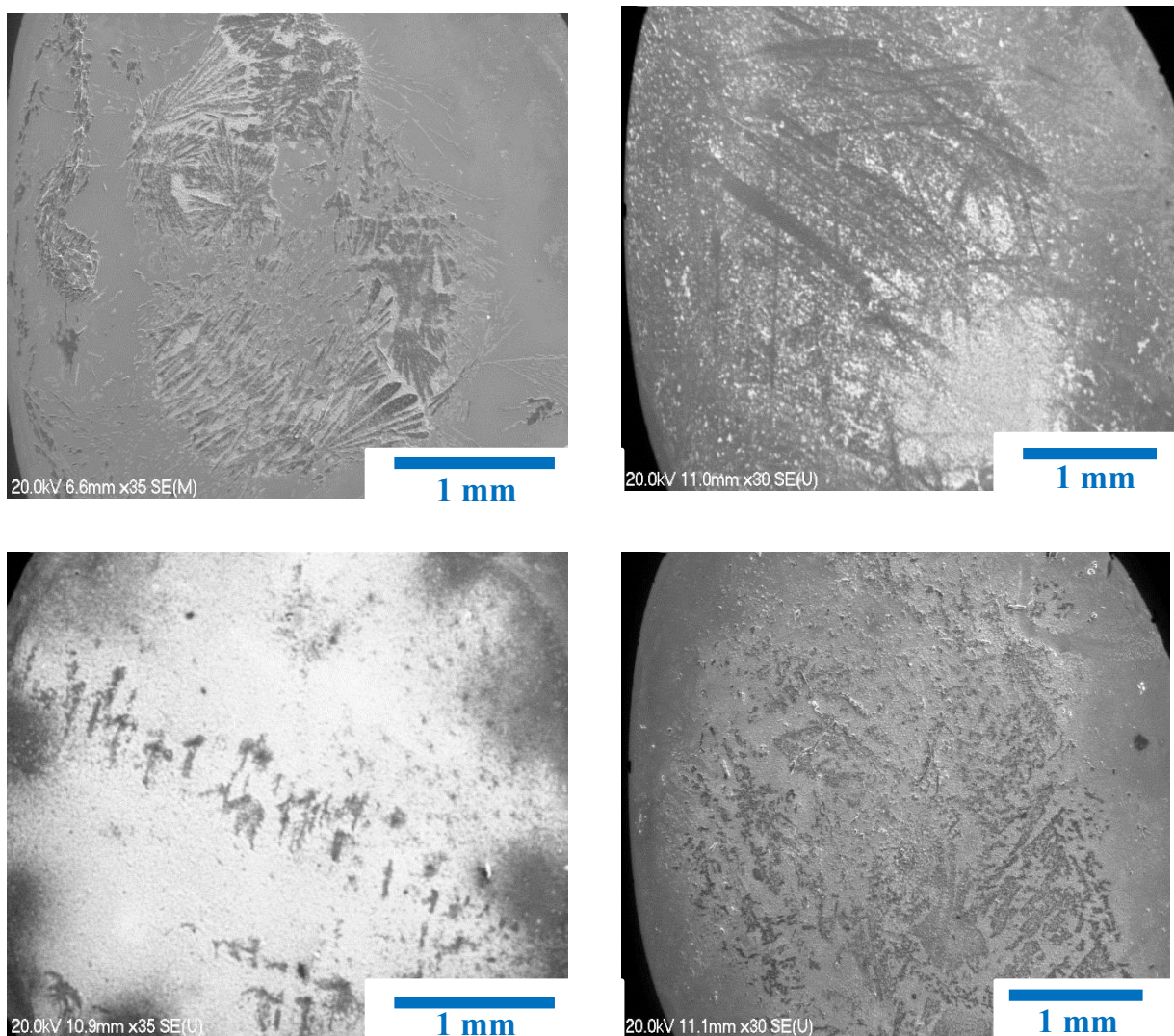
Figure 3.16: Electroflocculated IrO$_X$ NP films after varying lengths of time. a) 3 minutes of electroflocculation. b) 5 minutes of electroflocculation. c) 12 minutes of electroflocculation. d) 15 minutes of electroflocculation.

90

films that did not. This is more than likely due to O_2 production knocking the NPs off of the electrode when potentials high enough to induce water oxidation catalysis were applied.

When magnified further to 80,000x and 90,000x, the morphology of the films is more apparent, as seen in Figure 3.15. The films exposed to the lower pH buffers closely resemble that of the freshly electroflocculated film. The films tested in buffers of pH 7.5 and higher, however, seem to take a different shape at this magnification. Instead of seeing smaller particles clustered together, the film appears more globular, as if the NPs fused together into an agglomeration. This could be due to the phosphate ions that are present in the buffer. At the higher pH values, the more deprotonated phosphate anions are present, specifically HPO_4^{-2} and PO_4^{-3}, as shown in the distribution diagram in Figure 3.3. These could be interacting with the NPs differently as ligands and changing the nature of the NPs. Also, if NPs are fused together, it could explain the higher calculated coverages in the higher pH buffers as it would facilitate electron transfer throughout the film.

Figure 3.16 is the collection of images at 30 and 35x magnification of films exposed to the pH 3 phosphate buffer that each have different electroflocculation times. Though the contrast varies between the images, as the electroflocculation time increases, the film more
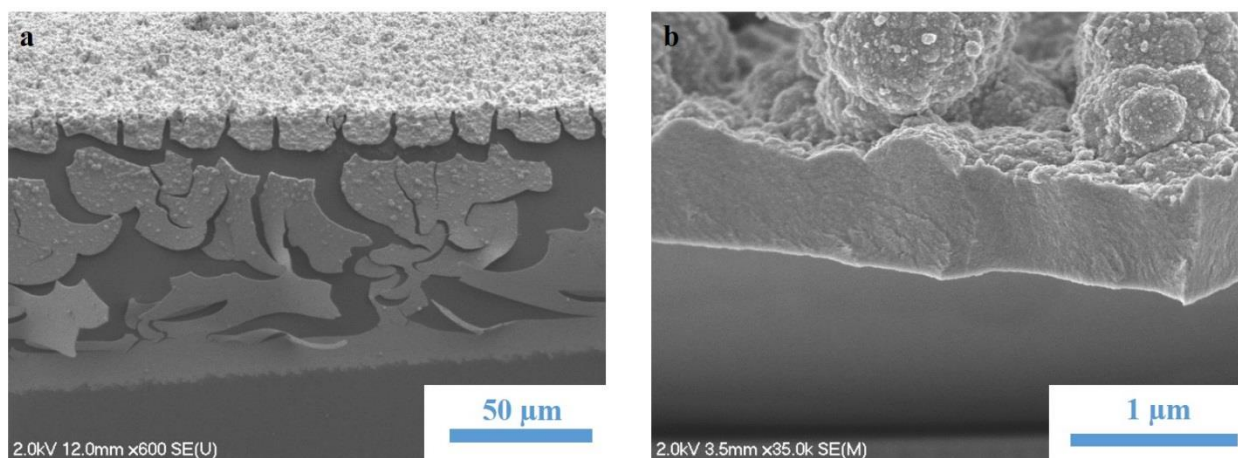
Figure 3.17: Cross-section SEM images of an electroflocculated IrO_X NP film on a Au coated glass slide. a) 600x magnification. b) 35,000x magnification.

91

evenly covers the electrode. There are clusters of IrOx NPs with bare electrode in between, confirmed by energy dispersive x-ray spectroscopy (EDS). As electroflocculation time increases, the bare spaces become fewer and at 15 min, the darker areas in the image still contain high percentages of Ir, inferring that the NPs are close to fully covering the electrode. This implies that as electroflocccuation time is increased, the coverage of the IrOx NPs also increases, as expected.

Figure 3.17 is a cross section of an IrO_X NP film on a Au coated glass slide after electroflocculation for 1 hour. The IrO_X NP film demonstrates complete coverage of the entire electrode, with a film thickness of ca. 1 μm. This corresponds to a thickness of about 500 IrO_X NPs, as they are ca. 2 nm in diameter. The films still maintain their mesoporous structure and rough morphology and this confirms that the original IrO_X NP islands formed at early
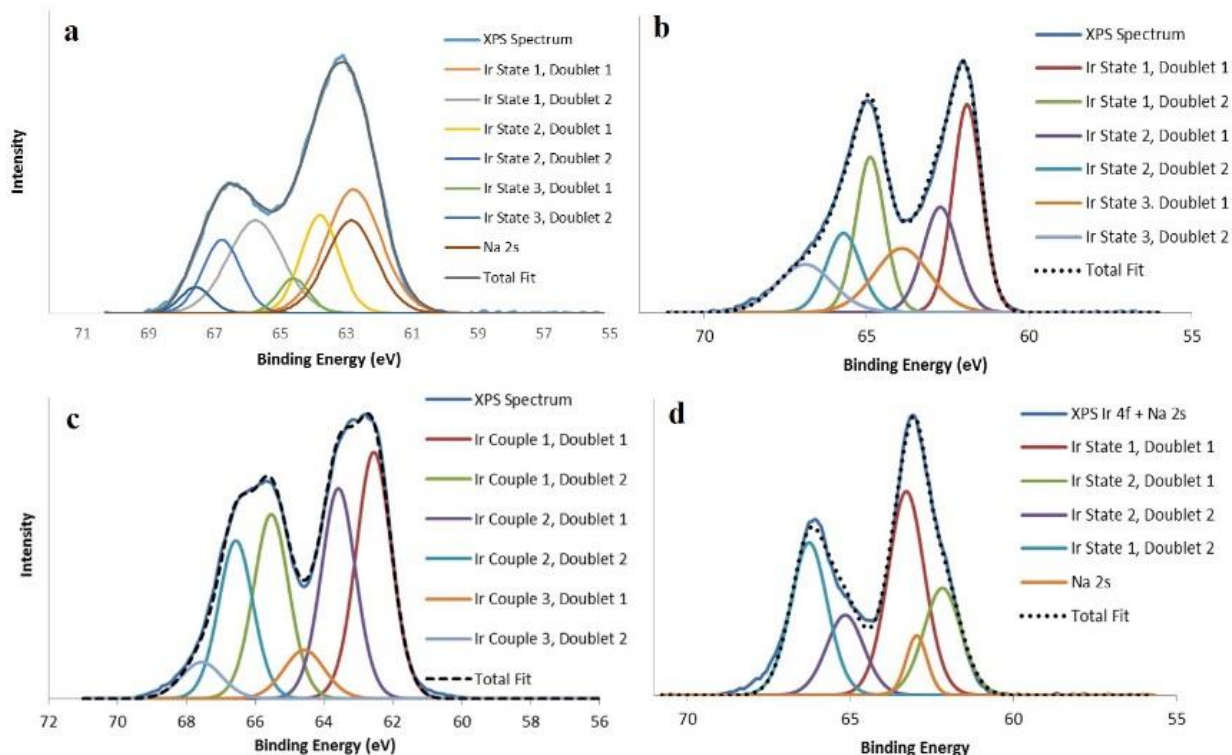
Figure 3.18: High resolution x-ray photoelectron spectra focused on the Ir 4f peak of IrO_X NPs in four different states. a) As-synthesized IrO_X NPs in 0.1 M NaOH (pH 13). b) Electroflocculated IrO_X NP film on a Au coated glass slide. c) Valeric acid capped IrO_X NPs in DCM. d) Chemically flocculated IrO_X NPs, precipitated via $(NH_4)_2Ce(NO_3)_6$.

electroflocculation times grow together to form a more uniform film across the electrode surface when the electroflocculation process is extended to longer periods of time.

3.3.6   X-ray Photoelectron Spectroscopy of Iridium Oxide Nanoparticles

Full x-ray photoelectron spectra were gathered of IrO$_X$ NPs prepared in various ways and each spectra confirmed the presence of Ir and O, as expected. The samples that were analyzed were the as-synthesized pH 13 IrO$_X$ NPs, an electroflocculated IrO$_X$ NP on a Au coated glass slide, the valeric acid capped IrO$_X$ NPs, which are further discussed in Chapter 4, and the $(NH_4)_2Ce(NO_3)_6$ chemically flocculated IrO$_X$ NP precipitate. All samples were deposited onto Au coated glass slides for analysis either by drop-casting or electroflocculation. High resolution scans of the Ir 4f doublet peaks were performed to analyze the change in shape of the different forms of IrO$_X$ NPs. These spectra, along with their fits of various Ir doublets are featured in Figure 3.18.

The first thing to note is that the Ir 4f peak overlaps with that of the Na 2s orbital. For the as-synthesized IrO$_X$ NPs and the chemically flocculated IrO$_X$ NPs, this is accounted for with the addition of a Na 2s peak into the fit. Both of these spectra show the presence of Na in the elemental analysis. This is because these samples were drop cast while in solutions that contained 0.1 M NaOH. Neither the electroflocculated film nor the valeric acid capped IrO$_X$ NPs exhibited Na in the elemental analysis of the samples.

Each Ir 4f high resolution scan required at least two different Ir couples to fit the spectra. These doublets correspond to the Ir 4f$_{7/2}$ and Ir 4f$_{5/2}$ orbitals, with the Ir 4f$_{7/2}$ appearing at a lower binding energy. The predicted ratio of the heights of Ir(4f$_{7/2}$):Ir(4f$_{5/2}$) is generally 4:3[130f] and this is accounted for in all of the fittings. Table 3.8 presents the binding energies for the Ir 4f$_{7/2}$ and Ir 4f$_{5/2}$ orbitals of each Ir species present in the different IrO$_X$ NPs. The areas of each fitted peak

were also found, so as to find the percentage each Ir species is present in the IrO_X NPs. This percentage is listed in the final column of Table 3.8.

Beginning with the as-synthesized IrO_X NPs in 0.1 M NaOH, the Ir 4f doublet is apparent, although the ratio of the two peaks is much larger than the expected 4:3. This is due to the

Table 3.8: Ir $4f_{7/2}$ and Ir $4f_{5/2}$ binding energies (eV) for each Ir species in the different preparations of IrO_X NPs. The percent of each Ir species is within the IrO_X NPs is also presented in the last column.

	Ir Species	Ir $4f_{7/2}$ BE (eV)	Ir $4f_{5/2}$ BE (eV)	% Area of Species
As-synthesized	1	62.77	65.75	58.7
	2	63.79	66.77	32.1
	3	64.59	68	9.2
Electroflocculated	1	61.9	64.88	45.5
	2	62.73	65.71	27.5
	3	63.91	66.89	27
Valeric Acid Capped	1	62.56	65.54	48.5
	2	63.6	66.58	40.4
	3	64.59	67.57	11.1
Chemically Flocculated	1	62.18	65.16	35
	2	63.27	66.25	65

overwhelming concentration of Na, which overlaps the Ir $4f_{7/2}$ peaks. As a comparison, metallic Ir exhibits binding energies of 60.9 and 63.8 eV for the Ir $4f_{7/2}$ and $4f_{5/2}$ orbitals, respectively, while those of the bulk material IrO_2 are 62.1 and 65.0 eV due to the oxidation of the iridium species.[130f] Three Ir species are required to fit the rest of the peak, where the lowest binding energy species makes up 58.7% of the Ir present in the nanoparticles. The other two species, combined, make up 43.1% of the nanoparticles. The lower binding energy species in the as-synthesized IrO_X NPs matches that of the bulk IrO_2. The two other species have higher binding

energies than those observed in the bulk material, suggesting there are Ir species with higher oxidation states present in the nanomaterial. The difference between bulk materials and their nanoparticle counterparts is the vast difference in surface area to volume ratio. As there are a higher number of surface species present in the nanoparticles, we may be able to observe them more clearly in XPS, which has a relatively low analysis depth. The two Ir species at higher binding energies may correspond to these surface species and their higher binding energies suggests they are at higher oxidation states than those within the core of the nanoparticle.

The Ir 4f high resolution spectrum of the electroflocculated IrO$_X$ NP films can also be fit using three different Ir species. The tailing can also be explained by the difference in oxidation state of the surface and core Ir species in the film. The Ir species that mostly closely resembles bulk IrO$_2$ comprises 45.5% of the Ir in the film. This is a slightly higher percentage of oxidized surface species, compared to the freely diffusing IrO$_X$ NP in 0.1 M NaOH. However, this appearance of a higher oxidization state Ir can be attributed to a phenomenon that occurs in bulk Ir materials. The overall shape, where there is significant tailing of the doublets, more closely matches that of the bulk IrO$_2$ films. Previous literature has attributed this to the screening response of the Ir 5d electrons in the bulk materials.[6] As an electroflocculated film, the IrO$_X$ NPs appear to behave more like the bulk IrO$_2$.

An attempt to manipulate the oxidation state of the electroflocculated IrO$_X$ NP film prior to XPS analysis and the results are shown in Figure 3.19. The potential of the electrode with the IrO$_X$ NP film was held at -0.3 V vs. Ag/AgCl for 10 minutes, at which point the slide was transported to another building on campus to run XPS on the film. Including the time to pump the x-ray photoelectron spectrometer down to vacuum, ca. 25 min elapsed between when the potential was held and when the spectrum was obtained. The potential that was applied was

negative enough to reduce the IrO$_X$ NP film to the Ir^{III} oxidation state. While there is a slight

shift to lower binding energies of the Ir 4f electrons which could indicate a slightly more reduced

Ir species, there is essentially no change to the peaks observed. Very similar results were

observed when the potential was held at a more positive potential, in order to oxidize the IrO$_X$

NP film to the Ir^V oxidation state. This indicates that while we can reversibly reduce and oxidize

these films electrochemically, the reduced and oxidized Ir species are short lived when the

potential is no longer being applied.

When capped with valeric acid, the Ir 4f spectrum (Figure 3.18c) of the IrO$_X$ NPs exhibits

a different shape than either the as-synthesized IrO$_X$ NPs or the electroflocculated NP film.

There are two distinct Ir doublets in this spectrum, with minor tailing at the higher binding
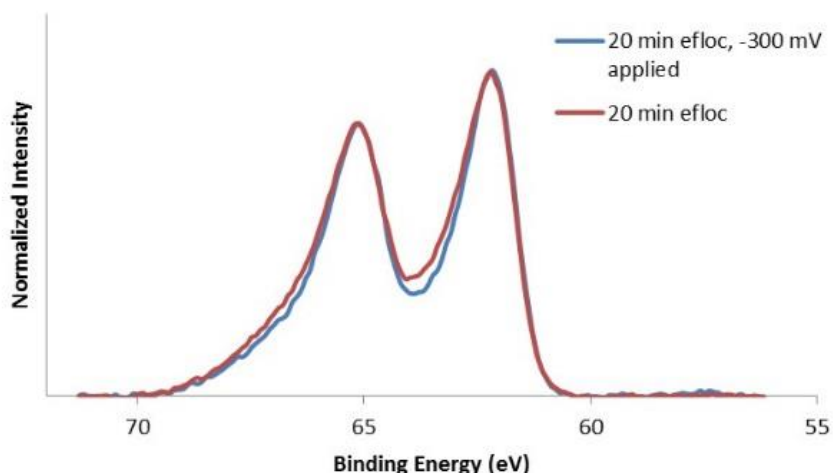
Figure 3.19: X-ray photoelectron spectra of an electroflocculated film before (red) and after (blue) holding the potential at -300 mV vs. Ag/AgCl.

energies. The ratio of the area of these two doublets is near 1:1. The other IrO$_X$ NPs have ratios

that are much closer to 2:1 and the third Ir species represents a much larger percentage of the Ir.

This could indicate that the addition of the carboxylic acid as a capping ligand may create a more

uniform surface species. The other two IrO$_X$ NP species mentioned above likely have a variety

of different oxide and hydroxide species on the surface. By capping them with an excess of

valeric acid, the surface becomes uniformly one oxidation state, controlled by the interaction with the carboxylic acid.

Figure 3.18d is the XPS spectrum of the chemically flocculated IrO$_X$ NPs. A chemical oxidant, $(NH_4)_2Ce(NO_3)_6$, was added to the as-synthesized IrO$_X$ NPs, which induced precipitation. Ce is also present in this precipitate (as explained in Chapter 2), due to the insolubility of $Ce(OH)_3$ in aqueous media. This is the only example of IrO$_X$ NPs where the higher binding energy couplet represents a higher percentage of the Ir species present, as seen in Table 3.8. This is likely due to the presence of Ce in the precipitate. The Ce can interact with the surface oxygen species of the IrO$_X$ NPs, pulling electron density away from the Ir sites, resulting in a higher observed binding energy. The presence of Ce appears to have a stronger oxidizing effect on the surface Ir sites, and possibly some of the core Ir species, than the carboxylic acid capping ligand.

From these experiments, it can be concluded that the IrO$_X$ NP environment greatly affects the binding energies of the Ir 4f electrons, especially those of the assumed surface species. We were able to shift these binding energies by replacing the capping ligand and changing the method of flocculation of the NPs.

3.4 CONCLUSIONS

From these characterization studies, much was learned about the IrO$_X$ NPs and their surface chemistry. The pH of the buffer which the film is exposed to can distinctly change the electrochemical behavior of the NP films, resulting in a higher resistance within the film. Catalytic Tafel plots established the similarity in water oxidation catalysis mechanisms for IrO$_X$ NP films in the same buffer, but different mechanisms for those obtained at different pH. UV-Vis spectroelectrochemistry demonstrated the spectral changes of the four different oxidation

states of Ir in the IrO$_X$ NPs and confirmed that the Ir^{VI} state is the active species in water oxidation catalysis. Zeta potential measurements demonstrated how the surface charge of the IrO$_X$ NPs changes depending on the buffer environment, when stabilized by phosphate species. Raman spectroscopy confirmed the short-lived rutile crystalline structure within the electroflocculated IrO$_X$ NPs, which further confirms that the ground state of these NPs is Ir^{IV}. XPS confirmed that changing the environment of the IrO$_X$ NPs can change binding energy of the electrons, simply based on what is near the surface Ir species.

3.5 ACKNOWLEDGMENTS

REFERENCES

(1)   Gottesfeld, S.; McIntyre, J. D. E. *J. Electrochem. Soc.* **1979**, *126*, 742.

(2)   Hillman, A. R.; Skopek, M. A.; Gurman, S. J. *Phys. Chem. Chem. Phys.* **2011**, *13*, 5252.

(3)   Huang, Y. S.; Lin, S. S.; Huang, C. R.; Lee, M. C.; Dann, T. E.; Chien, F. Z. *Solid State Communications* **1989**, *70*, 517.

(4)   Johnson, C. S.; Hupp, J. T. *J. Electroanal. Chem.* **1993**, *345*, 351.

(5)   Kaya, S.; Ogasawara, H.; Naslund, L. A.; Forsell, J.-O.; Casalongue, H. G. S.; Miller, D. J.; Nilsson, A. *Catalysis Today* **2013**, *205*, 101.

(6)   Kodintsev, I. M.; Trasatti, S.; Rubel, M.; Wieckowski, A.; Kaufher, N. *Langmuir* **1992**, *8*, 283.

(7)   Lioa, P. C.; Chen, C. S.; Ho, W. S.; Huang, Y. S.; Tiong, K. K. *Thin Solid Films* **1997**, *301*, 7.

(8)   Mailley, S. C.; Hyland, M.; Mailley, P.; McLaughlin, J. M.; McAdams, E. T. *Materials Science and Engineering* **2002**, *21*, 167.

(9)   McIntyre, J. D. E.; Peck, J., W. F.; Nakahara, S. *J. Electrochem. Soc.* **1980**, *127*, 1264

(10)   Minguzzi, A.; Locatelli, C.; Gappelletti, G.; Scanini, M.; Vertova, A.; Ghigna, P.; Rondinini, S. *J. Phys. Chem. A* **2012**, *116*, 6497.

(11)   Minguzzi, A.; Lugaresi, O.; Locaterri, C.; Rondinini, S.; D'Acapito, F.; Achilli, E.; Ghigna, P. *Anal. Chem.* **2013**, *85*, 7009.

(12)   Mo, Y.; Stefan, I. C.; Cai, W.-B.; Dong, J.; Carey, P.; Scherson, D. A. *J. Phys. Chem. B* **2002**, *106*, 3681.

(13)   Music, S.; Popovic, S.; Maljkovic, M.; Skoko, Z.; Furic, K.; Gajovic, A. *Materials Letters* **2003**, *57*, 4509.

(14)   Rogers, D. B.; Shannon, R. D.; Sleight, A. W.; Gillson, J. L. *Inorg. Chem.* **1969**, *8*, 841.

(15)   Thanawala, S.; Georgiev, D. G.; Baird, R. J.; Auner, G. *Thin Solid Films* **2007**, *515*, 7059.

(16)   Zou, S.; Chan, H. Y. H.; Williams, C. T.; Weaver, M. J. *Langmuir* **2000**, *16*, 754.

(17)   Zou, S.; Gomez, R.; Weaver, M. J. *Langmuir* **1997**, *13*, 6713.

(18) Kotz, R.; Stucki, S. *Electrochem. Acta.* **1986**, *31*, 1311.

(19) Kotz, R.; Stucki, S.; Scherson, D.; Kolb, D. M. *J. Electroanal. Chem.* **1984**, *172*, 211.

(20) Trasatti, S. *Electrochim. Acta.* **1984**, *29*, 1503.

(21) Tilley, S. D.; Cornuz, M.; Sivula, K.; Gratzel, M. *Angew. Chem.* **2010**, *122*, 6549.

(22) Walter, M. G.; Warren, E. L.; McKone, J. R.; Boettcher, S. W.; Mi, Q.; Santori, E. A.; Lewis, N. S. *Chem. Rev.* **2010**, *110*, 6446.

(23) Yagi, M.; Tomita, E.; Sakita, S.; Kuwabara, T.; Nagai, K.; J. Phys. Chem. B 2005, 21489 *J. Phys. Chem. B* **2005**, *109*, 21489.

(24) Nakagawa, T.; Beasley, C. A.; Murray, R. W. *J. Phys. Chem. C* **2009**, *113*, 12958.

(25) Zhao, Y.; Hernadez-Pagan, E. A.; Vargas-Barbosa, N. M.; Dysart, J. L.; Mallouk , T. E. *J. Phys. Chem. Lett.* **2011**, *2*, 402.

(26) Nakagawa, T.; Bjorge, N. S.; Murray, R. W. *J. Am. Chem. Soc.* **2009**, *131*, 15578.

(27) Gambardella, A. A.; Bjorge, N. S.; Alspaugh, V. K.; Murray, R. W. *J. Phys. Chem. C* **2011**, *115*, 21659.

(28) Gambardella, A. A.; Feldberg, S. W.; Murray, R. W. *J. Am. Chem. Soc.* **2012**, *134*, 5774.

(29) Hardcastle, F. D.; Wachs, I. E. *Journal of Raman Spectroscopy* **1995**, *26*, 397.

(30) Hoertz, P. G.; Kim, Y. L.; Youngblood, J. W.; Mallouk, T. E. *J. Phys. Chem. B* **2007**, *111*, 6945.

(31) Morris, N. D.; Suzuki, M.; Mallouk, T. E. *J. Phys. Chem. A* **2004**, *108*, 9115.

(32) Zhao, Y.; Vargas-Barbosa, N. M.; Hernandez-Pagan, E. A.; Mallouk, T. E. *Small* **2011**, *7*, 2087

(33) Wohler, L.; Witzmann, W. Z. *Anorg. Chem.* **1908**, *57*, 323.

(34) Augustynski, J.; Koudelka, M.; Sanchez, J. *J. Electroanal. Chem.* **1984**, *160*, 233.

(35) Casalongue, H. G. S.; Ng, M. L.; Kaya, S.; Friebel, D.; Ogasawara, H.; Nilsson, A. *Angew. Chem. Int. Ed.* **2014**, *53*, 7169.

(36) Wertheim, G. K.; Guggenheim, H. J. *J. Phys. Rev. B* **1980**, *22*, 4680.

(37) Gambardella, A. A., University of North Carolina at Chapel Hill, 2013.

(38)   Felberg, S. W., Comparison of the EC' Catalytic Mechanism When the Redox Intermediate is in Solution and When it is Bound to the Surface.

CHAPTER 4: Iridium Oxide Nanoparticles in Organic Media

4.1 INTRODUCTION

4.1.1 Electrochemistry of Iridium Oxide Nanoparticles

The electrochemistry of small (< 2 nm in diameter) iridium oxide nanoparticles (IrO_X NPs) has been thoroughly explored in aqueous solutions by both the Murray and Mallouk laboratories.[1-8] Both freely diffusing IrO_X NPs and films deposited of the same NPs exhibit two Nernstian behaved proton coupled electron transfer (PCET) couples, $Ir^{V/IV}$ and $Ir^{IV/III}$, before the onset of water oxidation. A figure (Figure 4.1) taken from an article published by the Murray lab depicts these shifts.[1] Both couples for the IrO_X NP films shift about 70 mV/pH, very close to the 60 mV/pH for a 1 e^-, 1 H^+ process. The freely diffusing IrO_X NPs also exhibit this behavior for the $Ir^{V/IV}$ couple and the $Ir^{IV/III}$ couple at in solutions below pH 6. Above pH 6, the formal potentials shift 116 mV/pH, which correlates more closely to a 1 e^-, 2 H^+ reaction.

The expected Ir redox reactions for the electroflocculated IrO_X NP films are presented in Scheme 4.1. The same reactions are expected for freely diffusing IrO_X NPs in solutions below

Scheme 4.1

$$NP]Ir^V(OH)(=O) + e^- + H^+ \rightarrow NP]Ir^{IV}(OH)(OH)$$

$$NP]Ir^{IV}(OH)(OH) + e^- + H^+ \rightarrow NP]Ir^{III}(OH)(H_2O)$$
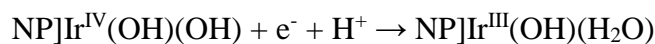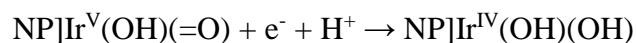
pH 6. For the freely diffusing IrO_X NPs in solutions above pH 6, however, the expected reactions are shown in Scheme 4.2. This is based on the suspected 1 e^-, 2 H^+ mechanism due to the Nernstian shift observed in Figure 4.1.

Scheme 4.2

$$NP]Ir^V(OH)(=O) + e^- + H^+ \rightarrow NP]Ir^{IV}(OH)(OH)$$

$$NP]Ir^{IV}(OH)(OH) + e^- + 2H^+ \rightarrow NP]Ir^{III}(H_2O)(H_2O)$$
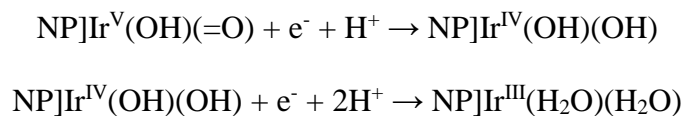
While these reactions are well defined, there has been little exploration into the IrO_X NP

behavior in organic and aprotic solvents. It is expected that these observed PCET changes would

be greatly diminished in aprotic media. The research presented below in Sections 4.3.1 and 4.3.2

explores the electroflocculated IrO_X NP behavior in completely aprotic media (DMSO). The

addition of aqueous media and organic acids is also explored to observe how the electrochemical

behavior changes as the films are changed from completely aprotic conditions to very low

concentrations of protons and then to media that are a 50:50 mixture of aprotic and aqueous

solutions.
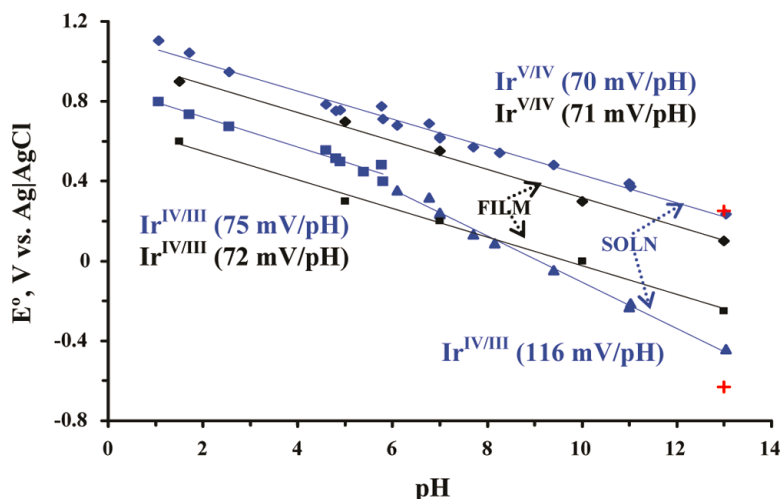
Figure 4.1[1]: pH dependency of the formal potentials of $Ir^{V/IV}$ and $Ir^{IV/III}$ for the freely diffusing IrO_X NPs (blue) and the electroflocculated IrO_X NP films (black) in various phosphate buffers.

4.1.2 Synthesis of Metal Oxide Nanoparticles with Organic Surfactant Shells

Iridium oxide nanoparticles are traditionally synthesized using a basic hydrolysis, based on

the Woehler method.[1-5,7-9] Hydrolytic synthetic methods can result in nanoparticles with poor

monodispersity and crystallinity.[10,11] As this could have significant effects on catalytic ability,

other synthetic methods were investigated to improve these qualities. Nanoparticles synthesized using a thermal degradation synthesis generally have both high crystallinity and good monodispersity.[12-14] For these synthesis, a metal salt is refluxed in a high boiling point solvent in the presence of a surfactant, such as oleic acid or oleylamine. Surfactants are selected for their functional groups and their interactions with metal oxide surfaces; both long carbon chain carboxylic acids and amines have been favored in the literature.[12-15] At these high temperatures, the metal salt decomposes and the nanoparticles start to nucleate. The surfactants form a shell around these nucleates and limit their growth; these syntheses rarely produce nanoparticles larger than 10 nm in diameter. The colloidal suspension that results from these syntheses can easily be precipitated with the addition of a polar solvent.

A wide variety of metal oxide nanoparticles have been successfully synthesized using this thermal degradation method, included ITO, ZrO_2, Fe_2O_3 and Fe_3O_4.[10-21] The research presented in Section 4.3.3 extends this method to the synthesis of small IrO_X NPs in an attempt to improve the monodispersity and crystallinity over the hydrolytic method mentioned above.

4.1.3   Ligand Modification of Metal Oxide Nanoparticles in Organic Media

Surface modification of metal oxide nanoparticles has been extensively studied, due to its wide variety of applications.[1,22-25] Simply changing the capping ligand can change the solubility of the nanparticles, increasing the applicability of a wider range of media.[1] Many organic functional groups are known to interact with metal oxide surfaces, including carboxylic acids, amines, silanes, phosphates and phosphonates.[26] Both amines and carboxylic acids interact via chemisorptive and physisorptive properties. There is an exchange equilibrium of these ligands on the surface of the nanoparticle and in solution. The Murray lab has previously shown exchange of the aqueous IrO_X NPs into dichloromethane (DCM) using a variety of carboxylic acids, in excess.[1,27] Silanes, phosphates and phosphonates form covalent bonds to metal oxide

surfaces, eradicating the equilibrium between surface bound and solvated ligands observed with carboxylic acids. These can then be used to quantify ligand attachment to the nanoparticle surface, using either an electrochemical or spectroscopic tag.[26]

Ligands with phosphate functional groups are an attractive option due to their stable P-O-Metal bonds.[26] There are limited phostphate functionalized compounds commercially available, so these ligands generally involve complex synthetic methods. One synthetic route which limits by-products and results in low hazard waste is to functionalize these ligands using click chemistry.[28] The Turro laboratory[29] developed an azide terminated phosphate ligand (**5** in Scheme 4.3), which they were able to further functionalize using an azide alkyne Huisgen cycloaddition in the presence of a Cu(I) catalyst. Using the same concept, the Xian laboratory clicked ethynyl ferrocene onto the surface of iron oxide nanoparticles.[16]

The research presented in Section 4.3.4 extends this method to valeric acid capped IrO_X NPs, using the phosphate functional group's affinity to metal oxide surface to electrochemically tag IrO_X NPs with ferrocene (Fc). Previous surface modification of these aqueous IrO_X NPs was successful with a wide variety of carboxylic acids. However, it was not quantifiable, due to the equilibrium and constant exchange of the ligands between the surface of the nanoparticles and solution. The use of a phosphate creates a covalent bond to the surface, eliminating this effect. The research presented below demonstrates the quantitative electrochemical analyses of these ferrocenated iridium oxide nanoparticles ($FcIrO_x$), so as to determine the number of ligands present on the surface, as well as the NP diffusion coefficient in a non-aqueous solution.

4.2 EXPERIMENTAL

4.2.1 Aqueous Hydrolysis of IrOx NPs

The $Ir^{IV}O_X$ nanoparticles were synthesized using a Wohler method,[9] in which a 2.5 mM

solution of K_2IrCl_6 (99%, Strem Chemicals) in nanopure H_2O was adjusted to pH 13 with 25%

w/w NaOH (50% w/w, Fisher Scientific). The solution was heated at 90 °C for 20 minutes and

then allowed to cool to RT and to rest for at least 24 hours after the synthesis, before

electroflocculation.

4.2.2 Electroflocculation of IrOx NP Films

For electroflocculations on Au coated glass slides, Au slides were first cleaned by

exposure to piranha solution (3:1 concentrated H_2SO_4 (Fisher Scientific) to H_2O_2 (30% w/w,

Fisher Scientific)), and then rinsed with nanopure H_2O and dried under a stream of Ar gas.

Piranha solution is highly oxidizing and should therefore be handled with care.

For films formed on Pt disk electrodes, the Pt electrode was first prepared by polishing

with varying sizes of silica, then sonicated to remove unwanted particles. The electrode was

further cleaned by potential cycling in 0.1 H_2SO_4. For films formed on glassy carbon (GC)

electrodes, the electrode was polished using 0.25 μm diamond spray and then sonicated to

remove any excess diamond particles.

The films were formed from unstirred pH 13 IrOx nanoparticle solutions by applying a

potential bias of 0.9 V *vs*. Ag/AgCl for 10 minutes. The films were rinsed with nanopure H_2O

and then cyclic voltammetry (CV) was performed in 0.1 M NaOH to verify the presence of a

film.

4.2.3 Non-Aqueous Electrochemistry of Iridium Oxide Nanoparticle Films

Electrochemical experiments were performed using a standard three electrode cell, where

an IrO$_X$ NP film atop a Au coated glass slide acted as a working electrode and Pt wire and Ag/AgCl (BASi) functioned as auxiliary and reference electrodes, respectively. Cyclic voltammetry of these films was performed in dimethyl sulfoxide (DMSO) (Fisher Scientific with 0.1 M tetrabutylammonium perchlorate (TBAP) (Sigma Aldrich) as supporting electrolyte. In the first experiment, nanopure water was added to the solution to gradually increase the H$^+$ concentration. In the second, 0.1 M NaOH (Fisher Scientific) in nanopure water was added to the DMSO, so as to more accurately control the pH of the solution.

4.2.4   Addition of Carboxylic Acids and Carboxylates

Two different carboxylic acid/carboxylate, hexanoic acid and valeric acid (Both from Sigma Aldrich), were used to probe the electrocatalytic ability of IrO$_X$ NP films towards the Kolbe reaction. The conjugate bases were prepared from the corresponding carboxylic acid by titrating with tetrabutylammonium hydroxide (TBAOH) (Sigma). The product, which was in methanol, was rotovapped, yielding a liquid-like solid, suspected of being an ionic liquid. This product was then dissolved in acetonitrile (CH$_3$CN) (Fisher Scientific) with 0.1 M TBAP as supporting electrolyte. Cyclic voltammetry was performed to investigate the IrO$_X$ NP film's ability to electrocatalytically oxidize each of the carboxylates.

In separate experiments, the carboxylic acids were dissolved in CH$_3$CN, along with 0.1 tetrabutylammonium hexafluorphosphate (TBAPF$_6$). Differential pulse voltammetry (DPV) was performed to examine how the IrO$_X$ NP Ir$^{IV/III}$ wave shifted during a titration with 0.1 M TBAOH.

4.2.5   Hot Injection Thermal Degradation Synthesis of IrO$_X$ NPs

This procedure was developed in the Murray laboratory[17,19] and was modified from a procedure published by the Fang laboratory.[13,18] 0.2 mmol Iridium acetylacetonate (Ir(acac)$_3$) (Sigma) and 1.9 mmol oleic acid (Sigma) were dissolved in octadecene (Sigma) in a 50 mL 3-

neck round bottom flask equipped with a magnetic stir bar, thermocouple and condenser. The vessel was evacuated and heated for 1 hour at 120 °C while stirring. The temperature was rapidly increased to 295 °C. 2.4 mmol oleylamine (Sigma) in 0.2 mL octadecene was injected via syringe at this temperature, causing the solution to turn black. This solution was refluxed for an hour at 320 °C and then allowed to cool to RT. 40 mL of ethanol (Fisher Scientific) was added to the suspension, which was then centrifuged at 3000 RPM for 10 minutes to induce precipitation of the nanoparticles. The precipitate was then resuspended in 3 mL of hexanes (Fisher Scientific), producing a dark blue solution.

4.2.6   Valeric Acid Exchange of IrO$_X$ NPs to Organic Media

5 mL of the aqueous IrO$_X$ NPs in pH 13 as-synthesized solution (0.0192 mM) was exchanged using an excess of valeric acid (1 mmol) in dichloromethane (DCM). The solution was stirred overnight and the organic layer was decanted from the aqueous layer ca. 24 hours later. A change in color of the DCM layer from colorless to dark purple was indication of a successful exchange.

4.2.7   Ferrocenation of IrO$_X$ NPs

Following Scheme 4.3, IrO$_X$ NPs were ferrocenated from the valeric acid capped NPs discussed in Section 4.2.6. Synthesis of the azo terminated phosphate ligand (**5**) was from previous literature from the Turro laboratory[29] and the click synthesis attachment of the ethylnyl ferrocene was reported by the Xian laboratory.[16] A 100 mL round bottom flask was flame-dried and Ar-purged. 55 mL of anhydrous ethylene glycol (**2**) (Sigma) was added along with a magnetic stir bar and cooled to 0 °C via icebath. 40.5 mmol of α-bromoisobutyryl bromide (**1**) (Sigma) was added dropwise via syringe and stirred vigorously for 3 hours. 100 mL of nanopure H$_2$O was added to quench the reaction and the product was extracted with chloroform (3 x 50

mL). The organic extract was dried over MgSO$_4$ (Sigma), filtered and concentrated via roto-vap to yield a viscous clear liquid (**3**).

9.5 mmol of **3** was dissolved in 15 mL of anhydrous dimethylformamide (DMF) (Fisher Scientific) in a flame-dried, Ar-purged 100 mL round bottom flask, equipped with a magnetic stir bar. 10.4 mmol of NaN$_3$ (Sigma) was added to the solution and stirred for 20 hours at RT. 20 mL of nanopure H$_2$O was added to quench the reaction and the product was extracted with chloroform (3 x 20 mL). The organic extract was again dried over MgSO$_4$, filtered and concentrated to yield a viscous clear liquid (**4**). This product was dried overnight *en vacuo* to remove excess DMF.

5.8 mmol of **4** was dissolved in 15 mL of anhydrous tetrahydrofuran (THF) (Fisher Scientific) in a flame-dried, Ar-purged round bottom flask, equipped with a magnetic stir bar. The solution was cooled to 0 °C via ice bath and 6.4 mmol triethyl amine (Sigma) was added. 6.4 mmol POCl$_3$ (Sigma) was added dropwise via syringe, forming a cloudy white solution. The
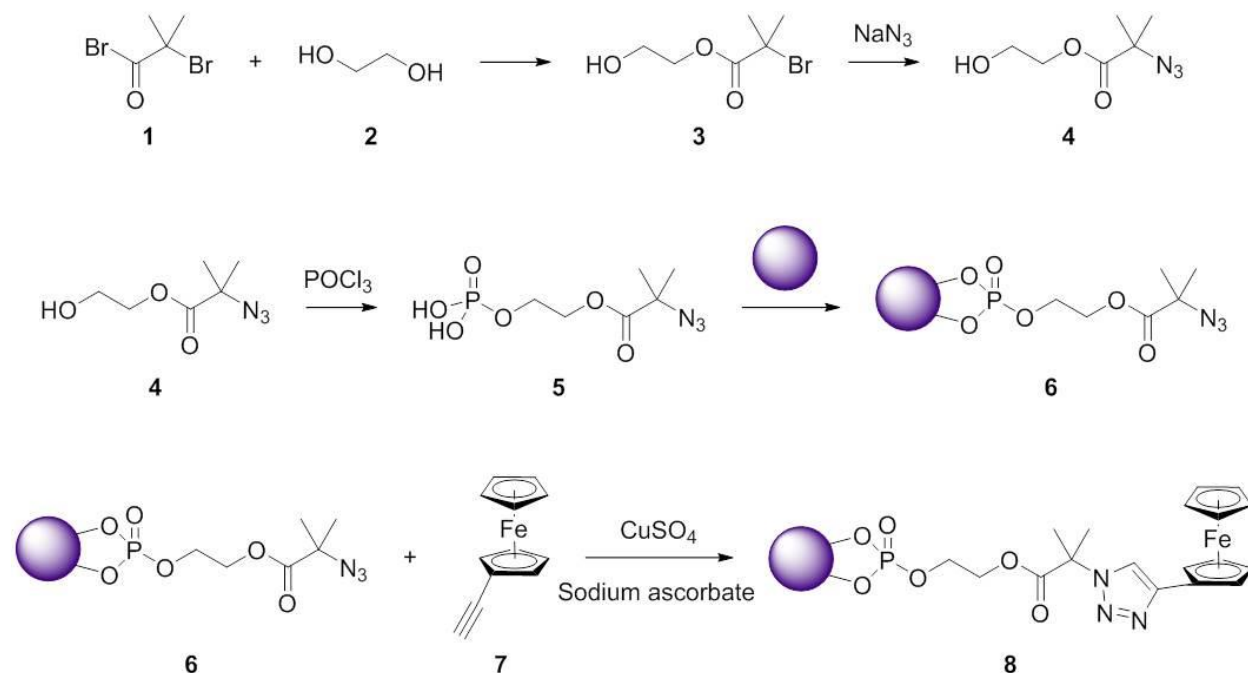
Scheme 4.3: Synthetic route for the Click Ferrocenation of IrO$_X$ NPs. The purple circle represents the IrO$_X$ NPs, which begin the synthesis as valeric acid capped NPs.

109

solution was warmed to RT and then stirred for an additional 3 hours. Over the course of

stirring, the solution changed from a cloudy white suspension to a light yellow solution. 10 mL

of nanopure H_2O was added to quench the reaction and the pH was adjusted to < 2. The product

was then extracted with chloroform (Fisher Scientific) (3 x 15 mL), before being dried over

$MgSO_4$, filtered and concentrated, resulting in a yellow, viscous oil (**5**).

A 1:1 ratio of **5**:IrO_X NPs by weight was added to 5 mL of chloroform. The solution was

stirred for 24 hours. Hexanes were added and then the solution was centrigued at 4000 RPM for

10 minutes. The precipitate (**6**) was collected after decanting off the excess liquid, and then

washed three times with hexanes.

6 was dissolved in 4:1 $DMSO$:H_2O. 0.124 mmol of ethynyl ferrocene (**7**) (Sigma), 0.008

mmol of $3CuSO_4 \cdot 5H_2O$ (Sigma) and 0.021 mmol sodium ascorbate (Sigma) were added to the

solution. The reaction was stirred for 24 hours at RT. 1 mL each of $CHCl_3$, acetone and ethanol

(All from Fisher Scientific) were added to the solution, which was then centrifuged at 4000 RPM

for 10 minutes. The precipitate (**8**) was collected and wasted three times with 4:1 $DMSO$:H_2O.

4.2.8   Instrumentation

4.2.8.1   High Resolution Transmission Electron Microscopy (TEM)

TEM images were obtained on a JEOL 2010F FasTEM on copper grids (200 carbon mesh,

carbon-coated Formvar, Ted Pella, Redding, CA).

4.2.8.2   Energy-Dispersive X-Ray Spectroscopy (EDS)

EDS elemental analysis was performed using an Oxford INCA EnergyTEM 250 TEM

microanalysis system within the JEOL 2010F FastTEM mentioned above.

4.2.8.3   Centrifugation

Samples were centrifuged in an Eppendorf 5810 centrifuge with a fixed angle rotator at

3000-4000 RPM for 10 minutes.

4.2.8.4 X-Ray Photoelectron Spectroscopy (XPS)

A Kratos Axis Ultra DLD system with monochromatic Al Kα x-ray source was used to obtain XPS specta. High resolution scans were taken at pass energy of 20 eV and the spectral energy axis was aligned at the C 1s peak (284.6 eV).

4.2.8.5 Electrochemsitry

All electrochemical experiments were performed on a CH Instruments 760c potentiostat.

4.3 RESULTS AND DISCUSSION

4.3.1 Electrochemistry of Iridium Oxide Nanoparticle Film in Non-Aqueous Media

Cyclic voltammetry of electroflocculated IrO_X NP films on Au coated glass slides were obtained in DMSO, a completely aprotic solvent. As all of the redox couples associated with the IrO_X NP films ($Ir^{IV/III}$, $Ir^{V/IV}$ and water oxidation catalysis) are proton coupled electron transfers (PCET), it was hypothesized that no electrochemically active species would be seen in the cyclic voltammetry under these conditions. This is largely true, as there are no distinct peaks within the window of -0.4 to 0.6 V vs. Ag/AgCl, as seen in Figure 4.2a. There is an increase in current around 0.6 V vs. Ag/AgCl, which may be water oxidation via IrO_X NPs of the residual water left in the mesoporous film from electroflocculation. When the potential window was expanded to -1.0 V vs. Ag/AgCl, a quasi-reversible redox couple is observed with a $E_{1/2}$ of -0.65 V vs.
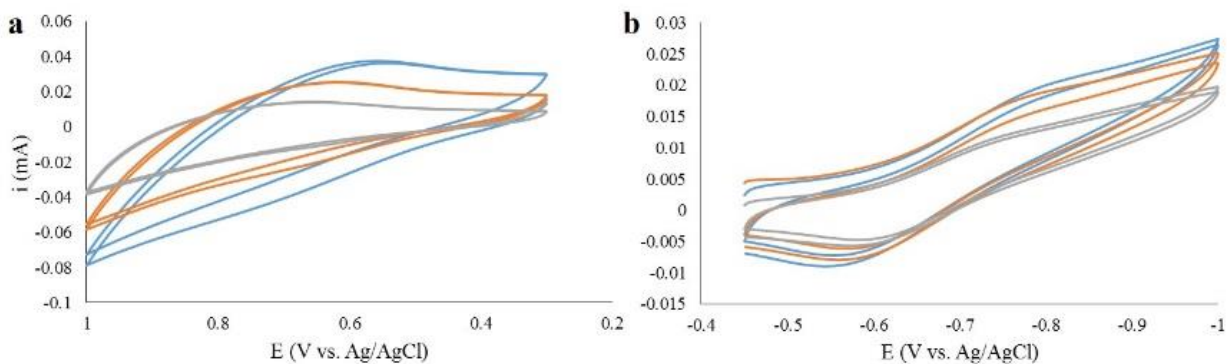
Figure 4.2: Cyclic voltammetry of an electroflocculated IrO_X NP film in DMSO with 0.1 M TBAP. Three different scan rates are represented in each potential window, 50 mV/s in blue, 25 mV/s in orange and 10 mV/s in purple.

111

Ag/AgCl and ΔE_p of 250 mV (Figure 4.2b). The i_p is linearly correlated with scan rate (v),

indicating that it is a surface species. However, it's $E_{1/2}$ is much more negative than any Ir redox

species that is generally observed for the IrO_X NP films.

It was hypothesized that this peak was the $Ir^{IV/III}$ redox couple, shifted to more negative

potentials due to the lack of protons available to undergo the expected PCET. In order to text

this hypothesis, nanopure water was added to the solution of 0.1 M TBAP in DMSO in 1 mL

increments (Figure 4.3a). The redox couple shifts positively with each respective addition of

H_2O. When the solution is 50% aqueous, the final $E_{1/2}$ of the couple is -0.35 V. Because of the

high aqueous character of the solution, however, the TBAP electrolyte is no longer soluble and
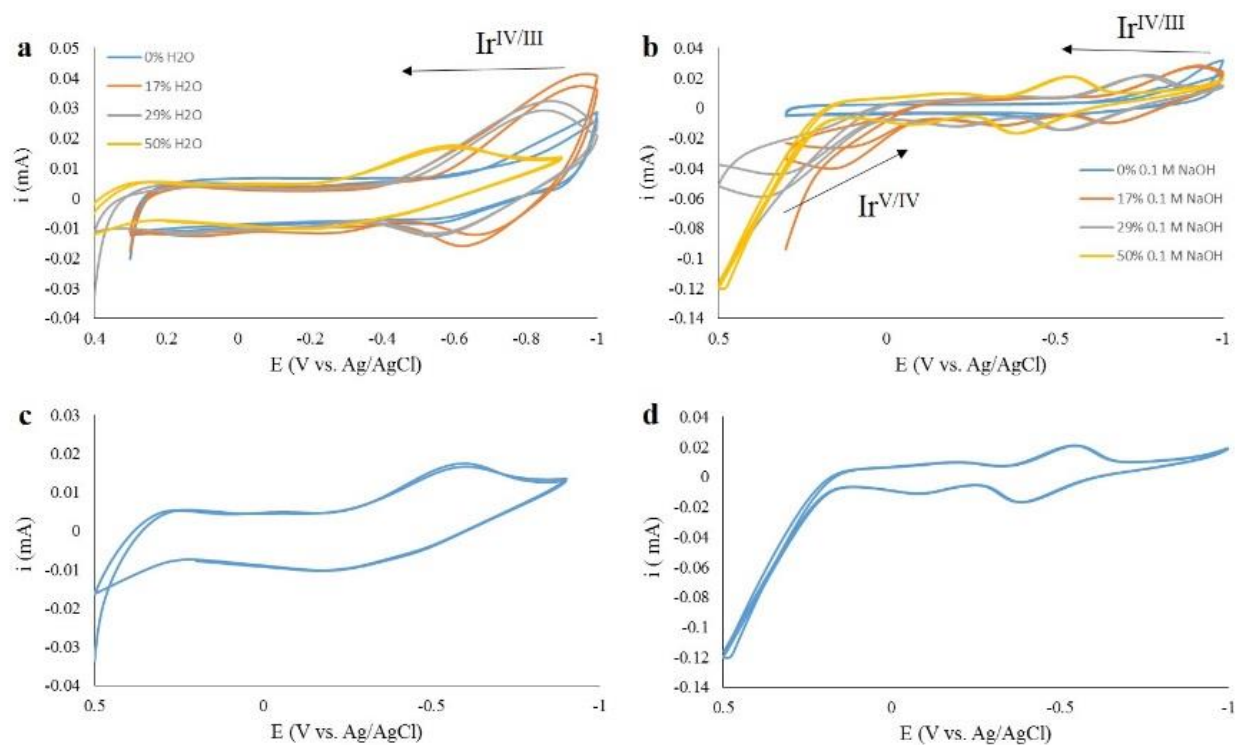
Figure 4.3: a) Cyclic voltammetry of an electroflocculated IrO_X NP film in DMSO with additions of nanopure H_2O. b) Cyclic voltammetry of an electroflocculated IrO_X NP film in DMSO with additions of 0.1 M NaOH in nanopure H_2O. c) Final CV of an electroflocculated IrO_X NP film in 50% DMSO, 50% H_2O. d) Final CV of an electroflocculated IrO_X NP film in 50% DMSO, 50% 0.1 M NaOH. Scan rate is 10 mV/s for all figures. Black arrows indicated the direction in which the Ir redox waves are shifting.

112

the high resistivity of solution results in a ΔE_p of 400 mV, instead of the near 0 mV expected

ΔE_p for a reversible surface species.

In order to combat the decrease in solubility of the electrolyte, the same experiment was

performed, but with additions of 0.1 M NaOH in nanopure H_2O instead (Figure 4.3b). The same

shift in $E_{1/2}$ is observed, with the final $E_{1/2}$ at 50% 0.1 M NaOH being 0.45 V vs. Ag/AgCl.

Because of the added supported electrolyte, the ΔE_p also decreases to 150 mV. The $E_{1/2}$ of this

species shifts towards that of the $Ir^{IV/III}$ species in 0.1 M NaOH (ca. -0.3 V vs. Ag/AgCl).

Because it is not in a completely aqueous solution, the aprotic solvent that is still present results

in a negative shift of the $E_{1/2}$. Also of note, the $Ir^{V/IV}$ redox wave is visible in these at -0.1 V vs.

Ag/AgCl, as is the increase in current normally associated with water oxidation catalysis. The

onset potential for what is presumed to be water oxidation catalysis is considerably lower than
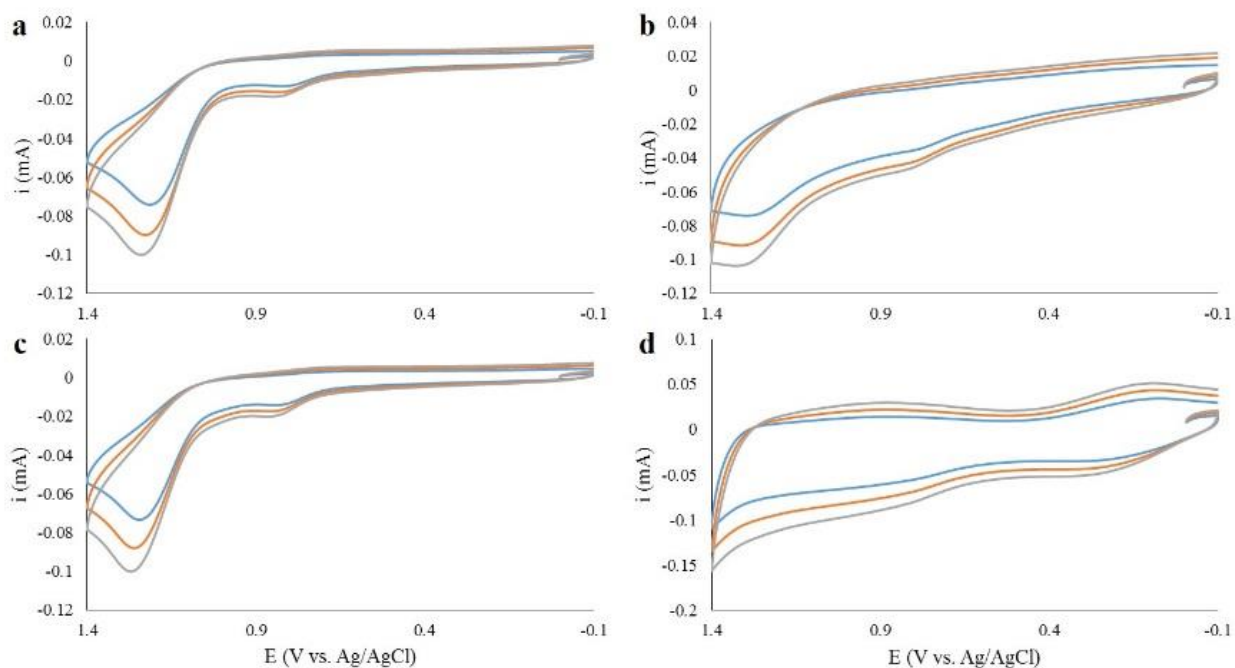
Figure 4.4: Cyclic voltammetry of various carboxylates in CH_3CN and 0.1 M TBAP. Various scan rates are shown, 200 mV/s in blue, 300 mV/s in orange and 400 mV/s in purple. a) 4 mmol tetrabutylammonium hexanoate with a GC working electrode. b) 4 mmol tetrabutylammonium hexanoate with an electroflocculated IrO_X NP film. c) 4 mmol tetratbutylammonium valerate with a GC working electrode. d) 4 mmol tetrabutylammonium valerate with an electroflocculated IrO_X NP film.

those previously reported.[2,4-8] At pH 13, the onset occurs at ca. 0.6 vs. Ag/AgCl. In the last CV

of these 50% solutions, the onset is at ca. 0.2 V vs. Ag/AgCl. Due to the aprotic nature of

DMSO, it is hard to quantify a pH of this solution, but it appears to make the solution more basic

and shift all PCET reactions to more negative potentials. If this is indeed water oxidation

catalysis, this is one of the lowest onset potentials reported for this reaction.

4.3.2   Addition of Carboxylic Acids and Carboxylates to Organic Media

In an effort to deduce whether the IrO_X NPs could act as an electrocatalyst for the Kolbe

reaction, cyclic voltammetry was performed in 0.1 M $TBAPF_6$ in CH_3CN. CVs of the hexanoate

and valerate with a GC working electrode and with an IrO_X NP film on the working electrode are

presented in Figure 4.4. The onset potentials for the oxidation of hexanoate are nearly identical

for the two different electrode surfaces. For the hexanoate oxidation via IrO_X NP film, there is

no increase in current that suggests further catalysis of this reaction. For the valerate solution, in

Figure 4.4d, the CV is largely dominated by the $Ir^{IV/III}$ and $Ir^{V/IV}$ waves of the film. If there is

any current from valerate oxidation, it is indistinguishable from the film electrochemistry. While

IrO_X NPs may be able to oxidize carboxylates, such as hexanoate and valerate, GC carbon

electrodes are also able to do so under the same conditions. Thus, there is no benefit in using

such as expensive electrode material to perform this reaction.

The IrO_X NP film electrochemical behavior in CH_3CN, 0.1 M TBAP was explored with

the addition of the same two carboxylic acids, as well as oxalic acid. Each carboxylic acid was

titrated with 0.1 M TBAOH in order to observe the shifts of the IrO_X NP redox couples. While

the measurement of pH in organic media is a complicated concept, the titration of the carboxylic

acid with TBAOH creates a more basic solution and the Ir redox couples shift accordingly. An
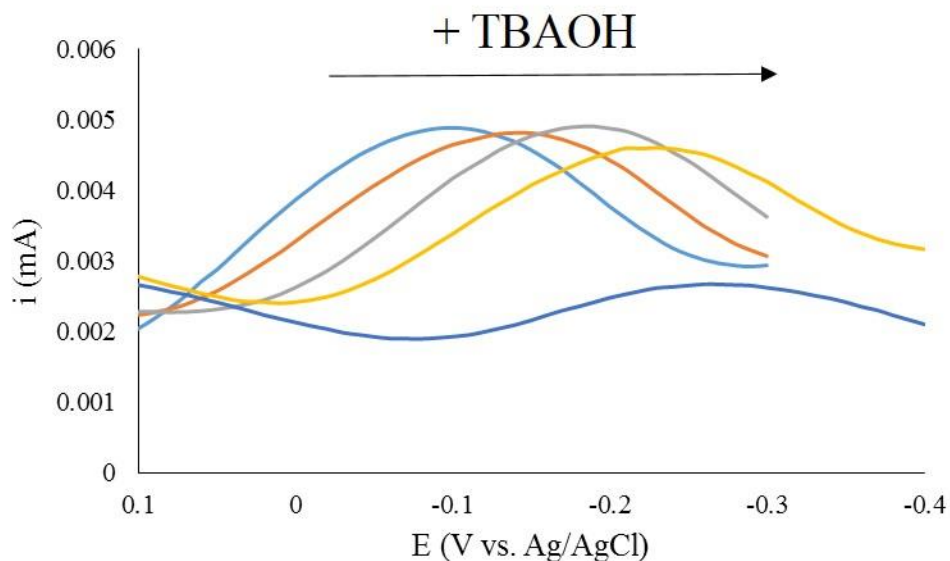
Figure 4.5: Differential pulse voltammetry of an electroflocculated IrO_x NP film in 0.1 TBAP, 10 mM hexanoic acid CH_3CN. 10 µL increments of 0.1 TBAOH were added to the solution and a negative shift of the redox couple is observed with each addition.

example of the shift of what is presumed to be the $Ir^{IV/III}$ redox couple with the titration of

hexanoic acid is presented in Figure 4.5. The E_p shifts from -0.075 to -0.25 V vs. Ag/AgCl.

After the addition of 50 µL of 0.1 M TBAOH, however, the current drops significantly. At this

point, the product of the titration, TBA hexanoate, is observed to precipitate, leading to a

decrease in current.

E$_p$ vs. the addition of TBAOH is presented in Figure 4.6a for the hexanoic and valeric

acid titrations and that of oxalic acid is in Figure 4.6b. The concentrations for these acids are 10

mM, 5 mM and 20 mM, respecitively. The difference in concentration accounts for the variance

in slopes in each titration; the slope for the valeric acid titration (ca. 0.0075 mV/µL) is about

twice that of the hexanoic acid titration (0.0035 mV/µL), which is double the slope of the oxalic

acid addition (0.0011 mV/µL). For a higher concentration analyte (carboxylic acid), there would

be a smaller change in E_p with each addition of titrant (TBAOH).
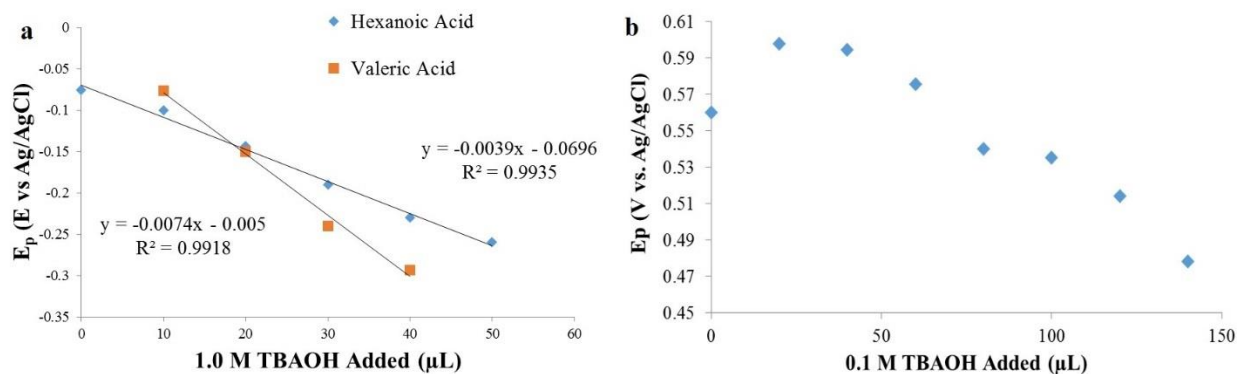
Figure 4.6: Shift of the peak potential via differential pulse voltammetry with the addition of 0.1 M TBAOH. a) Titrations of 10 mM hexanoic acid and 5 mM valeric acid. b) Titration of 20 mM oxalic acid.

For the valeric acid and hexanoic acid titrations, the starting potential and final potential are very similar: -0.077 and -0.29 V vs Ag/AgCl for valeric acid and -0.076 and -0.26 V vs Ag/AgCl for hexanoic acid. However, the potentials for the oxalic acid titration are drastically different; the starting and final potentials are 0.60 and 0.48 V vs Ag/AgCl, respectively. This is a big shift in potential, which can be partially explained by the difference in pK_a values of the various carboxylic acids. The pK_as of valeric acid (4.82) and hexaonic acid (4.88) are similar. Oxalic acid has two pK_as at 1.25 and 4.14, both lower than the other two acids. At the start of the titration, the relative pH in CH_3CN would be lower than the solutions of hexanoic and valeric acids. This would result in a shift of the IrO_X redox waves toward more positive potentials. As only one redox wave is observed for each titration, it is difficult to know which Ir reduction is occurring. The $Ir^{V/IV}$ redox couple usually occurs at more positive potentials than the $Ir^{IV/III}$ redox couple, so part of the shift between the two acids could also be due to looking at two different electrochemical reactions.

4.3.3 High Boiling Point Solvent Synthesis of Iridium Oxide Nanoparticles

A thermal degradation synthesis was attempted to synthesize IrO_X NPs in organic media in order to compare to those synthesized via a basic hydrolytic method, as previously discussed in this dissertation. This method results in IrO_X NPs capped with oleic acid and oleylamine;

116
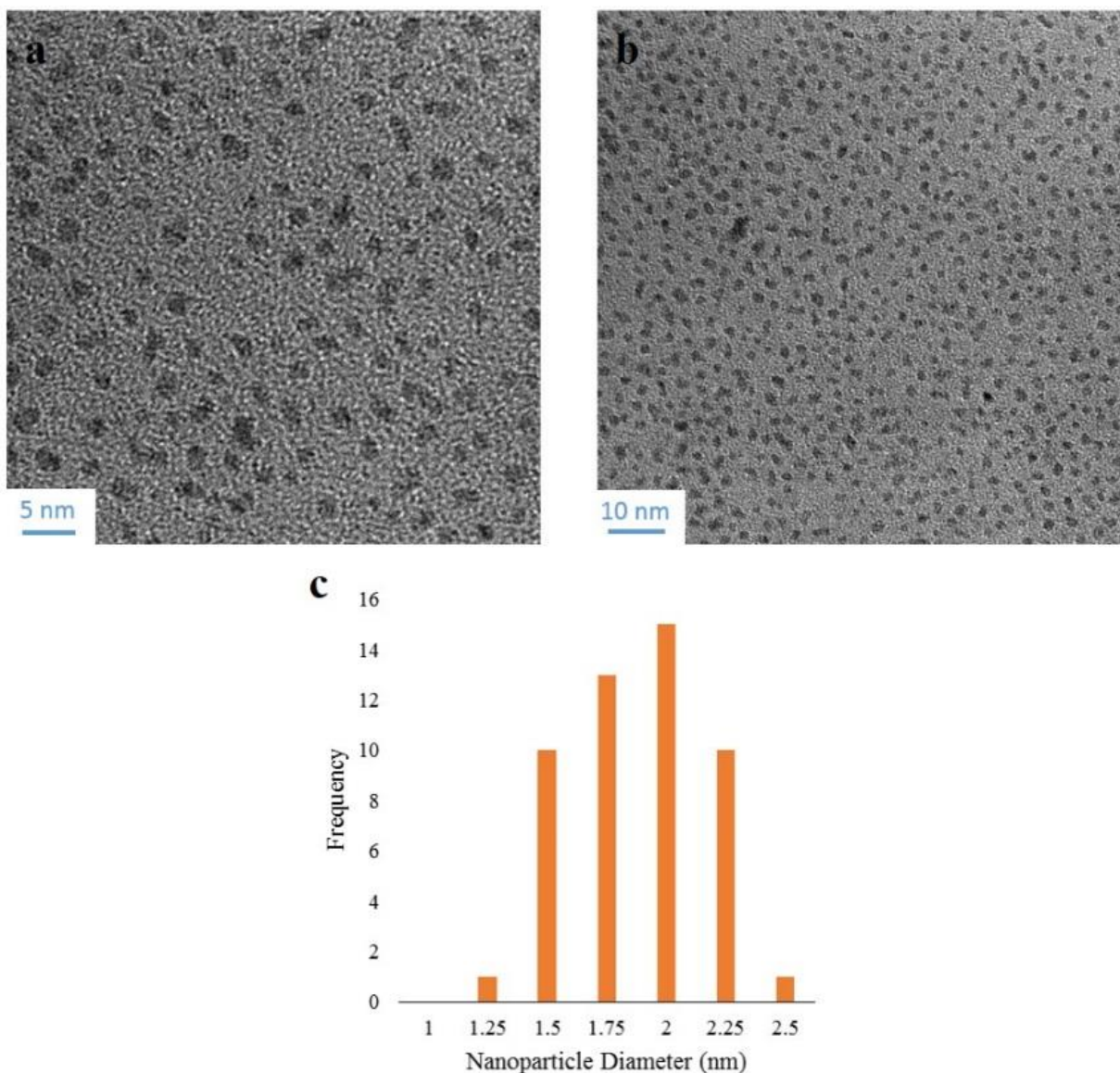
Figure 4.7: TEM images (a and b) and histogram (c) of the IrO$_X$ NPs sytnthesized via the hot injection thermal degradation synthesis.

these ligands have long carbon chains (C$_{18}$) which act as a surfactant shell for metal oxide

nanoparticles and control the size. Typically, these sort of syntheses result in more

monodisperse nanoparticles, compared to hydrolytic methods.[12-14]

Figure 4.7 is a TEM image of the IrO$_X$ NPs synthesized via the hot injection thermal

degradation method. The average diameter of these nanoparticles are 1.78 ± 0.28 nm, very

similar to the 1.8 ± 0.3 nm particles that result from the hydrolysis method. XPS and EDX both
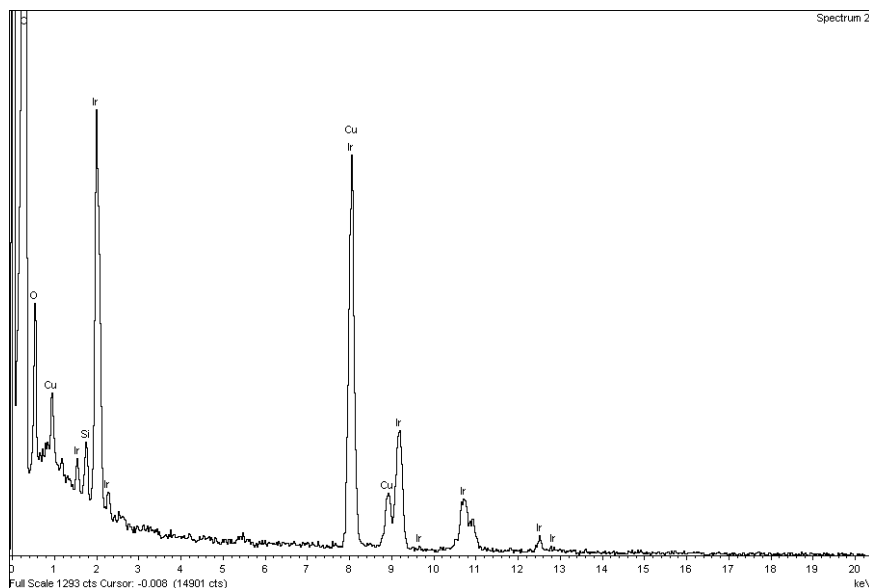
Figure 4.9: EDS spectrum of the hot injection, thermal degradation synthesis IrO_X NPs, demonstrating the presences of Ir in the NPs seen in the TEM images of Figure 4.6.
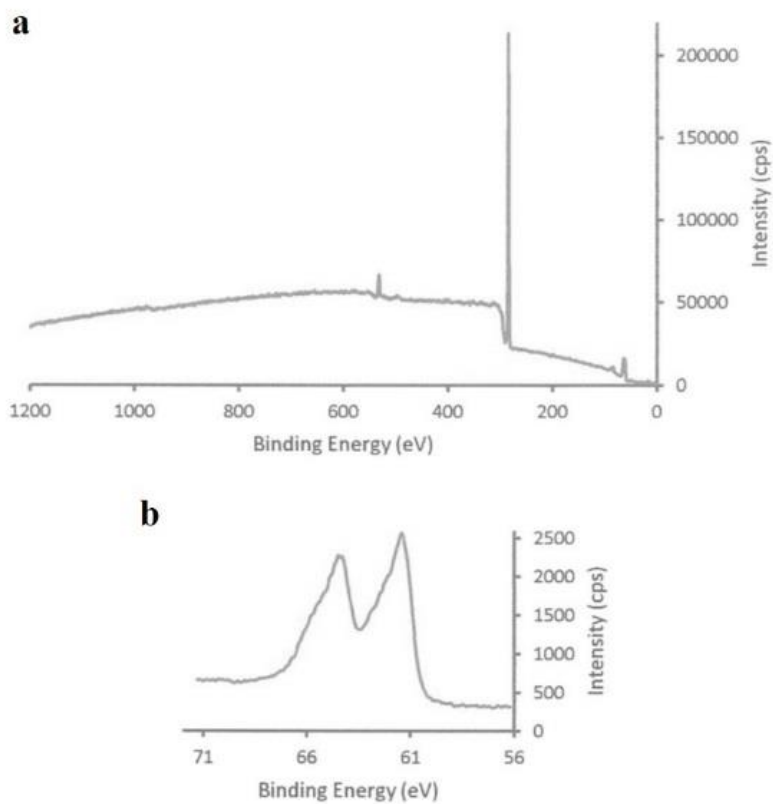
Figure 4.9: XPS of the hot injection, thermal degradation synthesis IrO_X NPs. a) Full spectrum demonstrates a large C s1 peak at 300 eV due to the surfactant shell. b) High resolution spectrum of the Ir 4f double peak.
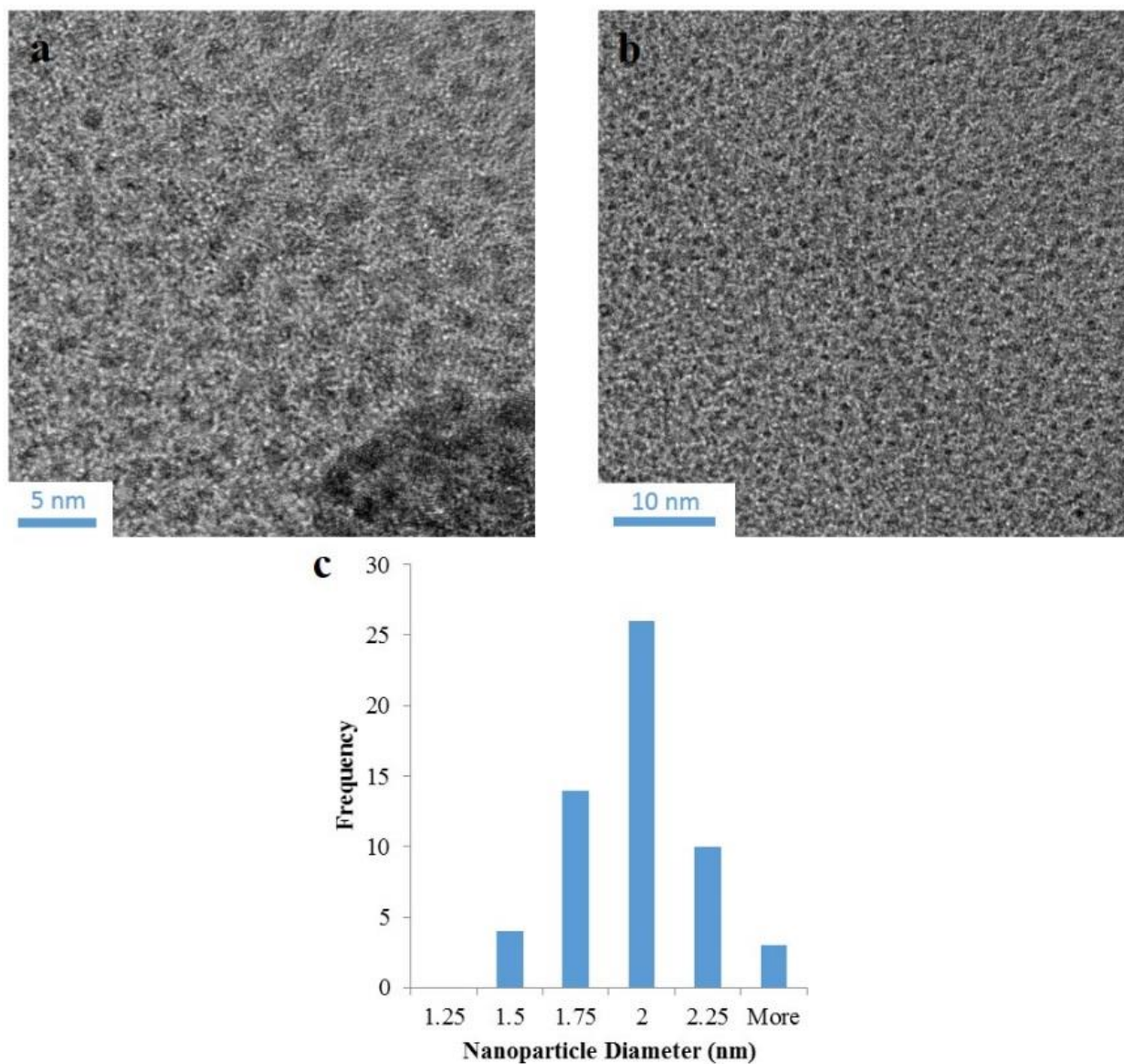
Figure 4.10: TEM images (a and b) of the valeric acid capped nanoparticles, as well as a histogram (c) of the nanoparticle diameter in nm.

confirmed the presence of Ir and are featured in Figure 4.8 and Figure 4.9, respectively. The

surfactant shell inhibits the signal of everything but the C 1s peak on the XPS spectra, but the Ir

4f peaks are visible via high resolution scans. As EDX has higher penetration depths, the Ir and

O signals are much stronger. This reveals an Ir:O ratio of 0.43, very close to the expected 0.5 for

a rutile structured IrO_2 species. However, there is no apparent increase in crystallinity or

monodispersity from the aqueous pH 13 IrO_X NPs. As the hydrolytic synthesis is much simpler

119
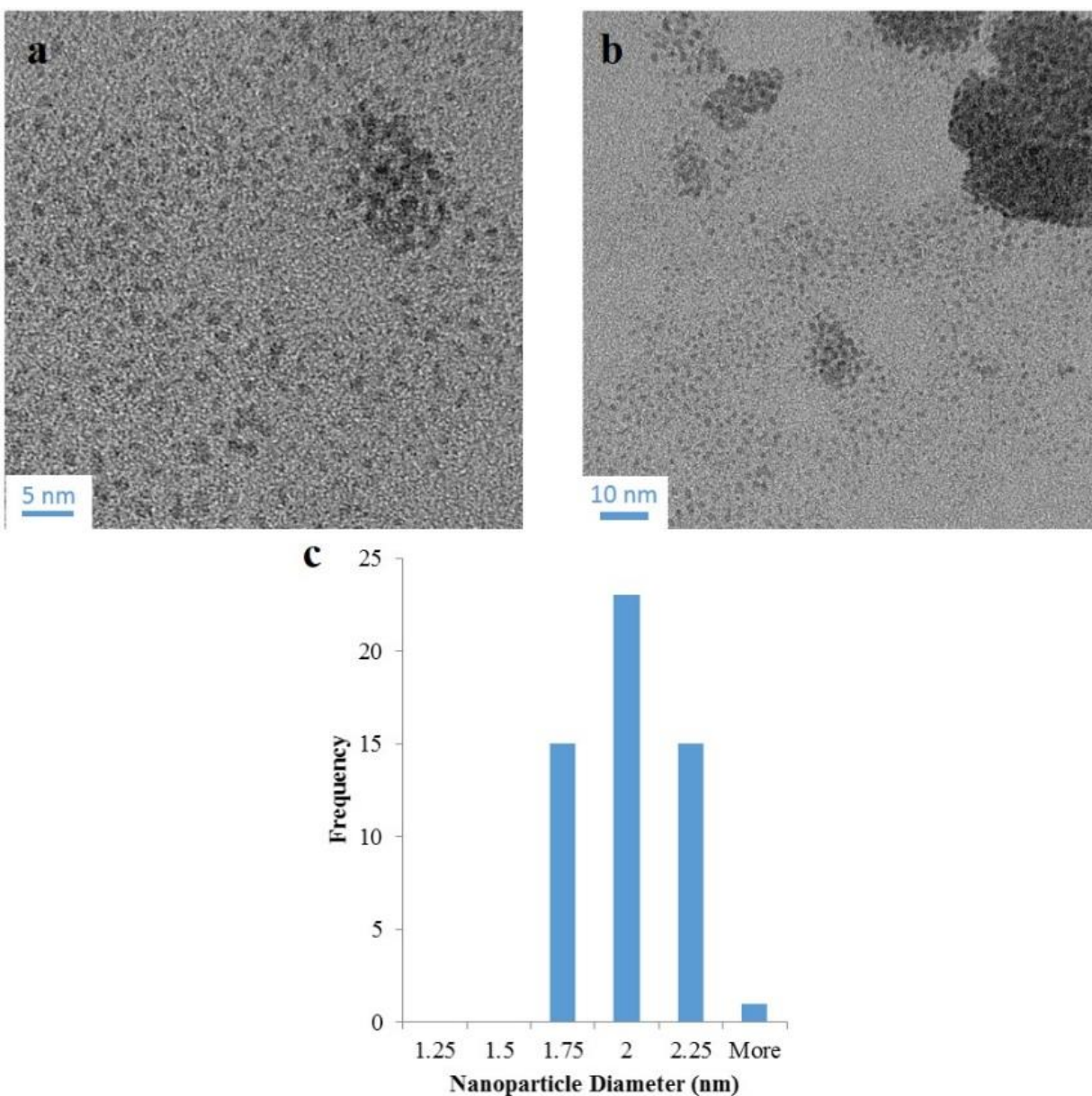
Figure 4.11: TEM images (a and b) of the N_3IrO_X NPs and a histogram of the nanoparticle diameter (c).

and doesn't result in an electrochemically inhibiting surfactant shell, all future research

continued with that particular synthesis.

4.3.4 Ferrocenation of Iridium Oxide Nanoparticles

The as-synthesized pH 13 IrO_X NPs were exchanged into dichloromethane (DCM) using

valeric acid as a capping ligand. This capping ligand has a minor effect on the diameter of these

nanoparticles, as seen in Figure 4.10. The valeric acid capped nanoparticles have a diameter of 1.86 ± 0.25 nm, slightly larger than the as-synthesized pH 13 diameter of 1.8 ± 0.3 nm.

Valeric acid capped IrO$_X$ NPs underwent a capping ligand exchange of valeric acid for **5**, in Scheme 4.3. While it is presumed that carboxylic acids merely cap metal oxides with a chemisorptive association, phosphate ligands, such as **5**, are suspected of forming covalent bonds with the metal oxide surface.[26] Compared to other covalently bonding ligands, such as silanes, they also have the added advantage of lack of polymerization, which would result in aggregated nanoparticles. With **5** has a capping ligand for the NPs, there was a significant change in polarity which resulted in successful separation of the products from the reactants via precipitation.
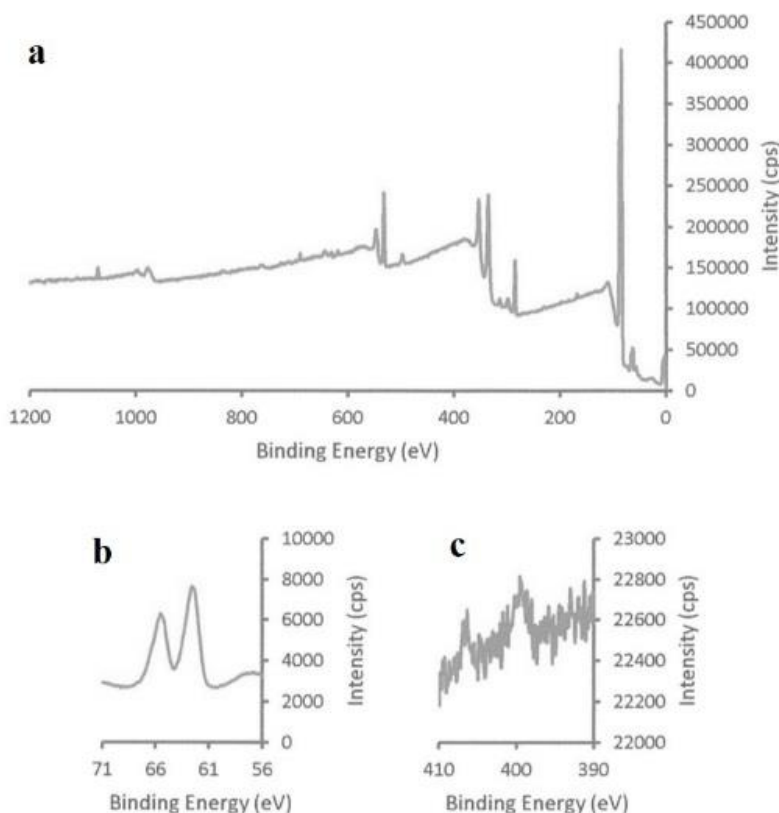
Figure 4.12: a) Full XPS spectrum of the N$_3$IrO$_X$ NPs. b) High resolution scan of the Ir 4f double peak. c) High resolution scan of the N 1s peak. A double peak at 399.5 and 406 eV indicates the presences of an N$_3$ species.

121
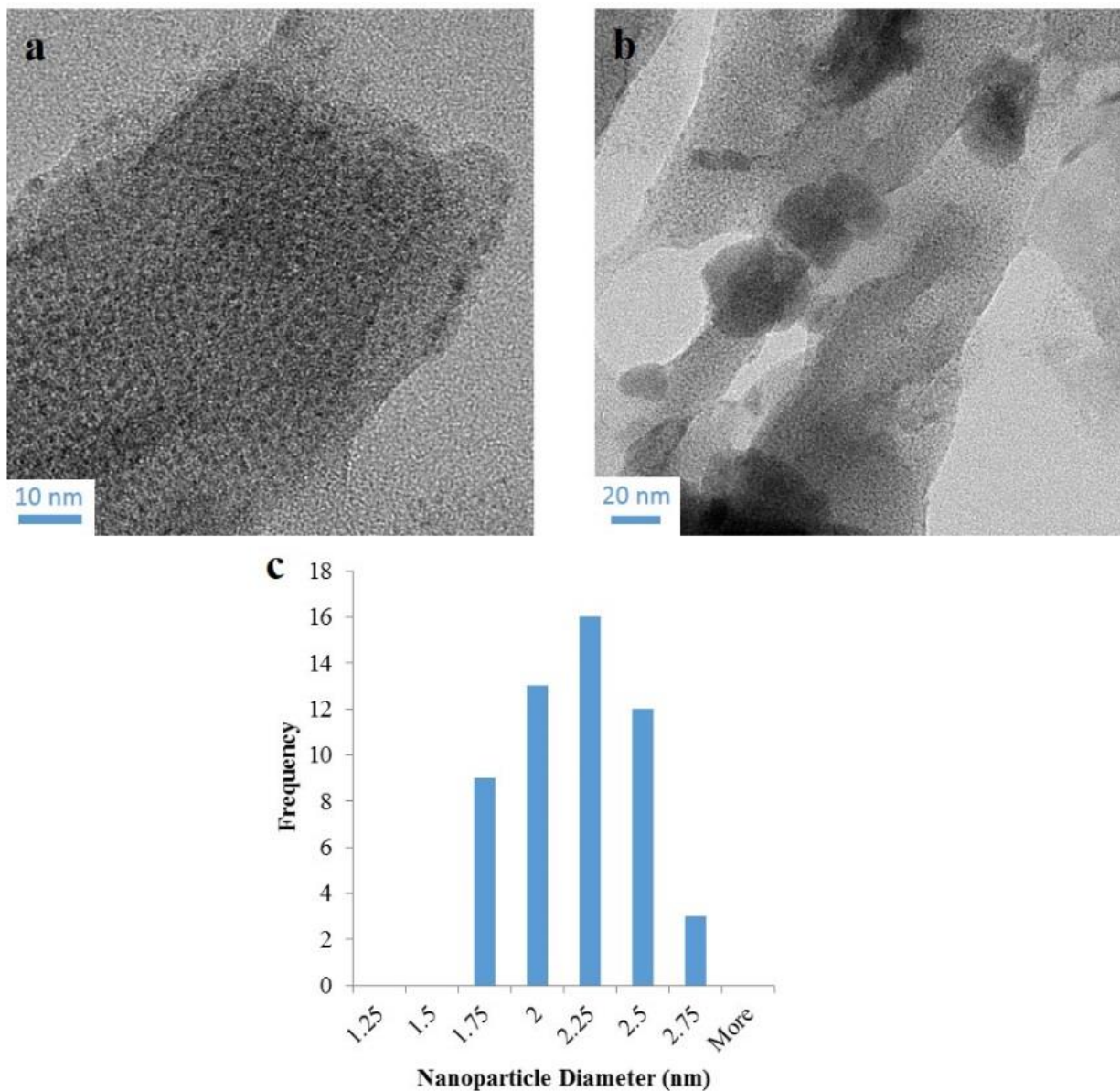
Figure 4.13: TEM images (a and b) of the FcIrO$_X$ NPs, as well as a histogram (c) of the nanoparticle diameters.

TEM of these N$_3$IrO$_X$ nanoparticles are shown in Figure 4.11. Their average diameter is 1.88 ± 0.19 nm, very similar to the valeric acid capped IrO$_X$. There is little change in size of these spherical NPs with the addition of this ligand. XPS of these nanoparticles (Figure 4.12a) confirms the presence of both Ir (Ir 4f peak in Figure 4.12b) and the azide terminated ligand (N 1p double peak in Figure 4.12c). Azides have a distinct XPS signal for their N 1s peak, instead of a single peak, it is split into two at 399.5 and 406 eV.
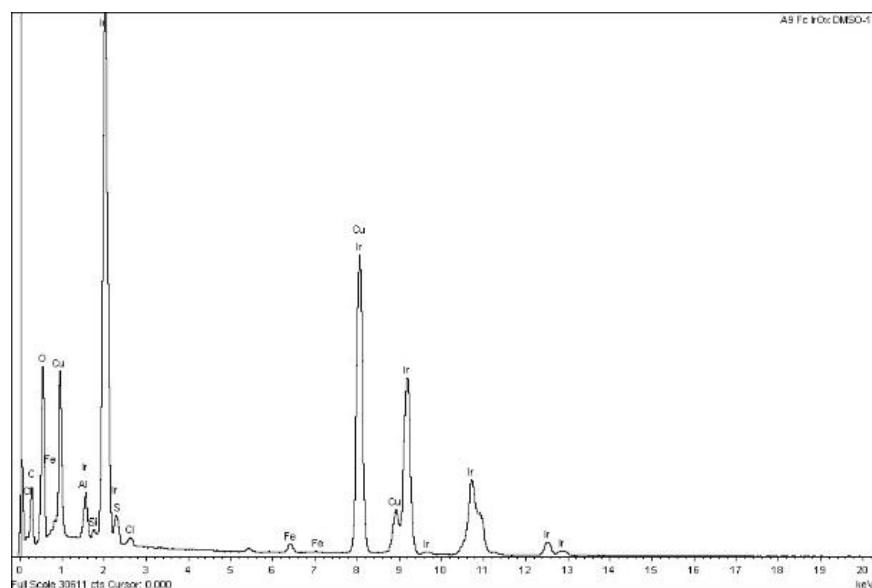
Figure 4.14: EDS of the FcIrO$_X$ NPs pictured in Figure 4.12, demonstrating the presence of both Ir and Fe.
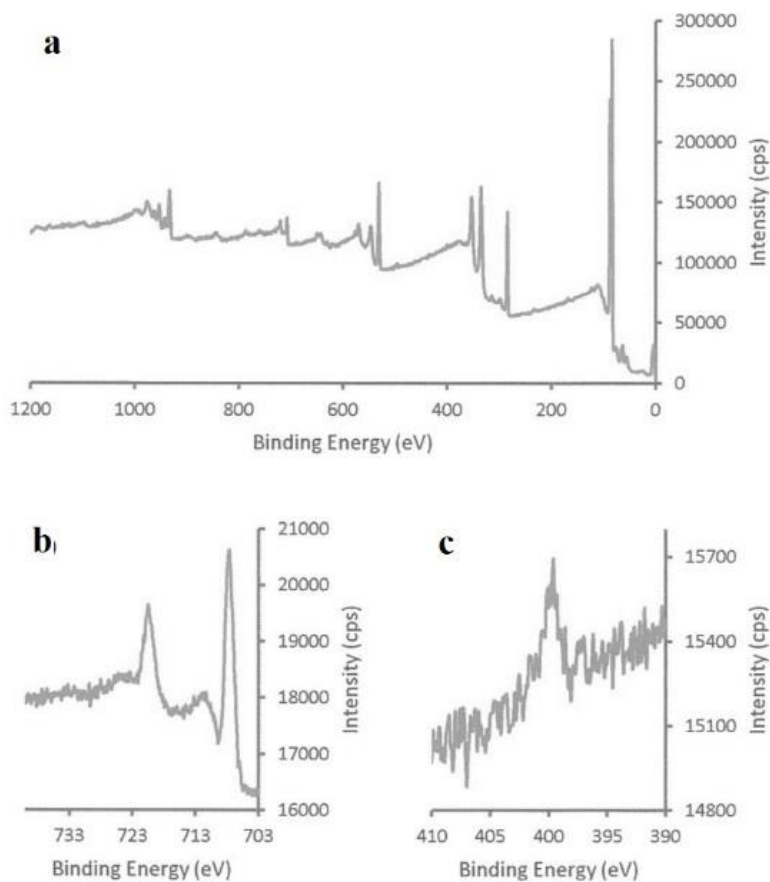
Figure 4.15: a) Full x-ray photoelectron spectrum of FcIrO$_X$ NPs. b) High resolution scan of the Fe 2p peak. c) High resolution scan of the N s1 peak.

A click reaction was then performed with ethynyl ferrocene to form complex **8** in Scheme 4.3. Click reactions are convenient for their lack of side products and close to 100% completion.[28] TEM images of these nanoparticles are in Figure 4.13. The capping ligand is substantially larger than the two previous capping ligands (azide terminated and valeric acid) with the addition of ferrocene and we observe an increase in average particle diameter to 2.08 ± 0.29 nm. XPS (Figure 4.15) and EDS (Figure 4.14) of the same nanoparticles confirmed the presence of both Ir and Fe. The azide double peak is no longer present in the XPS higher resolution scan of the N 1s peak, another indication of a successful click reaction. The Ir:Fe ratio was ca. 27:1 from the EDS elemental analysis. Assuming an average 130 Ir/NP based on the IrO$_2$ rutile structure, this corresponds on average to roughly 5 ferrocene ligands/NP.

Cyclic voltammetry of the FcIrO$_X$ NPs was performed in DMSO with 0.1 M TBAP supporting electrolyte. CVs of these diffusing species using both a Au coated slide and Au
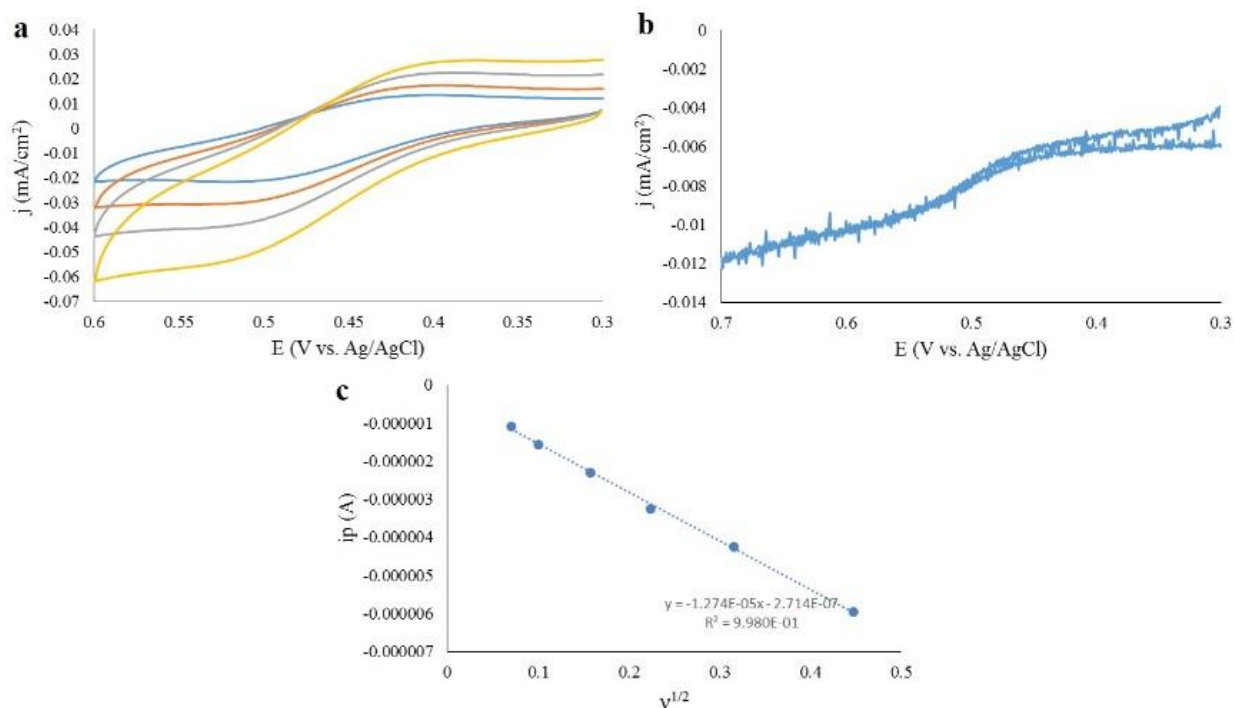
Figure 4.16: a) Cyclic voltammetry of the FcIrO$_X$ NPs in 0.1 M TBAP DMSO using a Au coated glass slide as a working electrode. b) Cyclic voltammetry of the FcIrO$_X$ NPs in 0.1 M TBAP DMSO using a Au microdisk working electrode. c) Peak current (i_p) vs. the square root of scan rate ($v^{1/2}$) from the CVs presented in (a).

microelectrode are presented in Figure 4.16. One reversible redox couple is observed at 0.47 V vs. Ag/AgCl, with a ΔE_p of 95 mV, very close to the expected 90 mV of an ideal reversible couple. This is presumed to be the Fc/Fc^+ reaction, since the IrO_X redox couples are unlikely to be observed in an aprotic solvent (see discussion in section 4.3.1.). The ultimate goal of these experiments was to find the diffusion coefficient (D) of these nanoparticles with the Fc tag.

An estimate of the diffusion coefficient can be made with the Stokes-Einstein equation (Equation 4-1), where k is the Boltzman constant, T is temperature, η is the viscosity of DMSO and r is the hydrodynamic radius of the nanoparticles.

Equation 4-1

$$D = \frac{kT}{6\pi\eta r}$$

TEM of the $FcIrO_X$ NPs estimated r to be ca. 2.08 nm, resulting in an estimated D of 1.03×10^{-6} cm^2/s. Previous studies with Au nanoparticles have shown this method of estimating the diffusion coefficient can be accurate within a factor of ca. two.[149]

A comparison of cyclic voltammetry using a macro and microelectrode can yield both the concentration of the analyte and the diffusion coefficient. The Randles-Sevcik equation (Equation 4-2) relates the peak current (i_p) to the square root of the scan rate ($v^{1/2}$), where n is the number of electrons, A is the area of the electrode and C is the concentration of the analyte.

Equation 4-2

$$i_p = 2.69 \times 10^5 n^{3/2} A D^{1/2} C v^{1/2}$$

If the analyte is a diffusing species, i_p will be linear with respect to $v^{1/2}$. As seen in Figure 4.16c, the i_p of $FcIrO_X$ correlates linearly with the square root of scan rate ($v^{1/2}$), verifying that the

species is diffusing. From the equation mentioned above, we are able to obtain a $D^{1/2}C$ value of 3.83 x 10^{-10} mol $s^{-1/2}cm^{-2}$.

The limiting current (i_{lim}) from the microdisk electrode cyclic voltammetry can used to find DC using Equation 4-3, where n is the number of electrons, F is Faraday's constant and r_0 is the microdisk electrode radius. A limiting current of 1.40 x 10^{-10} A was found for the FcIrO$_X$ NPs at

Equation 4-3

$$i_{lim} = 4nFDCr_0$$

$E_{1/2}$ of 0.49 V vs. Ag/AgCl, resulting in a DC of 7.23 x 10^{-13} mol s^{-1} cm^{-1}. A ratio of DC to the $D^{1/2}C$ obtained from the Randles-Sevcik equation yields the diffusion coefficient and concentration of the analyte, 3.56 x 10^{-6} cm^2/s and 0.20 mM, respectively. The D is on the same order of magnitude of the Stokes-Einstein estimated diffusion coefficient. Assuming complete conversion of IrO$_X$ NPs from start to finish, the ratio of Fc:IrO$_X$ NP is ca. 0.5 ligands/NP. However, TEM of each wash in the N$_3$IrO$_x$ NP synthesis and FcIrO$_x$ NP synthesis steps demonstrated the presence of IrO$_X$ NPs, suggested substantial loss of IrO$_X$ NPs with each step. The ligand:NP ratio is expected to be much higher, likely close to the ratio observed via EDS of 5:1.

4.4 CONCLUSIONS

The electrochemical behavior of IrO$_X$ NPs in organic media under a variety of conditions is presented. It is observed that a proton source, such as a protic solvent or carboxylic acid must be present for the NPs to be oxidized or reduced through the previously reported PCETs. In organic media, we are able to manipulate the $E_{1/2}$ of the IrO$_X$ redox couples with the addition of organic acids and bases.

IrO$_X$ NPs that are soluble in organic media can be synthesized with a surfactant shell, using a thermal degradation synthesis developed previously in the Murray lab.[17] They do not differ in size and shape from the NPs synthesized via basic hydrolysis. There is also no observed improvement in crystallinity or monodispersity.

Aqueous IrO$_X$ NPs can be exchanged into organic media and then electrochemically tagged with ferrocene using a click reaction. These nanoparticles exhibit one reversible redox couple in DMSO, attributed to the Fc/Fc$^+$ reaction. Using cyclic voltammetry from a maco and micro Au electrode, the diffusion coefficient and concentration of Fc in these solutions was determined to be 3.56 x 10^{-6} cm^2/s and 0.20 mM, respecitively. This equates to a >0.5 ligand:NP ratio, likely closer to 5:1 from the EDS elemental analysis of the NPs.

4.5 ACKNOWLEDGEMENT

REFERENCES

(1)   Gambardella, A. A.; Bjorge, N. S.; Alspaugh, V. K.; Murray, R. W. *J. Phys. Chem. C* **2011**, *115*.

(2)   Hoertz, P. G.; Kim, Y. L.; Youngblood, J. W.; Mallouk, T. E. *J. Phys. Chem. B* **2007**, *111*, 6945.

(3)   Michaux, K. E.; Murray, R. W. *Langmuir* **2013**, *29*, 12254

(4)   Morris, N. D.; Suzuki, M.; Mallouk, T. E. *J. Phys. Chem. A* **2004**, *108*, 9115.

(5)   Nakagawa, T.; Beasley, C. A.; Murray, R. W. *J. Phys. Chem. C* **2009**, *113*, 12958

(6)   Swierk, J. R.; McCool, N. S.; Saunders, T. P.; Barber, G. D.; Strayer, M. E.; Vargas-Barbosa, N. M.; Mallouk, T. E. *J. Phys. Chem. C.* **2014**, *118*, 17046

(7)   Zhao, Y.; Hernandez-Pagan, E. A.; Vargas-Barbosa, N. M.; Dysart, J. L.; Mallouk, T. E. *J. Phys. Chem. Lett.* **2011**, *2*, 402

(8)   Zhao, Y.; Vargas-Barbosa, N. M.; Hernandez-Pagan, E. A.; Mallouk, T. E. *Small* **2011**, *7*, 2087

(9)   Wohler, L.; Witzmann, W. Z. *Anorg. Chem.* **1908**, *57*, 323.

(10)   Han, C.-H.; Han, S.-D.; Gwak, J.; Khatkar, S. P. *Mater. Lett.* **2007**, *61*, 1701.

(11)   Liu, S.-M.; Ding, W.-Y.; Chai, W.-P. *Mater. Lett.* **2011**, *65*, 1272.

(12)   Sun, S.; Zeng, H.; Robinson, D. B.; Raoux, s.; Rice, P. M.; Wang, S. X.; Li, G. *J. Am. Chem. Soc.* **2003**, *126*, 273.

(13)   Sun, Z.; He, J.; Kumbhar, A.; Fang, J. *Langmuir* **2010**, *26*, 4246.

(14)   Zhang, Z.; Lu, M.; Xu, H.; Chin, W.-S. *Chemistry - A European Journal* **2007**, *13*, 632.

(15)   Gilstrap Jr, R. A.; Summers, C. J. *Thin Solid Films* **2009**, *518*, 1136.

(16)   Peng, R.; Zhang, W.; Ran, Q.; Liang, C.; Jing, L.; Ye, S.; Xian, Y. *Langmuir* **2011**, *27*, 2910.

(17)   Roberts, J. J. P.; Vuong, K. T.; Murray, R. W. *Langmuir* **2013**, *29*, 474.

(18)   Sun, Z.; Kumbhar, A.; Fang, J. *Langmuir* **2010**, *26*, 4246.

(19)   Roberts, J. J. P.; Westgard, J. A.; Cooper, L. M.; Murray, R. W. *J. Am. Chem. Soc.* **2014**, *136*, 10783.

(20)   Zhen, G.; Muir, B. W.; Moffat, B. A.; Harbour, P.; Murray, K. S.; Moubaraki, B.; Suzuki, K.; Madsen, I.; Agron-Olshina, N.; Waddington, L.; Mulvaney, P.; Hartley, P. G. *J. Phys. Chem. C* **2010**, *115*, 327.

(21)   Charles, J. C.; Ilia, N. I.; Salil, J.; Rosario, A. G. *Nanotechnology* **2009**, *20*, 145701.

(22)   Yiu, H. H. P. *Nanomedicine* **2011**, *6*, 1429.

(23)   Barrera, C.; Herrea, A. P.; Rinaldi, C. *J. Colloid Interface Sci.* **2009**, *329*, 107.

(24)   Gambardella, A. A.; Feldber, S. W.; Murray, R. W. *J. Am. Chem. Soc.* **2012**, *134*, 5774.

(25)   Hoertz, P. G.; Chen, Z.; Kent, C. A.; Meyer, T. J. *Inorg. Chem.* **2010**, *49*, 8179.

(26)   Neouze, M.-A.; Schubert, U. *Monatshefte fur Chemie/Chemical Monthly* **2008**, *139*, 183.

(27)   Gambardella, A. A., University of North Carolina at Chapel Hill, 2013.

(28)   Moses, J. E.; Moorhouse, A. D. *Chem. Soc. Rev.* **2007**, *36*, 1249.

(29)   White, M. A.; Johnson, J. A.; Koberstein, J. T.; Turro, N. J. *J. Am. Chem. Soc.* **2006**, *128*, 11356.

(30)   Wuelfing, W. P.; Templeton, A. C.; Hicks, J. F.; Murray, R. W. *Anal. Chem.* **1999**, *71*, 4069.

CHAPTER 5: Chromophore Catalyst Assemblies of RuP₂ and Iridium Oxide Nanoparticles

5.1 INTRODUCTION

The use of dye-sensitized photoelectrosynthesis cells (DSPEC) for water splitting has evolved rapidly.[1-5] In a DSPEC for water splitting, a chromophore-catalyst assembly is used for light absorption and injection into the conduction band of a high band gap oxide semiconductor such as TiO_2 or SnO_2, which act as photoanodes for water oxidation to O_2. Reduction of H^+/H_2O to H_2 occurs at an integrated cathode. Here we present a layer-by-layer assembly method for photocathodes of such cells, using a ruthenium chromophore and iridium oxide nanoparticles. This arrangement yields increases in photocurrent, relative to previous literature of similar assemblies that have utilized the surface chemistry of iridium oxide nanoparticles (IrO_X NPs) to modify them with various ligands, including the chromophore itself.[6-15] It is proposed here that the NPs should have a higher catalytic efficiency if they remain uncapped or as-synthesized at pH 13 capped with hydroxyl groups. In order to create a film without the addition of a deliberate ligand, a non-coordinating acid (perchloric acid) was added to adjust the pH of the as-synthesized IrO_X NPs so as to induce precipitation.[11,16] The uncapped film should favor increased water oxidation catalysis.

Improved performance has been achieved by application of Atomic Layer Deposition (ALD) in two ways. This gas phase, conformal technique was first used to form a thin shell of TiO_2 on a core of transparent conducting oxide, indium tin oxide (ITO, $Sn:In_2O_3$) in mesoscopic, nanoparticle films (*nano*ITO). The assembly was subsequently formed on the surface of the

130

TiO$_2$ shell by first surface binding of the phosphonated Ru(II) polypyridyl derivative [Ru(4,4'-PO$_3$H$_2$bpy)$_2$(bpy)]$^{2+}$ (RuP$_2$). In earlier studies, it was shown that in core/shell structures with thin 1-4 nm outer shells of TiO$_2$ on *nano*ITO, excitation and injection into the TiO$_2$ shell was followed by rapid transfer of the injected electron into the conducting core for transport to the cathode where H$_2$ is produced.[1,17] With an appended water oxidation catalyst, stepwise excitation-injection cycles build up multiple oxidative equivalents at the catalyst for oxidation of water to O$_2$.
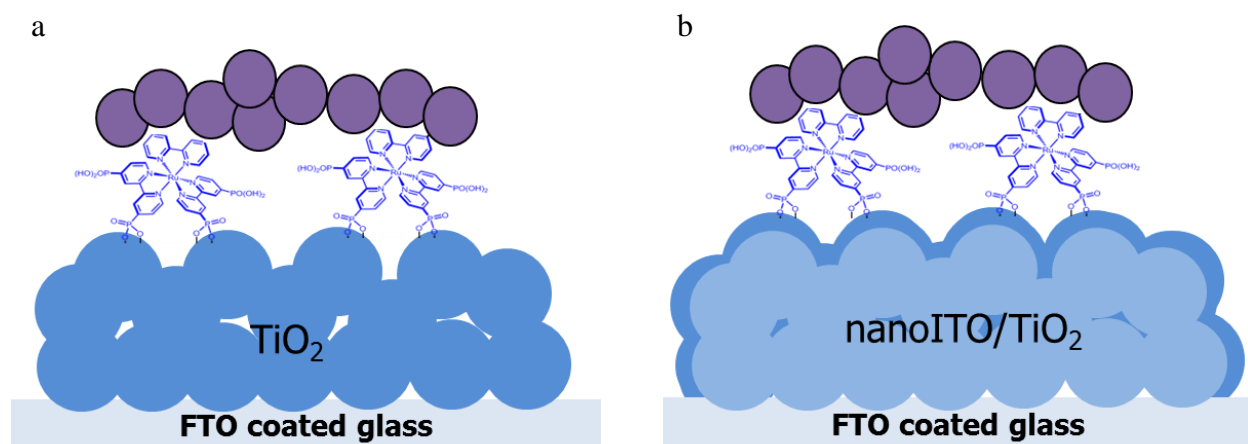
Figure 5.1: Diagram of the dipcoated layer-by-layer assembly of RuP$_2$ and IrO$_x$ NPs on various electrodes. A) Assembly is seen on the mesoporous TiO$_2$ substrate atop FTO coated glass. B) Assembly is built upon the core/shell electrode with a nanoITO core coated with a thin TiO$_2$ shell, deposited via atomic layer deposition.

In a second step, ALD was used to stabilize surface binding of the chromophore by depositing an overlayer of TiO$_2$ to stabilize its binding to the surface (Figure 5.11). In previous studies it has been observed that, although phosphonate-to oxide surface binding is stable under acidic conditions, hydrolysis from the surface is rapid as the pH is increased to 7 and above. Use of ALD to deposit thin TiO$_2$ or Al$_2$O$_3$ overlayers has been shown to stabilize phosphonate derivatives of chromophores, catalysts, and assemblies even at high pH.[18-26]

In this work, we describe the use of FTO|*nano*ITO|TiO$_2$ core/shell structures, derivatized by surface binding of RuP$_2$ followed by addition of IrO$_X$ NPs, to create photoanodes for DSPEC

131

water splitting. The stages in the formation of the photoanode are illustrated in Figure 5.1. The resulting surface-assembled structures on fluorine-doped tin oxide (FTO) optically transparent substrates – FTO|TiO$_2$|RuP$_2$,IrO$_X$ – and the core/shell analog – FTO|*nano*ITO|TiO$_2$-RuP$_2$,IrO$_X$ – have been evaluated as photoanodes for DSPEC visible light water splitting.

5.2   EXPERIMENTAL

5.2.1   Materials

The pH 5.8 buffers that were used in the aforementioned experiments were composed of 37.5 mM Na$_2$SiF$_6$ (Aldrich) and 80 mM NaHCO$_3$ (Aldrich) in nanopure water. 0.1 M HClO$_4$ solutions were prepared from concentrated HClO$_4$ (70%, GFS Chemicals) and nanopure water.

5.2.2   Synthesis of IrO$_X$ NPs

Synthesis of the IrO$_X$ NPs was based off of a Woehler method.[28] A 2.5 mM K$_2$IrCl$_6$ (Strem Chemicals) solution was adjusted to pH 13 using 50% w/w NaOH (Fisher Scientific). The resulting solution was heated at 90 °C for 20 minutes, then allowed to cool to RT.

5.2.3   Assembly of RuP2-IrO$_X$ NP systems

RuP$_2$ ([Ru(4,4'-(PO$_3$H$_2$)$_2$bpy)$_2$(bpy)]$^{+2}$) was dissolved into a 0.1 M HClO$_4$ solution, so that the concentration was 0.1 mM RuP$_2$. The as-synthesized IrO$_X$ NPs were adjusted to pH 1 with 0.1 M HClO$_4$. The electrodes were first soaked in 0.1 mM solutions of RuP$_2$ in 0.1 M HClO$_4$ for 1.5 h to bind the chromophore, followed by a second soaking in a solution of IrO$_X$ NPs (2.5 mM in Ir) also in 0.1 M HClO$_4$ for 1.5 h. Coverage of RuP$_2$ after 1.5 hours of soaking is $1 ^{ x }\ 10^8$ mol RuP$_2$/cm^2, based on the geometric area.

5.2.4   Fabrication of *nano*ITO-FTO substrates:

A 3 gram sample of *nano*ITO (Lihochem, Inc.) powder was added to a mixture of acetic acid (3 g) and ethanol (10 mL), giving a 5 M solution/suspension (22 wt %). After brief shaking, this mixture was sonicated for 20 minutes. The colloidal suspension was further sonicated with a

Branson ultrasonic horn outfitted with a flat microtip (70 % power, 50 % duty cycle; 5 minutes).

FTO glass substrates, 4 cm x 2.2 cm, were prepared and cleaned by sonication in EtOH for 20

min followed by acetone for 20 min. Kapton tape was applied to one edge to maintain a defined

area (1 cm x 2.5 cm). The *nano*ITO colloidal suspension was coated on FTO glass substrates by

a spin-coater (600 rpm, 10 s hold). *nano*ITO slides were annealed under air and then under 5%

H_2 with a method described previously.[21] Annealed films were measured to be 3.2 ± 0.5 μm

thick by surface profilometry.

5.2.5   ALD deposition

Atomic layer deposition (ALD) was performed in a commercial reactor (Savannah S200,

Cambridge Nanotech, Cambridge, MA). Titanium dioxide (TiO_2) was deposited using

tetrakis(dimethylamido)titanium (TDMAT) (99.999%, Sigma-Aldrich) and water. The reactor

temperature was 130°C. The TDMAT reservoir was kept at 75°C. The TDMAT was pulsed into

the reactor for 0.3 s and then held for 10 s before opening the pump valve and purging for 10 s.

Standard ALD coating conditions were 130°C and 20 Torr of N_2 carrier gas with a sequence of
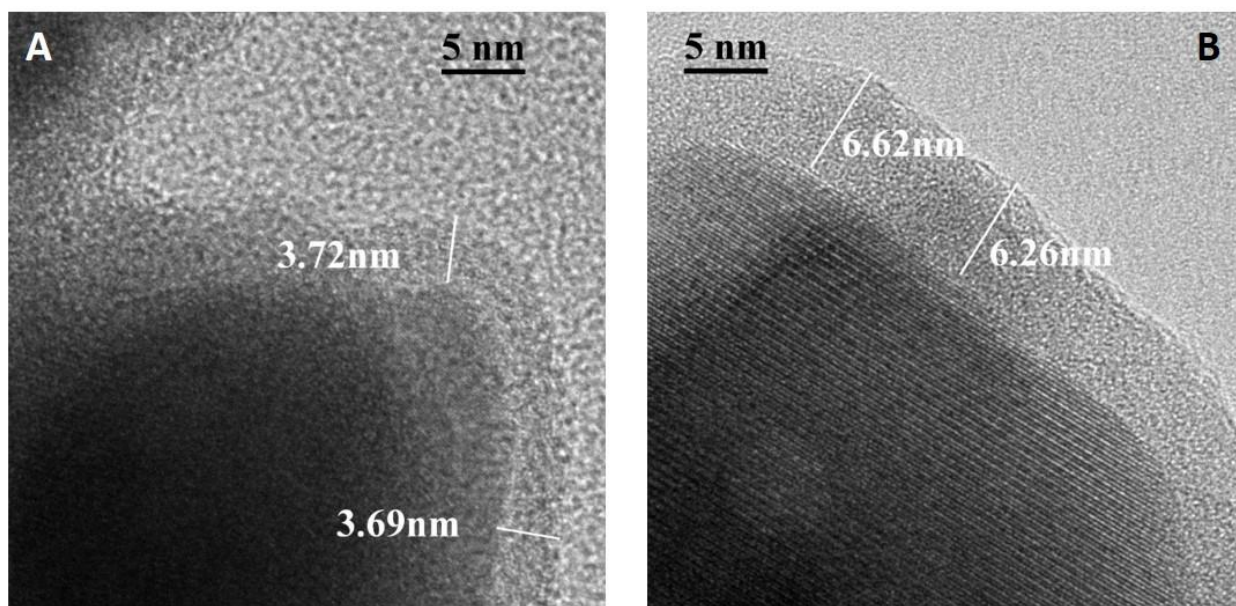
Figure 5.2: TEM images of A) the 50 cycles *nano*ITO/TiO_2 core/shell electrode and B) the 100 cycles *nano*ITO/TiO_2 electrode. The darker core represents the *nano*ITO coke and the surrounding layer is the TiO_2 shell, further pointed out by the bar lines.

0.3 s metal precursor dose, 10 s hold, 20 s N_2 purge, 0.02 s H_2O dose, 10 s hold, 20 s N_2 purge.

The growth rate under these conditions was 0.6 Å per cycle, as determined by ellipsometry on Si

wafers. The quality of the outer TiO_2 outer layers with 50 and 100 cycles ALD TiO_2 on *nano*ITO

are shown in the transmission electron micrograph (TEM) in Figure 5.2.

5.2.6 Spectroelectrochemical Characterization

Spectroelectrochemical characterizations were conducted in a three electrode cell with a

1 cm path length cuvette by using a CHI 670 potentiostat, and an Agilent UV-Vis spectrometer.

The data were analyzed by using SpecFit. The potential was varied in 0.02 V increments from -

0.2 to 1.2 V vs. Ag/AgCl with spectra recorded at each increment after holding the potential for

60 s. (The Ag/AgCl reference is +0.199V vs NHE.)

5.2.7 Photolysis Measurements

Photolysis experiments were conducted in a three electrode set-up, where the working

electrode and auxiliary electrode were separated from the reference electrode via a fine frit. A

Lumencor LED was used to back illuminate the working electrode at a 45° angle at 455 nm at

different intensities. The current change was monitored using a CHI 670 potentiostat. The

difference in current when the light was off and on was determined to be the photocurrent.

5.2.8 O_2 Detection

O_2 was detected using a four electrode set-up, where the two working electrodes were

attached to each other in a thin cell-like arrangement via epoxy, separated by thin pieces of glass

on either side. The two working electrodes were spaced 1 mm apart using glass spacers.

Working electrode 1 (WE1) was a *nano*ITO/TiO_2 core/shell electrode on FTO with the RuP_2-

IrO_X NP assembly; working electrode 2 (WE2) was an FTO electrode. Pt wire and Ag/AgCl

were used for the auxiliary and reference electrodes, respectively. WE1 was illuminated from

behind while a potential of 400 mV vs. Ag/AgCl was held at that same electrode. The potential

at WE2 was held at -900 mV vs. Ag/AgCl in order to measure the reduction of O_2 produced at WE1.

5.3   RESULTS AND DISCUSSION

5.3.1   Dip-Coating Layer-by-Layer Synthesis of RuP2 and IrO$_X$ NP Assemblies

The surface-bound chromophore-catalyst assemblies were synthesized using a simple layer-by-layer method. Preparation of the chromophore, RuP_2, is described elsewhere.[16] The chromophore RuP_2 becomes bound to the metal oxide electrode through the phosphonic acid linkers, a previously studied and reported process.[27] IrO$_X$ NPs were synthesized based on a
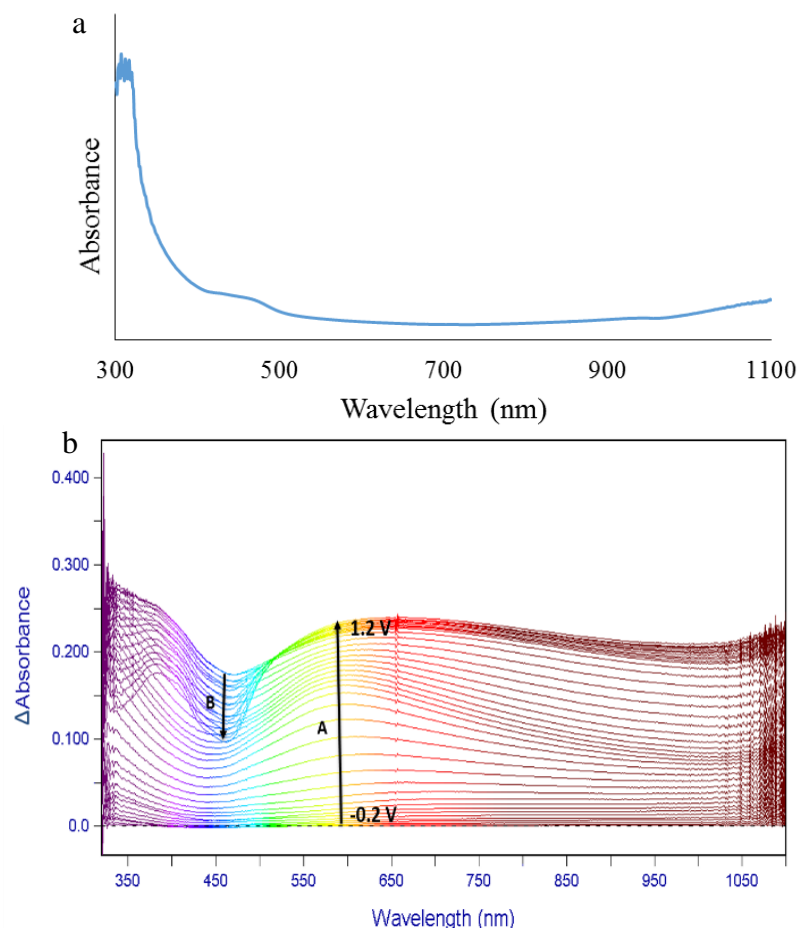
Figure 5.3: (a) UV-Vis absorbance spectrum of RuP_2-IrO$_X$ NP assembly on a nanoITO electrode. (b) UV-Vis difference spectra of RuP_2 – IrO$_X$ NP assembly on nanoITO in a pH 5.8 NaSiF$_6$ buffer, as the applied potential is varied (bottom to top) from -0.2 V to 1.2 V vs. Ag/AgCl. Two features are observed: A) increase in absorbance due to oxidation of Ir from Ir^{III} to Ir^{VI} where it becomes a black absorber and B) photobleaching of RuP_2 as it is oxidized from Ru^{II} to Ru^{III}.

Wohler method.[28] The NP synthesis was carried out at pH 13, resulting in nanoparticles capped

with hydroxyl groups. In order to form the assembly overlayer without adding a capping ligand,

solutions were acidified with 0.1 M $HClO_4$, which yields a non-coordinating perchlorate anion,

to induce precipitation-binding to the surface-bound layer. By adding the non-coordinating acid

as mentioned above, the IrO_X NPs precipitate and form an overlayer atop the RuP_2 layer.

5.3.2   UV-Vis Spectroelectrochemistry of RuP₂ and Iridium Oxide Nanoparticles on nanoITO

The resulting RuP_2/IrO_x assemblies were characterized by UV-Vis

spectroelectrochemistry at pH 5.8 in a $NaSiF_6$ buffer on *nano*ITO electrodes.

Spectroelectrochemical difference spectra for the assembly FTO|*nano*ITO|-RuP2,IrO_X is shown

in Figure 5.3, along with the absorbance spectra for the ground state assembly for reference.

Spectroelectrochemical data for RuP_2 is shown in Figure 5.4 and that of the IrO_X NPs was

previously discussed in Chapter 3. In Figure 5.3, two spectral features are present, the first (A)

assigned to the oxidation of Ir^{III} to Ir^{VI} and the second (B) assigned to the oxidation of Ru^{II} to

Ru^{III}. As the IrO_X NPs are oxidized through their various oxidation states, they change color

from green to purple to black. This is seen spectrally in the increase of absorbance at 540 nm as

the Ir sites are oxidized to the IV and V oxidation states. As the assembly is further oxidized, the
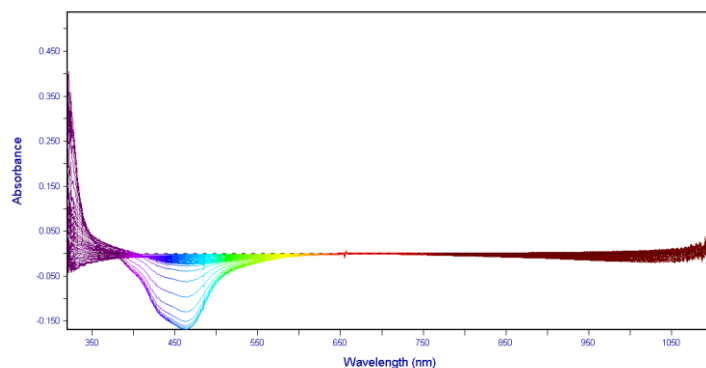
Figure 5.4: UV-Vis difference spectra of RuP2 on *nano*ITO/FTO coated glass with varying potential in a pH 5.8 $NaSiF_6$ buffer, as the applied potential is varied (bottom to top) from -0.2 V to 1.2 V vs. Ag/AgCl. Photobleaching of the chromophore as it is oxidized from Ru^{II} to Ru^{III} is observed at 455 nm.

NPs become black absorbers, observed as the increase in absorbance at all wavelengths. This change happens around the electrochemical onset of water oxidation catalysis, indicating Ir^{VI} as a participant in the process. When the RuP_2 chromophore is oxidized, there is a bleaching seen at 450 nm. The individual difference spectra of each species is featured in Figure 5.5, along with a concentration gradient of each species. The intercepts of each species in Figure 5.5a correspond to the redox potentials of $Ir^{IV/III}$, $Ir^{V/IV}$, $Ir^{VI/V}$ and $Ru^{III/II}$.

The UV-Vis difference spectra of the assembly are summations of the spectra of the individual species. The electrochemical redox potentials obtained from the concentration gradients derived from these spectra match those from the literature.[29] Both spectral and electrochemical integrity are maintained through the dip-coating process. This indicates that the
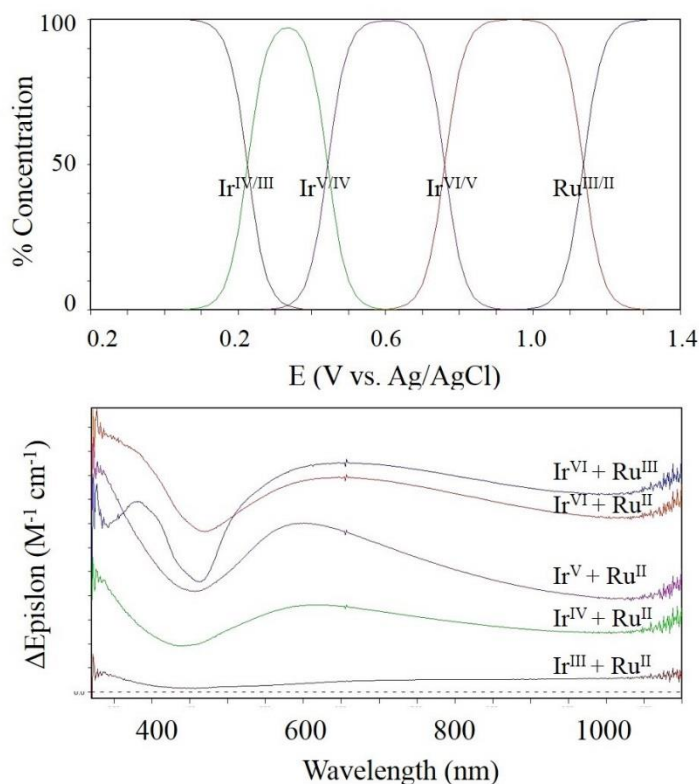
Figure 5.5: (Top): Concentration gradients of each redox species present from -0.2 to 1.4 V vs. Ag/AgCl at pH 5.8. (Bottom): Individual difference spectra of each oxidation species. The first four changes in spectra correspond to different oxidation states of Ir. The last change corresponds to the oxidation of the RuP_2.

two species remain unchanged in the assembly making process and furthermore, the IrO_X NPs remain uncapped – the overall goal of this synthesis.

5.3.3 Photolysis of RuP2 and Iridium Oxide Nanoparticle Assemblies at pH 1

While the UV-Vis spectra are additive, the photocurrents obtained from the assembly on a mesoporous TiO_2 electrode are significantly larger than the sum of the individual components, suggesting that water oxidation was occurring. Photolysis experiments were performed on three different electrode types at pH 1, featured in Figure 5.6. In these experiments, a potential bias of 0 V vs. Ag/AgCl was held and the current was measured with a 455 nm LED light on and off at various intensities. The difference between the light and dark current was considered the photocurrent at that potential bias.

Table 5.1: Photocurrent ($\mu A/cm^2$) of the RuP_2-IrO_X NP assemblies on three different electrodes in pH 5.8 $NaSiF_6$ solution, illuminated at 450 nm at 14.5 mW/cm^2 with an applied potential bias of 0 V. The core/shell electrode has an ALD TiO_2 layer that is 3.7 nm in thickness.

	RuP$_2$	**IrO$_X$ NPs**	**RuP$_2$ + IrO$_X$ NPs**
FTO|*nano*ITO	-0.98	-1.42	10.5
FTO|TiO$_2$	8.56	2.92	15.6
FTO|*nano*ITO|TiO$_2$	4.62	7.13	34.8

Figure 5.6a features the current of the individual components (RuP_2 and IrO_X NPs) and that of the assemblies on an FTO|*nano*ITO electrode. Despite the initial spikes of current when the light is turned on, there is very little difference in current between when the light is on and off after 10 s of decay for all three photoanodes. These figures are reported in Table 5.1. In the case of the RuP_2 and IrO_X NPs, individually, the photocurrent is negative. There is some photocurrent observed (10.5 $\mu A/cm^2$) for the assembly, though it is not as high as the assemblies on the other two electrodes, discussed below. The assembly on FTO|*nano*ITO also exhibits a

138

background current which slopes upward. This falsely gives the impression of higher photocurrents. The lack of photocurrent for assemblies on this electrode can be accounted for based on the conductivity of the electrode. *nano*ITO is a very conductive surface and lacks the charge separation feature observed in semiconductors, such as TiO_2. Because of this, when the chromophore (RuP_2) is excited, back electron transfer to RuP_2 is very common at the electrode surface. There is a very low level of electron injection into the circuit for these photoanodes.

Figure 5.6b depicts the same components as Figure 5.6a, but on an FTO|TiO_2 semiconductor electrode, as seen in Figure 5.1a. Compared to the assemblies on FTO|*nano*ITO, there is measureable photocurrent. These values are found in Table 5.1. As TiO_2 is a semiconductor material, there is sufficient charge separation within the material and the excited electrons from the chromophore are injected into the circuit. Also of note, the photocurrent for the assembly of -RuP_2, IrO_X is greater than that of the sum of the individual components. This is an indication that water oxidation catalysis is occurring at this low applied bias (0 V vs. Ag/AgCl).

The photocurrents in Figure 5.6c represent those of the individual components and the chromophore catalyst assembly on FTO|*nano*ITO|TiO_2 core/shell electrodes, depicted in Figure 5.1b. These particular electrodes underwent 50 cycles of atomic layer deposition and had a TiO_2 shell thickness of 3.7 nm, as seen in Figure 5.2a. The photocurrents for these anodes decay less quickly than those of the TiO_2 photoanodes, signifying more efficient electron injection. Within 10 s, a steady state current is reached, as opposed to the TiO_2 assemblies which continued to decay. Also of note, the photocurrents are greater for the core/shell electrodes. This is due to the thin semiconductor layer of TiO_2, which allows for charge separation and then injection into the conductive electrode material. Back electron transfer to the chromophore is sufficiently decreased in these electrodes, as previously reported by the Meyer lab.[17]
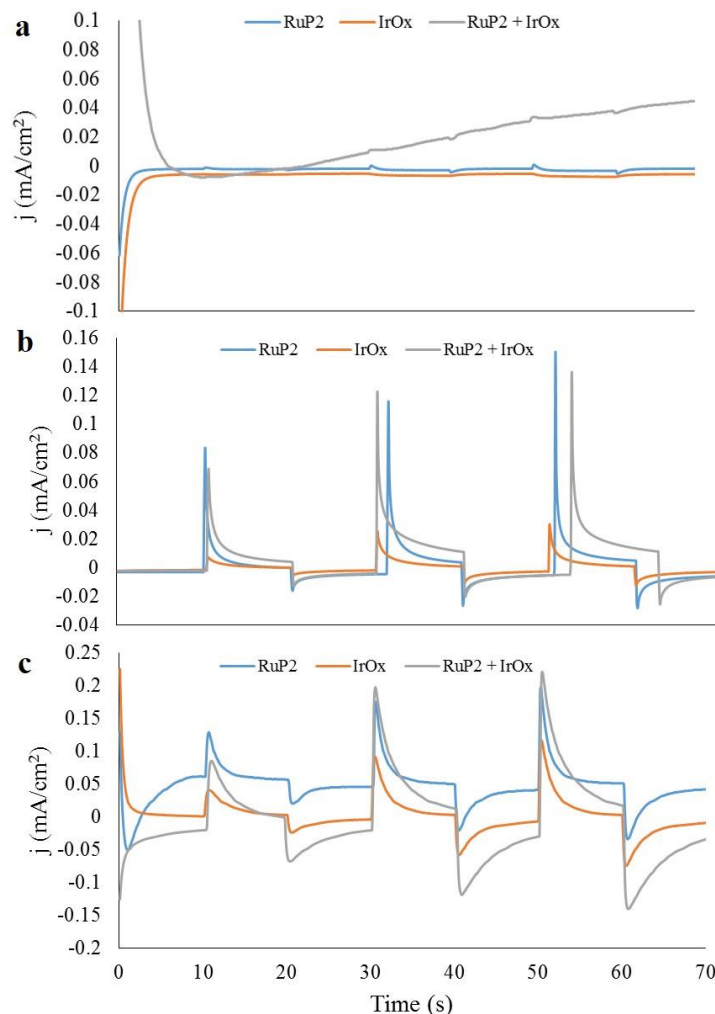
Figure 5.6: Photolysis of the chromophore (RuP_2), catalyst (IrO_X), and chromophore-catalyst assembly (RuP_2,IrO_X) on three difference electrode types: (a) FTO|*nano*ITO, (b) FTO|TiO_2 and (c) FTO|*nano*ITO|TiO_2. In each chart, the traces for RuP_2 alone is in blue, IrO_x alone is in orange and the assembly of the two is in purple. Three different light intensities. 10%, 50% and 100% correspond to 3.4, 14.5 and 23.1 mW/cm^2 at 455 nm, respectively. A potential bias of 0 V vs. Ag/AgCl was applied.

A potential bias study was performed using the FTO|*nano*ITO|TiO_2|RuP_2,IrO_X photoanodes with a 6.7 nm TiO_2 thickness; the results are featured in Figure 5.7. The potential bias ranged from 0 to 0.86 V vs. Ag/AgCl and the potentials are shifted from those discussed in the next section in Figure 5.10 using the Nernst Equation (60 mV/pH). With this photoanode, there is an increase in photocurrent with respect to applied potential, indicating fast electron transfer through the assembly. The potentials reported are all below the onset of water oxidation electrocatalysis via IrO_X NPs, which occurs at ca. 1.35 V vs. Ag/AgCl at pH 1.

140

Figure 5.7: Photocurrent density of the RuP_2-IrO_X NP assemblies on a FTO|*nano*ITO|TiO_2 core/shell electrodes at pH 1 with varied applied potential bias. These values are taken after 90 s of photolysis when illuminated by the Lumencor at 455 nm and 14.5 mW/cm^2. (The photocurrent density is based on the geometric area of the electrode.)

5.3.4   Photolysis of RuP2 and Iridium Oxide Nanoparticle Assemblies at pH 5.8

Photolysis experiments of the individual components and assemblies on various electrodes were also performed in a pH 5.8 solution, comprised of a $NaSiF_6$ and HCO_3 buffer. Photocurrents were significantly higher at this pH, at a potential bias of 0 V vs. Ag/AgCl, due to the Nernstian behavior of the water oxidation reaction. Currrent-time traces as a function of incident light intensity for a FTO|TiO_2|-RuP_2,IrO_x photoanode are shown in Figure 5.8a at an applied bias of 0 V vs. Ag/AgCl, compared to the individual components. Photocurrent data are summarized in Table 5.2. The current comparisons in Figure 5.8a demonstrate significantly enhanced photocurrents for the -RuP_2/IrO_X assembly on TiO_2 compared to -RuP_2 or IrO_X by

Table 5.2: Photocurrent (μA/cm^2) of the RuP_2-IrO_X NP assemblies on three different electrodes in pH 5.8 $NaSiF_6$ solution, illuminated at 450 nm at 14.5 mW/cm^2 with an applied potential bias of 0 V. 50 cycles and 100 cycles refer to 3.7 nm and 6.6 nm thickness of the TiO_2 shell.

	FTO|TiO₂	FTO|*nano*ITO/TiO₂ Core/Shell, 50 cycles	FTO|*nano*ITO|TiO₂ Core/Shell, 100 cycles
IrOₓ NPs	0.27	22	37
RuP₂	6.9	53	27
RuP₂ + IrOₓ NPs	37	88	100

themselves. These data are reported at 0 V vs. Ag/AgCl applied bias as the photocurrent after 10 seconds of photolysis. The photocurrent produced by these assemblies on the mesoporous TiO_2 electrodes is~3 x that reported in previous literature, largely due to the uncapped nature of the iridium oxide nanoparticles.[5-7,10,11,15]

Water oxidation catalysis was confirmed using a two electrode, generator-collector, pseudo-thin cell system (see Figure 5.9). The electrode set-up is described in the experimental section. Using Fc/Fc^+ as a model generator-collector reaction, collection efficiencies of 60-65% were observed. For the FTO|*nano*ITO|TiO_2|RuP_2,IrO_X generator and FTO collector set-up, collection efficiencies of O_2 were between 20-25%, similar to those previously reported.[7,8,10,11,15] Some loss of O_2 between the generator and collector electrodes is expected, as the space between the two electrodes is not sealed at the top and the bottom of the electrodes. As water oxidation catalysis is occurring at a rate where visible bubbles are produced, it is likely that some of these will dislodge and escape through the top of the apparatus before reaching the collector electrode. This would result in a decrease of collection efficiency.
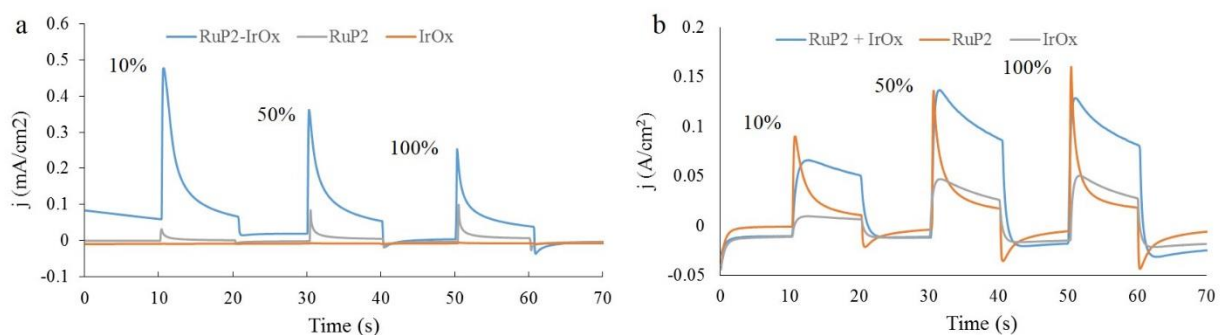
Figure 5.8: Photocurrent measurements of the RuP_2-IrO_X assembly, as well as the individual components. Photocurrents on a TiO_2 mesoporous electrode are featured on the left in (a) and photocurrents on a 100 cycle *nano*ITO/TiO_2 core/shell electrode are on the right in (b). Three different light intensities. 10%, 50% and 100% correspond to 3.4, 14.5 and 23.1 mW/cm^2 at 455 nm, respectively. A potential bias of 0 V vs. Ag/AgCl was applied.
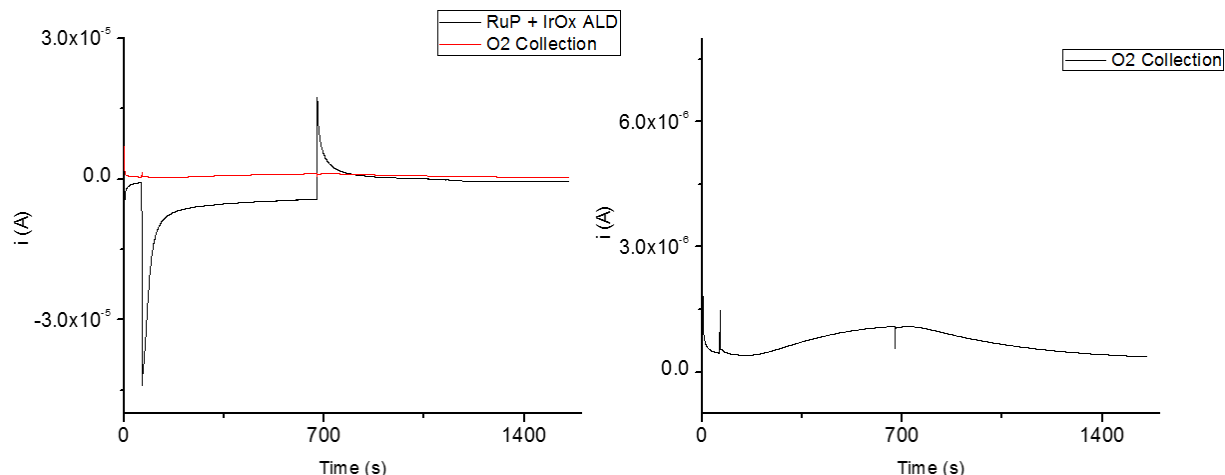
Figure 5.9: O_2 detection using a four electrode set up. On the left, the black trace is WE1 with the RuP-IrO$_x$ assembly and the red trace is the O_2 detection at WE2. The figure on the right is the same O_2 detection from the figure on the left. There is a time delay between when the light is switched on and when O_2 is detected due to the wide spacing between WE1 and WE2. Faradaic efficiencies of 20-25% were observed for these assemblies.

When the RuP$_2$-IrO$_x$ NP assemblies were combined with a nanoITO/TiO$_2$ core/shell electrode, the photocurrent was significantly increased, as seen in Figure 5.8b. This increase in photocurrent is due to the decrease in back electron transfer of the core/shell electrodes, as previously reported.[17] Comparison of these values to that of the undecorated TiO$_2$ mesoporous structure is made in Table 5.2. The increase in photocurrents for the core/shell electrodes is notable, reinforcing related observations in both DSPEC and DSSC applications.[1,17] The origin of the "core/shell" effect is dynamic. Following excitation and injection by the surface bound chromophore – FTO|*nano*ITO|TiO$_2$|-RuP$_2^{2+}$ $\xrightarrow{h\nu}$ FTO|*nano*ITO|TiO$_2$|-RuP$_2^{2+*}$ $\longrightarrow$ FTO|*nano*ITO|TiO$_2$(e$^-$)|-RuP$_2^{3+}$ – rapid transport through the thin TiO$_2$ shell to the conducting *nano*ITO shell provides a basis for electron transfer to the cathode allowing the accumulation of four oxidative equivalents at the catalyst for water oxidation.

Two different TiO$_2$ shell thicknesses were studied at various potentials vs. Ag/AgCl, as reported in Figure 5.10. Significant photocurrent is produced at an applied potential of 0 V vs. Ag/AgCl, with substantial further increases incited by increased applied potential through 0.5 V
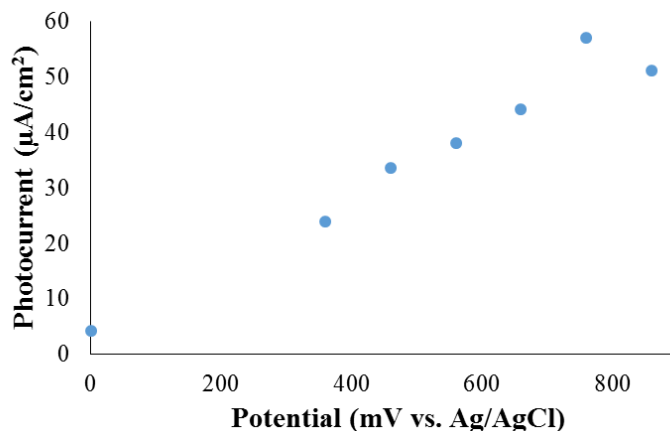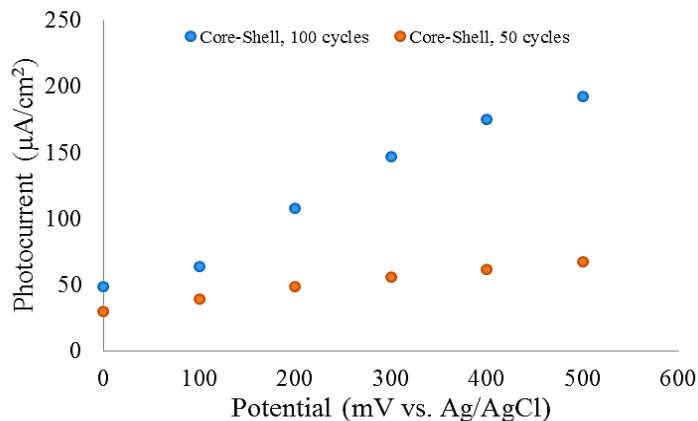
Figure 5.10: Photocurrent density of the RuP$_2$-IrO$_X$ NP assemblies on two different core/shell electrodes at pH 5.8 with varied applied potential. These values are taken after 90 s of photolysis when illuminated by the Lumencor at 455 nm and 14.5 mW/cm^2. (The photocurrent density is based on the geometric area of the electrode.)

vs. Ag/AgCl at pH 5.8. This increase in catalysis with applied potential suggests fast electron transfer throughout the system. As found earlier for related cells, the photocurrent output is dependent on applied bias with the dependence arising, at least in part, from meeting the driving force requirements for H$_2$ evolution at the cathode.[4] It is important to note, at the pH value reported, that these applied potentials are less positive than those producing the onset of direct electrocatalytic water oxidation of the IrO$_X$ NPs (~ 0.9 V vs. Ag/AgCl), i.e., direct electrolysis of water does not occur.

A shell thickness effect is also apparent in the data in Figure 5.10, with enhanced photocurrents observed for the TiO$_2$ shell thickness of 6.7 nm. The extent of photocurrent enhancement is bias dependent, increasing with applied bias, reaching a current enhancement of ~4 at 0.5 V vs. Ag/AgCl. Shell thickness effects in core/shell DSPEC and dye sensitized solar cells (DSSC) have been reported in previous studies.[17,23,25]

The data presented above were obtained on slides that were dipped in the chromophore and catalyst solutions for 1.5 hours each. In order to optimize these assemblies, the dipping time was varied in both the RuP$_2$ and IrO$_X$ NP solutions. Increasing the loading time for RuP$_2$ yielded

positive results, as there was a significant increase in photocurrent. The photocurrents measured at different applied biases for an assembly where the loading time for RuP$_2$ is 24 hours are listed in Table 5.3. Photocurrents up to 655 µA/cm^2 are reported for this assembly. As a comparison, the same assemblies with a 1.5 hr RuP$_2$ loading time only produced up to ~200 µA/cm^2.

Table 5.3: Photocurrent (µA/cm^2) of the RuP$_2$-IrO$_X$ NP assemblies, with a 24 hour loading time for RuP$_2$, in pH 5.8 NaSiF$_6$ solution, illuminated at 455 nm with various light intensities and applied biases. The core/shell electrode has an ALD TiO$_2$ layer that is 6.2 nm in diameter.

Applied Bias (V vs. Ag/AgCl)	Light Intensities (mW/cm^2)		
	3.4	14.5	23.1
0	77.9	164	196
0.3	120	388	542
0.6	119	436	655

Extending the loading time of the IrO$_X$ NPs, however, resulted in a decrease in photocurrent. An assembly with an IrO$_X$ NP loading time of 17 hours yielded photocurrent that was 50% of the photocurrent from an assembly with an IrO$_X$ NP loading time of 1.5 hours. This is likely due to the competing light absorbance from the IrO$_X$ NPs at 455 nm. A smaller percentage of the light is being absorbed by the chromophore, which results in a decrease in photocurrent. Electroflocculation was also explored as a film formation technique for the IrO$_X$ NPs in these assemblies. However, since this technique requires basic solutions as discussed in Chapter 2 and the RuP$_2$ chromophore detaches from the metal oxide surface as the pH approaches 7, electroflocculation was performed before the addition of the chromophore.

For the initial 10 s photolyses, the photocurrent of the electroflocculated assemblies is much less than that of the dip-coated assemblies (2.0 and -2.8 µA/cm^2 compared to 37 µA/cm^2). This indicates that the order of assembly plays a large role in the amount of photocurrent that is produced. When the chromophore is loaded onto the slide first, it is positioned at the metal

oxide semiconductor surface where it can more easily inject excited electrons. If the catalyst is

loaded

Table 5.4: Photocurrent ($\mu A/cm^2$) over time from assemblies of electroflocculated IrO_X NPs and RuP_2, where the arrangement of the photoanode is $FTO|TiO_2|IrO_X,RuP_2$. Two different electroflocculation times were explored, 10 and 20 minutes. The photoanodes were backlit at a 45° angle with a 455 nm LED at 14.5 mW/cm^2. A 0 V vs. Ag/AgCl potential bias was applied in pH 5.8 $NaSiF_6$ buffer.

	Photocurrent ($\mu A/cm^2$)	
Photolysis Time (s)	10 min Electroflocculation + RuP	20 min Electrofloculation + RuP
10	2.0	-2.8
30	0.52	- 0.34
60	0.36	- 0.21
90	0.33	- 0.18

first, such as in the electroflocculated assemblies, it blocks the chromophore from the

semiconductor surface and inhibits electron injection. The decrease in photocurrent from 20

minutes of IrO_X NP electroflocculation compared to 10 minutes of electroflocculation further

demonstrates this effect. Electroflocculating for longer periods of time results in higher coverage

of the semiconductor electrode surface; this further inhibits electron injection from the

chromophore, resulting in a decrease in observed photocurrent.

5.3.5   Atomic Layer Deposition of TiO₂ as Stabilization Technique

Long term photolysis of the FTO|*nano*ITO|TiO₂|RuP₂,IrOₓ assemblies demonstrated a

significant decrease in photocurrent over time. This is suspected to reflect the instability of the

RuP_2 chromophore's immobilization at the higher pH of the $NaSiF_6$ buffer used in these

experiments. As observed earlier for phosphonate-derivatized assemblies on TiO₂, surface

binding is unstable as the pH is increased toward 7 leading to rapid loss from the surface by

hydrolysis.[19,20] Further evidence of this is the loss in color of the slide and the increase in color

of the solution after prolonged photolysis. The Meyer and Hupp laboratories have
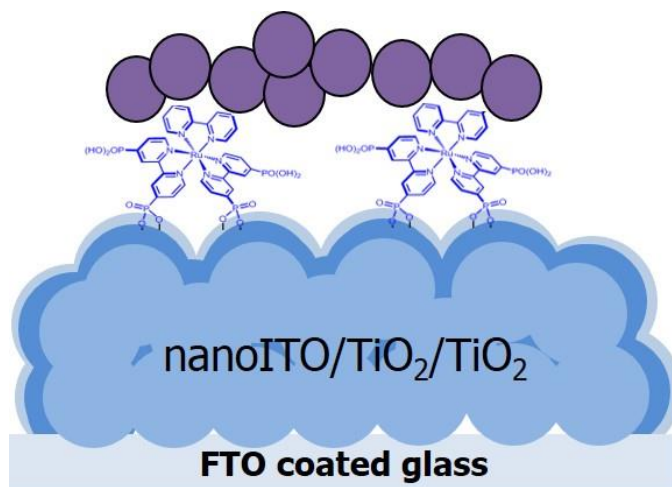
Figure 5.11: A cartoon of the assembly after an additional ALD of ~ 1 nm of TiO_2, represented by the light blue edge of the nanoparticles. This ALD layer is added after the chromophore (RuP2) is adsorbed to the surface, but before the IrO_X NPs are deposited. This creates a protective layer of TiO_2 around the phosphonic acid groups of the chromophore, which anchor the complex to the metal oxide surface.

previously reported on atomic layer deposition (ALD) as a means to stabilize the chromophores

on metal oxide surfaces.[21,24,26,30,31] A cartoon of this ALD stabilization layer on the assembly is

depicted in Figure 5.11. Figure 5.12 presents results that support this finding on the core/shell

electrode with 6.6 nm TiO_2 thickness. The effect of an added 10 cycle TiO_2 overlayer (less than

1 nm in thickness) added to stabilize -RuP_2 before addition of the IrO_x NPs is also shown in

Figure 5.12. After two hours of photolysis with a 300 mV applied bias vs. Ag/AgCl, the

photocurrent from the unstabilized assembly has fallen appreciably, to a level that is well below

that of the dark current (- 97 $\mu A/cm^2$). The stabilized electrode sustains a photocurrent of 110

$\mu A/cm^2$ over the photolysis period, indicating significant improvement in stability. Compared to

the photocurrent obtained from 90 s photolysis at the same potential bias (150 $\mu A/cm^2$), the loss

is significantly decreased with ALD stabilization.
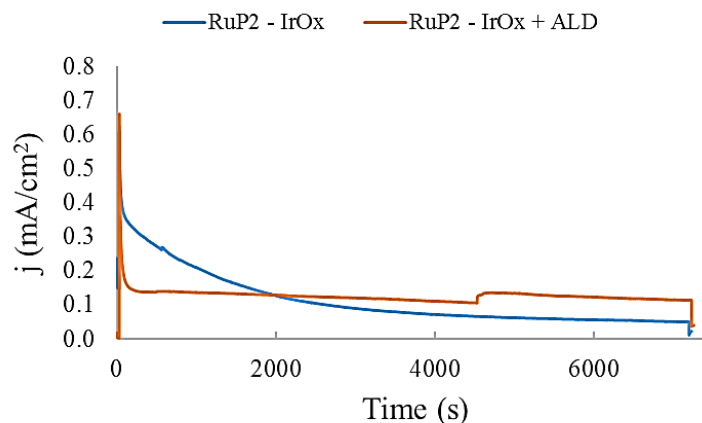
Figure 5.12: Photocurrent densities after 2 hours of photolysis for the RuP_2-IrO_X assemblies on the *nano*ITO/TiO_2 core/shell electrodes (TiO_2 thickness = 6.6 nm) with and with ALD stabilization (10 cycles) were 110 $\mu A/cm^2$ and 97 $\mu A/cm^2$, respectively. Photolysis conditions were at pH 5.8 with an applied potential bias of 300 mV vs. Ag/AgCl, while illuminating at 455 nm and 14.5 mW/cm^2.

A conductive polymer, poly(methacrylic acid) (PMAA), was also tested as a means to stabilize the RuP_2 chromophore in higher pH solutions. A solution of 3% PMAA was applied to the photoanode after RuP_2 loading, but before the slide was dipped in the IrO_X NP solution to load the catalyst. This was then allowed to air dry to form a protective layer. After loading the IrO_x NPs via the dip-coating method, there was no apparent purple color that usually accompanies these films. This suggested that the IrO_X NP did not precipitate onto the PMAA surface. Figure 5.13 is the 10 minute photolysis experiment performed with this assembly. The light was turned on at 60 s, as indicated by the black arrow. There is a slight spike in current when the light is turned on, but no apparent water oxidation catalysis occurs (as indicated by the lack of O_2 detection at the collector electrode). This further supports the theory that the IrO_X NPs do not deposit onto the PMAA surface. This is likely due to the more hydrophobic nature of the polymer, compared to that of TiO_2 and RuP_2.
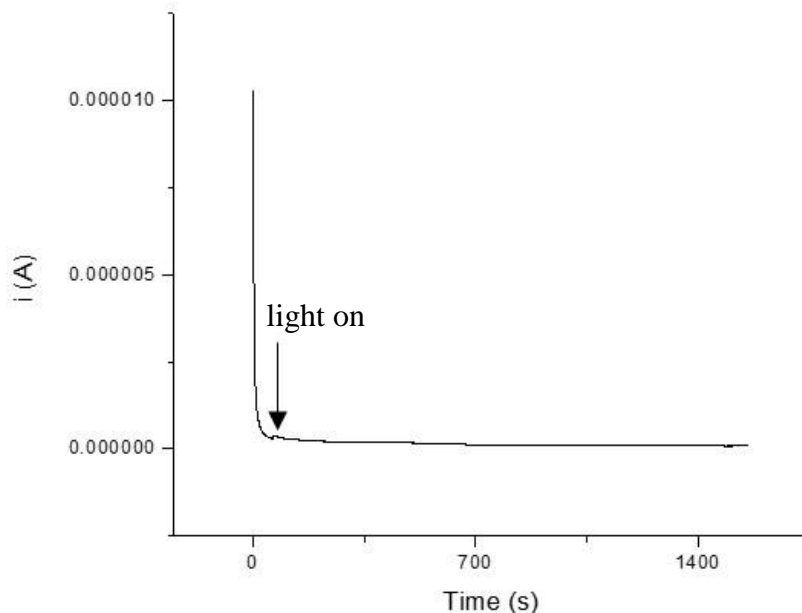
Figure 5.13: Photolysis of PMAA stabilized FTO|nanoITO|TiO_2|RuP_2, IrO_X assembly. The light (455 nm, 14.6 mW/cm^2) is turned on at 60 s, indicated by the arrow. A potential bias of 0.4 V vs. Ag/AgCl was applied in a pH 5.8 NaSiF$_6$ buffer.

5.4   CONCLUSIONS

The results described here are important in building on the earlier results of Mallouk and coworkers on the use of Ru(II) polypyridyl-IrO_x assemblies on semiconductor oxides to achieve visible light water splitting.[7,8,10,11,15] The use of *nano*ITO|TiO_2 core/shell structures results in impressive gains in photocurrent efficiency which increase with applied bias. Long term instability arising from hydrolysis and loss of the chromophore from the surface has been addressed by use of ALD overlayers of TiO_2. With the combination of enhanced efficiencies and surface stabilization this approach to self-assembly based on IrO_x nanoparticles offers promise as a platform for achieving relatively high efficiencies with extensions to chromophores and combinations of chromophores for extending light absorption further into the visible with surface stabilization by ALD.

5.5 **ACKNOWLEDGEMENT**

REFERENCES

(1)   Alibabaei, L.; Brennaman, M. K.; Norris, M. R.; Kalanyan, B.; Wenjing, S.; Losego, M. D.; Concepcion, J. J.; Binstead, R. A.; Parsons, G. N.; Meyer, T. J. *Proceedings of the National Academy of Sciences* **2013**, *110*, 20008.

(2)   Alstrum-Acevedo, J. H.; Brennanman, M. K.; Meyer, T. J. *Inorg. Chem.* **2005**, *44*, 6802

(3)   Meyer, T. J. *Nature Chemistry* **2011**, *3*, 757

(4)   Song, W.; Chen, Z.; Brennanman, M. K.; Concepcion, J. J.; Patrocinio, A. O. T.; Iha, N. Y. M.; Meyer, T. J. *Pure Appl. CHem.* **2011**, *83*, 749.

(5)   Youngblood, J. W.; Lee, S.-H. A.; Kobayashi, Y.; Hernandez-Pagan, E. A.; Hoertz, P. G.; Moore, T. A.; Moore, A. L.; Gust, D.; Mallouk, T. E. *J. Am. Chem. Soc.* **2009**, *131*, 926

(6)   Harriman, A.; Pickering, I. J.; Thomas, J. M.; Christensen, P. A. *J. Chem. Soc., Faraday Trans.* **1988**, *84*, 2795.

(7)   Hoertz, P. G.; Kim, Y. L.; Youngblood, J. W.; Mallouk, T. E. *J. Phys. Chem. B* **2007**, *111*, 6945.

(8)   Morris, N. D.; Suzuki, M.; Mallouk, T. E. *J. Phys. Chem. A* **2004**, *108*, 9115.

(9)   Nakagawa, T.; Beasley, C. A.; Murray, R. W. *J. Phys. Chem. C* **2009**, *113*, 12958

(10)   Zhao, Y.; Hernandez-Pagan, E. A.; Vargas-Barbosa, N. M.; Dysart, J. L.; Mallouk, T. E. *J. Phys. Chem. Lett.* **2011**, *2*, 402

(11)   Zhao, Y.; Vargas-Barbosa, N. M.; Hernandez-Pagan, E. A.; Mallouk, T. E. *Small* **2011**, *7*, 2087

(12)   Blakemore, J. D.; Mara, M. W.; Kushner-Lenhaff, M. N.; Schley, N. D.; Konezny, S. J.; Rivalta, I.; Negre, C. F. A.; Snoeberger, R. C.; Kokhan, O.; Huang, J.; Stickrath, A.; Tran, L. A.; Parr, M. L.; Chen, L. X.; Tiede, D. M.; Batista, V. S.; Crabtree, R. H.; Brudvig, G. W. *Inorg. Chem.* **2013**, *52*, 1860

(13)   Blakemore, J. D.; Schley, N. D.; Kushner-Lenhoff, M. N.; Winter, A. M.; D'Souza, F.; Crabtree, R. H.; Brudvig, G. W. *Inorg Chem.* **2012**, *51*.

(14)   Chuang, M.-C.; Ho, J. A. *RSC Adv.* **2012**, *2*, 4092

(15)   Swierk, J. R.; McCool, N. S.; Saunders, T. P.; Barber, G. D.; Strayer, M. E.; Vargas-Barbosa, N. M.; Mallouk, T. E. *J. Phys. Chem. C.* **2014**, *118*, 17046

(16)   Michaux, K. E.; Murray, R. W. *Langmuir* **2013**, *29*, 12254

(17)   Alibabei, L.; Farnum, B. H.; Kalyanyan, B.; Brennaman, M. K.; Losego, M. D.; Parsons, G. N.; Meyer, T. J. *Nano Letters* **2014**, *14*, 3255

(18)   Hanson, K.; Losego, M. D.; Kalanyan, B.; Asford, D. L.; Parsons, G. N.; Meyer, T. J. *Chemistry of Materials* **2013**, *25*, 3.

(19)   Hanson, K.; Losego, M. D.; Kalanyan, B.; Parsons, G. N.; Meyer, T. J. *Nano Lett* **2013**, *13*, 4802.

(20)   Vannucci, A. K.; Alibabaei, L.; Losego, M. D.; Concepcion, J. J.; Kalanyan, B.; Parsons, G. N.; Meyer, T. J. *Proceedings of the National Academy of Sciences* **2013**, *110*, 20918.

(21)   Jeong, N. C.; Son, H.-J.; Prasittichai, C.; Lee, C. Y.; Jensen, R. A.; Farha, O. K.; Hupp, J. T. *J. Am. Chem. Soc.* **2012**, *134*, 19820

(22)   Katz, M. J.; Vermeer, M. J. D.; Farha, O. K.; Pellin, M. J.; Hupp, J. T. *Langmuir* **2012**, *29*, 806

(23)   Martinson, A. B. F.; Elam, J. W.; Liu, J.; Pellin, M. J.; Marks, T. J.; Hupp, J. T. *Nano Lett.* **2008**, *8*, 2862

(24)   Son, H.-J.; Wang, X.; Prasittichai, C.; Jeong, N. C.; Aaltonen, T.; Gordon, R. G.; Hupp, J. T. *J. Am. Chem. Soc.* **2012**, *134*, 9537

(25)   Williams, V. O.; Jeong, N. C.; Prasittichai, C.; Farha, O. K.; Pellin, M. J.; Hupp, J. T. *ACS Nano* **2012**, *6*, 6185

(26)   Son, H.-J.; Prasittichai, C.; Mondloch, J. E.; Luo, L.; Wu, J.; Kim, D. H.; Farha, O. K.; Hupp, J. T. *J. Am. Chem. Soc.* **2013**, *135*, 11529

(27)   Norris, M. R.; Concepcion, J. J.; Glasson, C. R. K.; Fang, Z.; Lapides, A. M.; Asford, D. L.; Templeton, J. L.; Meyer, T. J. *Inorg. Chem.* **2013**, *52*, 12492.

(28)   Wohler, L.; Witzmann, W. Z. *Anorg. Chem.* **1908**, *57*, 323.

(29)   Gambardella, A. A.; Bjorge, N. S.; Alspaugh, V. K.; Murray, R. W. *J. Phys. Chem. C* **2011**, *115*.

(30)   Kim, D. H.; Losego, M. D.; Hanson, K.; Alibabaei, L.; Lee, K.; Meyer, T. J.; Parsons, G. N. *Physical Chemistry Chemical Physics* **2014**, *16*, 8615.

(31)   Vannucci, A. K.; Alibabaei, L.; Losego, M. D.; Concepcion, J. J.; Kalanyan, B.; Parsons, G. N.; Meyer, T. J. *Proceedings of the National Academy of Sciences* **2013**.

CHAPTER 6: Electrochemical Characterization of Quaterpyridine Ruthenium Complexes for Benzyl Alcohol Oxidation Catalysis

6.1 INTRODUCTION

6.1.1 Molecular Water Oxidation Catalysts

While heterogenous catalysts generally are easier to synthesize, molecular water oxidation catalysts (WOC) have the advantage when it comes to analysis of the mechanism.[1] Furthermore, there are more possibilities for modification of molecular complexes to enhance and promote facile catalysis. As discussed in the introduction, the original catalysts for water oxidation were based upon Photosystem II (PSII), the protein complex responsible for producing oxygen gas (O_2) in photosynthesis.[2] The water is oxidized by manganese ions that are within the complex and are bonded together by μ-oxo bridges.[3] Various mono-, di-, tri- and tetrametallic complexes have been synthesized as catalysts trying to mimic its behavior using ruthenium, manganese, rhodium, osmium and iridium metal centers.[4-8] They have polypyridal ligands, such as bipyridine, tripyridine, and phenanthraline which are good oxidizers, due to their ability to accept electrons in the conjugated π system.[9-17]

Although the majority of WOCs consist of one or two polypyridyl ligands bound to a ruthenium(II) centre with one coordination site free for a water molecule, coordinatively saturated ruthenium WOCs are being discovered.[17-22] Recently Thummel and coworkers reported the complex [Ru(dpp)(pic)$_2$] (dpp = 2,0-di(pyrid-2'-yl)-1,10-phenanthroline), which is active as a WOC in the presence of Ce^{IV}.[17] Studies with a related complex were reported by Lau et al. who demonstrated that the complex [Ru(qpy)(pic)$_2$] (qpy = 2,2':6',2":6",2"'-quaterpyridine) was oxidized in the presence of Ce^{IV} to form a qpy-N,N"'- dioxide complex, which acted as a

water oxidation catalyst.[16] The bis-aqua form of this complex had previously been reported by

Che *et al.* and its properties as an alcohol oxidation catalyst were tested.[23] The three complexes

presented in this chapter are derivatives of this [Ru(qpy)(L)$_2$] complex, as seen in Figure 6.1,

where the L groups in **1** are a chloro (Cl) and acetonitrile (MeCN), in **2**, both L groups are

MeCN and in **3**, the ligands are vinyl pyridine (VP). Their electrochemistry is presented in the

results and discussion below, which shows their potential as water oxidation catalysts.

6.1.2 Benzyl Alcohol Oxidation Catalysis
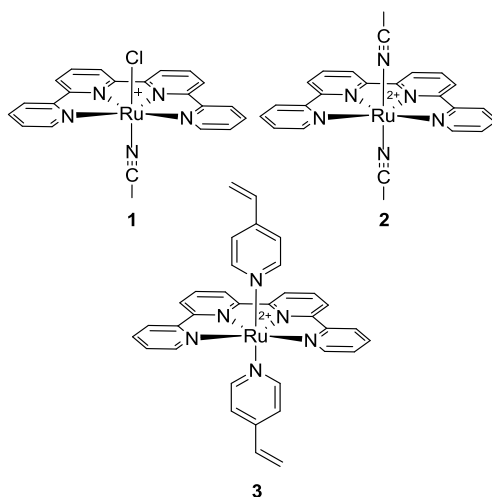
Figure 6.1: Structures of the three quaterpyridine complexes studied. In **1**, L = Cl, MeCN. In **2**, L = MeCN. In **3**, L = vinyl pyridine (VP).

One way of probing the mechanism for water oxidation via a homogeneous, molecular

catalyst is to investigate its properties as a benzyl alcohol oxidation catalyst.[24-28] Benzyl alcohol

(BnOH) is a readily oxidized compound that can undergo a two electron, two proton oxidation to

benzaldehyde. There is also the possibility of over-oxidizing the substrate to benzoic acid, which

would require another two electron, two proton reaction. This is analogous to water oxidation,

another four electron, four proton reaction. Many research groups, in particular the Meyer and

Hill laboratories, have used this reaction as a probe to study the intermediates of water oxidation

catalysts, largely polypyridal Ru based complexes.[25-29] Polypyridal Ru complexes have shown to be effective catalysts for the oxidation of alcohols, aldehydes, ketones, diols and aromatics hydrocarbons.[29-41] The extensive use of these complexes in mechanistic studies is largely due to their coordinative stability and their formation of stable intermediates at high oxidation states.[40]

These oxidations were found to be predominately second order and this rate constant, k_{cat}, dependent on a wide variety of factors, including solvent, electrolyte and ligand substitution on the catalyst.[27,35,36] Depending on conditions, the mechanism of BnOH oxidation catalysis varies, undergoing either a 1 or 2 electron (e^-) pathway. In water, the mechanism is believed to be a 2 e^- process, involving a hydride transfer step, seen in Scheme 6.4. There is no trend correlated between redox couple of the catalyst and rate of benzyl alcohol oxidation.[26] Additionally, derivitizing the aromatic ring of the benzyl alcohol substrates demonstrated little change in rate.[27] The Hill group found that there is a steric effect on rate of oxidation of benzylic alcohols via $[Ru(trpy)(4,4'-Me_2dppi)(OH_2)]^{2+}$ [4,4'-dppi = 3,6-di-(4-methylpyrid-2-yl) pyridazine], as adding carbon substituents on the benzylic carbon resulted in a decreased catalytic rate. This suggests that the rate determining step is the pre-association of the alcohol with the catalyst, as opposed to electron transfer.[26,27] A general mechanism for this reaction with a Ru polypyridal complex is presented below in Scheme 6.4.

Scheme 6.4

$$Ru^{IV}=O^{2+} + HC(OH)Ph \rightarrow Ru^{IV}=O^{2+}, HC(OH)Ph$$

$$Ru^{IV}=O^{2+}, HC(OH)Ph \rightarrow [Ru^{IV}=O\cdots H\cdots C(OH)Ph]^{2+} \rightarrow Ru^{II}\text{-}OH^+, PhCOH^+$$

$$Ru^{II}\text{-}OH^+, PhCOH^+ \rightarrow Ru^{II}OH_2 + PhC=O$$
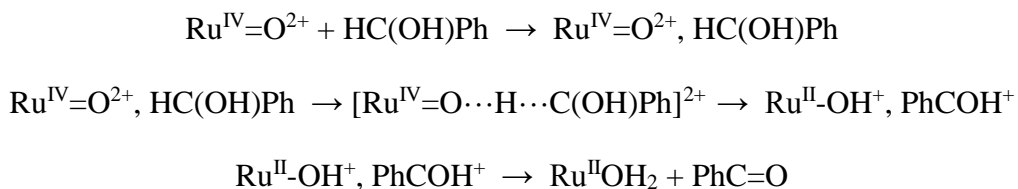
The Meyer lab has also demonstrated that BnOH oxidation can occur with

[Ru(Mebimpy)(bpy)(OH$_2$)]$^{2+}$ (Mebimpy = 2,6-bis(1-methylbenziidazol-2-yl)-pyridine; bpy =

2,2'-bipyridine) via four different intermediates, Ru^{IV}=O^{2+}, Ru^{IV}(OH)$^{3+}$, Ru^{V}=O^{3+} and

Ru^{V}(OO)$^{3+}$.[28] The Ru^{IV}=O^{2+} mechanism is accessible in higher pH solutions and undergoes a

similar mechanism to Scheme 6.4. The Ru^{IV}(OH)$^{3+}$ and Ru^{V}(OO)$^{3+}$ pathways are accessible in

lower pH solutions (pH 5, compared to > pH 9), with the Ru^{V}(OO)$^{3+}$ pathway yielding a higher

rate by a factor of two. The Ru^{V}(OO)$^{3+}$ intermediate would be reduced to Ru^{III}(OOH)$^{2+}$ upon

oxidation of BnOH, as seen in Scheme 6.5. It is hypothesized that it also undergoes a hydride

transfer mechanism, as with the Ru^{IV}=O^{2+} intermediates. BnOH oxidation catalysis occurring

from four different pathways of the same catalyst is important to note as it indicates that

mechanistic and kinetic studies may not be as simple as expected. This is especially true when

dealing with chemical oxidants, such as cerium ammonium nitrate (CAN), rather than direct

electrolysis, where multiple oxidation states of the catalyst may be coexisting.

Scheme 6.5

$$Ru^{V}(OO)^{3+} + PhCHOH \rightarrow Ru^{III}(OOH)^{2+} + PhCHO + H^+$$

Work also performed by the Meyer lab has recently proposed a base-catalyzed pathway for

BnOH oxidation catalysis using [Ru(Mebimpy)(bpy)(OH$_2$)]$^{2+}$, after exploring the effect of the

concentration of the buffer present on the rate of catalysis.[25] As opposed to proton coupled

electron transfers (PCET) noted above, this mechanism suggests concerted hydride proton

transfer (HPT) is occurring with the help of the base present in solution. This suggests that

performing these oxidations in solutions with higher pH may facilitate catalysis.

Initial BnOH oxidation catalysis studies for the three complexes in Figure 6.1 are presented in this chapter, as well as kinetic studies of BnOH oxidation catalysis via complex **1** and long term bulk electrolyses.

6.2   EXPERIMENTAL

6.2.1   Synthesis of the ruthenium quaterpyridine ligand and [Ru(qpy)$_2$(Cl)$_2$] complex

The ligand qpy[42] and the complex [Ru(qpy)$_2$(Cl)$_2$][43] were prepared according to literature procedures. [RuCl$_3$], dry solvents from Sigma Aldrich and chromatography solvents from Fisher Chemicals were all used as received. Size exclusion chromatography was carried out using Sephadex LH-20.

6.2.2   Synthesis of Complex 1

[Ru(qpy)(CH$_3$CN)Cl][BF$_4$] (**1**). Sixty mg (0.12 mmol) of [Ru(qpy)$_2$(Cl)$_2$] and 24.2 mg (1 eq., 0.12 mmol) of AgBF$_4$ were put into a flask, equipped with a stir bar, and evacuated and refilled with N$_2$ three times. Following addition of 15 mL dry acetonitrile the reaction was heated at reflux overnight. The solution was cooled to room temperature, filtered and the solvent removed *in vacuo*. The complex was purified using size exclusion chromatography with 1:1 acetonitrile:H$_2$O as eluent. The purple fraction was collected and dried yielding a purple powder. Yield: 35 mg, 49.0 %.

6.2.3   Synthesis of Complex 2

[Ru(qpy)(CH$_3$CN)$_2$][BF$_4$]$_2$ (**2**). Sixty mg (0.12 mmol) [Ru(qpy)$_2$(Cl)$_2$] and 55 mg (excess, 0.28 mmol) AgBF$_4$ were put into a flask equipped with a stir bar, and evacuated and refilled with N$_2$ three times. Following addition of 15 mL of dry acetonitrile, the reaction was heated at reflux overnight. The solution was cooled to room temperature, filtered and the solvent removed *in vacuo*. The complex was purified using size exclusion chromatography with 1:1 acetonitrile:H$_2$O

as eluent. The second fraction from the column was collected and the solvent removed *in vacuo* affording a dark red powder. Yield: 53.0 mg, 83.2 %

6.2.4 Synthesis of Complex 3

[Ru(qpy)(VP)$_2$][Cl]$_2$ (**3**). Sixty mg (0.12 mmol) [Ru(qpy)$_2$(Cl)$_2$] and 0.65 mL (50 eq., 6.0 mmol, 654 mg) vinyl pyridine were heated at reflux in 10 mL ethanol and 3 mL H$_2$O for 2 days. The reaction was then allowed to cool to room temperature and the solvent removed *in vacuo*. The resulting solid was dissolved in 1:1 methanol:H$_2$O and purified using size exclusion chromatography with 1:1 methanol:H$_2$O as the eluent. The dark purple fraction was collected and the solvent removed *in vacuo* affording a dark purple powder. Yield: 60.0 mg, 73.4%

6.2.5 Electrochemical experimental setup

Cyclic voltammetry was performed on a CH Instruments 660a potentiostat, using a conventional three electrode setup consisting of either a glassy carbon (GC) or boron doped diamond (BDD) working electrode, platinum wire auxiliary electrode and 3 M Ag/AgCl (BASi) reference electrode. 1 mM solutions of each complex in acetonitrile were used for these experiments, with 0.1 M tetrabutylammonium hexafluorophosphate (TBAPF$_6$) as supporting electrolyte. For the aqueous electrochemical measurements, a 1 mM solution of each complex was prepared in 0.1 M trifluoroacetic acid (TFA).

For the kinetic studies of benzyl alcohol oxidation, cyclic voltammetry was performed on 0.1 M TFA solutions with low concentrations of the catalyst (1 mM, 0.5 mM, 250 μM, 125 μM, 67.5 μM and 33.8 μM) and 20 mM benzyl alcohol in order to achieve a limiting current.

Bulk electrolyses were originally performed in 0.1 M TFA solutions, with 0.5 mM of each catalyst and 20 mM benzyl alcohol. A three electrode setup was used, where the working electrode (*nano*ITO on a FTO coated glass slide) was separated from the auxiliary electrode (Pt

wire) and reference electrode (3 M Ag/AgCl) via a fine frit. The electrolyte was later switched

to 0.1 M HClO$_4$ when it was discovered that the TFA electrochemically etched the *nano*ITO

surface when the potential was held oxidatively. Each bulk electrolysis lasted 13 hours and the

concentrations of the reactant (benzyl alcohol) and product (benzaldehyde) were detected using

gas chromatography.
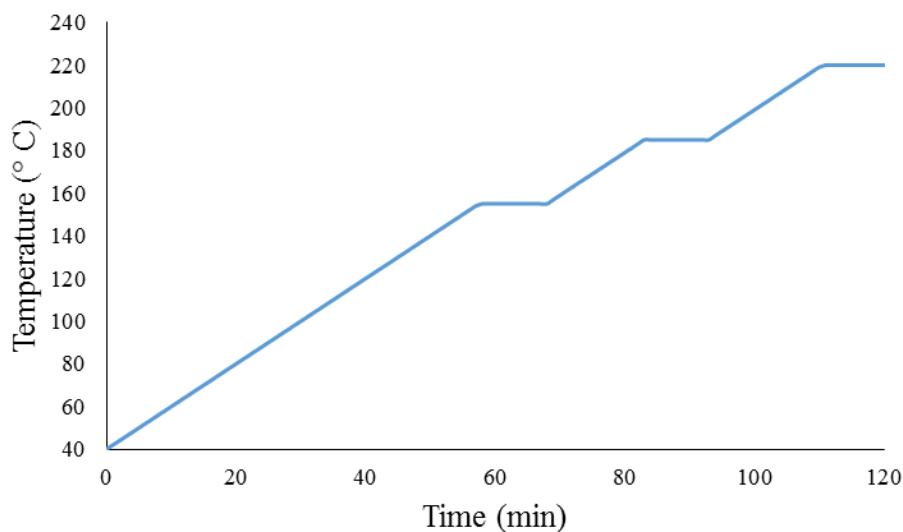
Figure 6.2: Heating program for GC detection of benzyl alcohol and benzaldehyde.

6.2.6   Detection of benzyl alcohol and benzaldehyde via Gas Chromatography

A Shimadzu GC-2014 gas chromatopgraph was used to detect the reactant and product of

the bulk electrolyses. The program used is shown in Figure 6.2, where the temperature is paused

twice just below the boiling point of benzaldehyde and benzyl alcohol. Two peaks are observed

in the typical gas chromatograph, one at 39 min and one at 60 min, corresponding to

benzaldehyde and benzyl alcohol, respectively.

6.3   RESULTS AND DISCUSSION

6.3.1   Electrochemistry of Ru(qpy)L$_2$ in Acetonitrile

As expected, all three complexes exhibited a Ru$^{II/III}$ redox couple in acetonitrile; the data

159

is summarized in Table 6.1 and depicted inFigure 6.3. For complexes **1** and **2** the redox wave was fully reversible and the potential of **1** was more negative than that of **2** due to the electron withdrawing nature of the chloride ligand.

Table 6.1: Formal potential of each of Complexes **1**, **2** and **3** in 0.1 M TBAPF$_6$ and MeCN.

Complex	Auxilary Ligands	E$_{1/2}$ (V vs. Ag/AgCl)
1	MeCN, Cl	0.898
2	MeCN	1.333
3	VP	0.956

Complex **3** exhibited behavior of an EC' reaction, where after the electrochemical oxidation of **3**, a chemical reaction, likely the polymerization of the vinyl ligands, immediately follows. Because of this, the voltammetry of **3** is irreversible, particularly at slower scan rates. A film is also observed on the electrode surface after multiple scans, which is further indication of polymerization on the electrode surface.
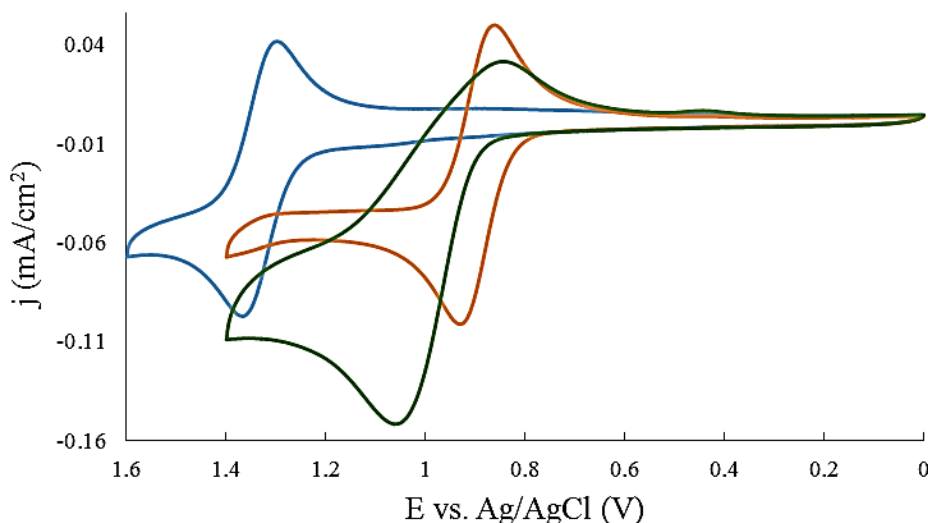

Figure 6.3: Cyclic voltammetry of complexes 1 (orange), 2 (blue) and 3 (green) in 0.1 M TBAPF$_6$ and MeCN, at 10 mV/s.

160

6.3.2 Electrochemistry of Ru(qpy)L₂ in Aqueous Media

Upon dissolution of **1** in 0.1M TFA solution three redox couples were observed in the cyclic voltammogram, Figure 6.4, which is evidence for the exchange of the acetonitrile ligand for an aquo ligand. These couples were assigned to $Ru^{II/III}$, $Ru^{III/IV}$ and $Ru^{IV/V}$ and the $E_{1/2}$ values are reported in Table 6.2. The potential for the $Ru^{II/III}$ couple has decreased by 320 mV compared to the measurement in acetonitrile. The exchange of the acetonitrile ligand for the aquo, combined with the low $Ru^{IV/V}$ redox potential indicates that this complex has the potential to act as a water oxidation catalyst.

Table 6.2: $E_{1/2}$ values for the aqueous electrochemistry of Complexes **1, 2,** and **3** in 0.1 M TFA.

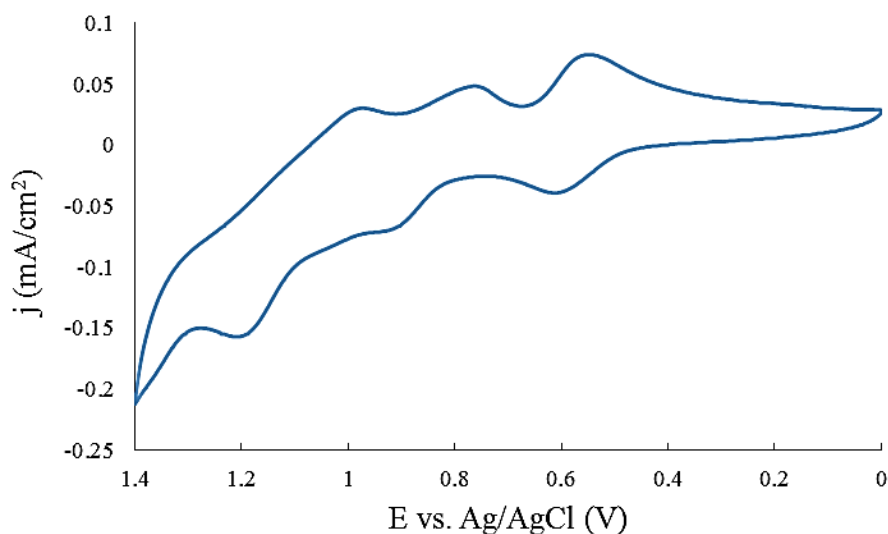| Complex | $E_{1/2}$ (V vs. Ag/AgCl) | | | |
	$Ru^{II/III}$	$Ru^{III/IV}$	$Ru^{IV/V}$	Vinyl Polymerization
1	0.578	0.874	1.092	
2	0.586	0.816	1.093	
3	0.975			0.54

Figure 6.4: Cyclic voltammetry of 1 in 0.1 M TFA at 25 mV/s.

Three redox couples are also observed for **2** in 0.1 M TFA solution, as seen in Figure 6.5. However, the cyclic voltammogram of the complex changes with each scan, with a shift in the $Ru^{V/IV}$ redox couple. In the return reduction of this couple, E_{peak} shifts more negative over time, likely due to the difficulty in exchanging two acetonitrile ligands for two water ligands. We propose that with each sequential scan a small amount of the bis-acetonitrile complex is converted into the bis-aquo complex and it is this that causes the CVs to look different with each scan. After 20 scans, the CV of **2** in 0.1 M TFA closely resembles the CV of Che *et al.*'s reported $[Ru(qpy)(OH_2)_2]$ complex[44], which gives confidence to this hypothesis.

The $E_{1/2}$ of **3** in 0.1 M TFA shows no change in aqueous media, when compared to the CV measured in MeCN. However, the peak appears more reversible than that of the complex in MeCN. This indicates that the MeCN is a likely co-participant in the polymerization of the vinyl ligand. Some polymerization is still observed in aqueous media, as observed by the peak that appears at 0.54 V vs Ag/AgCl in Figure 6.6. To try to reduce the polymerization on the GC electrode, a boron doped diamond (BDD) electrode was implemented as a working electrode (Figure 6.6). This effectively eliminated the appearance of the peak at 0.5 V and also reduced
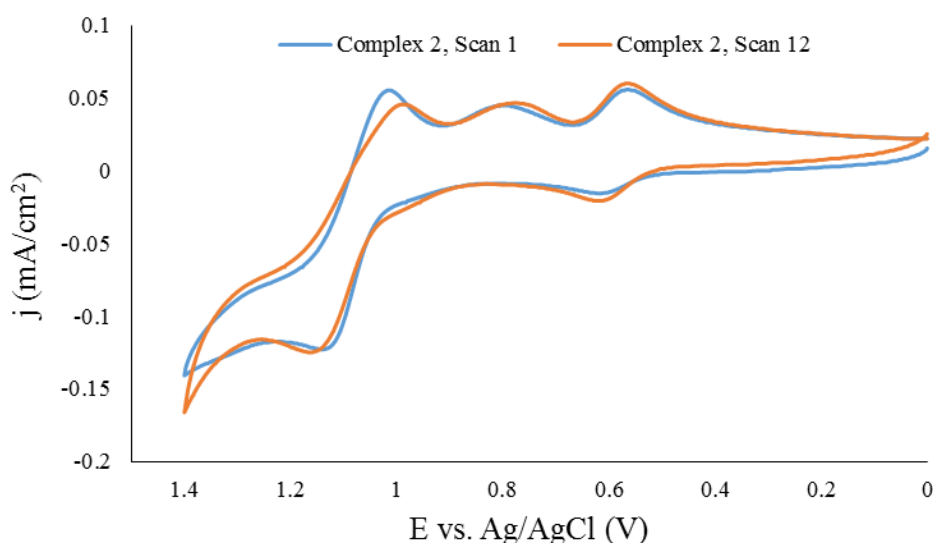

Figure 6.5: Cyclic voltammetry of Comlex **2** in 0.1 M TFA at 25 mV/s. Scan 1 is in blue and scan 12 is in orange. The CVs change over time due to MeCN exchange with H_2O.

162

the non-faradaic current observed. This is largely due to the nature of the surface of a BDD

electrode, compared to that of GC. While the surface of a GC electrode contains functional

groups ready for polymerization, that of the BDD electrode is considered to benign.[45] However,

as it is not possible to observe any oxidation states higher than the Ru^{III}, we do not expect this

complex to be an active catalyst for water oxidation or benzyl alcohol oxidation.
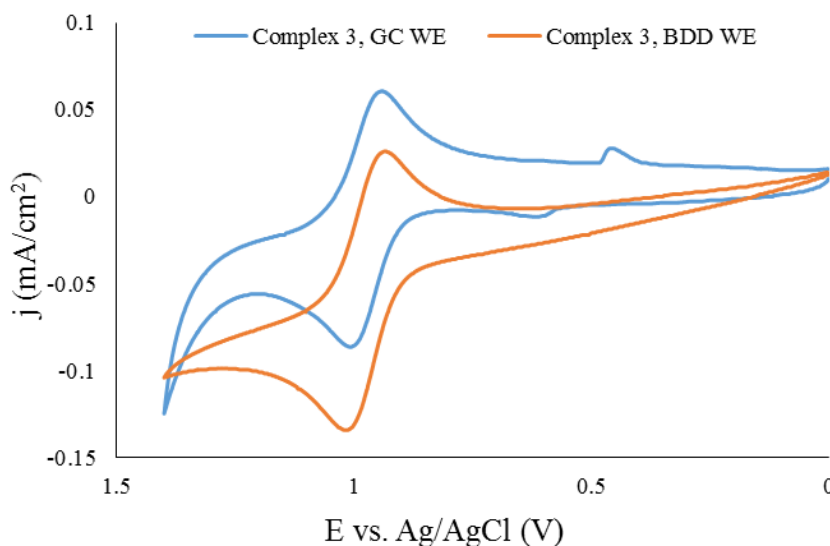

Figure 6.6: Cyclic voltammetry of Complex 3 in 0.1 M TFA. The blue curve corresponds to the GC
working electrode, where higher rates of polymerization are observed (the peak formation at 0.5 V). The orange
curve corresponds to the BDD working electrode, which observes no polymerization of the catalyst.

6.3.3 Addition of Benzyl Alcohol to Aqueous Ru(qpy)L₂ Solutions

20 mM benzyl alcohol was added to the aqueous solutions of each complex; the results

can be seen in Figure 6.7. Both Complex 1 Figure 6.7(a) and Complex 2 Figure 6.7(b) exhibit a

significant increase in oxidative current, with an onset potential of 1.2 V vs. Ag/AgCl. This is an

indication that catalysis of benzyl alcohol oxidation is occurring. For Complex **1**, the catalytic

current is saturated at 20 mM BnOH with 1 mM **1**, likely to due to the saturation of the alcohol-

complex association. There is virtually no change in the CV of Complex **3** with the addition of

BnOH, supporting the hypothesis that the lack of access to higher oxidation states of Ru inhibits

163

catalysis. Due to the changing nature of the cyclic voltammetry of Complex **2**, kinetic studies were only explored on Complex **1**.

The first approach for determining the rate constant of benzyl alcohol oxidation catalysis was to explore the relationship of i_c/i_p with respect to scan rate, as has been done frequently in the literature.[25,28] This is based on Equation 6-1, below, and the results are shown in Figure 6.8.

Equation 6-1

$$\frac{i_c}{i_p} = 2.24 \frac{n_c}{n_p} \sqrt{\frac{RT}{n_p F}} \sqrt{\frac{1}{v}} \sqrt{k_{obs}}$$

In this equation, i_c, i_p, n_c, n_p, R, T, F, v and k_{obs} correspond to the catalytic current, the peak current for a particular redox couple, the number of electrons for the catalytic reaction, the number of electrons for the redox couple mentioned for i_p, the gas constant, temperature, Faraday's constant, scan rate and the observed rate constant. The relationship between i_c/i_p and $v^{-1/2}$ is clearly not linear, as seen in Figure 6.8, largely due to the lack of steady state current in catalysis. This exponential relationship also suggests that the reaction is not first order. Three different applied potentials (1.3, 1.4 and 1.5 V vs. Ag/AgCl) were explored using this method. k_{obs} values of 320, 3800 and 7500 s^{-1} were found for each potential, respectively. While the higher potentials saw significantly higher rates of catalysis, it is likely that a competing reaction, water oxidation catalysis, is also occurring at this potentials, resulting in a falsely increased rate.

In order to compensate for the second order nature of the catalysis, Equation 6.2 was utilized, which takes the concentration of both the catalyst (C_O) and analyte (C_S) into consideration. In this equation, n, F, A, C_O, D, k_{cat} and C_S correspond to the number of electrons, Faraday's constant, the area of the electrode, concentration of the catalyst, diffusion coefficient of the catalyst, catalytic rate constant and concentration of the analyte, respectively. The catalytic rate
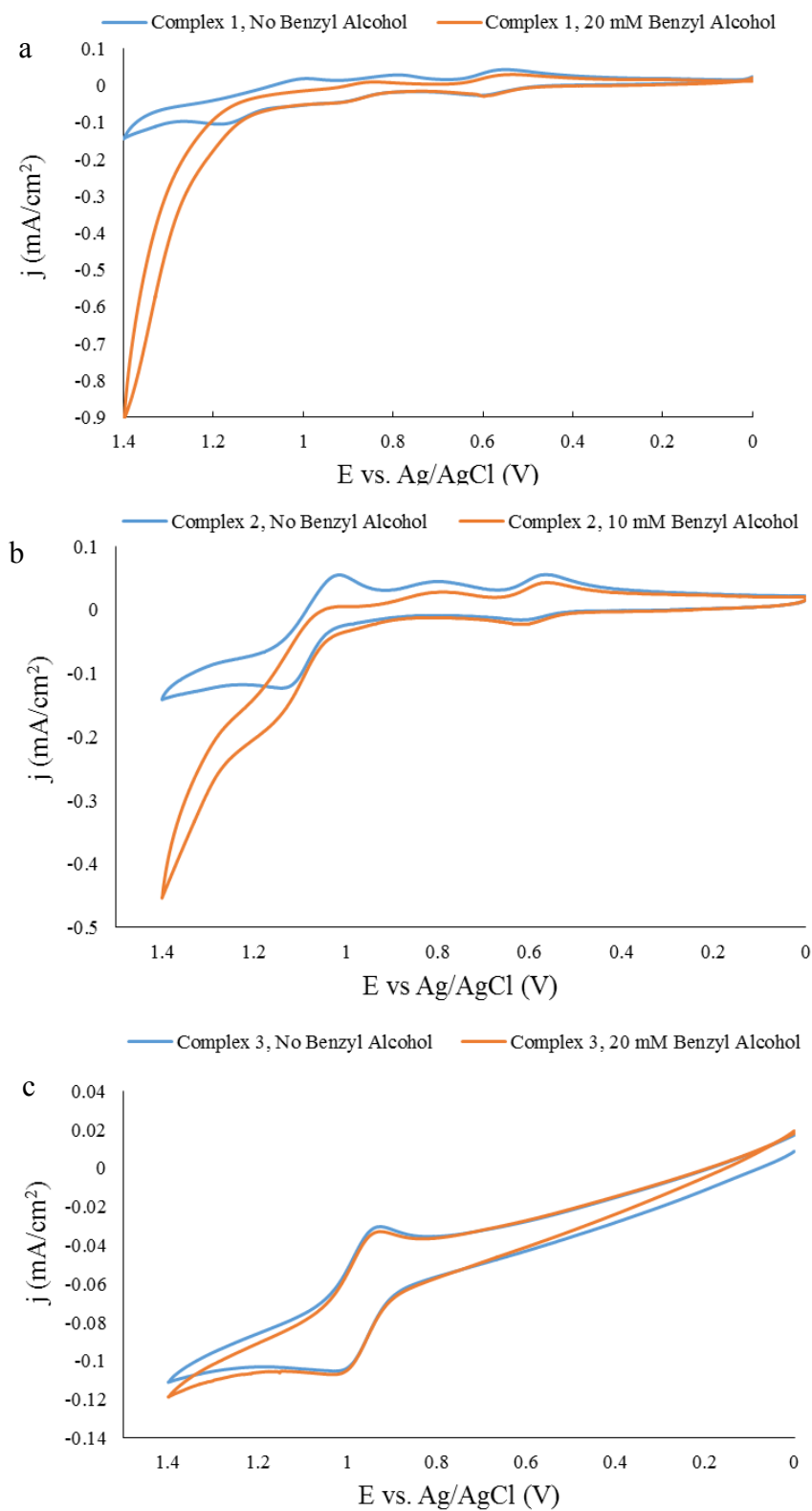
Figure 6.7: Cyclic voltammetry of Complexes **1** (a), **2** (b) and **3** (c) in 0.1 M TFA, without (blue) and with (orange) benzyl alcohol.
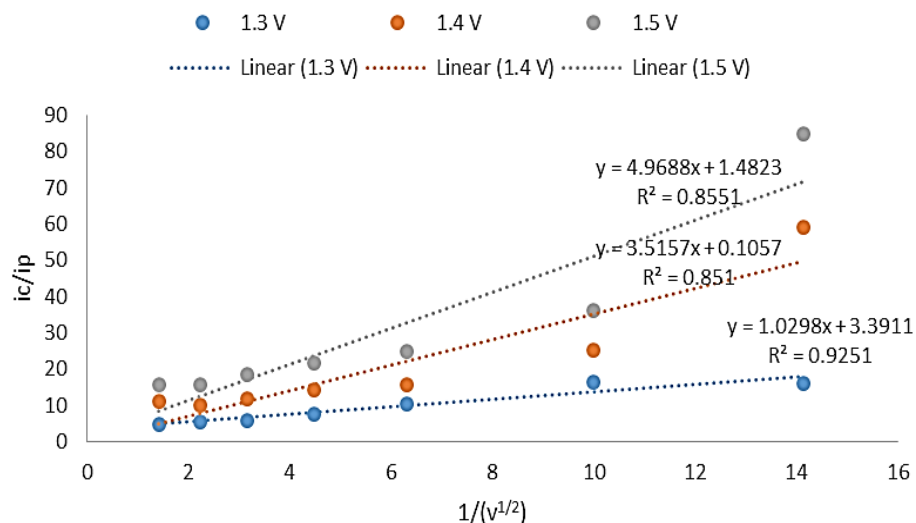
165

Figure 6.8: Plot of i_c/i_p vs. $v^{-1/2}$ for Complex **1** in 0.1 M TFA with 20 mM benzyl alcohol. CVs were performed using a BDD working electrode, Pt auxiliary electrode and Ag/AgCl reference electrode. Three different potentials were reported, each vs. Ag/AgCl. The k_{obs} derived from each potential was 320 s^{-1}, 3800 s^{-1} and 7500 s^{-1}, respectively.

constant (k_{cat}) derived from this equation is a second order rate constant with units of M^{-1}s^{-1}, provided that C_O is expressed in units of mol/cm^3 and C_S in M.

Equation 6-2

$$i_L = nFAC_O(Dk_{cat}C_S)^{1/2}$$

To find k_{cat}, a limiting current (i_L) for the catalysis reaction was needed. In order to obtain this information, very low concentrations of catalyst (discussed earlier in the experimental section) and slow scan rates (5 mV/s) were implemented. CVs of the low concentrations of catalyst with 20 mM benzyl alcohol are seen in Figure 5.9a. The ca. linear relationship between concentration of Complex **1** (C_O) and the limiting current (i_L) is depictred in Figure 5.9b. Linearity ceases at concentrations higher than 0.25 M Complex **1**, due to the lack of observed limiting current. The rate constant (k_{cat}) determined using Equation 6.2 was 470 M^{-1} s^{-1}. This is significantly higher
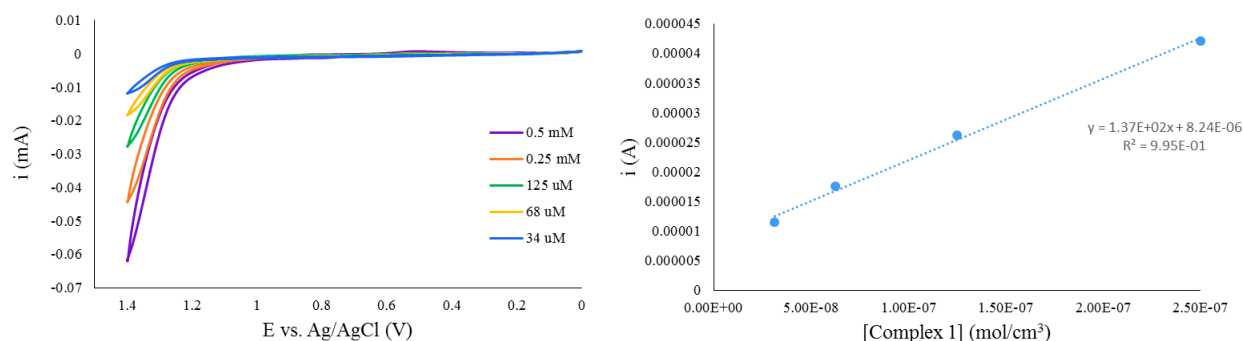
Figure 6.9: (a) Cyclic voltammetry of low concentrations of Complex **1** and 20 mM benzyl alcohol. (b) The linear relationship between the concentration of the catalyst, Complex **1,** and the limiting current.

than previous literature, where most catalytic rate constants were one to two orders of magnitude smaller.[24-26,28,29,36]

6.3.4 Bulk Electrolysis of Ru(qpy)(CH₃CN)(Cl) with Benzyl Alcohol

Bulk electrolyses of Complex **1** with 20 mM benzyl alcohol were performed in order to determine the efficiency of this process. Originally, the bulk electrolyses were performed under the same conditions as the voltammetry reported above (0.1 M TFA), with the substitution of a high surface area *nano*ITO electrode for the working electrode. However, low current efficiencies were observed (2-4%). It was determined that the source of current was the electrochemical etching of the *nano*ITO by the TFA electrolyte. The electrolyte was then switched to 0.1 M HClO₄, which resulted in a decrease in solubility of Complex **1**. To compensate for this, 20% MeCN was added to the solution. A bulk electrolysis at 1.25 V vs. Ag/AgCl yielded 1.8×10^{-5} mol of benzaldehyde with faradaic efficiency of 98%. As this is around the onset potential of catalysis, low turnover is expected, but the high faradaic efficiency is promising that the primary reaction occurring at this potential is the oxidation of benzyl alcohol.
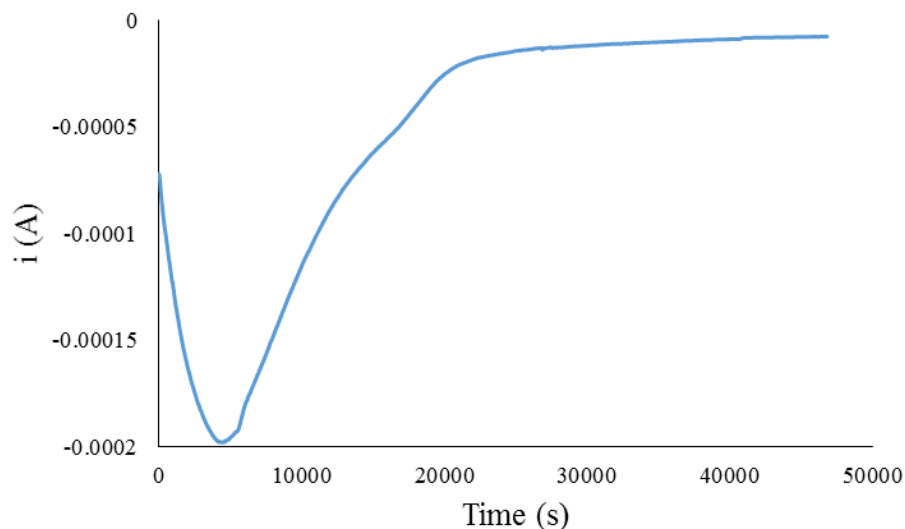
167

Figure 6.10: Chronoampergram of a bulk electrolyses of **Complex 1** and benzyl alcohol in 0.1 M HClO$_4$ and 20% MeCN, where the potential was held at 1.4 V vs. Ag/AgCl for 13 hours. *nano*ITO on FTO coated glass was used as a working electrode, with a Pt auxiliary electrode and 3 M Ag/AgCl reference electrode.

However, bulk electrolyses at higher potentials (> 1.3 V), seem to pose a dilemma in terms of current efficiency. As seen in Table 6.3, the calculated current efficiencies for the bulk electrolyses at 1.3 and 1.4 V were 136 and 182%, respectively. The gas chromatographs for these electrolyses showed complete conversion of benzyl alcohol to benzaldehyde and/or other products, such as benzoic acid. However, the charge from the bulk electrolyses suggested much lower yields of product. At these potentials, it appears that the benzyl alcohol was oxidized via non-electrochemical methods. One hypothesis for this might be oxidation via the electrolyte HClO$_4$, which is a known oxidant of organic compounds.[169]

Upon further inspection of the chronoamperograms such as in Figure 6.10, the current for the higher potential bulk electrolyses follows a unique pattern. There is a sudden increase in current for a short period of time and then the current decays away. This suggests that the electrode is becoming passivated in some way. Comparing the solutions before and after electrolysis, , the color changes from pink to orange, indicating possible decomposition of the catalyst during the bulk electrolysis. Furthermore, the *nano*ITO electrode has an orange film deposited onto the

168

Table 6.3: Current efficiencies of bulk electrolyses at various potentials.

	Potential Applied vs. Ag/AgCl		
	1.25 V	1.3 V	1.4 V
Current Efficiency	98%	136%	182%

surface, presumably the product of this reaction. This film deposition could explain the passivation of the electrode during electrolysis.

6.4 CONCLUSION

The electrochemical characterization of three $[Ru(qpy)L_2]^{+2}$ complexes is reported as well as the initial kinetic studies of benzyl alcohol oxidation via $[Ru(qpy)(MeCN)(Cl)]^+$. In MeCN, one redox couple is observed for each complex, corresponding to the $Ru^{III/II}$ couple. Under acidic aqueous conditions, the MeCN ligands are exchanged for aqua groups, resulting in the accessibility of higher oxidation states of Ru, suggesting a possible water oxidation catalyst. Benzyl alcohol oxidation catalysis was observed for $[Ru(qpy)(MeCN)(Cl)]^+$, with a high rate constant of 470 M^{-1} s^{-1}. At low potentials, high selectivity for this reaction is observed. At high
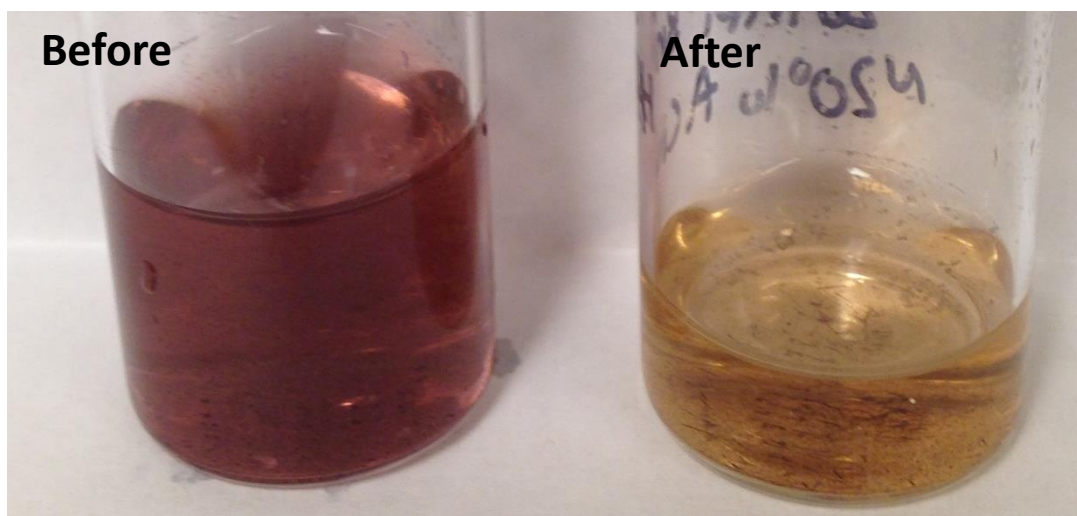

Figure 6.11: Complex **1** in 0.1 M HClO$_4$ and 20% MeCN before (left) and after (right) bulk electrolysis. The complex undergoes a color change from pink to orange, indicating the catalyst may be decomposing.

potentials, the catalyst may experience decay and other methods of benzyl alcohol oxidation may also occur.

6.5 ACKNOWLEDGEMENT

REFERENCES

(1)   Dau, H.; Limber, C.; Reier, T.; Rish, M.; Roggan, S.; Strasser, P. *Chem Cat. Chm.* **2010,** 2, 724.

(2)   Walter, M. G.; Warren, E. L.; McKone, J. R.; Boettcher, S. W.; Mi, Q.; Santori, E. A.; Lewis, N. S. *Chem. Rev.* **2010**, 110, 6446.

(3)   Saveant, J.-M. *Chem. Rev.* **2008**, 108.2348.

(4)   Blakemore, J. D.; Schley, N. D.; Olack, G. W.; Incarvito, C. D.; Brudvig, G. W.; Crabtree, R. H. *Chem. Sci.* **2011**, 2, 94.

(5)   Chen, Z.; Concepcion, J. J.; Meyer, T. J. *Dalton Trans.* **2010**, 40, 3789.

(6)   Jurss, J. W.; Concepcion, J. J.; Norris, M. R.; Templeton, J. L.; Meyer, T. J.; *Inorg. Chem.* **2010**, 49, 3980.

(7)   White, T. A.; Whitaker, B. N.; Brewer, K. J. *J. Am. Chem. Soc.* **2011,** 133, 15332.

(8)   White, T. A.; Knoll, J. D.; Arachchige, S. M.; Brewer, K. J. *Materials* **2012**, 5, 27.

(9)   Sala, X.; Poater, A.; Romero, I.; Rodriguez, M.; Llobet, A.; Solans, X.; Parella, T.; Santos, T. M. *Eur. J. Inorg. Chem.* **2004**, 612.

(10)   Zong, R.; Wang, B.; Thummel, R. P. *Inorg. Chem* **2012**, 42, 8385.

(11)   Sens, C.; Rodriguez, M. Romero, I.; Llobet, A. *Inorg. Chem.* **2003,** 42, 8385

(12)   Chanda, N.; Mondal, B,; Puranik, V. G.; Lahiri, G. K. *Polyhedron,* **2002**, 21, 2033.

(13)   Dobson, J. C.; Meyer, T. J. *Inorg Chem.***1986**, 27 3283

(14)   Che, C.-M.; Wong, K.-Y.; Leung, W.-H.; Poon, C.-K. *Inorg. Chem.* **1986**, 25, 345

(15)   Che, C.-M.; Wong, K.-Y.; Lee, W.-O. *J. Electroanal. Chem.* **1991,** 309, 303.

(16)   Liu, Y.; Ng, S.-M.; Yiu, S. M.; Lam, W. W. Y.; Wei, X.-G.; Lau, K.-C.; Lau, T. C.; *Angew. Chem. Int. Ed.* **2014,** 53, 14468.

(17)   Muckerman, J. T. ; Kowalczyk, M.; Badiei, Y. M.; Polyanksy, D. E.; Concepcion, J. J.; Zong, R.; Thummel, R. P.; Fujita, E.; *Inorg. Chem.* **2014**, 53, 6904.

(18)   Duan, L.; Bozoglian, F. Mandal, S.; Steward, B.; Privalov, T.; Llobet, A.; Sun, L. *Nat. Chem.* **2012,** 4, 418.

(19)   Duan, L.; Araujo, C. M.; Ahlgust, M. S. G.; Sun, L. *Proc. Nat. Acad. Sci.* **2012,** 109, 15584.

(20)   Staehle, R.; Tong, L.; Wang, L.; Duan, L.; Fischer, A.; Ahlquist, M. S. G.; Sun, L. Rau, S. *Inorg, Chem.* **2014**, 53, 1307.

(21)   Deng, Z.; Tseng, H. W.; Zong, R.; Wang, D.; Thummel, R.. *Inorg. Chem*, **2008**, 47, 1835.

(22)   Kaveevivitchai, N; Kohler, L.; Zong, R.; El Ojaimi, M.; Mehta, N.; Thummel, R. P. *Inorg Chem.* **2013**, 52, 10615.

(23)   Chan, C. W.; Lai, T. F.; Chen, C. M.; *J. Am. Chem. Soc. Dalton Transactions.***1994**, 6, 895

(24)   Guadalupe, A. R.; Chen, X.; Sullivan, B. P.; Meyer, T. J. *Inorg. Chem.* **1993**, 32, 5502.

(25)   Paul, A.; Hull, J. F.; Norris, M. R.; Chen, Z; Ess, D. H.; Concepcion, J. J.; Meyer, T. J. *Inorg. Chem.* **2011**, 50, 1167.

(26)   Catalano, V. J; Heck, R. A.; Ohman, A.; Hill, M. G. *Polyhedron*, **2000**, *19,* 1049.

(27)   Catalano, V. J.; Heck, R. A.; Immoss, C. E.; Ohman, A; Hill, M. G. *Inorg. Chem.* **1998**, 37, 2150.

(28)   Vannucci, A. K.; Hull, J. F>; Chen, Z.; Beinstead, R. A.; Concepcion, J. J.; Meyer, T. J. *J. Am. Chem. Soc.* **2012**, 134, 3972.

(29)   Kutner, W.; Meyer, T. J.; Murray, R. W. *J. Electroanal. Chem.* **1985**, 195, 375.

(30)   Li, C. K; Tnag, W. T.; Chen, Cm. M.; Wong, K. Y.; Wang R. J.; Mak, T. C. W. *J Chem. Soc. Dalton Trans.***1991**, 1909.

(31)   Sussuchi, E. M; de Lima, A. A.; de Giovani, W. F.   *J Molecular Catalysis A; Chemical* **2006,** 259, 302.

(32)   Geneste, F.; Moinet, C. *New. J. Chem.***2004**, 28, 722.

(33)   Roecker, L.; Meyer, T. J *J. Am. Chem. Soc.***1987**, 109, 746.

(34)   Meyer, T. J. *J. Electroanal. Chem. Soc.***1984**, 131, 221C.

(35)   Thompson, M. S.; Meyer, T. J. *J. Am Chem. Soc.* **1982**, 104, 5070.

(36)   Navarro, M.; de Giovani, W. F.; Romero, J. R.; *J. of Molecular Catalysis A; Chemical* **1998**, 135, 249.

(37)   Zhou, X. T.; Ji, H. B.; Liu, S. G. *Tetrahedron Letters* **2013**, 19, 1563.

(38)   Ohzu, S.; Ishizuka, T.; Hirai, Y.; Fukuzumi, S.; Kojima, T. *Chem. Eur. J.* **2013,** 19, 1563.

(39)   Thompson, M. S.; de Giovani, W. F.; Moyer, B. A.; Meyer, T. J. *J. Org. Chem.* **1984**, 49, 4972.

(40)   Sook, W. K.; Meyer, T. J. *J. Am Chem. Soc.* **1988**, 110, 7358.

(41)   Thompson, M. S.; Meyers, T. J.; *J. Am. Chem. Soc*, **1982**, 104, 4106.

(42)   Hu. Y. Z.; Xiang, Q.; Thummel, R. P. *Inorg, Chem.* **2002,** 41, 3423.

(43)   Zong, R.; Wang, B.; Thummel, R. P. *Inorg. Chem.* **2012,** 5, 51.

(44)   Chan, C. W.; Lai, T. F.; Che, C. M. *J. Chem. Soc. Dalton Trans.* **1994**, 895.

(45)   Luong, J. H. T.; Male, K. B.; Glennon, J. D. *Analyst* **2009**, 134, 1965.

(46)   Committee, A. M. *Analyst* **1959**, 84. 214.